Institut für Geodäsie und Geoinformation der Universität Bonn

Professur für Astronomische, Physikalische und Mathematische Geodäsie

Enhancing Numerical Simulation of Mass Density in Earth's Upper Atmosphere using Data Assimilation

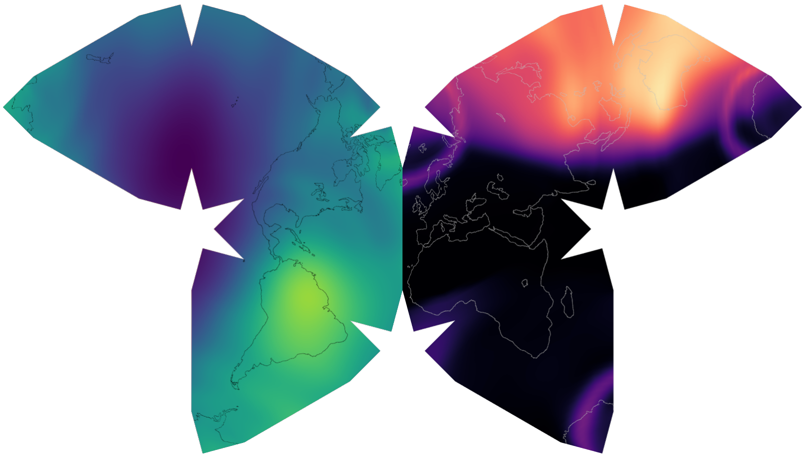

Dissertation
zur Erlangung des Grades
Doktor der Ingenieurwissenschaften (Dr.-Ing.)
der Agrar-, Ernährungs- und Ingenieurwissenschaftlichen Fakultät
der Rheinischen Friedrich-Wilhelms-Universität Bonn

von
Armin Corbin
aus Aachen

Bonn 2025

Referent: Prof. Dr.-Ing. Jürgen Kusche (Universität Bonn)
Korreferent: Prof. Dr.-Ing. Michael Schmidt (DGFI - TU München)
Korreferent: Prof. Dr. Yuri Shprits (GFZ Potsdam)

Tag der mündlichen Prüfung: 1st July 2025
Angefertigt mit Genehmigung der Agrar-, Ernährungs- und Ingenieurwissenschaftlichen Fakultät der Universität Bonn

Front cover picture: The output of the TIE-GCM is visualized using the Waterman butterfly projection. The left wing indicates the mass density and the right wing the electron number density for 10 April 2010 at about 200 km altitude.

Abstract

The atmosphere's mass density is variable in space and time and directly proportional to atmospheric drag, which decelerates all objects in the atmosphere. Thus, the mass density should be specified with high accuracy and precision for applications depending on atmospheric drag acceleration, such as precise orbit determination, satellite lifetime assessment, and satellite re-entry prediction. The lower a satellite's orbit, the larger the atmospheric drag. Thus, atmospheric drag is especially of concern for low-Earth orbiting satellites. The mass density is not directly observed along satellite orbits but is simulated by physics-based numerical or empirical models. Numerical models providing the mass density suffer from simplifications, assumptions, discretization, uncertain parameters, idealized external forcings with limited temporal resolution, and unrealistic boundary conditions. Thus, the mass density predictions of numerical models show significant differences compared to other models and observations. Data assimilation is the combination of observations and models, taking into account their uncertainties. Several studies demonstrated that data assimilation enhances the prediction skills of numerical atmosphere models. However, data assimilation experiments require significant computational resources and typically cover only periods lasting a few days. In addition, the uncertainty of the model forecasts is tailored to the specific conditions of the assimilation experiment and is not transferable to other periods. Moreover, spurious correlations in the model covariances often require localization, which limits the improvements of the models to the vicinity of the sparse observations. Here, I implement a new assimilation system for the Thermosphere Ionosphere Electrodynamics General Circulation Model using the Parallel Data Assimilation Framework to address those limitations. Time-variable perturbations of the model inputs allow a realistic representation of the model's uncertainty. They reduce spurious long-range correlations in the model covariances and adapt to the time-variable conditions in the Earth's space environment. The assimilation of accelerometer-derived mass densities enhanced the models' prediction skills globally in three about two-week-long validation periods covering solar minimum and maximum conditions, quiet times, and geomagnetic storms. As semi-empirical atmosphere models represent a harmonized collection of a substantial record of observations, it is much more straightforward to assimilate their output instead of assimilating the corresponding observations separately. This approach corrected the model's mass density estimation during geomagnetic quiet conditions. As the physical and chemical processes within the atmosphere couple the electron number density and the mass density, the assimilation of one can correct the estimate of the other. However, the assimilation of electron number densities from an empirical model did not improve the mass density prediction compared to accelerometer-derived mass densities. Co-estimation of model parameters enables the correction of model dynamics. Here, a single parameter, the Joule heating factor, was co-estimated. The default Joule heating factor was found to fit well with the corresponding period.

Zusammenfassung

Die Massendichte der Atmosphäre ist zeitlich und räumlich variabel und dirket proportional zum Luftwiderstand, der alle Objekte in der Atmosphäre abbremst. Daher muss die Massendichte für Anwendungen, die von der Beschleunigung durch den atmosphärischen Luftwiderstand abhängen, wie z. B. die genaue Bestimmung der Umlaufbahn, die Ermittlung der Lebensdauer von Satelliten und die Vorhersage des Wiedereintritts von Satelliten, mit hoher Genauigkeit und Präzision vorgegeben werden. Je niedriger die Umlaufbahn eines Satelliten ist, desto größer ist der Luftwiderstand. Daher ist der Luftwiderstand besonders für Satelliten in niedrigen Erdumlaufbahnen von Bedeutung. Die Massendichte wird nicht direkt entlang der Satellitenbahnen beobachtet, sondern stammt aus Simulationen physikalisch basierter numerischer oder empirischer Modelle. Die Genauigkeit numerische Modelle, die die Massendichte simulieren, wird durch Vereinfachungen, Annahmen, Diskretisierung, unsicheren Parametern, idealisierten externen Kräften mit begrenzter zeitlicher Auflösung und unrealistischen Randbedingungen limitiert. Daher weisen die Massendichtesimulationen numerischer Modelle im Vergleich zu anderen Modellen und Beobachtungen erhebliche Unterschiede auf. Datenassimilation ist die Kombination von Beobachtungen und Modellen unter Berücksichtigung ihrer Unsicherheiten. Mehrere Studien haben gezeigt, dass die Datenassimilation die Vorhersagefähigkeiten von numerischen Atmosphärenmodellen verbessert. Allerdings erfordern Datenassimilierungsexperimente erhebliche Rechenressourcen und decken in der Regel nur Zeiträume von wenigen Tagen ab. Darüber hinaus ist die Unsicherheit der Modellvorhersagen auf die spezifischen Bedingungen des Assimilationsexperiments zugeschnitten und nicht auf andere Zeiträume übertragbar. Außerdem erfordern Scheinkorrelationen in den Modellkovarianzen oft eine Lokalisierung, die die Verbesserungen auf die Umgebung der spärlichen Beobachtungen beschränkt. Daher, implementiere ich ein neues Assimilationssystem für das Thermosphere Ionosphere Electrodynamics General Circulation Model unter Verwendung vom Parallel Data Assimilation Framework, um diese Einschränkungen zu beheben. Zeitvariable Störungen der Modelleingaben sorgen für eine realistische Darstellung der Modellunsicherheit. Sie reduzieren störende langreichweitige Korrelationen in den Modellkovarianzen und passen sich den zeitvariablen Bedingungen in der Weltraumumgebung der Erde an. Die Assimilation der von Beschleunigungsmessern abgeleiteten Massendichten verbesserte die Vorhersagefähigkeiten der Modelle weltweit in drei etwa zweiwöchigen Validierungsperioden, die solare Minima und Maxima, ruhige Zeiten und geomagnetische Stürme abdeckten. Da halb-empirische Atmosphärenmodelle eine harmonisierte Sammlung einer beträchtlichen Anzahl von Beobachtungen darstellen, ist es viel einfacher, ihre Ergebnisse zu assimilieren, anstatt die entsprechenden Beobachtungen separat zu assimilieren. Mit diesem Ansatz wurde die Schätzung der Massendichte des Modells während geomagnetisch ruhiger Bedingungen korrigiert. Da die physikalischen und chemischen Prozesse in der Atmosphäre die Elektronenzahldichte und die Massendichte koppeln, kann die Assimilation der einen Dichte die Schätzung der anderen

Dichte korrigieren. Die Assimilation von Elektronenzahldichten aus einem empirischen Modell konnte jedoch die Massendichteabschätzung im Vergleich zu den aus Beschleunigungssonden abgeleiteten Massensichten nicht verbessern. Das Mitschätzen von Modellparametern ermöglicht die Korrektur der Modelldynamik. Hier wurde ein einziger Parameter, ein Faktor für das Stromwärmegesetz, mitgeschätzt. Es zeigte sich, dass der Standardwert bereits gut zum entsprechenden Zeitraum passte.

Acknowledgments

This thesis was written at the Institute of Geodesy and Geoinformation within the Astronomical, Physical and Mathematical Geodesy Group, which offers great conditions–especially nice colleagues–for writing a thesis. Over the years, many people have supported me and made this thesis possible. I want to thank my supervisor Prof. Dr.-Ing. Jürgen Kusche who gave me a lot of freedom in my research without losing sight of the overall goal. I want to thank my referees Prof. Dr. Yuri Shprits and Prof. Dr.-Ing. Michael Schmidt.

I thank Dr. rer. nat. Lars Nerger for his continuous PDAF support, answering many questions related to data assimilation and proofreading the chapter on data assimilation. My colleague Dr.-Ing. Kristin Vielberg contributed to this thesis by providing the accelerometer-derived mass densities, many fruitful discussions, and proofreading the aeronomy section and model chapter. I thank Prof. Dr. tech. Wolf-Dieter Schuh for discussing covariance functions on several occasions.

I appreciate that my brother Dr. rer. nat. Gregor Corbin proofread the chapter about aerodynamics, Dr.-Ing. Anno Löcher proofread the chapter about observations, Dr. rer. nat. Benjamin D. Gutknecht proofread the space weather and aeronomy chapter, M.Sc. Kerstin Schulze proofread the chapter about the implementation, and Dr.-Ing. Helena Gerdener proofread the chapter about the experiments. I am thankful for M.Sc. Anna Verwey and M.A. Janick Patschorke for their feedback on the introduction.

TIE-GCM PDAF ran on many different clusters during its development until it found a home on *Marvin* (University Bonn). The development would not have been possible without the other clusters: *LWFHPC-1* (Landwirtschaftliche Fakultät University of Bonn), *Bonna* (University of Bonn), *JUREACA* (Jülich Supercomputing Centre), and *Noctua 2* (Paderborn Center for Parallel Computing).

This thesis was enabled by funding from the German Research Foundation (DFG): the TIPOD Project (Development of high-precision Thermosphere models for Improving Precise Orbit Determination of Low-Earth-Orbiting satellites) within the DFG SPP 1788 Dynamic Earth and the DFG Research Unit MIPT (Magnetosphere, Ionosphere, Plasmasphere and Thermosphere, as a coupled system).

Many open source software was used for this thesis. Without the open source licenses of the PDAF and TIE-GCM this thesis could never been written. This document itself was created using LaTeX. The figures were created with the help of Ti*k*Z, PGFPLOTS, matplotlib, cartopy, inkscape, gnuplot, and blender. A first look at the results was often done via Panoply, which is a great tool for inspecting NetCDF files. The code was compiled using the GNU compiler collection.

I really appreciate my parents' (Ricarda and Georg) and siblings' (Dagmar and Gregor) encouragement and interest in my work.

Contents

Symbols

Aerodynamics

$\boldsymbol{C}_a$	aerodynamic coefficient 51–53
C_A	axial force coefficient 52, 53, 61
b	ballistic coefficient 56
L	characteristic length 50, 51
C_D	drag coefficient 52, 53, 55, 56
q_∞	freestream dynamic pressure 52, 53
ρ_∞	freestream mass density 51, 52, 61
$\boldsymbol{v}_\infty$	freestream velocity 51–53, 55, 61
K	Knudsen number 50, 51
C_L	lift force coefficient 52, 53
S	molecular speed ratio 55
A	reference area 51–53, 56, 61

Aeronomy

n	amount of substance 12–14
N_A	Avogadro constant ($6.022\,14 \times 10^{23}\,\mathrm{mol}^{-1}$) 13–15
k_B	Boltzmann constant ($1.380\,65 \times 10^{-23}\,\mathrm{J\,K}^{-1}$) 14, 15, ii
H_C	density scale height 15, 16, iii
g	gravitational acceleration 15–17, 73, i, ii, v–vii
B	magnetic flux density 122, 125
m	mass 12–14, 52, 56, 61
ρ	mass concentration, mass density 5, 13–15, 56, 68, 110, 121, 123, 132, 133, 139, 154, i, ii, v, vi
w	mass fraction 12–15, 55, 71, 110, 121, 123, 131, 140, 146, 151
$\overline{m}$	mean mass of a gas mixture 14, 15, ii
$\overline{M}$	mean molar mass of a gas mixture 14, 15, 17, 68, v, vi
x	molar fraction, number fraction 13, 14
R	molar gas constant ($8.314\,\mathrm{J\,mol}^{-1}\,\mathrm{K}^{-1}$) 15, 17, 55, 110, v, vi
M	molar mass 13–15, 55, 110
C	number concentration, number density 13–15, 68, 71, 121, 123, 146, ii–iv
N	particle number 12–14
p	pressure 14, 15, 110, i, ii, v, vi
H	pressure scale height 15, 16, ii–iv

T	temperature 14, 15, 17, 55, 68, 71, 110, 121, 123, 131, 140, 146, 151, ii–vi
V	volume 12–14

Data assimilation

$\boldsymbol{z}$	augmented state vector 95
n_y	dimension of the observation vector 84, 88
n_x	dimension of the state vector 83, 84, 88, 89, 91, 92, 123
$\boldsymbol{c}$	dynamics vector, calibration parameters 95
$\boldsymbol{L}$	ensemble in error subspace 91, 92, 95
$\boldsymbol{X}$	ensemble matrix contataining ensemble members in columns 88–92, 94–96, x, xi
$\boldsymbol{S}$	ensemble perturbation matrix in observation space 89, 90, x–xii
$\boldsymbol{d}$	innovation 86, 88, 90, 92, 95
$\boldsymbol{K}$	Kalman matrix 86, 88, ix–xi
$\boldsymbol{M}$	linearized model operator 84, 85, 88
$\boldsymbol{H}$	linearized observation operator 84–86, 88–90, 92, 95, vii–xi
$\boldsymbol{\eta}$	model error 83, 85, 86
$\mathcal{M}$	model operator 83–86
n_e	number of ensemble members 88–92, 95, 101, 104, 123, x–xii
$\boldsymbol{\varepsilon}$	observation error 84, 85
$\mathcal{H}$	observation operator 84–86, 88, 110, 141
$\boldsymbol{y}$	observation vector 84, 86, 88, 141, vii–ix
$\boldsymbol{\xi}$	state error 85
$\boldsymbol{x}$	state vector 83–86, 88–90, 94, 95, 110, 141, vii–ix
$\boldsymbol{T}$	transform matrix 90, 92, 95, xi, xii
$\boldsymbol{F}$	variance covariance matrix of innovation 89, 90, xi, xii
$\boldsymbol{Q}$	variance covariance matrix of model error 85
$\boldsymbol{R}$	variance covariance matrix of observations 85, 86, 88–90, 92, 95, 139–141, vii–xii
$\boldsymbol{P}$	variance covariance matrix of the state 85, 86, 88–90, 93, 95, vii–xi
$\overline{\boldsymbol{w}}$	weights for updating ensemble mean 89, 90, 92, 94, 95
$\hat{\boldsymbol{W}}$	weights for updating ensemble perturbations 89, 90, 92, 94, 95

Earth

$R_\oplus^{eq}$	Earth radius at equator (semi major axis of ellipsoid) xxxi
$R_\oplus$	mean Earth radius (sphere with same volume) 17, 112, vii, xxx–xxxii
$\mu_\oplus$	standard gravitational parameter of Earth (Gravitational constant times mass) 56, vi, vii

Matrix algebra

$\mathbb{1}$	identity matrix 86, 89–92, 95, viii–xii
$\boldsymbol{I}$	vector/matrix containing only ones 82, 91

Height systems

z	geometric height 17, vii

W	geopotential 16, vi, vii
$H_{\mathbf{pot}}$	geopotential height 16, 17, v–vii
C	geopotential number 16, v, vii

Acronyms

CDF	cumulative distribution function 40, 78
CHAMP	Challenging Minisatellite Payload 5, 8, 61, 62, 65, 75, 76, 98–101, 113–115, 118, 127–133, 135–139, 144, 145, 149, 151–159
CIR	corotating interaction region 3, 4, 33
CME	coronal mass ejection 3, 4, 33
CTIPe	Coupled Thermosphere Ionosphere Plasmasphere Electrodynamics 76, 99, 101, 102
DART	Data Assimilation Research Testbed 99, 101
DORIS	Doppler Orbitography and Radiopositioning Integrated by Satellite 62
DTM	Drag Temperature Model 68, 74–76
EAKF	Ensemble Adjustment Kalman Filter 101
EKF	Extended Kalman Filter 86, 88
EnKF	Ensemble Kalman Filter 89, 101, 102
ESA	European Space Agency 2, 161
ESTKF	Error-Subspace Transform Kalman Filter 77, 91–95, 97, 98, 101, 131, 135, 140, 146, 151, 157, 158
ETKF	Ensemble Transform Kalman Filter 90–92
EUV	extreme ultraviolet 19, 22, 24–28, 31, 67, 70, 83, xiii, xiv
FUV	far ultraviolet 28
GCRS	geocentric celestial reference system 99, xxix
GITM	Global Ionosphere Thermosphere Model 99–101
GNSS	global navigation satellite system 62, 65, 146
GPS	Global Positioning System 61, 99, 101
GRACE	Gravity Recovery And Climate Experiment 8, 61, 62, 65, 75, 76, 98–102, 127–130, 132, 133, 135–139, 144, 145, 149, 152, 154–159, 161
GRACE-FO	Gravity Recovery And Climate Experiment-Follow On 41, 62, 65, 76, 145, 161
GSE	geocentric solar ecliptic 34, 35, 107, xxix, xxx
GSM	geocentric solar magnetospheric 39, 107, 108, 129, 130, 142, xxix, xxx
GSWM	Global Scale Wave Model 71, 109, 117, 160
HASDM	High Accuracy Satellite Drag Model 75
HRGEM	high resolution global electron density model 145–148
HWM	Horizontal Wind Model 109, 117, 118, 160
IGRF	International Geomagnetic Reference Field 36, 98, 108, 160
IMF	interplanetary magnetic field 3, 31–36, 39, 68, 70, 98, 105, 107, 108, 121, 122, 124, 129, 130, 142, 158, 159, xv

IR	infrared 25, 28
IRI	International Reference Ionosphere Model 23, 45, 145
ISS	International Space Station 1, 2
ITRS	International Terrestrial Reference System 99, 113, xxix
LEO	low Earth orbit 1–4, 59–61, 67, 159
MPI	Message Passing Interface 70, xix, xx
MUV	middle ultraviolet 19, 25, 28
NASA	National Aeronautics and Space Administration 64, 113, 161
NOAA	National Oceanic and Atmospheric Administration 38, 40
NRLMSIS	Naval Research Laboratory Mass Spectrometer and Incoherent Scatter radar 16, 19, 21, 42, 43, 45, 46, 68, 74–76, 98, 101, 102, 109, 113–118, 127, 128, 138, 140, 142–144, 159, 160
NUV	near ultraviolet 28
OLS	open loop simulation 8, 102, 103, 117, 118, 125–129, 132–136, 138–140, 142–144, 147–150, 152–156, 158–160, xxvi, xxviii, xxxiv
PDAF	Parallel Data Assimilation Framework , 8, 93, 97, 101, 112, 157, xix–xxi
PDF	probability density function 40, 77, 78, 80–82, 84, 85, 89
RMSE	root mean square error 76, 132, 133, 135, 137–141, 154, 158, 159
SEE	Solar EUV Experiment 26
SEIK	Singular Evolutive Interpolated Kalman 91, 92, 94
SLR	Satellite Laser Ranging 62, 76
TEC	total electron content 6, 98, 99, 101, 149
TIDA	Thermosphere Ionosphere Data Assimilation 99, 101
TIE-GCM	Thermosphere Ionosphere Electrodynamics General Circulation Model , 5, 8, 9, 11, 31, 68, 70–74, 76, 77, 88, 95, 97–99, 101–103, 106–114, 117–120, 123, 125, 127–129, 131, 132, 134, 137, 139, 140, 144–148, 150–152, 155–157, 159–161, xv–xix, xxi, xxii, xxv, xxxiv
TSI	total solar irradiance 24, 25
UTC	coordinated universal time 99
VCM	variance covariance matrix 77, 80–82, 85–90, 92, 93, 95, 104, 114, 116, 119, 133, 138–141, 158, x, xi
VIS	visible light 28
XUV	soft X-rays 19, 22, 25, 26, 28, 70

> Captain's Log, supplemental. The Enterprise, spiraling down out of control. Ship's outer skin heating rapidly due to friction with planet atmosphere.
>
> *(Star Trek TOS 1x06 'The Naked Time')*

1. Introduction

After the launch of the first artificial satellite into orbit around the Earth in 1957, the number of satellites and their use for society has skyrocketed in recent years. McDowell (2025) reports 28 282 satellites in an orbit around the Earth in February 2025. Satellites orbiting Earth enable global broadcasting, communication, cartography, surveying, navigation, Earth observation but also military reconnaissance and espionage (e.g., Maini and Agrawal, 2014, Part II). 83 % of the satellites orbiting Earth are in the low Earth orbit (LEO) regime[1], which are all orbits up to 2000 km above the Earth's surface. According to Kepler's third law, a satellite orbits Earth in 127 min at an altitude of 2000 km and in 88 min at an altitude of 200 km. Examples of LEO satellites are altimeter satellites (e.g., Stammer and Cazenave, 2017) measuring the sea level, satellites measuring Earth's gravitational potential (e.g., Hofmann-Wellenhof and Moritz, 2006), and the International Space Station (ISS).

In addition to Earth's gravity (e.g., Hofmann-Wellenhof and Moritz, 2006), which forces satellites into orbit around the Earth, satellites are affected by non-gravitational forces (e.g., Montenbruck and Gill, 2000). For satellites flying below about 1000 km, atmospheric drag is the largest non-gravitational force. It is caused by the collision of the satellites with the particles of the rarefied upper atmosphere[2]. The atmospheric drag is proportional to the mass density of air (e.g., Anderson, John D. and Cadou, Christopher P., 2023).

Although the air in the upper atmosphere is very thin–at 100 km, the mass density of the air is about seven orders of magnitude lower than on the ground, and at 1000 km 14 orders of magnitude lower–the lifetime of LEO satellites is limited to several years due to atmospheric drag, which slows the satellites down and reduces their altitude (e.g., King-Hele, 1987). Atmospheric mass density decreases roughly exponentially with altitude, so drag is less significant for satellites above the LEO. On the other hand, the atmospheric mass density increases exponentially as satellites lose altitude, intensifying drag and accelerating orbital decay. Eventually, atmospheric drag becomes so intense that satellites burn and disintegrate. Fragments may fall to Earth unless they are completely incinerated during re-entry (e.g., Klinkrad et al., 2006). When planing a satellite mission, reliable mass density forecasts along the satellite's orbit are required for predicting its lifetime. During a LEO satellite mission that is not equipped with instruments to measure acceleration, precise and accurate mass density estimates are required for determining

---

[1] McDowell (2025) lists 23 560 LEO satellites.

[2] The term 'upper atmosphere' is not consistently defined. In Prölss (2004, p. 29), it begins at the mesopause (above about 90 km), while others define it to start above the tropopause (above about 15 km). Those layers are explained later in Section 2.2. In this thesis, 'upper atmosphere' refers to the atmosphere above an altitude of 90 km unless otherwise indicated.

a highly reliable orbit (e.g., Montenbruck and Gill, 2000). At the end of a satellite mission, the mass density is also needed to predict the re-entry time and position (e.g., Klinkrad et al., 2006).

On 7 March 2024, ESA published an article about the impending re-entry of battery packages of the ISS, which crashed on 8 March 2024:

> The European Space Agency (ESA) Space Debris and Independent Safety Offices are closely monitoring the reentry of a pallet of used ISS batteries and calculating estimates for when and where the reentry will occur.
>
> The batteries, nine in total, were released on 11 January 2021 and will undergo a natural reentry, which is now predicted for around 18:56 CET on 8 March [2024] +/- 0.4 days.
>
> The total mass of the batteries is estimated at 2.6 metric tonnes, most of which may burn up during the reentry. While some parts may reach the ground, the casualty risk – the likelihood of a person being hit – is very low.
>
> The reentry will occur between -51.6 degrees South and 51.6 degrees North. Large uncertainties, primarily driven by fluctuating levels of atmospheric drag, prevent more precise predictions at this time. The closer we get to the expected reentry window, the better the concerned region can be geographically constrained.
>
> [...] (*Reentry of International Space Station (ISS) Batteries into Earth's Atmosphere* 2024)

This quote illustrates the current limits in predicting orbits of LEO satellites. It should be noted here that the probability of being killed by re-entering space debris is very low as the following comparison of exposure time spans of equivalent fatality probability demonstrates:

> The annual risk of a person being killed by a re-entering man-made space object is equivalent to the risk of being killed while traveling 1 meter in a car, doing 10 seconds of skiing, working 1 second as a fire fighter, or spending 5 minutes of your life at the age of 60. (Klinkrad et al., 2006, p. 271)

1.1. Factors Determining the Mass Density of the Upper Atmosphere

The upper atmosphere's mass density depends on the conditions in Earth's space environment (also called space weather, e.g, Luhmann and Solomon 2014; Prölss 2004; Yau et al. 2019a) and the lower atmosphere (e.g., H.-L. Liu, 2016). Figure 1.1 shows an overview of the processes impacting Earth's mass density. Most of the ultra violet radiation emitted by the Sun is absorbed in the upper atmosphere. This heats the atmosphere and causes an up-welling of denser air. Moreover, the absorption of solar radiation ionizes the atmosphere. The number of charge carriers in the upper atmosphere is several orders of magnitude lower than the number of electrically neutral components. The charged part of the atmosphere is called the ionosphere, and the electrically neutral part is referred to as the neutral atmosphere.

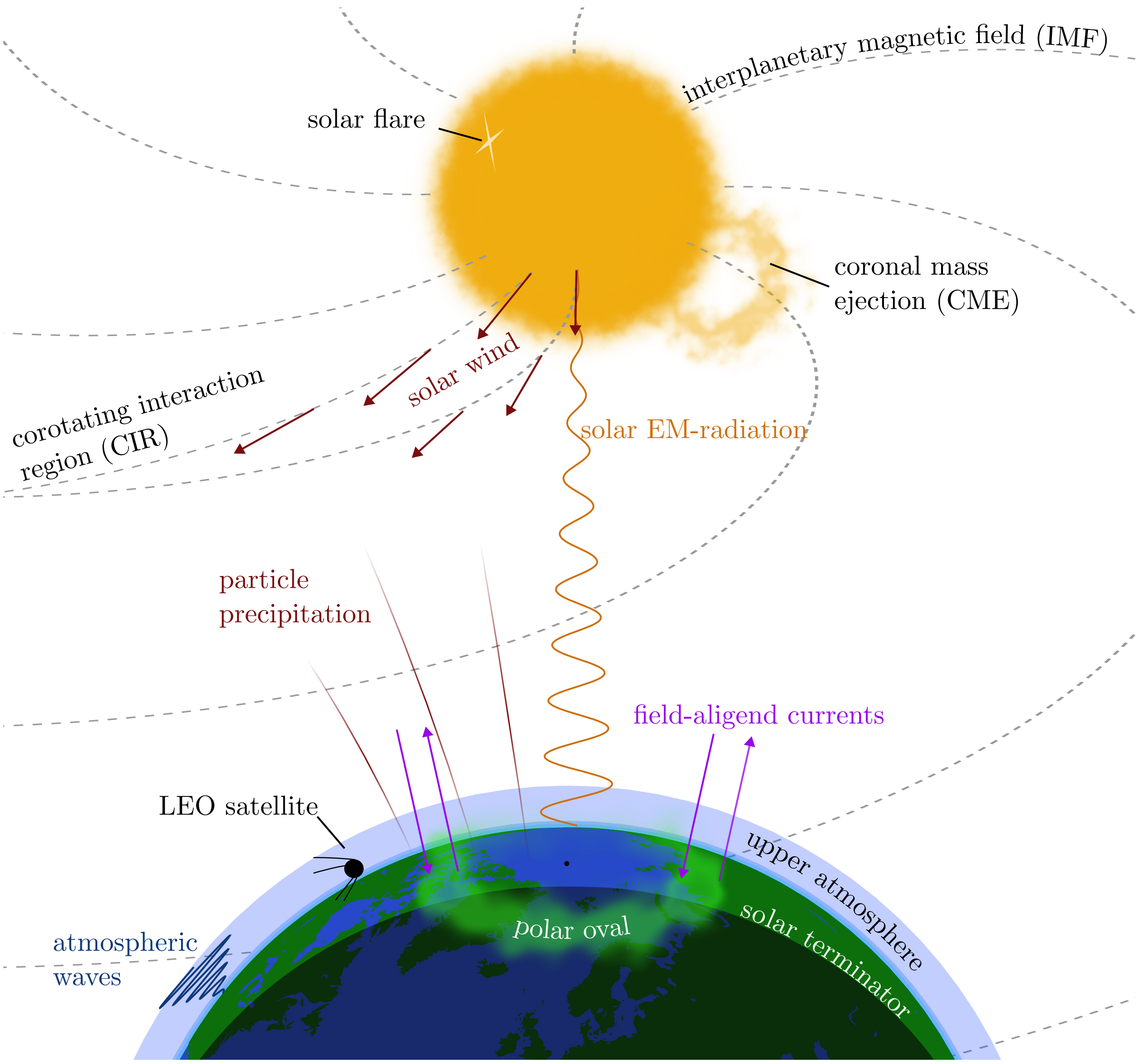

Figure 1.1.: This sketch (not to scale) illustrates the primary energy inputs of the upper atmosphere. The Sun continuously emits electromagnetic radiation in a wide spectrum and a plasma called solar wind. Moreover, the Sun generates the interplanetary magnetic field (IMF). The solar wind streamlines and the IMF field lines coincide. Regions where fast-moving solar wind streams meets slower-moving solar wind streams are called corotating interaction regions (CIRs). The highly energetic part of solar radiation is absorbed in the upper atmosphere, which heats and ionizes the atmosphere. Solar radiation is only absorbed on the day-side. Thus, on the night-side, separated by the solar terminator, conditions are significantly different. Most of the solar wind is shielded by Earth's magnetic field. Solar wind particles precipitating in the atmosphere generate additional heat. Solar flares and coronal mass ejections (CMEs) are outbursts on the Sun. Solar flares, CMEs, and CIRs can cause geomagnetic storms when hitting Earth. Around each magnetic pole, an oval with high electron density is formed. Field-aligned currents are electric currents aligned to Earth's magnetic field that vertically couple the atmosphere around the poles. Waves from the lower atmosphere arising, for example, from atmospheric tides, volcanic eruptions, or tsunamis propagate upwards into the upper atmosphere. All those processes affect the neutral density, and accordingly, the atmospheric drag acting on a LEO satellite as it orbits Earth. Thus, LEO satellites experience very different conditions in the atmosphere.

The solar radiation emission is subject to various temporal variations, which are also seen in the mass density. Prominent features are the eleven-year activity cycle of the Sun and the 27-day rotation cycle of the Sun. Nonperiodic events such as solar flares, coronal mass ejections (CMEs), or corotating interaction regions (CIRs) may cause geomagnetic storms when hitting Earth that induce severe mass density variations in the upper atmosphere and endanger the technical infrastructure (e.g., M. Hapgood, 2019). For example, a geomagnetic storm can affect electric power grids on Earth's surface, disrupt communication, including navigation signals from satellites, and also destroy circuits aboard spacecraft. The three most severe geomagnetic storms according to Cliver et al. (2022, Figure 39) are the Carrington event in 1859 (Carrington, 1859; Hodgson, R., 1859), the Chapman–Silverman storm in 1872 (Hayakawa et al., 2023), and the New York Railroad Storm in 1921 (Love et al., 2019).

> [...] In the last extreme geomagnetic storm on record, the great Halloween Storm of 2003, anecdotal testimony from USAF operators during the storm recounts that the majority of LEO satellites were temporarily lost, requiring several days of around-the-clock work to reestablish the catalog. (T. E. Berger et al., 2020)

Even minor geomagnetic storms can have practical and financial consequences, as the loss of 38 Starlink satellites on 3 February 2022 illustrates (M. Hapgood et al., 2022).

1.2. Challenges in Observing and Modeling the Mass Density in the Upper Atmosphere

The mass density in the atmosphere is observed by different remote sensing and in-situ measurements. Observations with high temporal resolution are derived from accelerometer measurements onboard satellites (e.g., Doornbos, 2012; Vielberg, 2024). However, those observations are sparse and require careful accelerometer calibration, accurate and precise simulation of non-gravitational accelerations and gas-surface interaction, as well as, accurate and precise information about the free stream velocity, mass, and orientation of the satellite. One can also derive the mass density by analyzing the orbital decay of any tracked satellite. The downside of this approach is the limited temporal resolution. Inverting acceleration or orbital delay to mass density requires an accurate aerodynamic model. The lack of such a model limits the accuracy of these mass densities.

Direct measurements of the neutral and ion density, and also the composition are possible by mass spectrometers. However, there is no current mission equipped with a mass spectrometer to observe Earth's upper atmosphere. Remote sensing techniques such as incoherent scatter radar and radio occultation provide electron density observations.

Many models have been developed to get access to the mass density at an arbitrary point in time and space. These are especially helpful for LEO satellites that are not equipped with suitable instruments to measure the neutral mass density or the non-gravitational accelerations. There are numerical models and (semi-) empirical models. Numerical models forward a given initial state by applying first principles/physical laws. To this end, the atmosphere is discretized in space and time. Discretization, assumptions, simplifications, uncertain initial states, boundary conditions, external forcings, and model parameters limit the prediction skills of numerical

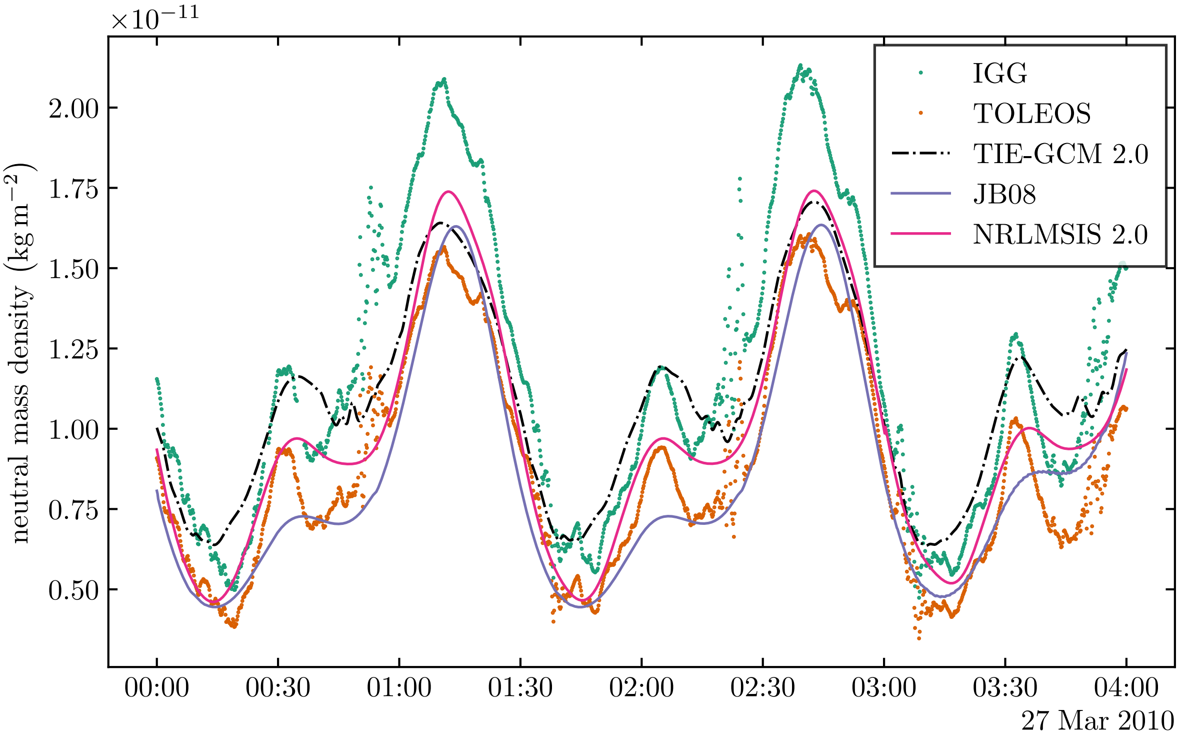

Figure 1.2.: The time series show the neutral mass density along the orbit of CHAMP. The dotted lines are accelerometer-derived densities (IGG: Vielberg et al. (2021), TOLEOS: Doornbos (2012), March et al. (2021), and Siemes et al. (2016). Solid lines are densities obtained from semi-empirical models, and the dashed-dotted line corresponds to the mass density of a numerical model (TIE-GCM 2.0). More details about the models can be found in Chapter 5.

models. Semi-empirical models are mathematical functions fitted to observations. The temporal and spatial resolution of the observations, the temporal resolutions of the external forcings used as model drivers, the drivers themselves, and assumptions limit empirical models.

Figure 1.2 shows simulated and observed mass densities along the orbit of the Challenging Minisatellite Payload (CHAMP) satellite mission (Section 4.1.1) flying at $\sim 300\,\mathrm{km}$ altitude for a four hour period. Within the period shown, the mass densities differ by up to a factor of two at the same time and place. These discrepancies are caused by the limitations of the models and observations explained before. Doubling the density approximately leads to an error of 17 m within one orbital revolution and more than 4 km after one day[1]. Although the mass density differences are typically lower, this illustrates the importance of improving the accuracy of mass density models.

The misfit of different mass density estimates has been examined in many studies. In summary, model performance depends on solar activity and the location on Earth (Section 5.3). Recent models capture observations of neutral mass density roughly within ± 5 %-15 %. However,

---

[1] These errors are computed by exploiting that the drag acceleration is directly proportional to the mass density (Equation 3.5) and assuming a constant reference drag acceleration a_0 of $1.15 \times 10^{-6}\,\mathrm{m\,s^{-2}}$. After the time Δt has passed, the difference in the satellite's path length is $\Delta s = \frac{1}{2} a_0 \left(1 - \frac{\rho}{\rho_0}\right) \Delta t^2$, with the scale factor for the mass density $\frac{\rho}{\rho_0}$.

average misfits between different models of up to 70 % have also been reported during periods of increased solar activity.

1.3. Challenges in Upper Atmosphere Data Assimilation

The core functionality of numerical models of the upper atmosphere is based on physics and chemistry. Combining physics and observations can improve the fidelity of the simulation of the upper atmosphere. An established tool for that is data assimilation, which seeks to combine models and observations optimally, taking into account their uncertainty (e.g., Asch et al., 2016; Lahoz et al., 2010). For large-scale non-linear systems such as the upper atmosphere, ensemble-based Kalman filters have been developed. These methods are derived from the Kalman filter (Kalman, 1960) and employ an ensemble of model instances to implicitly represent the model uncertainty (e.g., Evensen, 1993; Evensen et al., 2022; Vetra-Carvalho et al., 2018). At predefined points in time, called *assimilation steps*, the Kalman filter updates the state of the system with the observations available at that time.

While ensemble-based Kalman filters render large-scale problems feasible, their computational demands remain significant. An advantage of ensemble-based data assimilation is the straightforward derivation of model uncertainty.

A few studies have already demonstrated that data assimilation can improve the prediction skills of upper-atmosphere models. Section 7.1 provides an review of these studies. The studies showed how assimilating accelerometer-derived mass densities, electron density profiles from radio occultation, and total electron content (TEC) measurements improves mass density forecasts. Nevertheless, the review in Section 7.1 revealed the following challenges for upper atmosphere data assimilation.

Runtime Assimilation experiments are computationally expensive and require longer run times compared to standalone model runs. However, the runtime of assimilation experiments is often longer than necessary because of the use of so-called offline implementations, which require reinitialization of the model after each assimilation step. Additionally, slightly more efficient assimilation algorithms operating in the *error subspace* have been developed, but they were not employed in these studies.

Periods covered by assimilation experiments Because of the long runtime and high computational costs, most studies cover only a few days and either focus on a sequence of geomagnetic quiet days or a single storm event. It is desirable, however, to extend the period, ideally to the whole lifetime of a satellite.

Ensemble Generation As a consequence of the previous aspect, the ensemble generation is often tailored to the study's specific solar and geomagnetic conditions, rendering it useless for other conditions. To conduct assimilation experiments over long periods, the ensemble must reflect the varying space weather conditions. The ensemble represents the uncertainty of the model, and the correlation encoded in it controls how ensemble-based Kalman filters update the state. Additionally, the ensemble typically contains spurious long-range correlations that cause unrealistic state updates when assimilating data. So-called localization schemes can suppress those spurious long-range correlations. However, they result in updates that affect only states in the vicinity of the observations.

Sparsity of accelerometer-derived mass densities When using localization schemes to suppress spurious long-range correlations within the ensemble, the state update is limited to the vicinity of the satellites whose mass densities are assimilated. Since only a few satellite missions are equipped with accelerometers suitable for determining the mass density, localization restricts the state update to a small fraction of the upper atmosphere.

High temporal resolution of accelerometer-derived mass densities Although accelerometer-derived mass densities have a temporal resolution of a few seconds, the data is assimilated less frequently. Older studies assimilate the data every 90 min whereas more recent studies assimilate data every 10 min. Thus, the full potential of the high temporal resolution is not used. The frequency of assimilation steps is also connected to the runtime, as an increased frequency of data assimilation update steps requires additional computational resources.

Model Dynamics For convergent systems, like the upper atmosphere, the model dynamics tend to restore the original state that the model would have predicted without assimilation after some time. This is further discussed in Section 6.2 and exemplarily shown in Figure 7.2. For persistent updates, one can co-estimate the model dynamics.

1.4. Objective of the Thesis

Derived from the challenges described in the preceding section, a new assimilation system is developed that is used to test the following hypotheses:

(H 1) Implementing an assimilation system without the need for model reinitialization and using efficient error-subspace filters allows performing data assimilation experiments over periods from several weeks to a few years and exploiting the high temporal resolution of accelerometer-derived mass densities with reasonable computational resources.

(H 2) This requires the generation of an ensemble that adapts to space weather conditions and provides a realistic uncertainty quantification of the model forecast over the complete period of the assimilation experiments.

(H 3) The ensemble can be generated without severe spurious long-range correlation, making localization for the assimilation system optional and enabling global state updates.

(H 4) The mass density prediction skills of the assimilation system exceed those from (semi)-empirical models.

(H 5) Because semi-empirical models of the upper atmosphere are condensed from many different observations that are globally available, one can assimilate them to improve the density estimation of numerical models.

(H 6) Persistent model updates can be enabled by co-estimation of model dynamics.

Developing a numerical model from scratch is challenging, so I use the established Thermosphere Ionosphere Electrodynamics General Circulation Model (TIE-GCM; Qian et al. 2014) developed at the High Altitude Observatory in Boulder, Colorado, as a basis. It is published under an open source academic research license and has been used already successfully in many assimilation experiments (Section 7.1). For the first time, data assimilation is implemented into the TIE-GCM by binding it to the Parallel Data Assimilation Framework (PDAF; Nerger 2024; Nerger et al. 2020) developed at the Alfred Wegener Institute in Bremerhaven. The implementation supports the assimilation of data located on trajectories (e.g., in-situ observations of satellites) or on regular grids (e.g., data derived from semi-empirical models). The implementation allows the assimilation of an arbitrary number of datasets located on trajectories or grids simultaneously. The computations require high-performance computers with hundreds of physical processor cores.

1.5. Outline of the Thesis

Chapters 2 to 6 provide the background information required to understand the implementation of the assimilation system (Chapter 7) and the assimilation experiments conducted with it (Chapter 8). Chapter 2 describes the processes summarized in Figure 1.1 in more detail. They are fundamental for understanding the models of the upper atmosphere, the mapping from the model forecasts to the observations, the generation of the state ensemble, and interpreting the experiments. Chapter 3 introduces the aerodynamics for satellites, which are necessary for understanding the link between drag acceleration and mass density. Observations and models of the upper atmosphere are summarized in Chapter 4 and Chapter 5, respectively. The emphasis is on accelerometer-derived mass densities and the TIE-GCM, as they are fundamental to this thesis. Data assimilation is introduced in Chapter 6 on a general level followed by an in depth description of error subspace filters, that are used for the assimilation system.

Based on the preceding chapters, Chapter 7 explains the implementation of the assimilation system. To test the Hypotheses H 1 - H 6 open loop simulation (OLS) and data assimilation experiments are conducted in Chapter 8. I assimilate mass densities derived from the accelerometers aboard the CHAMP, Gravity Recovery And Climate Experiment (GRACE), and Swarm-C satellites directly into the TIE-GCM with and without localization. As expected, localization successfully suppresses long-range correlations but at the cost of limiting the update to the vicinity along the orbits of the satellites from which the density data were obtained. The global filter (a filter that does not apply localization) performs slightly worse along the orbit of the assimilated data but achieves notable improvements along the orbits of other satellites.

Instead of assimilating the enormous datasets from which semi-empirical models are constructed, assimilating the output of the semi-empirical model is much more straightforward. The observations are already harmonized, and the model interpolates them into any position. To exploit this, I developed a two-step approach (Corbin and Kusche, 2022) that assimilates the mass density prediction of a semi-empirical model into the TIE-GCM. In the first step, an empirical model is calibrated with accelerometer-derived mass densities. In the second step, the model is globally evaluated on a regular grid and assimilated. While the two-step approach can improve the estimation of the average mass density, it fails to correct sudden changes since the temporal resolution is limited to three hours. I show in this thesis that for this conditions direct assimilation performs better.

Given the coupling between the neutral upper atmosphere and the ionosphere, it is possible to assimilate electron number density data in order to enhance the mass density estimation. Here, I assimilate electron number densities from a three-dimensional multi-layer Chapman model constructed from observations. The TIE-GCM electron number density is corrected towards the multi-layer model. However, the mass density prediction capabilities are not improved when compared to accelerometer derived mass densities over the time period studied.

For a persistent correction of the model estimates, one can co-estimate the model dynamics. In this thesis, I co-estimated the Joule heating factor. It was found that the default value is already well chosen for the investigated period.

2. Space Weather and Terrestrial Aeronomy

The state of the Earth's upper atmosphere, including but not limited to the mass density, is strongly influenced by the time-varying emission of electromagnetic radiation and plasma from the Sun, the Sun's magnetic field, and waves propagating from the lower atmosphere. These external influencing factors are responsible for many (periodic) effects visible in the time series of the data assimilation experiments in Chapter 8. In addition, these external influencing factors must be considered in constructing upper atmosphere models, which are discussed in Chapter 5. In Chapter 7, the uncertainty of the state predicted by the TIE-GCM is computed considering the uncertainty of the variables used to represent the external influencing factors. The basic physics and assumptions used to construct numerical and semi-empirical models (Chapter 5) and equations to link the observations to model states which is required in Chapter 7 are summarized in this chapter.

The atmosphere is a mixture of gaseous particles surrounding Earth and bound by its gravity. There are electrically neutral and charged particles in the atmosphere. The latter are affected by and influence electric and magnetic fields. Unfortunately, there is no universal or conventional definition of space weather. However, as the two examples illustrate, there is some agreement on the concept.

> Space weather refers to the dynamic, highly variable conditions in the geospace environment including those on the sun, in the interplanetary medium, and in the magnetosphere-ionosphere-thermosphere system. (Baker, 1998)

> We understand space weather to mean all influences and effects of the sun and other cosmic sources on the state of near-Earth space down to the Earth's surface. (Berdermann et al., 2015, translated from German into English)

Space weather (e.g., Luhmann and Solomon, 2014; Yau et al., 2019a) is the most significant energy input into the upper atmosphere and, accordingly, has a huge impact on satellite drag.

Aeronomy (e.g., P. M. Banks and Kockarts, 1973a,b; Bauer and Lammer, 2004) is "the study of the physics and chemistry of the upper atmosphere of a planet" (Bauer and Lammer, 2004). Within the atmospheric sciences, the term is used to distinguish it from meteorology, which is mainly concerned with the lower atmosphere (Bauer and Lammer, 2004). As space weather significantly affects the upper atmosphere, aeronomy cannot be studied in isolation from it.

The first Section 2.1 covers the fundamentals of gas mixtures and aerostatics. The second Section 2.2 explains the terminology used to subdivide the atmosphere into horizontal layers. Section 2.3 provides a short summary of our Sun, which is the origin of space weather. Section 2.3.1 explains how the electromagnetic radiation emitted by the Sun affects the atmosphere. The subsequent Section 2.3.2 is about the interaction of the plasma emitted by the Sun and the

Earth's environment with an emphasis on the upper atmosphere. Vertical coupling is discussed in Section 2.4. The last Section 2.5 gives an overview of spatial and temporal variations of the neutral mass density in the upper atmosphere.

2.1. Fundamentals

Models of the upper atmosphere (Chapter 5) use different representations for its composition. The links between those representations are explained in Section 2.1.1. Section 2.1.1 also explains how the total mass density is obtained given the composition which is required later for constructing the observation operator (Section 7.3). Recent models of the upper atmosphere assume the atmosphere is an ideal gas (Section 2.1.2) and most models assume aerostaic equilibrium (Section 2.1.3). Numerical models frequently use pressure as vertical coordinate. The conversion from pressure to geometric height is descried in Section 2.1.4. This conversion is required in Section 7.3 to interpolate the modeled state to the observations.

2.1.1. Gas Mixtures

There are several quantities suited to describe the composition of the atmosphere. A concise description of mixtures is given by Cvitas (1996) that is summarized in the following: A mixture consists of two or more different particle types. The special case of a mixture containing two particle types is called a binary mixture. Measures for the occurrence of a single particle type are the volume V, the mass m, the particle number N, and the amount of substance n. To characterize a mixture, one uses the ratio, fraction, concentration, or molality of those measures.

Table 2.1 contains the definition for the corresponding fractions, concentrations, and ratios. However, only fractions and concentrations are relevant for this thesis. The notation in this section corresponds to the one in Renner (2007). Although the focus is on gas mixtures here, the quantities are also valid for substances in different states of matter. The particle types of a gas mixture are also called species.

mass fraction Given a gas mixture consisting of s species the total mass of the composition

$$m = \sum_{i=1}^{s} m_i \tag{2.1}$$

is the sum of the individual masses of each species m_i. The mass fraction of a species is the ratio of the mass of the species and the total mass

$$w_i = \frac{m_i}{m}, \tag{2.2}$$

with the sum of all mass fractions

$$\sum_{i=1}^{s} w_i = 1 \tag{2.3}$$

being one.

Table 2.1.: Overview of quantities describing gas mixtures. The indices i and j refer to the corresponding particle type within the mixture. The definitions in this table are taken from Cvitas (1996).

	fraction	concentration	ratio
mass (m)	$w_i = \frac{m_i}{\sum m_j}$	$\rho_i = \frac{m_i}{V}$	$\zeta_{i,j} = \frac{m_i}{m_j}$
molar (n)	$x_i = \frac{n_i}{\sum n_j}$	$c_i = \frac{n_i}{V}$	$r_{i,j} = \frac{n_i}{n_j}$
number (N)	$x_i = \frac{N_i}{\sum N_j}$	$C_i = \frac{N_i}{V}$	$r_{i,j} = \frac{N_i}{N_j}$
volume (V)	$\phi_i = \frac{V_i}{\sum V_j}$	$\sigma_i = \frac{V_i}{V}$	$\psi_{i,j} = \frac{V_i}{V_j}$

amount of substance fraction Analogously, the total amount of substance in a gas mixture n is the sum of the amount of substance of each species

$$n = \sum_{i=1}^{s} n_i. \tag{2.4}$$

The molar fraction is

$$x_i = \frac{n_i}{n}, \quad \text{with} \sum_{i=1}^{s} x_i = 1. \tag{2.5}$$

particle number fraction The particle number N and amount of substance n are related by the Avogadro constant $N_A = 6.02214 \times 10^{23} \frac{1}{\text{mol}}$ via

$$N = N_A n. \tag{2.6}$$

Since this is a constant factor, the amount of substance in Equation 2.4 and Equation 2.5 can be replaced with the particle number N.

conversion of fractions Given the molar fraction x_i and the molar mass (mass per amount of substance) M_i of each species, the mass fraction is computed by

$$w_i = \frac{x_i M_i}{\sum_{j=1}^{s} x_j M_j}. \tag{2.7}$$

Introducing the mean molar mass of a gas mixture

$$\overline{M} = \frac{m}{n} = \frac{1}{\sum_{j=1}^{s} \frac{w_j}{M_j}} = \sum_{j=1}^{s} x_j \, M_j, \tag{2.8}$$

Equation 2.7 can be written as

$$w_i = x_i \frac{M_i}{\overline{M}}. \tag{2.9}$$

From 2.9 one can express the molar fraction as a function of mass fraction

$$x_i = w_i \frac{\overline{M}}{M_i}. \tag{2.10}$$

number concentration The number concentration, which is equivalent to the number density, of a species is the ratio of particle number N_i and volume V

$$C_i = \frac{N_i}{V}. \tag{2.11}$$

mass concentration The mass concentration

$$\gamma_i = \frac{m_i}{V} = \rho_i \tag{2.12}$$

is mass per volume and is equivalent to the mass density.

conversion of concentrations Given the mean molar mass of a gas mixture, the relation between the number density and mass density of the gas mixture is

$$\rho = \frac{\overline{M}}{N_A} C = \overline{m} C, \tag{2.13}$$

with the mean mass $\overline{m} = \dfrac{m}{N} = \dfrac{\overline{M}}{N_A}$.

2.1.2. Ideal Gas

An ideal gas is

> a theoretical gas composed of many randomly moving point size particles that do not interact with each other except when they collide elastically. Although in reality, there is no such thing as an ideal gas, most gases behave close enough to ideal that the ideal gas law can effectively describe their behavior. Generally, a gas behaves more like an ideal gas at higher temperatures and lower pressures. (Gaffney and Marley 2018, p. 198)

For ideal gases, the ideal gas law

$$p = C k_B T, \tag{2.14}$$

is valid. It relates the pressure p, the number density C, and the temperature T by means of the Boltzmann constant $k_B = 1.380\,65 \times 10^{-23}\,\mathrm{J\,K^{-1}}$. Inserting Equation 2.14 into Equation 2.13

and using the gas constant $R = k_B N_A$ one can compute the mass density with

$$\rho = \frac{p\overline{M}}{RT} = \frac{p\overline{m}}{k_B T} \tag{2.15}$$

Given the mass fraction, mean molar mass, pressure, and temperature, the number density of a single species is

$$C_i = \frac{w_i}{M_i} \frac{p\overline{M}}{k_B T}. \tag{2.16}$$

2.1.3. Aerostatic Equation

The aerostatic equation (derived in Appendix A.1) states that the vertical pressure gradient is proportional to the mass density and gravitational acceleration g

$$\frac{dp(z)}{dz} = -\rho(z)\, g(z) \tag{2.17}$$

if the pressure force and gravitational force are in equilibrium. This equation is only valid for an atmosphere at rest, which means there are no winds or other mass transport processes.

Inserting Equation 2.15 into the right side of Equation 2.17 leads to the barometric law (see Appendix A.2 for a derivation)

$$p(h) = p(h_0) \exp\left(- \int_{h_0}^{h} \frac{1}{H(z)} dz \right) \tag{2.18}$$

with the pressure scale height

$$H(h) = \frac{k_B\, T(h)}{\overline{m}(h) g(h)} = \frac{R\, T(h)}{\overline{M}(h) g(h)}. \tag{2.19}$$

Assuming a constant scale height one obtains $p(h) = p(h_0) \exp\left(-\frac{h-h_0}{H}\right)$. In that case, the scale height is the height difference at which the pressure has increased by factor e or decreased by $\frac{1}{e}$. Considering Equation 2.19 plotted in Figure 2.1 for an exemplary column, it is obvious that the scale height is not constant for Earth's atmosphere.

One can define a similar equation for the number density (see Appendix A.3)

$$C(h) = C(h_0) \exp\left(- \int_{h_0}^{h} \frac{1}{H_C(z)} dz \right) \tag{2.20}$$

with the number density scale height

$$\frac{1}{H_C(h)} = \frac{1}{H(h)} + \frac{1}{T(h)} \left. \frac{dT}{dz} \right|_{z=h}. \tag{2.21}$$

In the case of Earth's Atmosphere, both the derivative of the temperature w.r.t. the altitude and the reciprocal temperature get lower with increasing height. Thus, $H_C \approx H$ for heights above $\sim 200\,\mathrm{km}$.

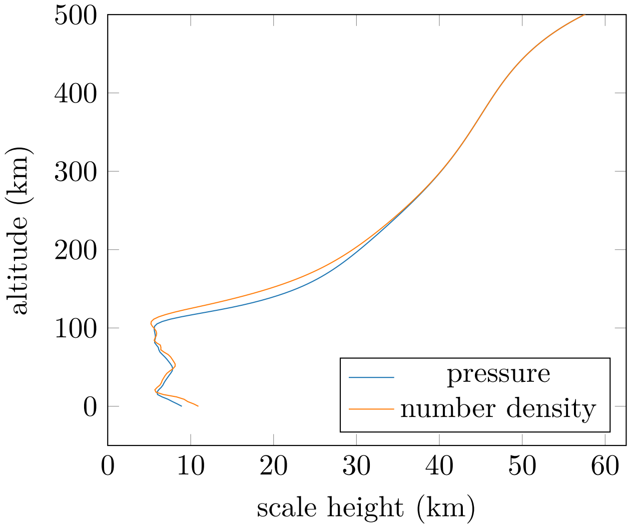

Figure 2.1.: Example of a pressure and number density scale height profiles computed from the NRLMSIS 2.0 model at 23.5°N 0°E 21 June 2019 12:00 UTC+0.

2.1.4. Height systems

The geopotential difference between two points is given by

$$\Delta W = W_B - W_A = -\int_\gamma \boldsymbol{g}(\boldsymbol{r}) \cdot d\boldsymbol{r} \tag{2.22}$$

(Hofmann-Wellenhof and Moritz, 2006, p.158) with geopotential W_A and W_B at point A and B, respectively. The geopotential difference ΔW is independent of the curve $\gamma : [a, b] \to \mathbb{R}^3$ connecting both points, since the gravity field $\boldsymbol{g}$ is a conservative force field. The geopotential number

$$C = W_0 - W_A = \int_\gamma \boldsymbol{g}(\boldsymbol{r}) \cdot d\boldsymbol{r} \tag{2.23}$$

is the negative geopotential difference between a point on the geoid and another point located at an arbitrary position. The potential difference is converted into a *physical height* by dividing it by gravitational acceleration g

$$h = \frac{C}{g}. \tag{2.24}$$

Height systems differ in the way g is calculated. In atmospheric science g is frequently chosen as a constant g_0 reflecting the gravity at the surface (e.g., Minzner et al., 1976; Wallace and Hobbs, 2006). The resulting height

$$H_{\text{pot}} = \frac{C}{g_0} \tag{2.25}$$

is called geopotential height. The geodetic community uses the term dynamic height instead. Geopotential heights do not have a geometric interpretation (Hofmann-Wellenhof and Moritz, 2006, p.160). Given the temperature T and mean molar mass $\overline{M}$ of the atmosphere along

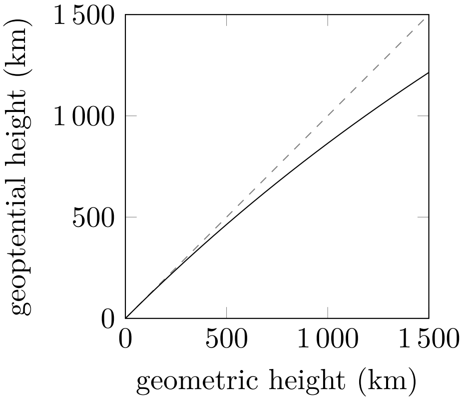

Figure 2.2.: For a given geometric height, the corresponding geopotential height is computed using Equation 2.27. A spherical Earth with a homogeneous density distribution is assumed.

a vertical column in pressure level coordinates, one can compute the geopotential height at pressure level k with (see Appendix A.5)

$$H_{\mathrm{pot}}(k) = H_{\mathrm{pot}}(k_0) + \frac{R}{g_0}\int_{k_0}^{k} \frac{T(\xi)}{\overline{M}(\xi)} d\xi. \tag{2.26}$$

Assuming a spherical Earth with radius $R_\oplus$ and homogeneous density distribution, the relation between geopotential height H_{pot} and geometric height z is (see Appendix A.5.2)

$$H_{\mathrm{pot}} = \frac{R_\oplus\, z}{R_\oplus + z} \tag{2.27}$$

or

$$z = \frac{R_\oplus H_{\mathrm{pot}}}{R_\oplus - H_{\mathrm{pot}}}. \tag{2.28}$$

As shown in Figure 2.2 the geometric height is greater than the geopotential height at the same location. The higher the altitude, the higher the difference between both.

Equations 2.26 and 2.28 are useful to calculate the geometric height of models that use pressure or pressure levels as vertical coordinate.

2.2. Characterization of Atmospheric Layers

There are significant variations in the characteristics of the Earth's atmosphere in the vertical direction. Therefore, it is frequently divided into distinct vertical layers based on different properties (see Figure 2.3). The upper atmosphere mass density is often associated with the thermosphere, which is defined by the temperature of the neutral species (Section 2.2.1). However, the neutral temperature alone cannot explain the vertical mass density profile in the upper atmosphere. Gravitational binding (Section 2.2.2), composition (Section 2.2.3), and ionization (Section 2.2.4) are also relevant to understanding the vertical mass density profile.

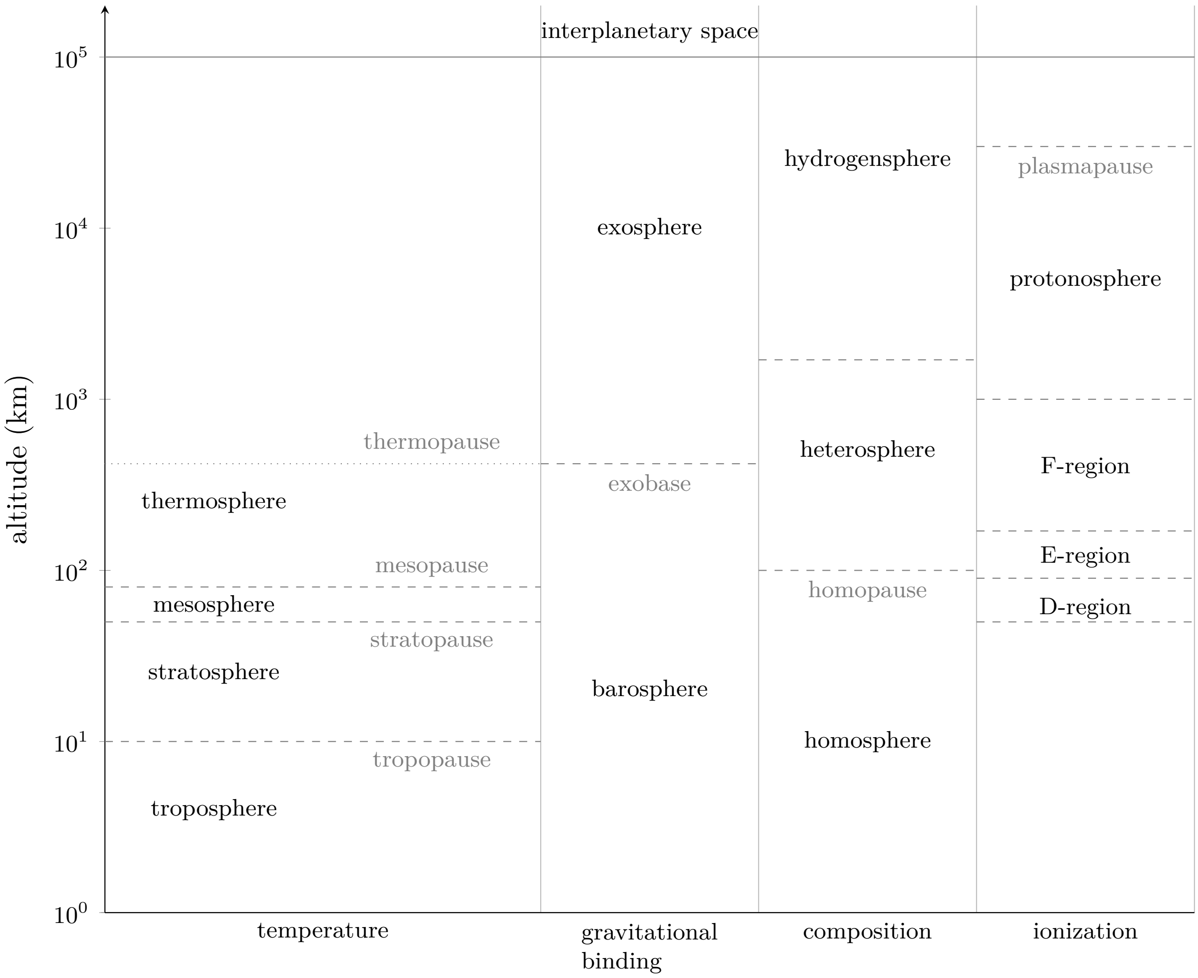

Figure 2.3.: Characterization of atmospheric layers by different quantities. Adopted from Prölss (2004, Figure 2.13). The location of the layers is subject to variations and depends on the location and time.

2.2.1. Temperature Profile of the Atmosphere

A prominent parameter for this division is the *neutral temperature*, which is the temperature of the neutral particles within the atmosphere, assuming they are in thermal equilibrium. This distinction is necessary since charged and neutral particles are not necessarily in thermal equilibrium. In fact, for Earth's atmosphere, charged particles have considerably higher temperatures on the day-side (e.g., Prölss 2004, Figure 4.3, R. Schunk and Nagy 2009, Figure 11.17). A typical neutral temperature profile is given in Figure 2.4. Vertical neutral temperature profiles depend on location and time but maintain certain characteristics (e.g., Prölss, 2004, Section 2.2): Starting from the ground, the temperature decreases to a height of about 10 km. This first inflection point is called tropopause (lowest dashed horizontal line in Figure 2.4). The troposphere is the layer between the ground and tropopause. Here, most of the water vapor accumulates and the majority of weather phenomena occur. Above the tropopause, the ozone concentration increases. The absorption of solar radiation with wavelength greater than 242 nm (located in the middle ultraviolet (MUV) band, see Table 2.3) by ozone increases the temperature. The local temperature maximum is located at about ~ 40 km altitude. This inflection point is the

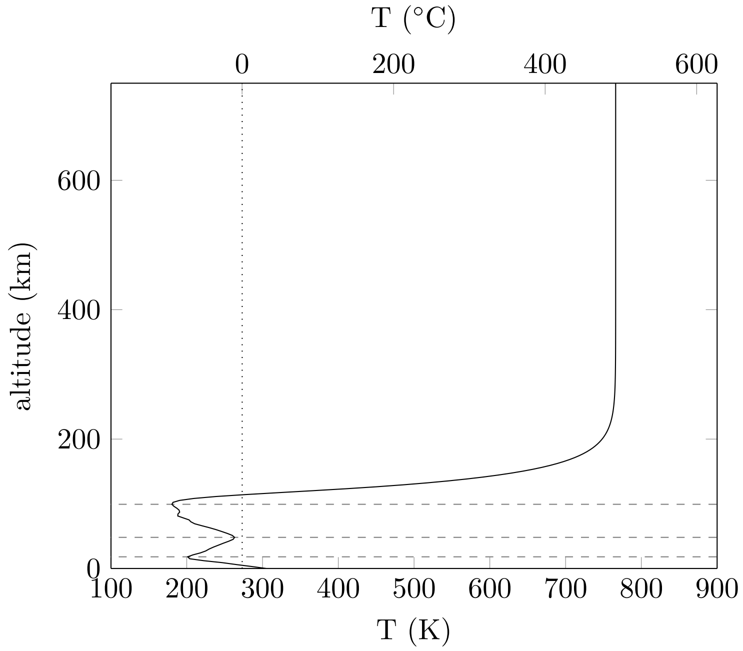

Figure 2.4.: Height profile of neutral temperature during quiet solar activity conditions, simulated by the Naval Research Laboratory Mass Spectrometer and Incoherent Scatter radar (NRLMSIS) 2.0. The boundaries of the layers are highlighted with dashed horizontal lines: Tropopause, Stratopause, and Mesopause from bottom to top. The profile is located at 23.5°N 0°E on 21 June 2019, at 12:00 UTC+0. At this time and location, solar radiation enters the atmosphere almost orthogonally.

stratopause (second dashed horizontal line), and the corresponding layer is the stratosphere. The layer above the stratosphere is called mesosphere. The temperature decreases again in this layer, due to decreasing ozone levels. At about 90 km altitude the neutral temperature reaches a local minimum which is the mesopause (upper horizontal dashed line). Above the mesopause, the temperature increases exponentially and approaches the limiting exospheric temperature. This upper layer is called the thermosphere. The temperate increase is caused by the absorption of solar extreme ultraviolet (EUV) and soft X-rays (XUV) radiation. In fact, the thermosphere protects all lifeforms on Earth against this ionizing radiation.

The upper boundary of the thermosphere cannot be defined based on the neutral temperature profile, which lacks distinguishing features beyond the mesopause. Instead, the exobase–introduced in the following Section 2.2.2–is often used as the upper limit and sometimes referred to as the thermopause.

2.2.2. Exosphere and Barosphere

Two conditions must be satisfied for a particle to escape from Earth's atmosphere. First, its velocity must exceed Earth's escape velocity to overcome gravitational attraction. Second, the density must be low enough to avoid collisions which scatter it back to lower altitudes.

Based on gravitational binding (second column from left in Figure 2.3) the atmosphere is separated into *barosphere* and *exosphere* (e.g., P. M. Banks and Kockarts 1973b, Chapter 16; Bauer and Lammer 2004, Section II.3; Prölss 2004, Section 2.4.1; R. Schunk and Nagy 2009,

Table 2.2.: Properties of important electrically neutral species found in Earth's atmosphere

species				
symbol	name	atomic number ()	mass number ()	molar mass ($\mathrm{g\,mol^{-1}}$)
H	Hydrogen	1	1	1.008
He	Helium	2	4	4.0026
Ar	Argon	18	40	39.948
O	atomic Oxygen	8	16	15.999
O_2	molecular Oxygen	16	32	31.998
N_2	molecular Nitrogen	14	28	28.014

Section 10.10). While particles in the exosphere have the chance to escape from the atmosphere, it is virtually impossible for a particle in the barosphere to do so.

The *exobase* is the boundary between the exosphere and the barosphere. It is defined as the altitude at which radially outward moving particles collide only once on average (e.g., Prölss, 2004, Section 2.4.1). Its exact location depends on the exospheric temperature and is approximately at 420 km altitude (Prölss, 2004, Section 2.4.1). The aerostatic equation (Equation 2.18) is only applicable to the barosphere since it does not allow for sources or sinks.

2.2.3. Vertical Composition of Neutral Atmosphere

The neutral part of Earth's atmosphere is a gas mixture (see Section 2.1.1) whose six most important neutral species are listed in Table 2.2. The composition of this mixture has a strong vertical dependency, as shown in Figure 2.5 and is another criterion for characterizing atmospheric layers (third column from left in Figure 2.3).

From the ground to about 100 km the atmosphere is well mixed and the mass/number fractions of the species are almost constant. Accordingly, the mean molar mass is constant, too. This part of the atmosphere is called the *homosphere*. The homosphere is dominated by molecular nitrogen, which accounts for 76 % of its mass. Molecular oxygen accounts for 23 %. The remaining species only contribute to 1 % of the mass. The region above the homosphere is the *heterosphere* (e.g. P. M. Banks and Kockarts, 1973b, Chapter 14). It is characterized by gravitational separation, that causes vertical variations of the composition: Heavier particles are found more often in lower altitudes, while lighter particles are found at high altitudes more frequently (see Figure 2.5c and d). The boundary between homosphere and heterosphere is called *homopause*. Above the homopause, the molecular nitrogen and molecular oxygen levels decrease gradually, and atomic oxygen becomes dominant at about 400 km. The origin of atomic oxygen in the atmosphere is the dissociation of molecular oxygen caused by the absorption of photons from the Sun (Prölss, 2004, Section 2.3.7). Above the atomic oxygen peak, the fraction of lighter hydrogen and helium atoms gradually increases. The upper region where hydrogen dominates the atmosphere is called hydrogensphere.

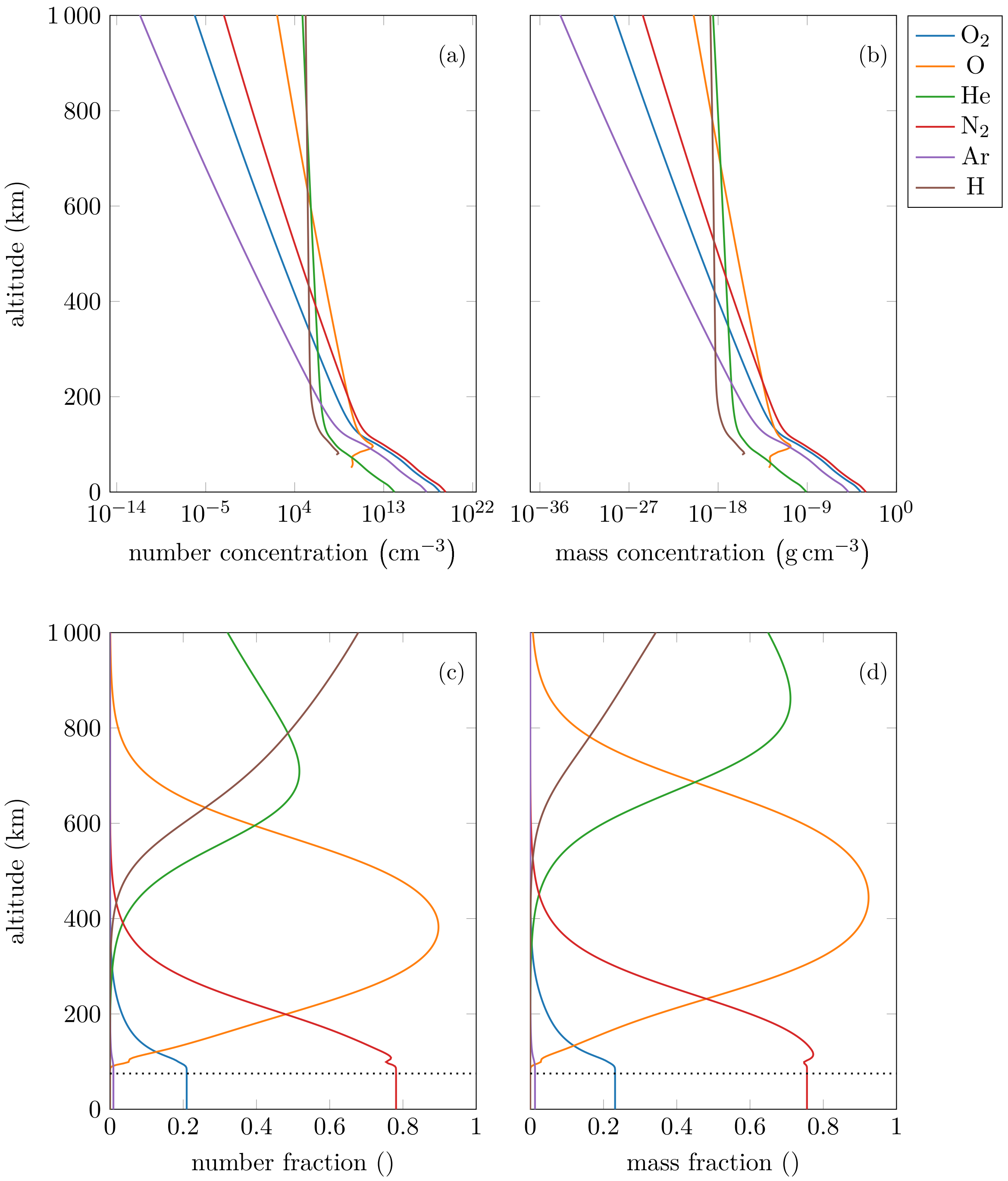

Figure 2.5.: This figure illustrates the vertical dependence of Earth's atmospheric composition. Each color corresponds to a species whose properties are listed in Table 2.2. The number concentration profiles in panel a were computed with the NRLMSIS 2.0. The profiles in the other panels were derived from panel a using the relations described in Section 2.1.1. The profiles are located at 23.5°N 0°E on 21 June 2019, at 12:00 UTC+0. At this time and location, solar radiation enters the atmosphere almost orthogonally. In panel c and d the location of the homopause is marked with a horizontal dotted line.

2.2.4. Ionosphere

Above an altitude of approximately 60 km, charge carriers (ions and electrons) populate the atmosphere. This ionized part of the atmosphere expands beyond 1000 km altitude and is called *ionosphere* (R. Schunk and Nagy, 2009). An exemplary simulated height profile of the ion and electron density is given in Figure 2.6. The ionosphere is a quasi-neutral gas mixture at each location. Thus, the number of electrons and negative ions is equal to the number of positive ions (assuming all ions are singly ionized). The global electron density maximum is located between 220 km and 400 km altitude and has values between $10 \times 10^5\,\mathrm{cm}^{-3}$ and $3 \times 10^6\,\mathrm{cm}^{-3}$ (Prölss, 2004, Section 4.1). Compared with the neutral number density (Figure 2.5a), the electron number density in the terrestrial ionosphere is several orders of magnitude lower. At roughly 1000 km altitude, protons (H^+) are the dominant ion species. Accordingly, this region is called *protonosphere*.

The primary source of charge carriers in Earth's ionosphere is *photoionization* arising from solar EUV and XUV radiation. Photoionization produces pairs of free electrons and positively charged ions when a photon with sufficient energy collides with a neutral atom or molecule. If the electrons have sufficient energy, they can trigger a secondary ionization. Additionally, at high latitudes, particle precipitation is an important charge carrier source (e.g., Prölss 2004, Section 4.2.1, R. Schunk and Nagy 2009, Chapter 9). The population of charge carriers is balanced by recombination processes (Prölss 2004, Section 4.2.2, R. Schunk and Nagy 2009, Section 8.4).

The ionosphere is subdivided into D-, E-, and F-region[1] (Last column in Figure 2.3). However, the boundaries of those regions are not well defined (Davies, 1990, Section 1.1), and only distinct on mid-latitudes at the day-side (R. Schunk and Nagy, 2009, Section 11.4). They are described by plasma frequency (R. Schunk and Nagy, 2009, Section 11.4) or ion composition (Prölss 2004, Section 4.1, R. Schunk and Nagy 2009, Section 2.4).

The D-region is dominated by cluster ions[2] and negative ions (not considered in Figure 2.6). Its upper boundary is located roughly at 90 km altitude. The E-region is the region dominated by molecular ions such as NO^+, ${O_2}^+$, and ${N_2}^+$. It is located roughly between 90 and 170 km. The number density of ions is six orders of magnitudes lower than the number density of neutral species. The F-region is dominated by atomic oxygen ions O^+. It is located between 170 km and 1000 km altitude and contains the global electron density maximum. The ion density at the peak is about two orders of magnitude lower. The region above the maximum is called *top-side ionosphere*. The F-region below the electron density maximum is further subdivided into a F1 and F2-region.

---

[1] The letters have no meaning and do not start from "A", as the number of regions could not be determined in advance (Silberstein, 1959).

[2] "An ion formed by the combination of two or more ions or atoms or molecules of a chemical species often in association with a second species." (Todd, 1991, p. 1549)

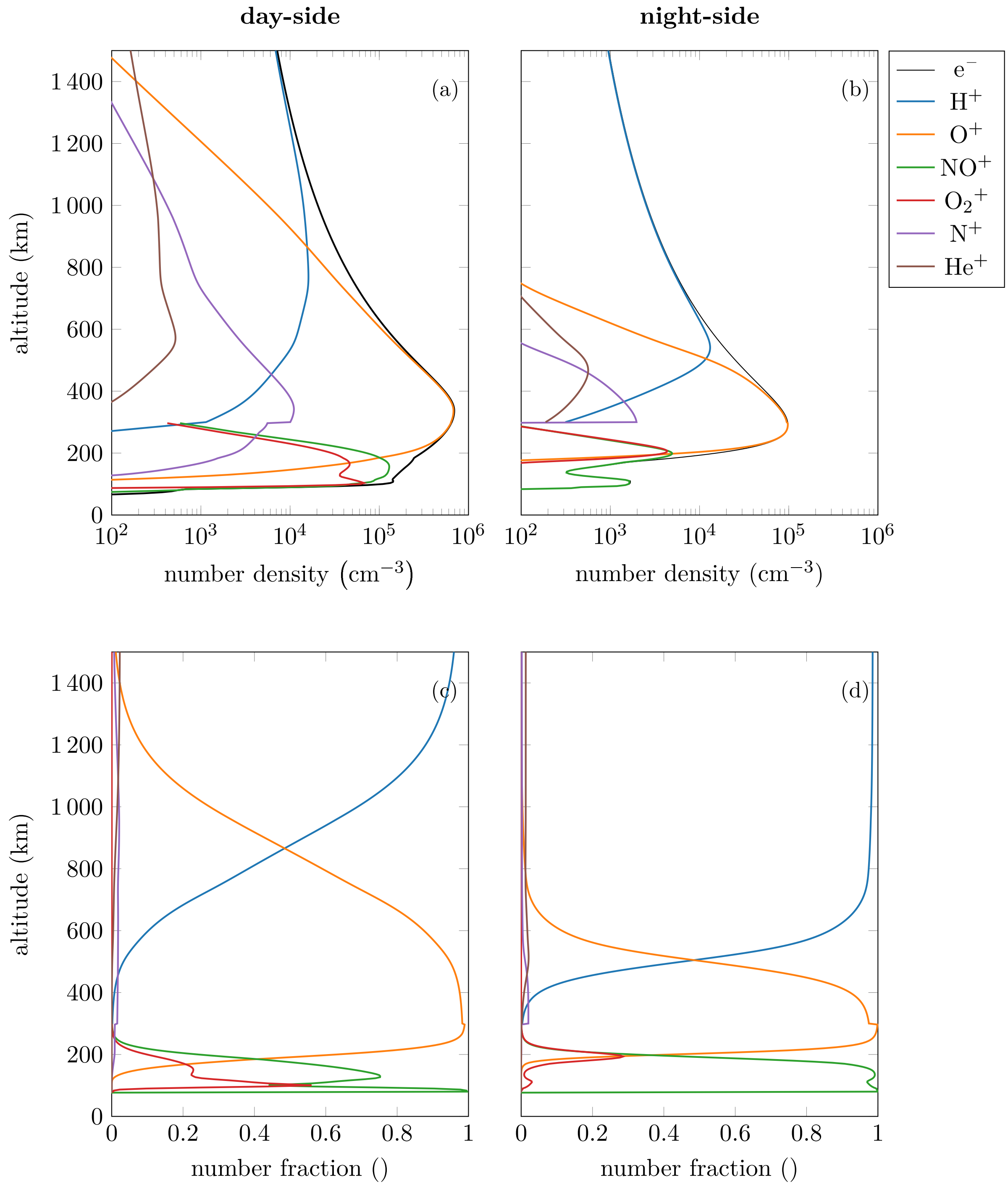

Figure 2.6.: This figure illustrates the vertical dependence of the charge carrier composition in the Earth's atmosphere. The profile was computed with the International Reference Ionosphere Model 2022 (IRI-2022, Bilitza et al. 2022) using default settings. The model assumes a quasi-neutral mixture, i.e., the number of electrons and negative ions is equal to the number of positive ions. The day-side profiles are located at 23.5°N 0°E on 21 June 2019, at 12:00 UTC+0. At this time and location, solar radiation enters the atmosphere almost orthogonally. The location of the night-side is in the opposite location. Panels c and d contain the number fraction w.r.t. the total number of ions, i.e., at each altitude the fractions sum up to one.

2.3. The Sun's Impact on Earth's upper Atmosphere

The source of space weather is the Sun (Luhmann and Solomon, 2014, p.479). The Sun is the heaviest body (1.99×10^{30} kg) of our solar system containing 99.9 % of its total mass (Prölss, 2004, Chapter 3). In terms of mass fraction the Sun mainly consists of Hydrogen (72 %) and Helium (26 %). Cecilia Payne was the first to discover that Hydrogen and Helium are the dominant species of stars (Payne, 1925, Table XXVIII). The remaining 2 % are particles with a mass number greater than four (Prölss, 2004, Chapter 3). Defining the visible solar disk as the Sun's surface (photosphere), the radius of the Sun is 6.957×10^{8} m (Prša et al., 2016, Table 1). The Sun is assumed to be 4.6×10^{9} years old (Aschwanden, 2014, Table 11.1) and has an energy production rate or luminosity of 3.828×10^{26} W (Prša et al., 2016, Table 1). The interior structure of the Sun is primarily explained by the equilibrium of pressure force and gravitational force. Since the gravitational force increases towards the center, the pressure and temperature get higher to keep the balance. Similar to the atmosphere, the density in the Sun almost decreases exponentially from its center to its surface (Prölss, 2004, Chapter 3).

A point located on the Sun's equator completes a full revolution approximately every 26.6 days as seen from Earth; this is called the synodical equatorial rotation period. The corresponding sideral period is about 24.8 days (Prölss, 2004, Chapter 3). The period depends on the solar latitude ϕ and can be approximated with (Aschwanden, 2014, p. 241)

$$T = \frac{360^\circ}{14.522\,^\circ\,\mathrm{d}^{-1} - 2.84\,^\circ\,\mathrm{d}^{-1}\sin^2(\phi)}. \tag{2.29}$$

The mean distance to Earth—one astronomical unit (AU)—is 149.6×10^{9} m. The minimal distance (January) is 147.1×10^{9} m and the maximal distance (July) 152.1×10^{9} m (Prölss, 2004, Table 3.1).

2.3.1. Electromagnetic Emission of the Sun

Of particular interest is the radiation emitted by the Sun since it interacts with the particles of Earth's upper atmosphere. The radiation is a product of the nuclear fusion inside the Sun (Prölss, 2004, Chapter 3). The time series in Figure 2.7b shows the total solar irradiance (TSI)—that is, the power per unit area over the entire spectrum—normalized to 1 AU. Compared with the mean value, the variations are three orders of magnitude lower. Thus, one can argue that the Sun has a quite constant energy output. Nevertheless, the total solar irradiance (TSI) variations are strong enough to affect Earth's atmosphere significantly. The most striking feature is the oscillation with a period of about eleven years. It is called the *solar activity cycle.* In fact, the mean period length of the solar cycle is eleven years with a standard deviation of 14 months (Hathaway, 2015, Figure 24).

Solar activity is described by various indices (see Section 2.3.1.2). The most prominent is the F10.7 index, which is the solar irradiance at 10.7 cm wavelength at the Earth's surface. It is often used as a proxy for EUV radiation, which cannot be measured from the ground since it is absorbed by the atmosphere (details follow in Section 2.3.1.1). The time series of the F10.7 index in Figure 2.7a shows the same eleven-year period associated with the solar activity

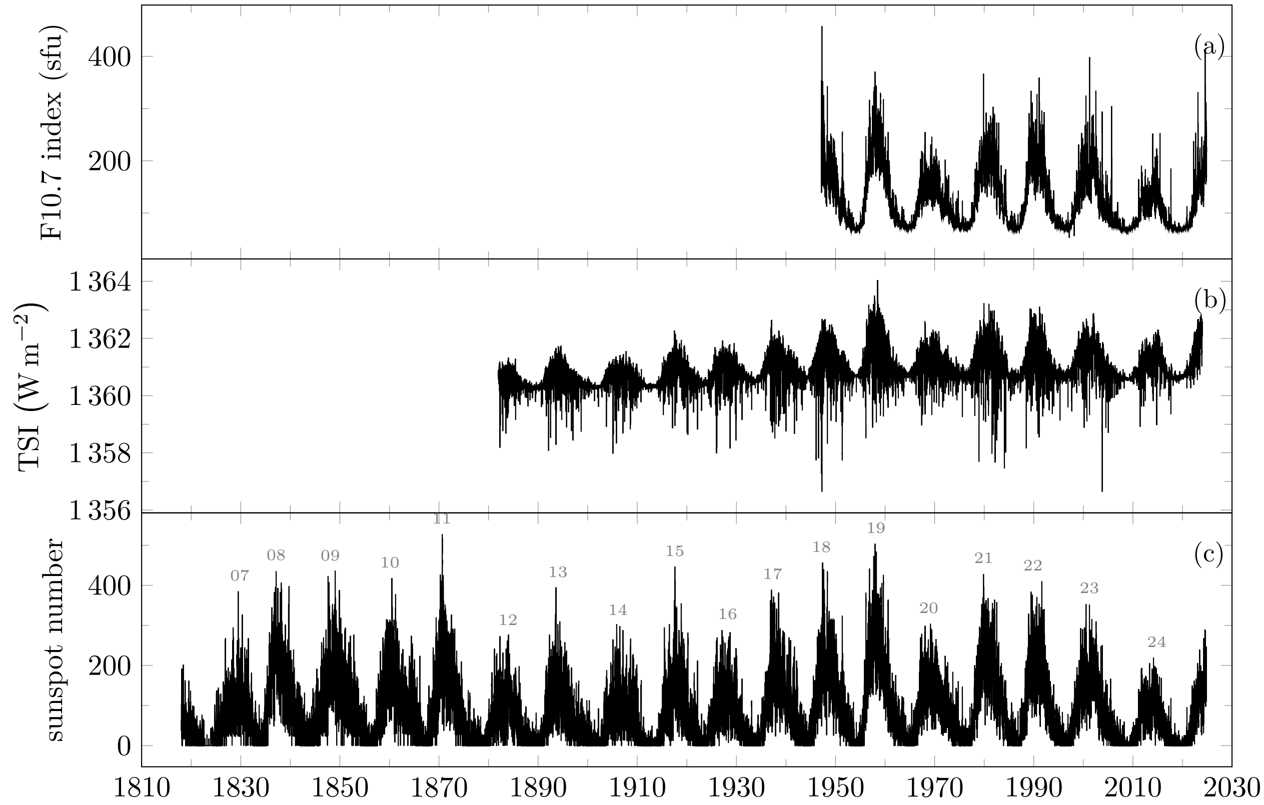

Figure 2.7.: Panel a is the Penticton solar radio flux at 10.7cm adjusted to 1 AU. Panel b is the total solar irradiance (TSI) normalized to 1 AU computed from NRL2 model (Coddington et al., 2016), and panel c shows the international sunspot number (SILSO World Data Center, 1818–2024). The solar cycles are numbered consecutively starting in 1755. The gray numbers in panel c indicate the corresponding solar cycle.

cycle. The same holds for the time series of the sunspot number in Figure 2.7c. Sunspots are "dark patches on the Sun where intense magnetic fields loop up through the surface from the deep interior" (Hathaway, 2015, p. 9). The solar cycle was discovered by Schwabe (1844), who counted the sunspots for fifteen years in sequence. The terms *solar maximum* and *solar minimum* are frequently used for time periods close to the maximum and minimum sunspot number, respectively. The solar cycle is associated with an inversion of the magnetic polarity at the solar maximum (Hathaway, 2015).

The Sun's radiation has a broad spectrum covering the range between gamma-rays and radio frequencies. In Figure 2.8, the spectrum before passing Earth's atmosphere ranging from XUV to infrared (IR) is presented for two different days. 1 November 2003 represents solar maximum conditions (sunspot number: 153, F10.7: 210 sfu) and 1 June 2008 solar minimum conditions (sunspot number: 0, F10.7: 67 sfu). When comparing quiet and active conditions, the largest differences w.r.t. the order of magnitude are within the XUV and EUV range (see Table 2.3 for specifications of those ranges). Beginning at the MUV range, it is hard to detect any difference between solar minimum and maximum conditions. The striking peak at 121.6 nm corresponds to the Lyman-α radiation of hydrogen (Liddle and Loveday, 2008; Lyman, 1906). At 58.4 nm

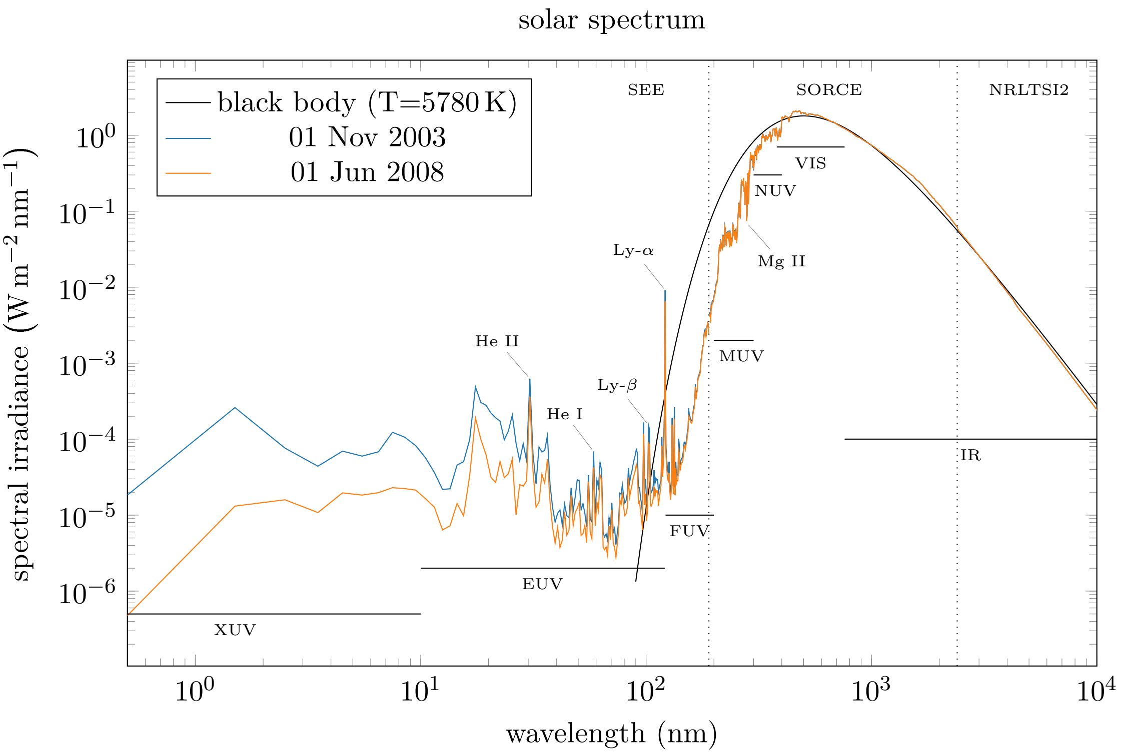

Figure 2.8.: Solar emission spectrum from 0.5 nm to 10 000 nm for solar maximum (2003) and minimum (2008) conditions. The spectra are averaged over a day and normalized to 1 AU. The spectra refer to solar radiation before it passes through the Earth's atmosphere. The data for this plot comes from three sources. The wavelengths between 0.5 nm to 190 nm are observations from the Solar EUV Experiment (SEE; T. N. Woods et al. 2005, level 3 data). The range from 190 nm to 2400 nm are observations from the SORCE mission (T. Woods et al., 2021) and wavelengths from 2400 nm to 10 000 nm are computed by the NRLSSI2 model (Coddington et al., 2016). The bands of the electromagnetic spectrum, indicated by horizontal black lines, are listed in Table 2.3.
In addition, a solid black line shows the idealized spectrum that the Sun would emit if it were a black body with a temperature of 5780 K.

and 30.4 nm, one can see the emission lines of neutral Helium (He I) and single ionized Helium (He II), respectively. The global maximum is located in the visible spectrum at about 479 nm.

The irradiance can be considered as an energy flux density with units $\frac{\mathrm{J}}{\mathrm{m}^2\mathrm{s}} = \frac{\mathrm{W}}{\mathrm{m}^2}$. Given the spectral irradiances S (units $\frac{\mathrm{W}}{\mathrm{m}^2\mathrm{m}}$) in the interval $[\lambda_0, \lambda_1]$ one can compute the energy flux density with

$$\Phi = \int_{\lambda_1}^{\lambda_2} S(\lambda) d\lambda. \tag{2.30}$$

The time series in Figure 2.9 showing the flux densities of the bands in Table 2.3 were computed by applying Equation 2.30 to the corresponding bands. The time series is almost eleven years long, so one can observe several periodic effects. Following Prölss (2004, p.99), variations in XUV (Figure 2.9a), EUV (Figure 2.9b) and radio frequency (Figure 2.9h) are caused by geometric

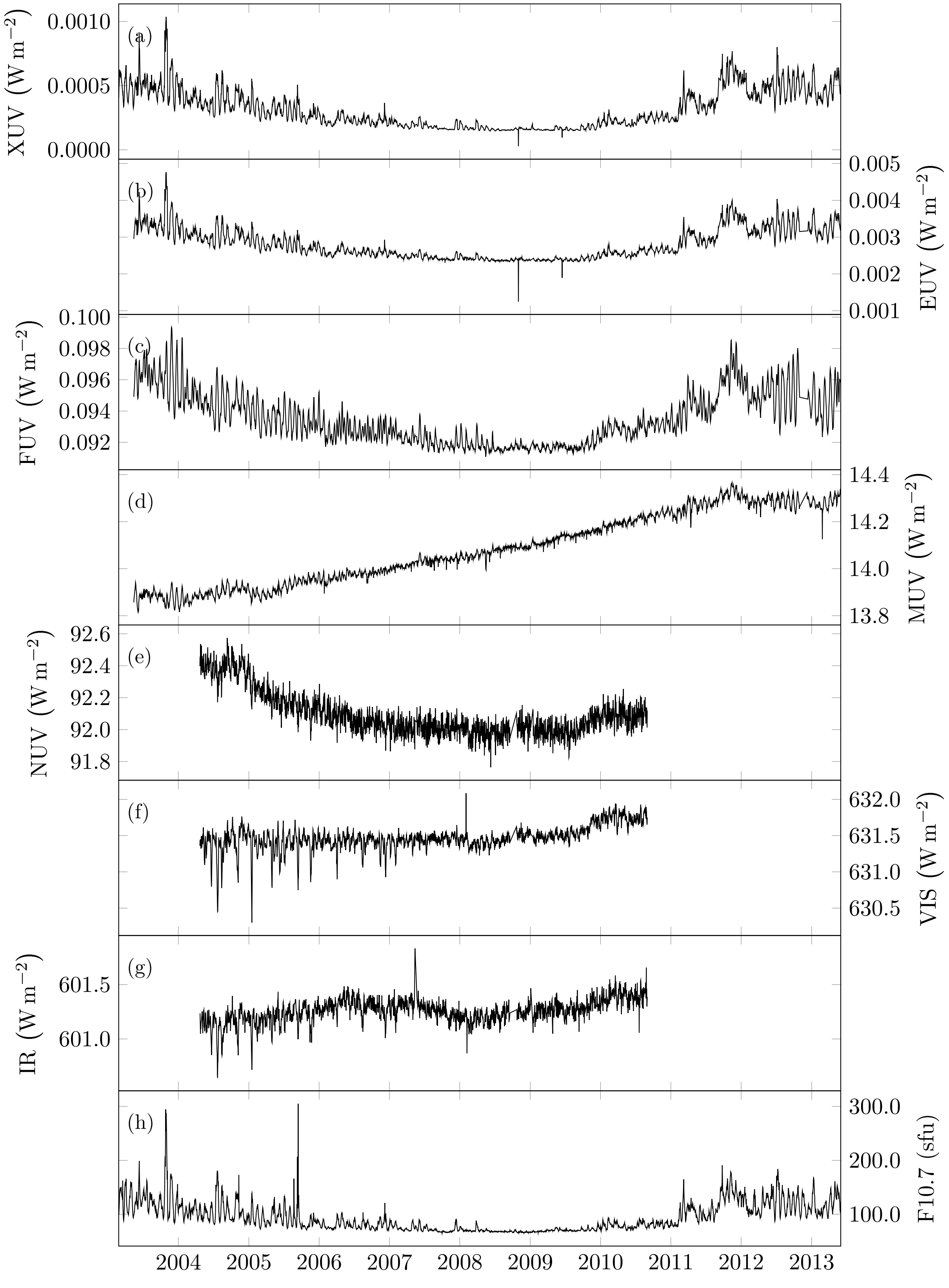

Figure 2.9.: The data source for panels a-g is the daily SORCE data (T. Woods et al., 2021). The fluxes of the corresponding wavelength ranges were computed by integrating the spectral irradiance over the wavelength using the trapezoidal rule. It is easy to identify the synodical rotation and solar activity cycle in panels a, b, c and h. By comparing panel b and panel h, it becomes obvious why the F10.7 index is used as a proxy for the EUV radiation.

Table 2.3.: Bands of the electromagnetic spectrum

		wavelength interval (nm)	
short name	name	*ISO 21348* (2007)	observed by SORCE
XUV	soft X-rays	$0.1 \leqslant \lambda < 10$	$0.50 \leqslant \lambda < 9.50$
EUV	extreme ultraviolet	$10 \leqslant \lambda < 121$	$0.50 \leqslant \lambda < 120.50$
	Hydrogen Lyman-α	$121 \leqslant \lambda < 122$	$\lambda = 121.5$
FUV	far ultraviolet	$122 \leqslant \lambda < 200$	$122.50 \leqslant \lambda < 199.50$
MUV	middle ultraviolet	$200 \leqslant \lambda < 300$	$200.50 \leqslant \lambda < 299.50$
NUV	near ultraviolet	$300 \leqslant \lambda < 400$	$300.50 \leqslant \lambda < 399.79$
VIS	visible light	$380 \leqslant \lambda < 760$	$380.04 \leqslant \lambda < 758.01$
IR	infrared	$760 \leqslant \lambda < 10^6$	$761.26 \leqslant \lambda < 2412.34$

effects and intrinsic variations of the Sun. The geometric effects are the rotation of the Sun and the orbit of the Earth. The rotation of the Sun causes an oscillation with 27 days (synodical equatorial rotation period). By reason of the elliptical orbit of the Earth, the distance to the Sun varies within one year, changing the energy flux density. However, the time series in Figure 2.9 are adjusted to 1 AU so that this effect is eliminated. The intrinsic variations are the solar cycle (eleven years), expansion of emission centers (days to weeks), and solar flares (minutes to hours) (Prölss, 2004, p.99). Relative variations in the MUV (Figure 2.9d), near ultraviolet (NUV) (Figure 2.9e), visible light (VIS) (Figure 2.9f) and IR (Figure 2.9g) are lower compared with the other spectra. Although the F10.7 index is observed in the radio frequency range, it is highly correlated with the EUV and XUV time series: The Pearson correlation between F10.7 index and XUV as well as EUV is 0.95.

2.3.1.1. Absorption in Earth's Atmosphere

In a large-scale picture, the atmosphere has two windows that permit radiation with corresponding frequency to reach the ground. Outside those windows, radiation cannot pass. One window is located around the visible light range, and the other is found in the radio frequency range (see Figure 2.10a). Radiation with a frequency in the MUV range or higher is stopped by the atmosphere, making life on Earth as we know it possible by shielding it from most of the ionizing radiation emitted by the Sun (see Figure 2.8). Ozone, primarily located in the stratosphere, is important for the absorption of MUV radiation (Figure 2.10d). The two windows are separated by an opaque block in the far infrared range, mainly associated with absorption by water vapor in the troposphere (Figure 2.10b). For wavelengths about below 10 m (30 MHz), the electrons in the ionosphere act like a mirror making the atmosphere opaque above this limit (e.g. Prölss, 2004, Section 4.7.3).

Where radiation is absorbed in the Earth's atmosphere depends on the composition along the path of the photon flux through the atmosphere. For example, a significant amount of MUV radiation is absorbed by ozone in the stratosphere, where its concentration is highest. Further important factors for the absorption are the absorption cross-sections and activation energies of the gas particles as well as the amount and energy of the photons entering the atmosphere (P. M. Banks and Kockarts, 1973a, Chapter 11). Figure 2 in Bowman et al. (2008b) shows the

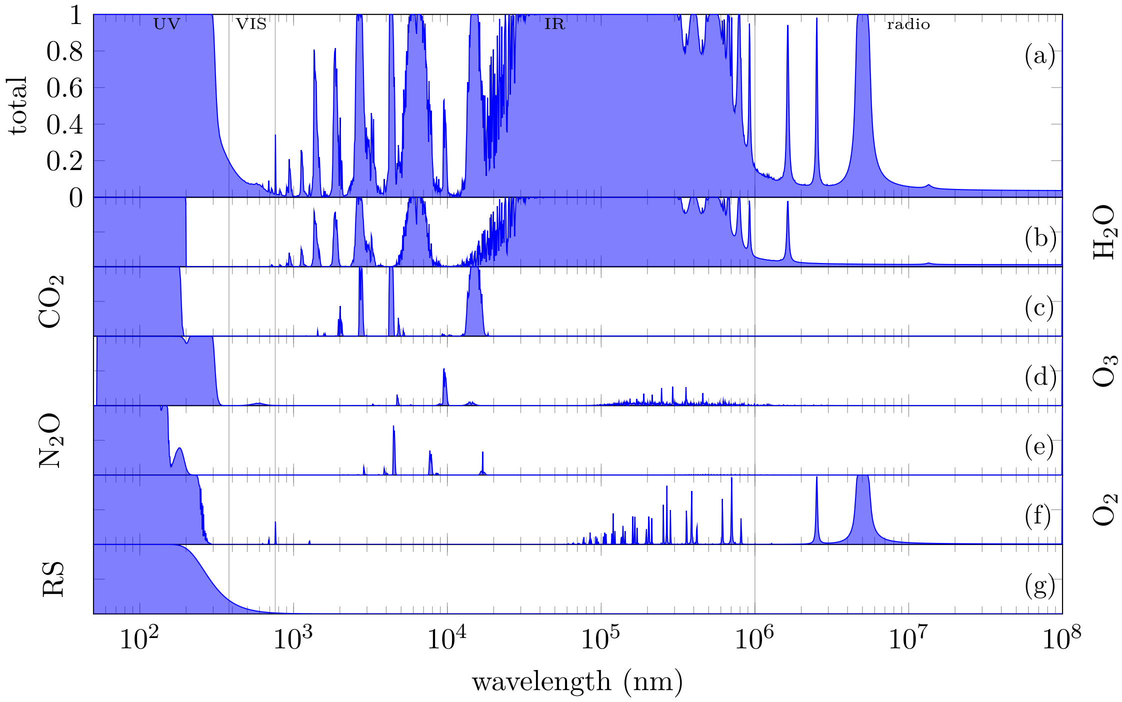

Figure 2.10.: Atmospheric zenith opacity computed with the Planetary Spectrum Generator (Villanueva et al., 2018) developed at Goddard Space Flight Center. A value of one means that no radiation at the corresponding wavelength reaches the ground. A value of zero means the atmosphere is transparent at the corresponding wavelength. The upper panel shows the opacity of the atmosphere, while the other panels contain the contribution of some important species and Raylight scatter (RS). The atmosphere becomes opaque outside the plot at wavelengths longer than 10 m. The opacity was computed at the subsolar point on 21 June 2023 at 12:00 UTC+0. Thus, the radiation enters the atmosphere in an almost orthogonal way.

altitude of the maximum rate of absorption as a function of the wavelength. There are three important absorption processes in the upper atmosphere: photodissociation, photoionization, and dissociative photoionization (Prölss, 2004, Section 3.2.1). Photodissociation (e.g., P. M. Banks and Kockarts, 1973a, Chapter 8) is the separation of a molecule into parts triggered by the absorption of a photon with sufficient energy to overcome the molecular binding. Photoionization (e.g., P. M. Banks and Kockarts, 1973a, Chapter 7) releases free electrons originating from atoms or molecules when hit by photons with sufficient energy. Dissociative photoionization is the combination of both processes.

The number of absorbed photons depends on the incident solar photon flux and the neutral number density of the atmosphere, both of which vary with altitude. At high altitudes, the neutral density is so low that the photon flux passes through the atmosphere with almost no chance of collision. As altitude decreases, the probability of collision increases due to the increase in neutral density, but each collision reduces the photon flux. Therefore, at low altitudes where the density is high, collisions are unlikely because the majority of the photons have already been absorbed. The absorption maximum can be found between those extremes (e.g., Prölss 2004, Section 4.2.1 or Baumjohann 2012, Section 4.3.1). The absorption of solar radiation produces ions, free electrons, and heat. For idealized conditions, a height profile of the ion production

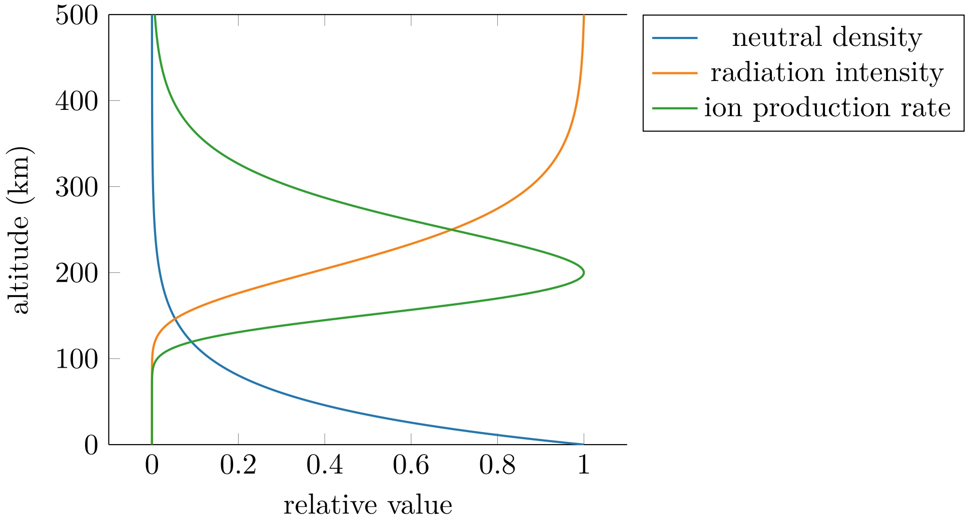

Figure 2.11.: The height profile of ion production (green line) is determined by two processes. Firstly, the neutral density increases from the top of the atmosphere towards the ground (blue line). Secondly, the photon flux decreases with each (non-elastic) collision with atmospheric particles on the way from the Sun to the ground (orange line). At high altitudes, collisions are unlikely due to the rarefied atmosphere. At low altitudes with high density, collisions are less frequent because most of the photons have already collided. All functions are normalized with their maximum to plot them together in one panel. The figure illustrates an idealized scenario for an isothermal atmosphere with parallel plane layers, featuring only one exponentially decreasing species and monochromatic solar radiation entering the atmosphere perpendicularly. In that case, it is described by the Chapman production function. This figure is adopted from Prölss (2004, Figure 4.4) and Baumjohann (2012, Figure 4.6).

rate is shown in Figure 2.11. This profile is called the Chapman production function. For actual conditions involving a multi-species atmosphere with different absorption cross-sections, a broad solar spectrum, and a curved non-isothermal atmosphere, the Chapman function does not agree well with the actual profile. However, the individual contributions from photons associated with a narrow frequency band can be explained well by the Chapman production function (Prölss, 2004, Figure 4.6). The number of ions and electrons is reduced by recombination processes. Thus, in the night-side upper atmosphere, the number of charge carriers is small except for the polar oval introduced later in Section 2.3.2.1.

During the absorption process, a fraction of the energy of the photon is transformed into heat (e.g., Prölss, 2004, Section 3.3). This transfer increases the temperature of the electrons, ions, and neutral particles in the upper atmosphere. The electron gas is hotter than the ion gas, which in turn is hotter than the neutral gas (e.g., Prölss, 2004, Figure 4.3). An excessive heating of the atmosphere is averted by radiative cooling and heat conduction (e.g., Prölss, 2004, Section 3.3.3).

The temperature increase caused by the absorption of solar radiation has two opposite effects on the mass density: an expansion of the gas and an upward transport of air. While the expansion decreases the density at a given altitude, the upward transport of denser air from below increases the density at the same altitude. At about two scale heights above the heat input altitude, the transport-induced effect is greater than the decrease (see Appendix A.4). Therefore, the air on the day-side is denser compared with the night-side.

In summary, the absorption of solar UV-radiation turns the atmosphere into a conducting medium (the ionosphere), changes the composition, and increases the density.

2.3.1.2. Solar Indices

The main energy input of Earth's upper atmosphere is EUV radiation absorbed in the lower thermosphere. By reason of the absorption, solar EUV cannot be observed from the ground directly (see Figure 2.10), but only from satellites outside the atmosphere. As mentioned above, on the ground, one can observe radiation that is not absorbed (e.g., radio waves) as a proxy for solar EUV. There are several solar indices (Tobiska et al., 2008b, Table 1). Solar indices generally combine information from different spectral bands into a single number. This compression facilitates the construction of models, as constructing a model from the full spectra is difficult.

A very frequently employed solar index is the F10.7 index (e.g., Tapping, 2013). Since Earth's atmosphere is transparent in the radio frequency range, one can measure the solar radio flux from Earth's surface. The F10.7 index is a time series of the solar flux at 10.7 cm wavelength used as a proxy for EUV. Typically, it is given in solar flux units (sfu) which correspond to $10^{-22}\,\mathrm{W\,m^{-2}\,Hz^{-1}} = 10\,000\,\mathrm{Jy}$. It has been regularly observed since 1947 from radio telescopes located in Canada. Currently, the measurements are being carried out by the Dominion Radio Astrophysical Observatory near Penticton. Tapping (2013) states that the uncertainty of the F10.7 index is $\max\left(1, \frac{F10.7}{100}\right)$ sfu. Figure 2.7 shows the F10.7 index, the sun spot number, and total solar irradiance. The solar cycle is clearly visible in all time series. The F10.7 index is used as a proxy for EUV since they are highly correlated (see Figure 2.9).

Additional solar indices used by some models discussed in Chapter 5 are summarized in Appendix B.1.

2.3.2. Solar Wind and Interplanetary Magnetic Field

The solar wind and interplanetary magnetic field are drivers of the TIE-GCM. The corresponding model inputs are perturbed in Chapter 7 to compute the uncertainty of the TIE-GCM.

The solar wind (e.g. Prölss 2004, Section 6.1 or Gosling 2014) is a supersonic plasma continuously emitted by the Sun. Hence, the interplanetary space is not a vacuum but is filled by this plasma. The solar wind consists mainly of protons (H^+), electrons, and α-particles (H^{++}). The plasma travels about 3-4 days from the Sun to Earth.

The median velocity of the solar wind at Earth orbit (1 AU) is $442\,\mathrm{km\,s^{-1}}$. 90 % of all velocities (centered around the median) are between 320 and $710\,\mathrm{km\,s^{-1}}$. The median number density of the solar wind at 1 AU is $6.9\,\mathrm{cm^{-3}}$. 90 % of all solar wind number density values (centered around the median) are between 3 and $20\,\mathrm{cm^{-3}}$. The median number ratio of α-particles compared with protons is 4.7 % (Gosling, 2014, Table 12.1). The Sun's mass loss due to solar wind is about $6.8 \times 10^{16}\,\mathrm{kg\,year^{-1}}$ (Gosling, 2014). The yearly loss is 14 orders of magnitude lower than the total mass of the Sun.

The Sun's outward plasma stream and magnetic field are coupled. A simplified model of the plasma stream and magnetic field in the interplanetary space is described by Parker's spiral

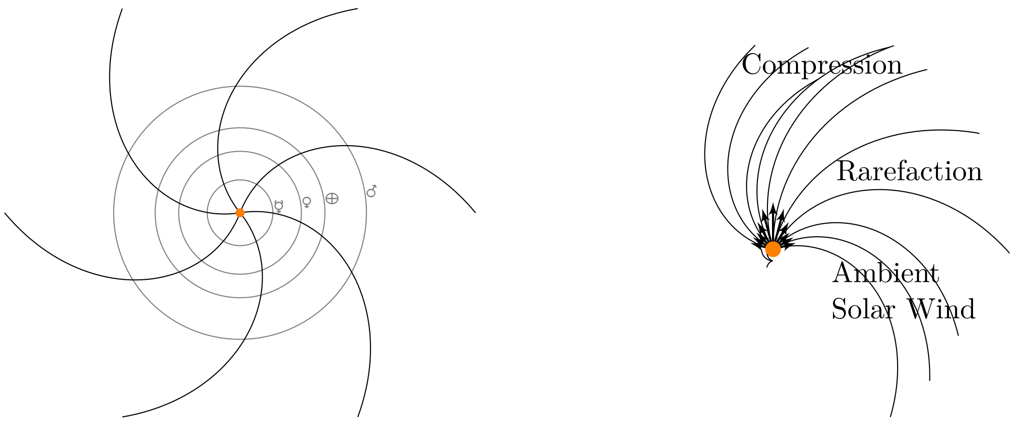

(a) The Parker spiral (E. N. Parker, 1958) describes the steady-state magnetic field of a rotating star with spherically symmetric plasma outflow. The outward-streaming solar wind drags the magnetic field of the star to infinity. By reason of rotation, the field lines (solid black lines) are spirals, whose footprints are anchored at the surface of the star (Marchaudon, 2019, Section 8.3). Here, the IMF of our solar system is shown. The distances of the planets to the Sun are illustrated by gray circles. The Parker model is valid for distances to the star where solar gravitation and outward acceleration by high coronal temperature are negligible. It depends on the angular velocity of the star and the velocity of the solar wind.

(b) Schematic illustration of the solar wind structure in the ecliptic with varying plasma velocities indicated by arrows. The stream lines associated with slow velocities have a larger curvature. The fast-moving streams overtake the slower streams, causing compression and, at the same time, rarefaction where slow streams are outrun. The varying velocities cause oscillations in the solar wind parameters associated with the rotation of the Sun. This figure is based on V. Pizzo (1978, Figure 1).

Figure 2.12.: Structure of the IMF and solar wind in ecliptic. The illustrations only provide a simple picture. More sophisticated models can be found, for example, in (Lhotka and Narita, 2019).

(E. N. Parker, 1958): Since the solar wind has an enormous electrical conductivity, it drags the magnetic field of the Sun outwards. The magnetic field is assumed to be frozen-in[1] into the plasma: The stream lines of the plasma flow and the field lines of the Sun's magnetic field coincide. Since the footprints of the field lines are anchored at the Sun's surface and the Sun rotates the shape of the streamlines and magnetic field lines is a spiral (see Figure 2.12a). Its shape depends on the velocity of the plasma flow and the angular velocity of the Sun. The spatially extended magnetic field of the Sun in the heliosphere is called interplanetary magnetic field (IMF; e.g., Lhotka and Narita 2019). Parker's spiral provides the "lowest-order picture" (Lhotka and Narita, 2019, p. 299) of the IMF.

In Figure 2.12a, a spherically symmetric plasma outflow is assumed. However, the corona is spatially variable, leading to considerable variations in plasma outflow. The corona has regions with opened and closed magnetic field lines[2]. Coronal holes are regions dominated by open

---

[1] More details about frozen field lines can be found, for example, in Baumjohann (2012, Section 5.1.2), Keith and Heikkila (2020, Section 1.5) or Kelley, Michael C. (2009, Section 2.5.2)

[2] The Maxwell equations prohibits the existence of magnetic monopoles (Gauss's law for magnetism). As a consequence magnetic, field lines are closed curves or extend to infinity. Thus, the term 'open field lines' does not mean that the field line does not close, but that the field line does not close within a particular region (Owens et al., 2011, Section 2.1).

magnetic field lines (e.g., Aschwanden, 2014, Section 5). The solar wind arising from coronal holes has higher velocities compared with other regions of the Sun. By reason of the variability of the corona, slow and fast plasma streams reach Earth alternating, as the Sun rotates. "Faster moving plasma overtakes slower moving plasma ahead while outrunning slower moving plasma behind" (Gosling, 2014, p. 266). This causes a compression and rarefaction of the solar wind, as illustrated in Figure 2.12b. Compressive regions in the solar equatorial plane where faster plasma overtakes slow plasma are called corotating interaction regions (CIR; e.g., Gosling and V. J. Pizzo 1999).

Figure 2.13 shows the time series of selected solar wind parameters and the IMF for an exemplary six-month period close to the solar minimum observed from various spacecrafts at the L1 Lagrange point. Figure 2.14 contains the power spectra of the same selected solar wind parameters and the IMF. All spectra have a strong peak associated with the rotation of the Sun. The spectra also contain distinct harmonics of the solar rotation. For the IMF, the solar rotation is the dominant period. For the plasma flow speed and proton temperature, the solar cycle is dominant. The IMF also shows a pronounced yearly dependency.

Among the periodic oscillations, there are also irregular and sudden short-term events such as solar flares and CMEs affecting the solar wind and the IMF. Solar flares and CMEs are eruptive phenomena in the solar corona driven by magnetic reconnection (Aschwanden, 2014, Section 6). They occur isolated or as a combination. A CME is an outburst of plasma that propagates through interplanetary space, expands in size, and carries the frozen-in magnetic field. A solar flare describes the rapid release of electromagnetic radiation in almost all wavelengths, including γ-radiation in case of large flares (Aschwanden, 2014, Section 6). The time series in Figure 2.13 contain a CME that hit Earth on 5 April 2010, causing a geomagnetic storm. At that point in time, the solar wind velocity and proton temperature rapidly increase and the IMF has large peaks. According to Figure 2.17, storms only occur during 5 % of the time, and only a small fraction of the storm time is severe. S. C. Chapman et al. (2020) instigated the occurrence of severe space weather events during the solar cycle and found that there is a roughly 4.4 years lasting quiet interval per cycle.

2.3.2.1. Interaction with Earth

The interaction of solar wind (Section 2.3.2) with Earth's environment is essential for understanding and modeling the upper atmosphere since it is an important energy input and perturbs the neutral density (e.g., Prölss, 2011).

The first encounter of the solar wind with Earth's environment is the (terrestrial) bow shock (e.g., Balogh and Treumann 2013, Section 10.2.1 or Prölss 2004, Section 6.4) that is a (supercritical) collisionless shock (Balogh and Treumann 2013 or Baumjohann 2012, section 13.2) caused by the interaction of Earth's magnetic field with the solar wind. The concept is similar to an ordinary gas, where shock waves are produced by objects flying with relative velocities faster than the speed of sound. However, the mean free path of the solar wind is so large (almost 1 AU at Earth orbit) that particle collisions cannot create this shock. Therefore, the shock is categorized as collisionless. Instead, the shock is caused by long-range electromagnetic

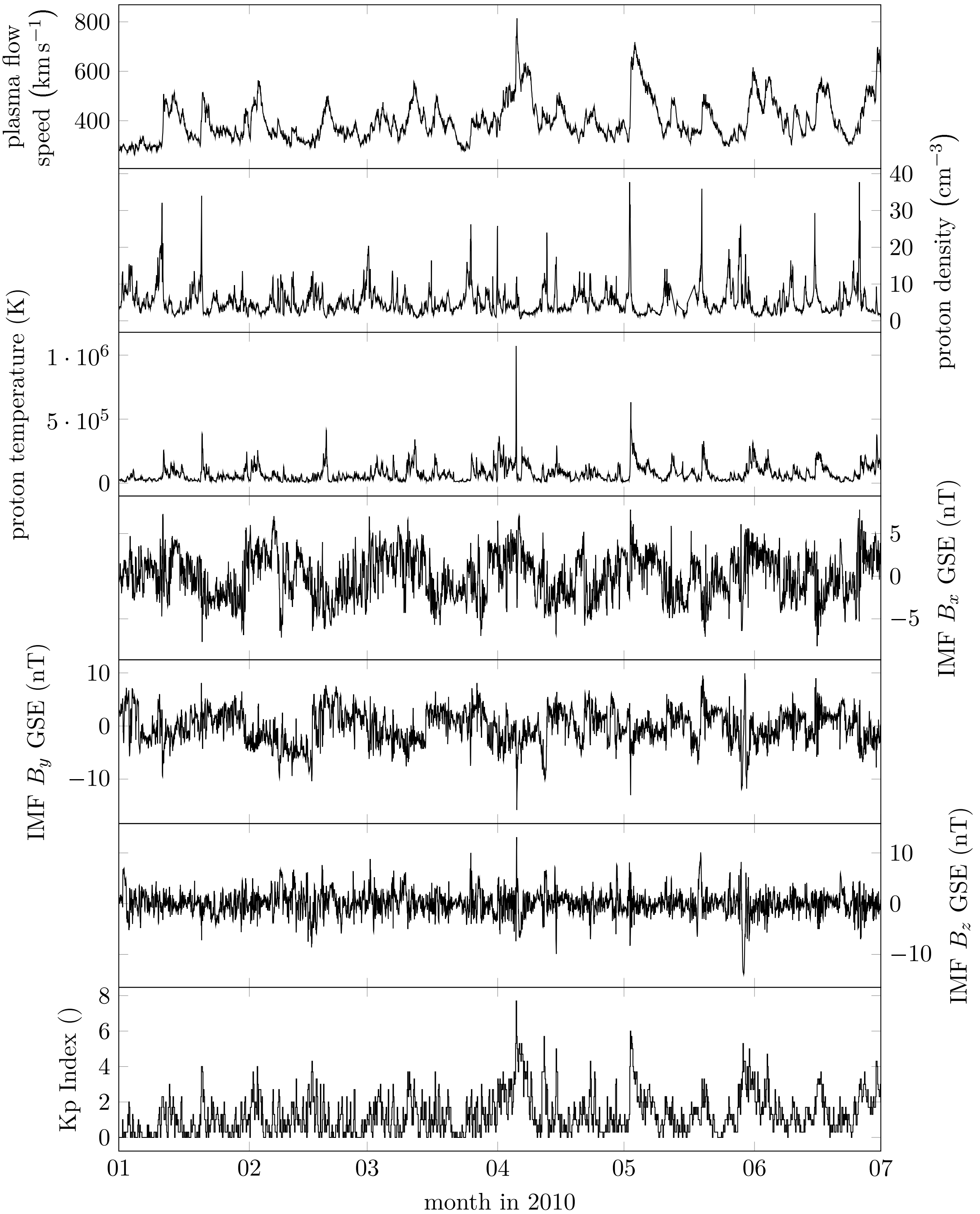

Figure 2.13.: Time series of selected solar wind parameters, the IMF (in geocentric solar ecliptic (GSE) frame, see Appendix E.2) and the Kp index in the first half of 2010 using the OMNI2 dataset with hourly resolution (Papitashvili and King, 2020c). The Kp index is measured at the Earth's surface, while the other time series are observed from the L1 Lagrange point.

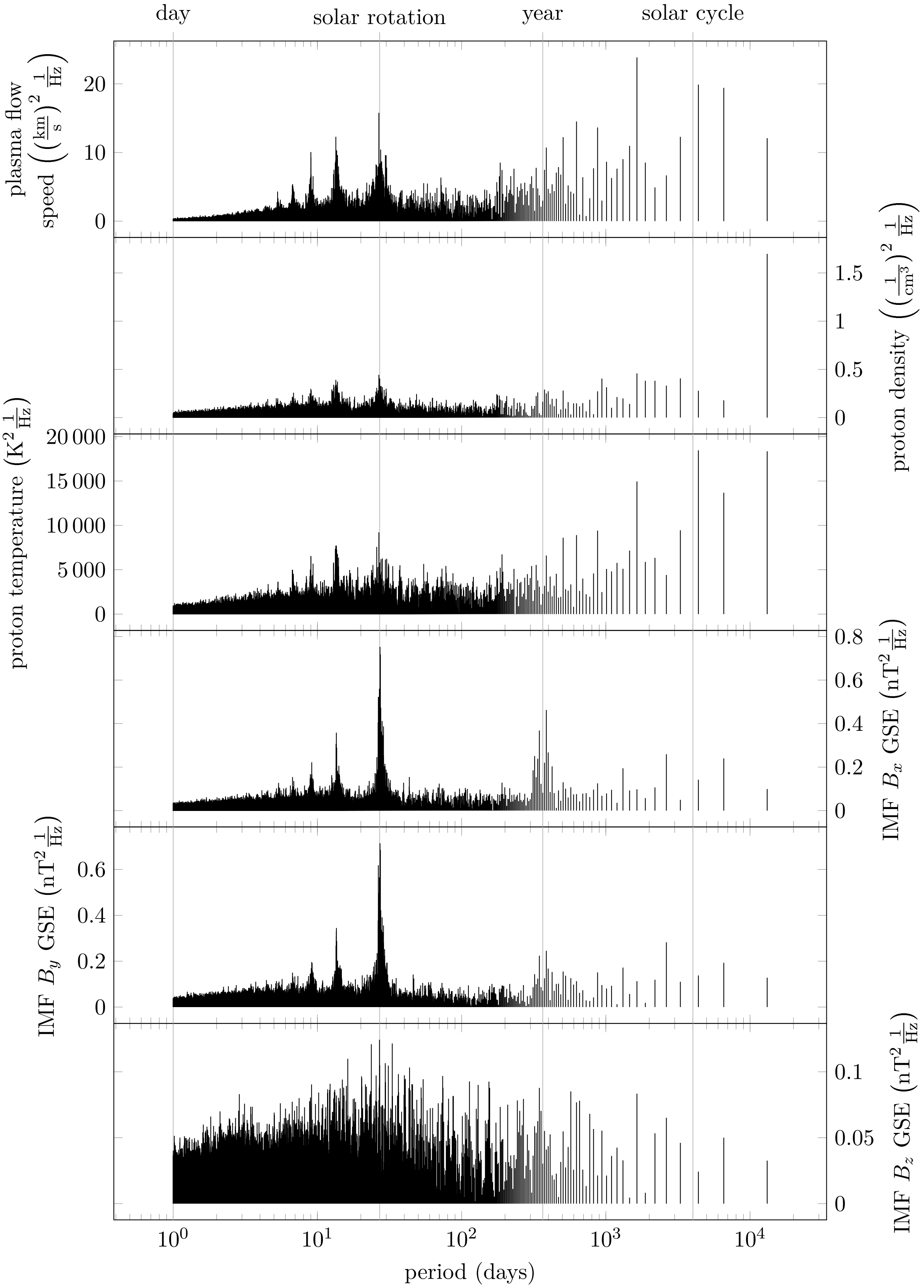

Figure 2.14.: Power spectra of selected solar wind parameters and the IMF (in GSE frame, see Appendix E.2) computed from OMNI2 dataset with hourly resolution (Papitashvili and King, 2020c) using FFT and data between 1984 and 2020. Distinct peaks corresponding to the Sun's rotation and corresponding harmonics are visible in all spectra.

interaction (Prölss, 2004, Section 6.4.5). The shock slows down the plasma to subsonic speeds. About 90 % of the solar wind is diverted by the shock (Keith and Heikkila, 2020, Section 1.3.1).

The geomagnetic field in the vicinity of the Earth (roughly six Earth radii) is approximately a dipole field that is tilted w.r.t. Earth's rotation axis (e.g., Prölss, 2004, Section 5.2). However, it is subject to spatial and temporal variations, which are described, for example, by the International Geomagnetic Reference Field (IGRF; Alken et al. 2021) .

The magnetosphere is "the region above the ionosphere in which the magnetic field of the Earth has a dominant control over the motions of gas and fast-charged particles [...]" (Gold, 1959). The outer boundary of the magnetosphere is called the magnetopause (see Figure 2.15). "It separates the solar wind plasma and the IMF from the geomagnetic field and plasma of primarily terrestrial origin" (Keith and Heikkila, 2020, p. 34) and "is determined by the pressure balance between the solar wind and the planetary magnetic field" (Parks, 2015, p. 1). The solar wind shapes the magnetopause as sketched in Figure 2.15. The distance from the magnetopause on the day-side to Earth is about 10 Earth radii (measured from the subsolar point) and is known to fluctuate about a few Earth radii, mainly depending on the dynamic pressure of the solar wind. The night-side magnetosphere is also called magnetotail because of its extended field lines whose shape is similar to the tail of a comet (Prölss, 2004, Section 5.5.1). The extent of the magnetotail is not well known but it exceeds 100 AU (Parks, 2015, p.1). The region between the bow shock and the magnetopause is the magnetoheath (e.g., Keith and Heikkila, 2020, Section 1.8).

The region where the magnetic field lines are separated between the day-side and night-side is called cusp (Prölss, 2004, Section 5.5.1). Here, solar wind particles can enter the magnetosphere.

The interaction of the IMF with the terrestrial magnetic field is explained by the Dungey Cycle (Dungey, 1961): When the field lines of the IMF encounter the terrestrial field lines at the magnetopause, they merge. The merged field line splits into two 'open' field lines with one footprint on Earth (blue field lines in Figure 2.15). The solar wind carries the 'open' field lines in the opposite direction to the Sun, over the poles, and to the magnetosphere's tail. At the end of the tail, the 'open' field lines reconnect, causing a plasma transport from the tail towards Earth (Baumjohann 2012, Section 5.2.1 or Section 2.2.1 Milan and Grocott 2021).

If the equilibrium between solar wind pressure and magnetic pressure shaping the magnetopause is disturbed, for example, by reconnection of magnetic field lines (Dungey Cycle), large-scale magnetospheric flows are excited to rebalance the system (Milan and Grocott, 2021, Section 2.3). "In a steady state this causes a continuous circulation of the magnetospheric flux and plasma, and this magnetospheric convection is coupled to the ionosphere by tension forces and gives rise to ionospheric convection." (Milan and Grocott, 2021, p. 27)

The plasma sheet is located within the region of 'closed' field lines (see Figure 2.15) located around the equatorial plane. The lower boundary is located at around 6 Earth radii (Gabrielse et al., 2022). The plasma in the solar wind, magnetoheath, plasmasheet, plasmasphere, and lobes can be distinguished by the temperature and density (see Gabrielse et al. 2022, Figure 4.1 or Baumjohann 2012, Figure 1.2).

The charge carriers in the magnetosphere and ionosphere cannot move freely in the magnetic and electric fields, instead one observes gyro-, oscillatory-, drift- and composite charge carrier

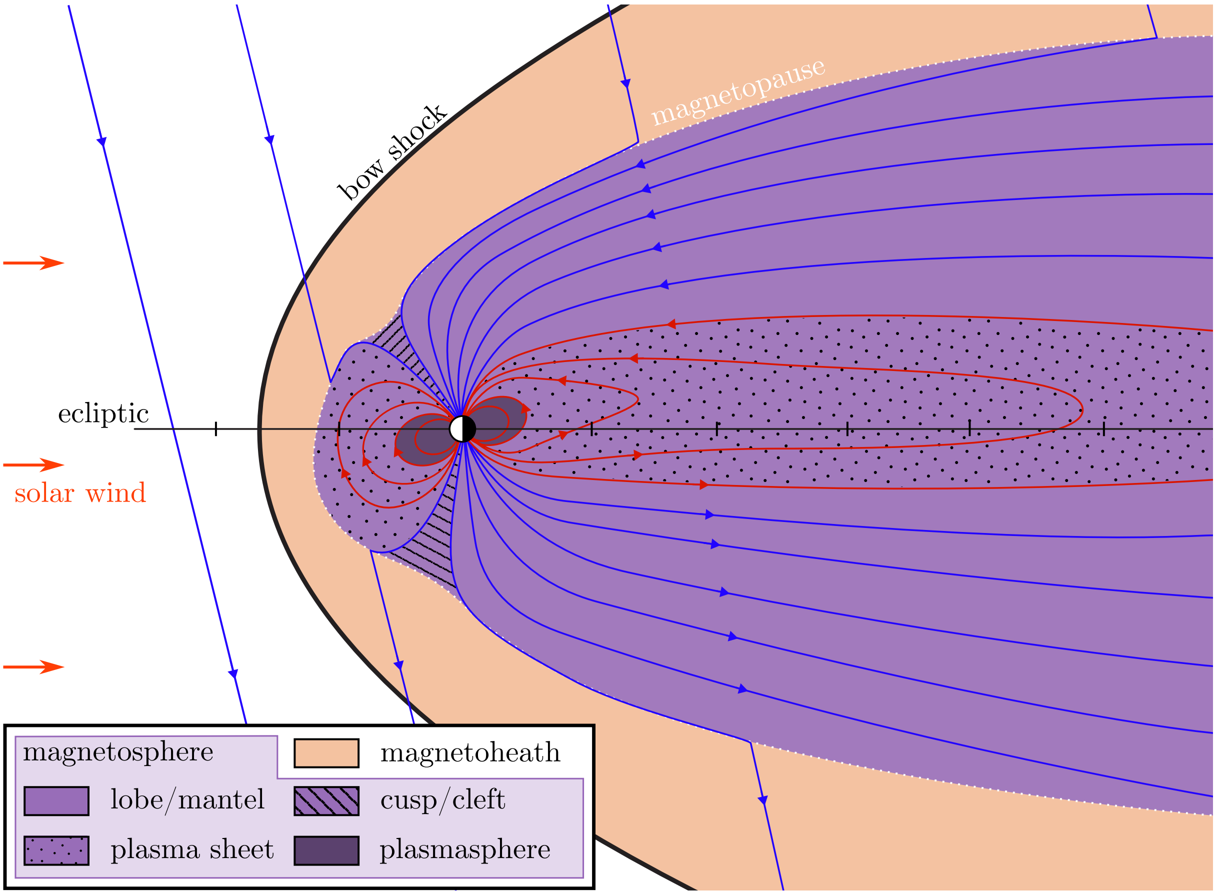

Figure 2.15.: Schematic cross-section of the magnetosphere in the x-z plane of the geocentric solar magnetospheric (GSM) system (see Appendix E.2) based on Milan (2009, Figure 1). The distance between two ticks is ten Earth radii. The field lines of the IMF merge with the terrestrial field lines and reconnect at the end of the magnetotail (not visible in this Figure, see Baumjohann (2012, Figure 5.5) for more details of this process). The merged field lines (only one footprint on Earth) are called 'open' field lines (blue lines in this figure). The field lines that are not interconnected across the magnetopause with the IMF are called 'closed' field lines (red lines). At the bow shock, the supersonic solar wind decelerates to subsonic speed. The magnetosphere is the part of the magnetic field dominated by Earth's magnetic field. The boundary layer of the magnetosphere is called magnetopause (white dotted line). The region between the bow shock and magnetopause is the magnetoheath. At the cusp (marked with a pattern of parallel lines), the field lines are separated between those entering the magnetotail and those headed towards the Sun. This cross-section only provides a limited picture of the magnetosphere. Three-dimensional drawings of the magnetosphere can be found, for example, in Yau et al. (2019b, Figure 2.5.1) or Keith and Heikkila (2020, Figure 1.1).

motion (e.g., Prölss 2004, Section 5.3; Baumjohann 2012, Chapter 2; Milan and Grocott 2021, Section 2.2.2; or Keith and Heikkila 2020, Section 1.4.5).

The polar oval (auroral oval) is a ring-like structure at both magnetic poles. Here, the northern and southern lights occur. The inner radius is approximately 15°. The center is shifted a few degrees from the magnetic pole towards the night-side. The outer radius is a few degrees larger than the inner radius. The oval is wider in the midnight sector. The size of the polar oval

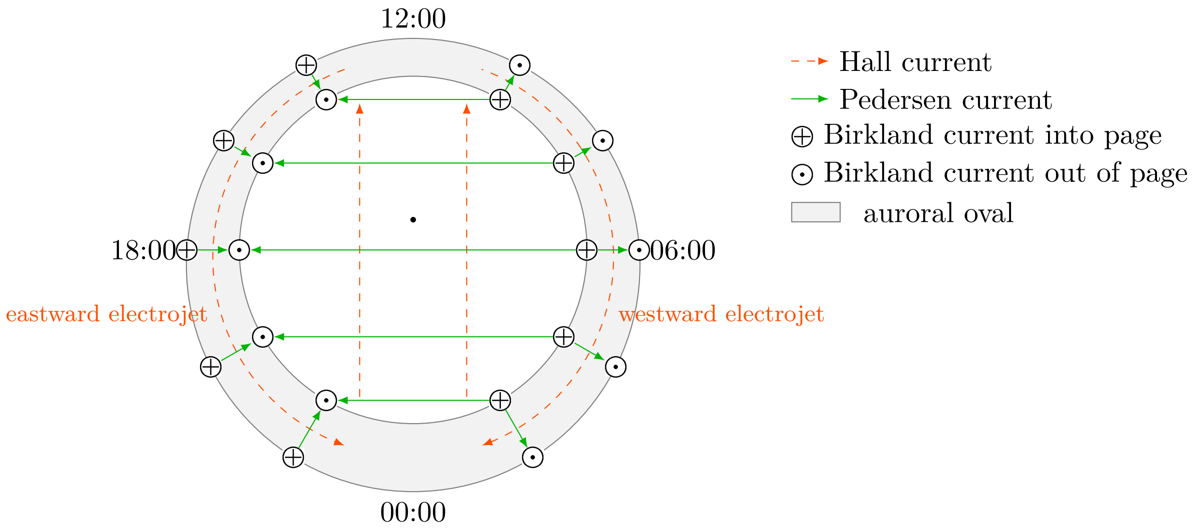

Figure 2.16.: Schematic of electrical currents at high latitudes adopted from Prölss (2004, Figure 7.10). The magnetic north pole is marked with a black dot. The orientation is given by the local time. Birkland currents are also called field-aligned currents. Birkland currents located at the outer and inner circle are called Region 2 and Region 1 currents, respectively. A three-dimensional version of this plot can be found, for example, in Palmroth et al. (2021, Figure 6).

is subject to temporal variations. A geomagnetic storm causes an expansion of the oval. The region surrounded by the inner edge of the polar oval is called polar cap. The magnetic field lines going through the polar cap are those associated with the lobes of the magnetotail. The field lines from the night-side polar oval connect to the plasma sheet, and the field lines from the day-side polar oval to the cusp and magnetospheric boundary layer (Prölss, 2004, Section 7.1).

Several electrical currents within the magnetosphere are created by the motion of the electrons and ions in opposite directions. There are currents that flow perpendicular to the magnetic field lines and currents that are aligned to the field lines. Examples of perpendicular currents are the ring current, the electrojets within the auroral ovals, and the equatorial electrojet above the magnetic equator. The large-scale field-aligned currents connect the currents of the polar ionosphere with the magnetosphere (Baumjohann, 2012, Section 1.3).

Figure 2.16 shows the current system in the auroral region. Hall and Pedersen currents are perpendicular to the magnetic field. Pedersen currents are parallel to the electric field, while Hall currents are parallel to it. The electrojets in the polar oval are Hall currents flowing eastward and westward from the noon to the midnight sector. Within the polar cap, Hall currents connect the midnight and noon sectors. Birkland currents (field-aligned currents, Birkland 1908) are parallel to the magnetic field lines. They are located at the inner (region 1) and outer (region 2) edge of the polar oval (Iijima and Potemra, 1978). The upper atmosphere and magnetosphere are coupled by region 1 and 2 currents. The region 1 currents are aligned to the 'closed' night-side magnetic field lines and 'open' day-side field lines extending to the magnetotail. The magnetic field lines associated with region 2 currents extend to 7-10 Earth radii (Prölss, 2004, Section7.6.6). Within the polar oval, region 1 and 2 Birkland currents are connected by Pedersen currents. The region 1 Birkland currents are connected through the polar cap by Pedersen currents. The Hall and Pedersen currents (Figure 2.16) have the greatest intensity where the corresponding conductivity is greatest. Thus, both currents are strongest in the E-region (Prölss, 2004, Section 7.3.4). The Pedersen currents heat the atmosphere by *Joule heating* (e.g., Richmond, 2021), which is caused by the friction between the charge carriers colliding with the neutral particles (Prölss, 2004, Section 7.5.2).

Aurora/polar lights are caused by the incidence of energetic particles, mostly electrons. The particles originate not directly from the solar wind but from the plasma reservoirs connected via magnetic field lines with the auroral oval: the night-side plasma sheet and the day-side magnetospheric boundary layer (Prölss, 2004, Section 7.4). The collisions of the energetic particles with the gas in the upper atmosphere result in scattering, ionization, dissociation, and excitation. The dominant emissions of the aurora caused by excitation are the yellow-green line and the red lines of atomic oxygen, the blue-violet band associated with singly ionized molecular nitrogen, and the dark red bands of neutral molecular nitrogen (e.g., Prölss, 2004, Figure 7.14). Only a small fraction of the energy provided by the incident particles is converted to radiation (about 1 % or less). Most of the energy is converted to heat or potential chemical energy. In contrast to the heating associated with the absorption of solar UV radiation, this heating mechanism also occurs on the night-side (Prölss, 2004, Section 7.4.2).

The heat generated in the polar oval through particle precipitation (aurora) and Joule heating (ionospheric currents) causes an upward expansion. It drives horizontal winds, which distribute the heat over a wider area. The vertical wind affects the composition of the atmosphere: The fraction of heavier species increases while the fraction of lighter species decreases accordingly (Prölss, 2004, Section 7.5.3).

2.3.2.2. Geomagnetic Indices

Geomagnetic activity can be considered as the variation of Earth's magnetic field. There are several indices constructed to represent this variation (Love and Remick, 2007).

A prominent geomagnetic index is the Kp index (Bartels, 1949; Matzka et al., 2021a)–p stands for *planetary*–which is a combination of the K index (Bartels et al., 1939) acquired at thirteen subauroral observatories. The K-index is computed from the variation of the horizontal magnetic field component within 3 h at a specific location (see Love and Remick, 2007, Figure M32). Thus, there are eight values per day starting at midnight UTC+0. The Kp and K indices have 28 different values between zero and nine. Based on Kp values, the National Oceanic and Atmospheric Administration (NOAA) has introduced a scale for the classification of geomagnetic storms (NOAA, 2023). When applying the NOAA scale to the official Kp values (Matzka et al., 2021b), 95.1 % of the Kp values indicate quiet conditions. About two thirds of all storms are minor; only 0.01 % of the Kp values correspond to extreme storm conditions (see Figure 2.17).

Additional geomagnetic indices used by some models discussed in Chapter 5 are summarized in Appendix B.2.

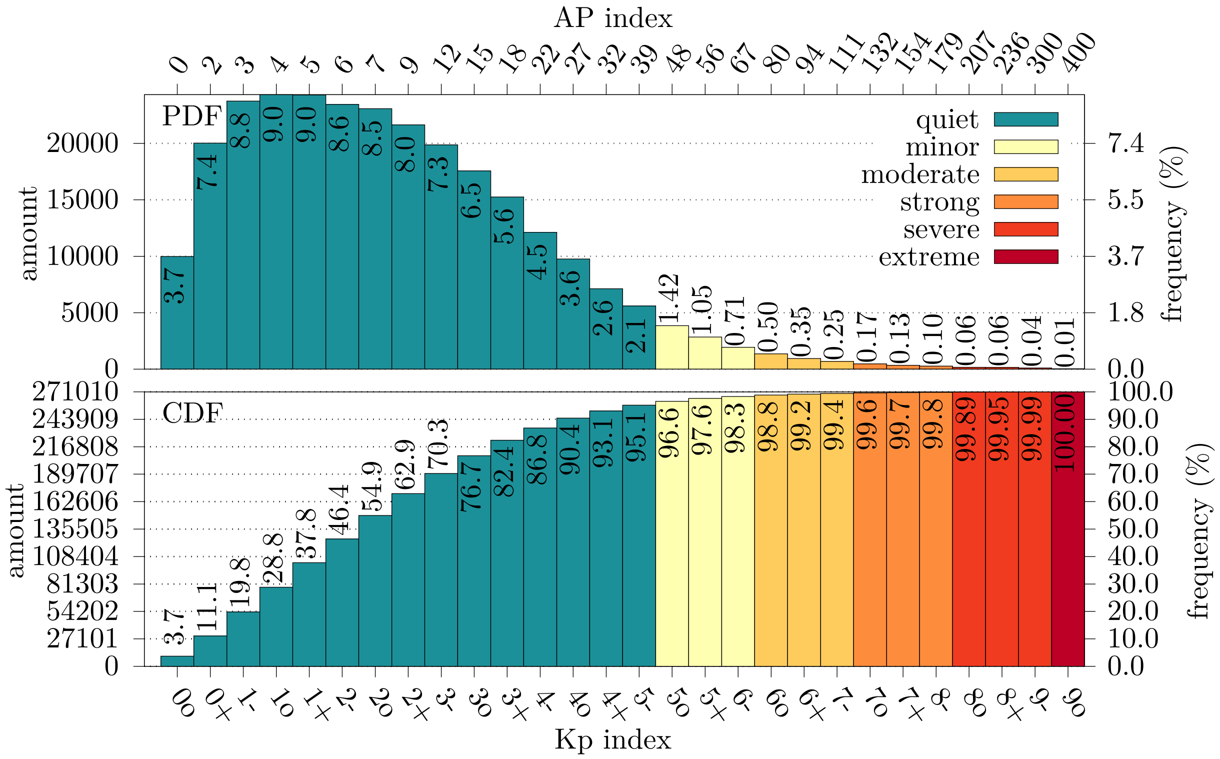

Figure 2.17.: Histogram of all observed Kp values from 1 January 1932 till 30 Sep 2024 provided by Matzka et al. (2021b). The upper and lower panels show the probability density function (PDF) and the cumulative distribution function (CDF), respectively. PDFs and CDFs are explained in Section 6.1. The Ap index is the Kp index transformed to a linear scale. The color of the bars indicates the geomagnetic storm scale from the NOAA (NOAA, 2023).

2.4. Vertical Coupling of the Atmosphere

Although the thermosphere is primarily controlled by space weather, it is also affected by the processes in the atmosphere below (e.g., H.-L. Liu, 2016). In this context, atmospheric tides (e.g., Oberheide et al., 2015; Schindelegger et al., 2023)–oscillations of neutral temperature, wind, composition, and density–are important as upward-propagating atmospheric tides originating in the lower atmosphere contribute to the longitudinal, seasonal-latitudinal, and day-to-day variability in the ionosphere and thermosphere (e.g., Schindelegger et al., 2023, Section 4.1 and references therein). Yue et al. (2023) found that the day-to-day variation of neutral mass density at 120 km altitude is 'exclusively controlled by the lower atmosphere', while at 300 km the Sun is the major driver. Yamazaki and Richmond (2013) describes how upward-propagating tides affect the density of the charge carriers via electrodynamic and mixing effects.

Atmospheric tides can be represented as zonally propagating waves that are periodic in longitude and time. The tidal spectrum includes many modes that can propagate upwards or downwards from the height at which they are excited. As tidal waves ascend in Earth's atmosphere, the density decreases, and their amplitude increases as a consequence of energy conservation (e.g., Schindelegger et al., 2023, Section 1). "Thus, tidal perturbations, which make up only a fraction of the meteorologically interesting variations in the troposphere, profoundly affect the large-scale dynamics of the mesosphere and lower thermosphere [...].” (Schindelegger et al., 2023)

Atmospheric tides are mainly generated by the Sun and the Moon. Solar tides are mainly caused by periodic heating, while lunar tides are associated with time-varying perturbations in Earth’s gravitational field. The semi-diurnal and diurnal solar tides have the largest impact. The amplitudes of the lunar tides are about an order of magnitude lower (Schindelegger et al., 2023).

A recent study by Dhadly et al. (2018) could not find evidence for a dependency of the migrating (sun-synchronous) semi-diurnal and diurnal tides on the solar cycle.

Apart from those periodic phenomena, isolated events such as volcanic eruptions (e.g., Li et al., 2023) or tsunamis (e.g., Garcia et al., 2014) can affect the thermosphere. For example, the eruption of Hunga Tonga-Hunga Ha’apai in 2022 (Vadas et al., 2023) caused density variations that were detected in 500 km altitude by the accelerometers onboard the GRACE-FO mission (Li et al., 2023).

2.5. Mass Density Variations

As established in Section 2.3.1 and 2.3.2, the solar radiation and solar wind are responsible for many spatial and temporal variations of the mass density of the upper atmosphere (e.g., Qian and Solomon, 2012). The impact of the Sun on satellites was discovered at the very beginning of the space era. Jacchia (1959b) found oscillations in the orbit of Sputnik II (1957 β 1) that could not explained by gravity. He attributed those oscillations to the rotation of the Sun (see Section 2.3). Jacchia (1959a) also discovered an anomaly in the orbit of the launch vehicle of Sputnik 3 (1958δ1), which was caused by a geomagnetic storm (Prölss, 2011). A few years later, Paetzold and Zschorner (1961) discovered the semiannual variation of the neutral density.

The following discussion is based on data from the NRLMSIS 2.0 empirical model (see Section 5.2.1). This model was fitted from many different observations and represents the average state of the atmosphere well. Other models yield different values, but the general structure of the atmosphere discussed in this section can be produced with all recent models.

Figure 2.18 shows the neutral mass density from 100 to 500 km altitude. The neutral mass density on the day-side is generally greater than on the night-side. This is explained by the heating and associated up-welling of denser air caused by absorption of solar radiation (see Section 2.3.1.1). At an altitude of 100 km, the difference between the day and night sides is less pronounced compared with higher altitudes. This is because, at this altitude, upward propagating atmospheric tides excited in lower layers are the dominant source of density variations. The maximum of the neutral mass density (white triangle) is on the day-side and delayed w.r.t. the subsolar point (white circle) since the impulse response of the atmosphere to heating is not zero. In Figure 2.18, the delay is roughly 3 h at 500 km altitude and 2 h at 100 km. The height dependency of this delay is also indicated in Figure 2.19 a and b with a red line, which connects the locations of the density maxima at each altitude. The angle between the Sun (12:00) and the maximum mass density increases with altitude. Comparing the contour lines (solid white lines) in Figure 2.19 with the dashed white lines of equal altitude reveals the bulge in the neutral density following the motion of the Sun. When comparing the outermost contour

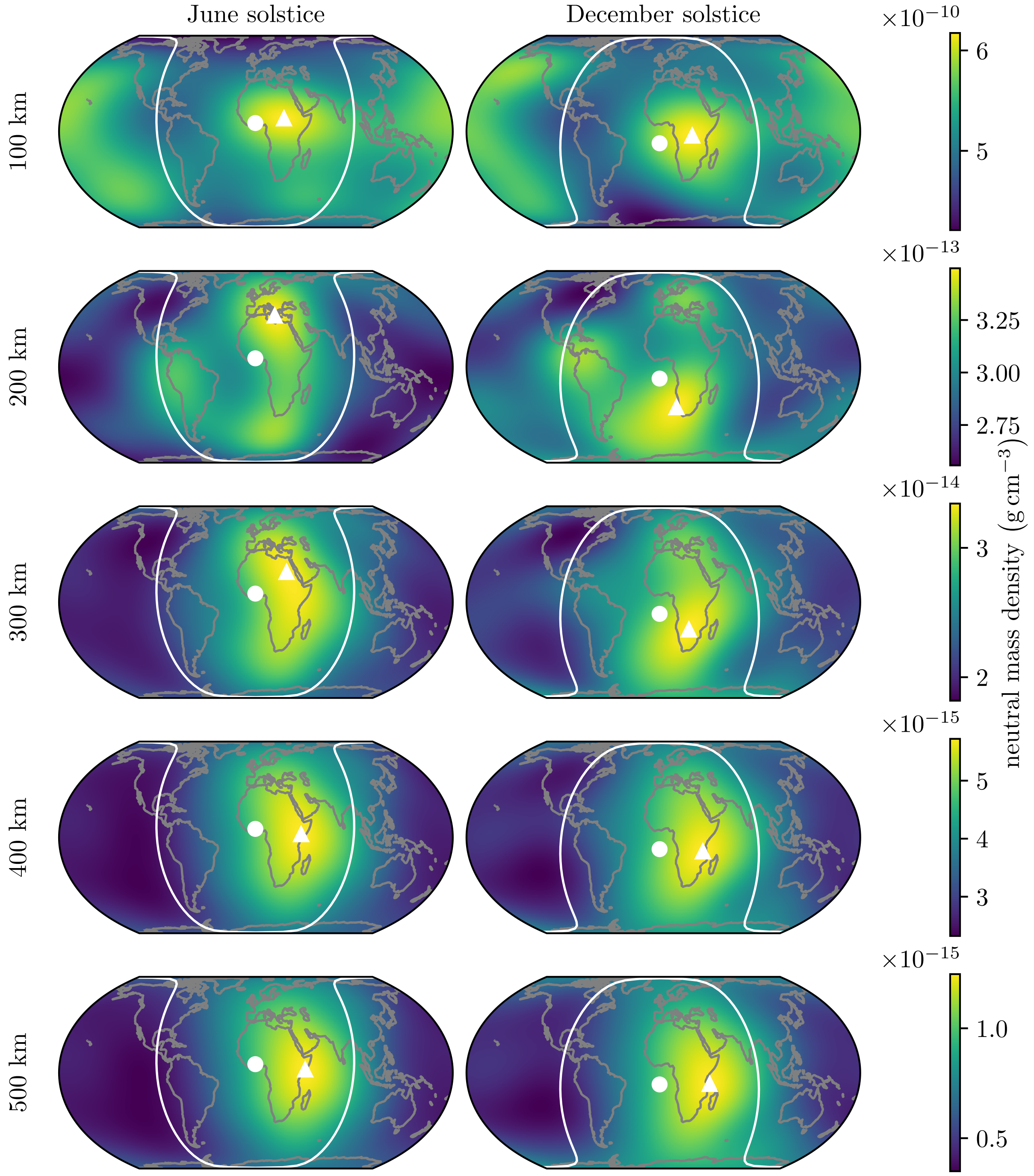

Figure 2.18.: The maps show the neutral mass density at various altitudes computed with the NRLMSIS 2.0 at the solstices of the year 2011 at 12:00 UTC+0. The white dot is the subsolar point, the white line is the solar terminator, and the white triangle is the global density maximum. The density maximum is between 1 and 3 h behind the Sun. The density on the night-side is lower than on the day-side because there is no solar radiation to absorb.

line during maximum and minimum conditions, one can see how the stronger solar radiation vertically expands the atmosphere.

Figure 2.20 shows the average height profiles of neutral mass density and neutral temperature for solar minimum and maximum conditions. For aerostatic equilibrium conditions (see Section 2.1.3) and constant density scale height, one would expect linear functions on the logarithmically scaled axes (simple exponential decay of neutral density). However, the atmosphere is not in aerostatic equilibrium since there is mass transport in the entire atmosphere and particle escape in the exosphere (Section 2.2.2). Besides, the scale height is not constant. However, for small vertical increments, the change in the scale height is small, and an exponential function may be employed for extrapolation and interpolation.

The neutral mass density and temperature are generally higher during solar maximum conditions. During the year 2003 (solar maximum), the median exospheric temperature is 261 K higher than during the year 2008 (minimum conditions). At 100 km altitude, the median neutral mass density is almost identical during solar minimum and maximum conditions. The largest difference of the median neutral mass density (solid line) between solar minimum and maximum in Figure 2.20 is at around 560 km, where it is 7.5 times larger. At the same altitude, the maximum neutral mass density (dashed line on the right-hand side) in 2003 was 771 times larger than the minimum density in 2008.

Figure 2.21 shows the median neutral mass density time series for different altitudes over two solar cycles. The lower the altitude, the lesser the amplitude of the temporal variations. The solar cycle, with a period of eleven years, is the most striking oscillation. Superimposed on that, one can detect annual and semiannual variations. The neutral mass density is also subject to solar-rotational, daily, and sub-daily variations that cannot be detected on this scale.

Long-term cooling is observed in the upper atmosphere, which also causes a long-term decrease in neutral density. Roble and Dickinson (1989) simulated the effect of increasing greenhouse gas concentrations in the mesosphere and thermosphere. They found that a doubling of CO_2 and CH_4 concentrations cools the global mean temperature of the thermosphere by 50 K. For a 30-40 K cooling, Rishbeth and Roble (1992) simulated a 20-40 % decrease in neutral density and a 15 km decrease in F2-layer peak height. Incoherent scatter radar (see Section 4.4) observations indicate an even higher temperature decrease (Donaldson et al., 2010; Holt and S. R. Zhang, 2008), which is twenty times larger than the simulation (W. L. Oliver et al., 2013). Thus, factors other than greenhouse cooling should also be considered. W. L. Oliver et al. (2013) suggest an increased gravity wave action that removes energy in the lower thermosphere as the main driver of the cooling. Cnossen (2020) attributed rising CO_2 levels to the temperature trends in the thermosphere, using a 65-year long WACCAM-X simulation. She found only small and not significant influence of altered gravity wave forcing on long-term cooling in the thermosphere. However, the influence of gravity waves could not be ruled out by this study and it remains an open question. The study of W. E. Parker et al. (2025) suggests that the greenhouse gases induced cooling reduces the satellite carrying capacity of orbits between 200 km and 1000 km by 50-65 % to the end of the century.

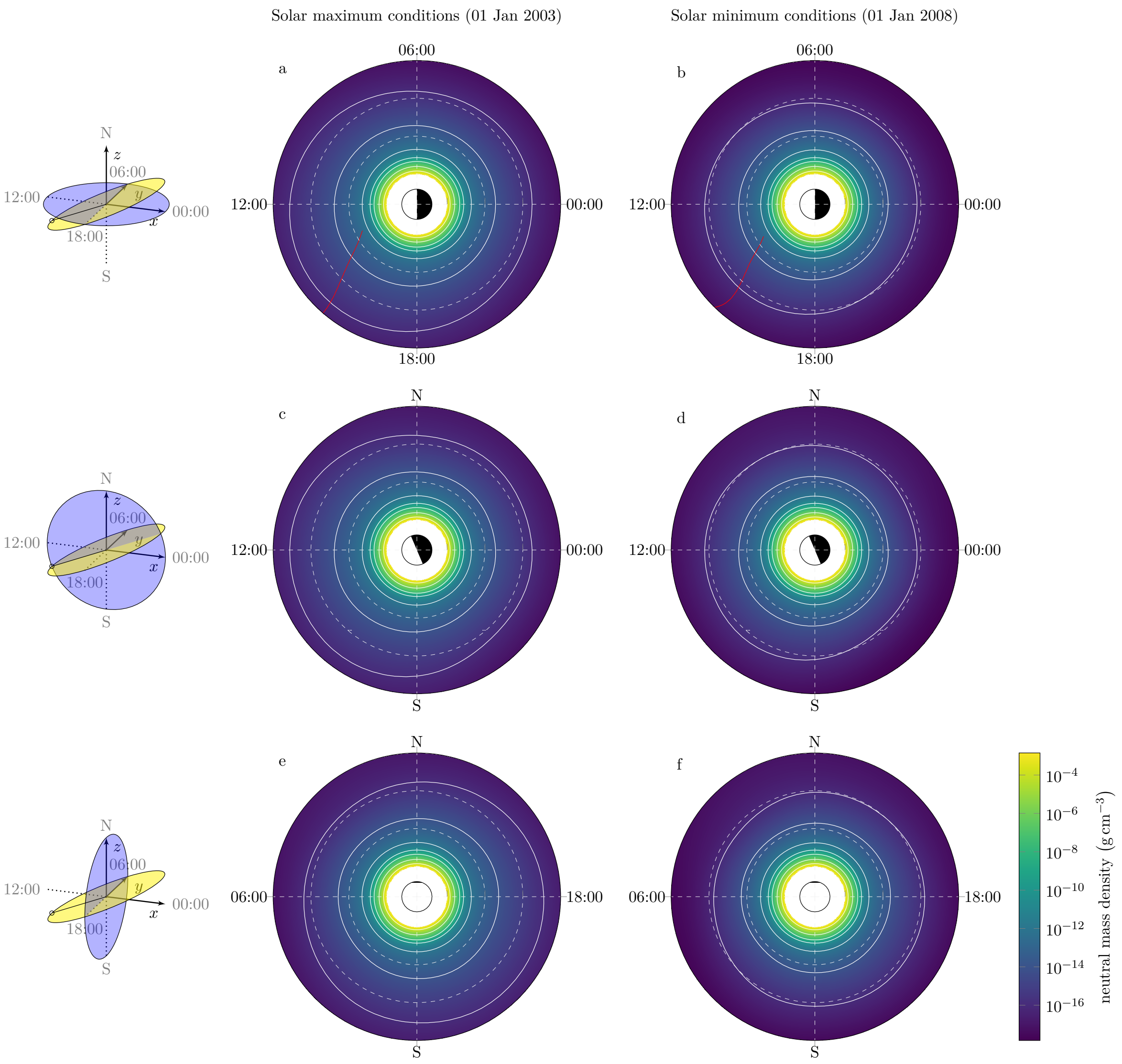

Figure 2.19.: Neutral mass density cross-sections through the xy-, xz-, and yz-plane of the Earth fixed frame for solar maximum and minimum conditions. The blue plane represents the cross-section, and the yellow plane the ecliptic. The partly filled circle located in the center shows the day- and night-side of the Earth. The altitude ranges from 0 km-750 km. The concentric dashed circles indicate 250 km and 500 km altitude. The white contour lines correspond to the tics of the color bar. The solar bulge can be easily detected by comparing the concentric dashed circles with the contour lines. At high solar activity the density is higher in the thermosphere. The red lines in panels a and b correspond to the density maximum at each altitude starting at 200 km altitude. The angle between the Sun (12:00) and the density maximum increases with altitude. For lower altitudes, the location of the maximum does not show a smooth vertical dependency.

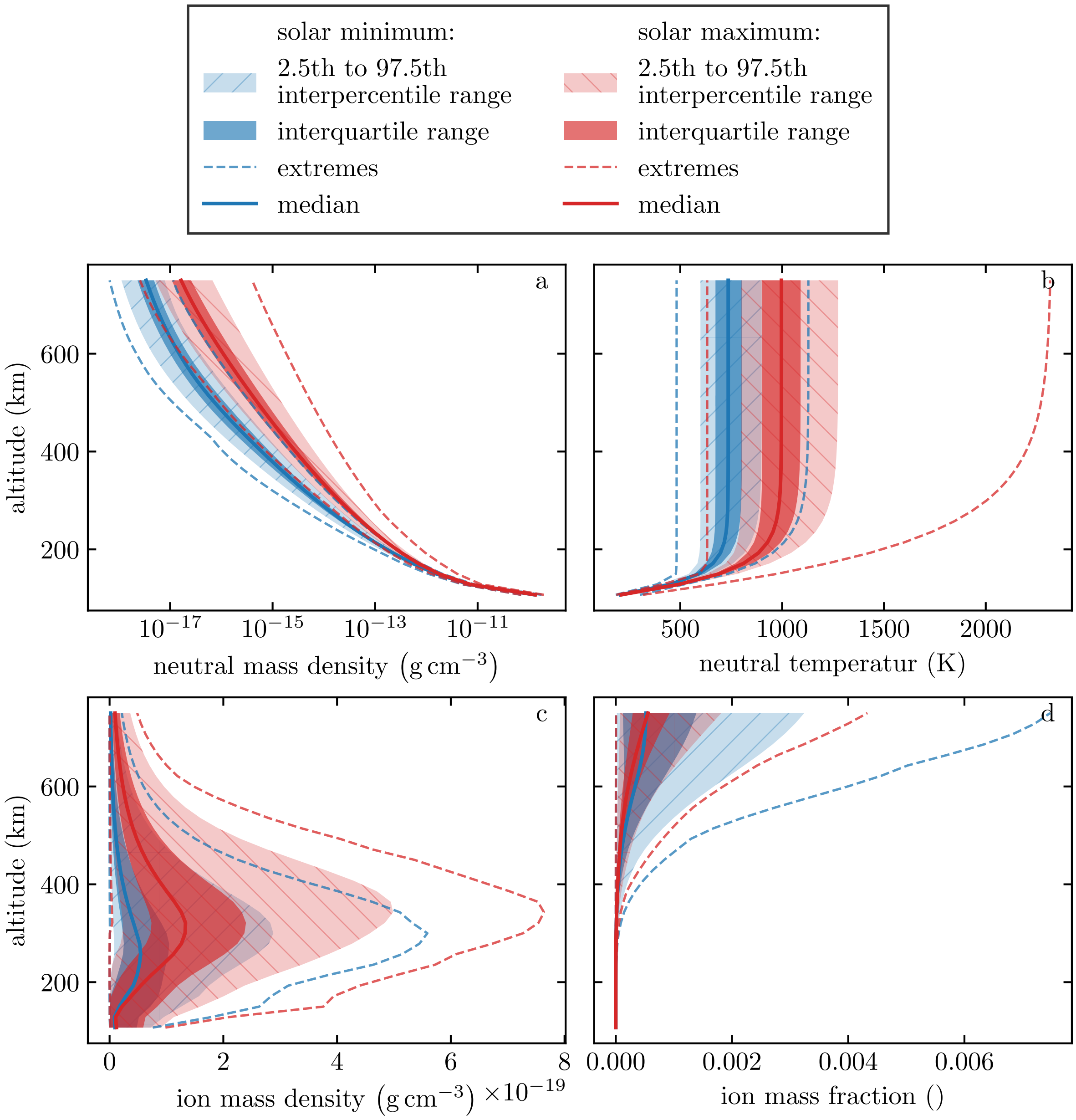

Figure 2.20.: Temporally and horizontally averaged height profiles for solar minimum conditions (2008) and solar maximum conditions (2003). The NRLMSIS 2.0 and IRI-2022 were evaluated hourly for each year on a grid partitioned into cells of equal surface area and similar shape on a sphere using the algorithm developed by B. Beckers and P. Beckers (2012). For each altitude and hemisphere, 125 grid cells were evaluated. The neutral quantities in panels a and b were computed from the NRLMSIS 2.0 and the ion mass density in panel c from the IRI-2022. Accordingly, panel d is computed from both models. Neutral mass density and neutral temperature are generally larger during solar maximum conditions. At 450 km, the median neutral mass density is about 6 times larger. The median neutral temperature is 261 K warmer. The ion mass density is much lower compared with the neutral mass density. The contribution of the ions to the total mass increases with altitude (panel d). The maximum ion mass fraction is 0.75 % at 700 km altitude. At 500 km it does not exceed 0.14 %. However, the NRLMSIS 2.0 and IRI-2022 are not coupled. Thus, these results should be considered as an approximation.

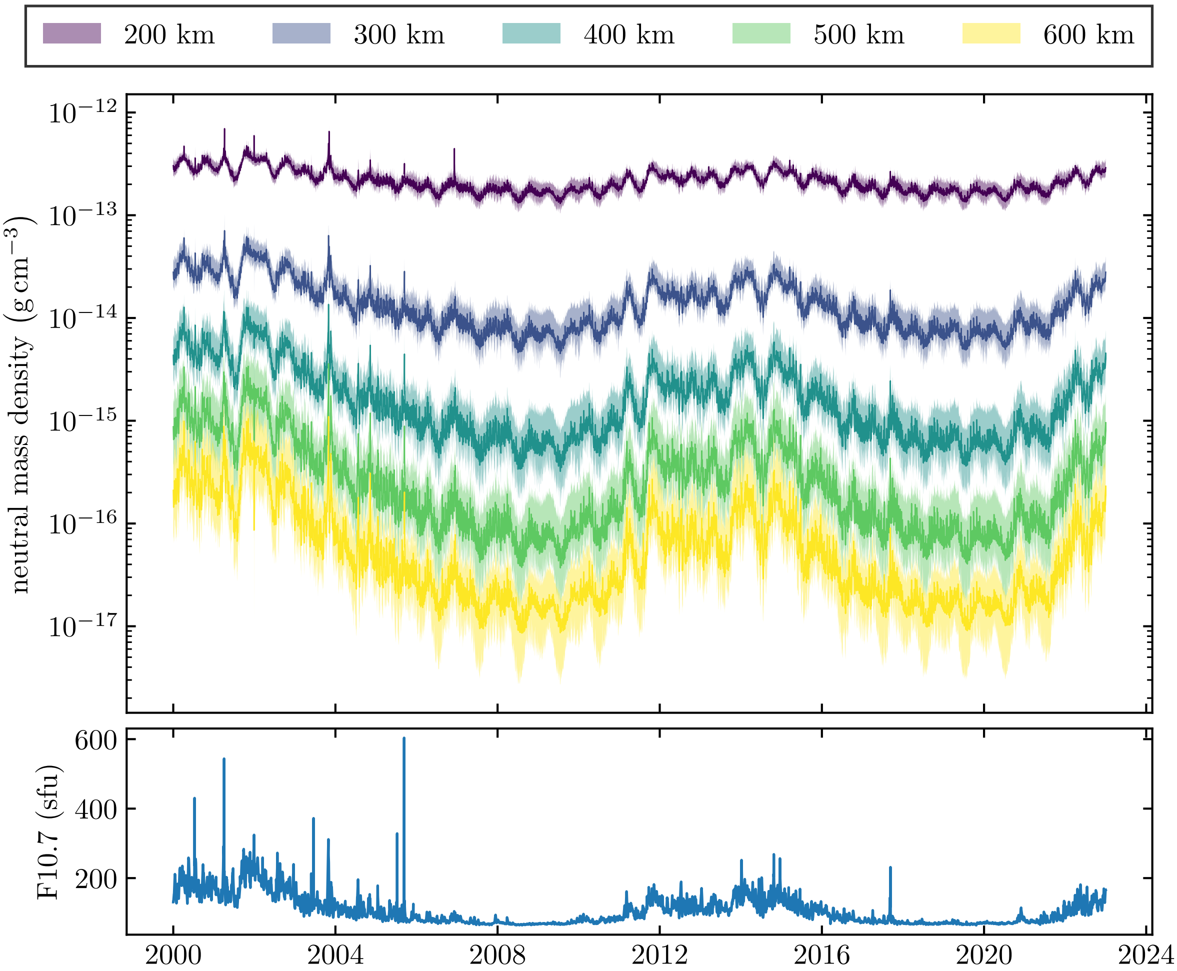

Figure 2.21.: The solid lines show the median neutral mass density of the corresponding color-indicated altitude. The transparent areas mark the 2.5th to 97.5th interpercentile range. To generate this figure, the NRLMSIS 2.0 was evaluated hourly on a grid partitioned into cells of equal surface area and similar shape on a sphere using the algorithm developed by B. Beckers and P. Beckers (2012). For each altitude and hemisphere, 125 grid cells were evaluated.

3. Satellite Aerodynamics

The aerodynamic acceleration is the largest non-gravitational acceleration acting on satellites close to Earth and, therefore, is important for precise orbit determination of those satellites. Moreover, the aerodynamic acceleration is crucial for satellite lifetime assessment and re-entry prediction. Aerodynamic acceleration depends on the geometry of the satellite, its surface materials, its velocity, and the properties of the surrounding gas, especially the mass density. Atmospheric drag is the acceleration acting opposite the satellite's flight direction relative to the motion of the atmosphere. The two other components of the acceleration vector, the lift and cross-track acceleration are generally much lower than the drag. Since the drag is proportional to the mass density of the surrounding gas, which decreases with altitude, the drag decreases accordingly. For satellites, the drag acceleration is dominant at altitudes below 850 km at solar minimum conditions and below 1750 km during solar maximum conditions (Montenbruck and Gill, 2000, Figure 3.1). Above those altitudes, solar radiation pressure (see Section 4.1) is the largest non-gravitational acceleration. Above 1000 km and 2000 km Earth radiation pressure becomes greater than the atmospheric drag for solar minimum and maximum conditions, respectively (Montenbruck and Gill, 2000, Figure 3.1). At an altitude of about 150 km, the remaining lifetime of typical (uncontrolled) satellites is shorter than one day (see Figure 3.4), and at about 78 km, they break up and disintegrate eventually. Thus, the density below this altitude is relevant for re-entry simulations but not for the operational phase of satellites.

To accurately simulate the aerodynamic acceleration acting on a satellite, the properties of the surrounding gas, especially the mass density, are required. Additionally, the velocities of the satellite and the atmosphere are needed. Moreover, accurate information on the energy and momentum transfer caused by the collisions of the atmospheric particles with the satellite is needed. The energy and momentum transfer depends on the material properties of the surface and its coating. Satellites with complex shapes, including concave geometries and superstructures such as antennas or solar panels, require a three-dimensional satellite macro model (e.g. March, 2020, Section 2.3) to calculate the angle of attack on a surface element and account for self-shadowing and multiple reflections. While this thesis focuses on providing highly-reliable mass densities, the satellite gas-surface interaction is also an active research area (e.g., March et al., 2021).

First, the type of gas flows that satellites may experience are introduced in Section 3.1. The basic equations for computing the aerodynamic acceleration acting on satellites are provided in Section 3.2. In Section 3.3, the gas-surface interaction modeling providing the drag coefficient for the computations in the previous section is summarized. Finally, a short description of satellite lifetime and the re-entry is given in Section 3.4.

Table 3.1.: Gas flow regimes are characterized by the Knudsen number. There is no exact definition and different authors use slightly different ranges of Knudsen numbers for the regimes.

		range of Knudsen number	
regime	rarefaction	Wu (2022)	Sentman (1961)
continuum flow	ordinary	$K < 0.001$	$K < 0.01$
slip flow	slightly	$0.001 < K < 0.1$	
transition flow	moderately	$0.1 < K < 10$	$0.01 < K < 10$
free molecular flow	highly	$10 < K$	$10 < K$

3.1. Gas Flow Regimes

One can divide gas dynamics into different gas flow regimes (e.g., Chambre and Schaaf 2017, p. 4 or Wu 2022, p. 9), corresponding to different degrees of rarefaction. Typically, a distinction is made between the *continuum-*, *slip-*, *transition-*, and *free molecular* flow regime. The continuum-regime is dominated by intermolecular collisions, whereas the free molecular flow regime is dominated by molecule-surface interactions. In the slip flow and transition flow regime, both intermolecular collisions and molecule-surface interactions are important.

The continuum and slip flow regime can be modeled with the Navier-Stokes-Fourier equations, but in the transition regime, these equations break down (e.g. Wu, 2022, Section 1.2). For the transition and free molecular flow regime the Boltzmann equation (e.g., S. Chapman 1970, Chapter 3; Gombosi 1994, Chapter 5; or Wu 2022, Chapter 2.3) is typically employed.

To characterize a flow into a regime the Knudsen number (e.g., Chambre and Schaaf, 2017; Sentman, 1961)

$$K = \frac{\bar{l}}{L} \tag{3.1}$$

is employed, which is the ratio of the mean free path $\bar{l}$ to a characteristic length L. The mean free path (e.g., S. Chapman 1970, p. 86, *USSA76* 1976, p. 17) is the mean distance a particle travels without any collision. L is a length that is characteristic of the considered scenario. In the case of a satellite, L is a characteristic length of the satellite itself. A Knudsen number greater than one means that the mean free path is longer than the geometry under consideration.

Typical values for the Knudsen number associated with a regime are given in Table 3.1 and Figure 3.1 shows the Knudsen number for different altitudes and characteristic lengths. At about 150 km, typical geodetic satellites enter the transition flow regime. As shown in Figure 3.4, satellites at that altitude survive one day without thrusters. Thus, typical Earth observation satellites are within the free molecular regime for most of their lifetime and enter the transition regime only at the end. Therefore, the focus is on the free molecular regime:

> The free molecule flow regime is the regime of extreme rarefaction. The molecular mean free path is by definition many times the characteristic dimension of the body which is assumed to be located in a gas flow of infinite extent. The molecules which hit the surface of the body and are then reemitted on the average travel very far before

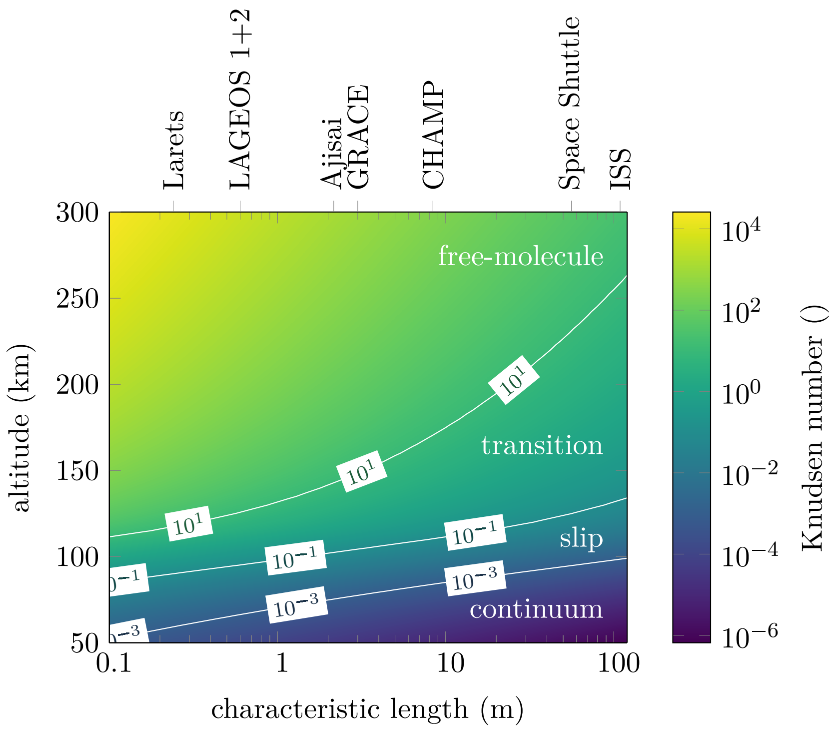

Figure 3.1.: Knudsen number for different characteristic lengths and altitudes. The mean free path is taken from the *USSA76* (1976). The maximum dimensions of some spacecraft are given for reference. The gas flow regimes are labeled according to Wu (2022)

> colliding with other molecules. It is consequently valid to neglect the effect of the reemitted particles on the incident stream, at least so far as effects on the body itself are concerned. The incident flow is therefore assumed to be entirely undisturbed by the presence of the body. This is the basic assumption of free molecule flow theory. It is a consequence of this basic assumption that no shock waves are expected to form in the vicinity of the object. (Chambre and Schaaf 2017, p. 8)

Sentman (1961) and Wu (2022) define the free molecular regime by $K > 10$. To decide whether an entire satellite is in a free molecular flow, L should be chosen as the largest dimension of the satellite (Sentman, 1961, pp. 5–1).

3.2. Aerodynamic Acceleration

The aerodynamic force acting on a satellite is typically represented by (e.g., Doornbos, 2012, Section 3.2.1)

$$\boldsymbol{F}_{\text{aero}} = \frac{1}{2}\boldsymbol{C}_a\, A\, \rho_\infty\, |\boldsymbol{v}_\infty|^2. \tag{3.2}$$

The freestream velocity $\boldsymbol{v}_\infty$ is the relative velocity of the atmosphere w.r.t. the motion of the satellite before the satellite affects the stream (e.g. Anderson, John D. and Cadou, Christopher P., 2023). In the case of free molecular flow, where the stream is assumed not to be affected by the satellite, this is the velocity at the position of the satellite. In other cases, it is the velocity that is far ahead of the satellite. Here, ρ_∞ is the freestream mass density. Again, in the case of free molecular flow, this is the density at the position of the satellite. The three-dimensional force coefficient vector $\boldsymbol{C_a}$ is a unit-less and scaled version of the aerodynamic force vector. It is introduced to account for the gas-surface interaction that depends on the geometry and material of the satellite (more details are explained in Section 3.3). In literature, it is more common to provide projections of the coefficient vector (see Figure 3.2), for example, the drag, lift, normal or axial coefficients (e.g. Anderson, John D. and Cadou, Christopher P., 2023). The reference surface area of the body is given by A. The choice of the reference surface area is not critical, but it is important to use the reference surface area that is associated with the force coefficients in all calculations (Anderson, John D. and Cadou, Christopher P., 2023). In other words, the reference surface area can be defined as desired, provided that the product of $\boldsymbol{C_a}$ and A remains constant. For satellites, the reference surface area is typically chosen as the satellite's projection on a plane perpendicular to the freestream velocity (cross-sectional surface area). Thus, for a spherical satellite, the reference surface area is typically the surface area of a circle with the same radius as the sphere. Assuming a perfectly spherical satellite, the cross-sectional surface area is independent of the satellite's attitude. This is not the case for satellites with more complex shapes.

The drag force

$$F_{\text{drag}} = q_\infty \, A \, C_D \tag{3.3}$$

is the projection of the aerodynamic force on the freestream velocity (see Figure 3.2) with the freestream dynamic pressure (e.g., Chassaing, 2022, Equation 3.20a)

$$q_\infty = \frac{1}{2}\rho_\infty |\boldsymbol{v}_\infty|^2. \tag{3.4}$$

This pressure is the contribution to the fluid's total pressure explained by its relative velocity and corresponds to “the increase in pressure when low-speed air is brought to rest” (King-Hele, 1987, p. 20). Even though the factor $\frac{1}{2}$ has no significance for high-speed aerodynamics, it is kept for compatibility. The drag coefficient C_D is the projection of the aerodynamic coefficient $\boldsymbol{C_a}$ on the freestream velocity $\boldsymbol{v}_\infty$. One obtains the drag acceleration

$$a_{\text{drag}} = \frac{q_\infty \, A \, C_D}{m_{\text{sat}}} \tag{3.5}$$

by dividing the force by the mass of the satellite. There are equivalent formulations for lift, axial, and normal acceleration

$$\begin{align} a_{\text{lift}} &= \frac{q_\infty \, A \, C_L}{m_{\text{sat}}} \tag{3.6} \\ a_{\text{axial}} &= \frac{q_\infty \, A \, C_A}{m_{\text{sat}}} \tag{3.7} \\ a_{\text{normal}} &= \frac{q_\infty \, A \, C_N}{m_{\text{sat}}} \tag{3.8} \end{align}$$

with C_L, C_A, and C_N being the projection of $\boldsymbol{C_a}$ on the corresponding axes. The components of

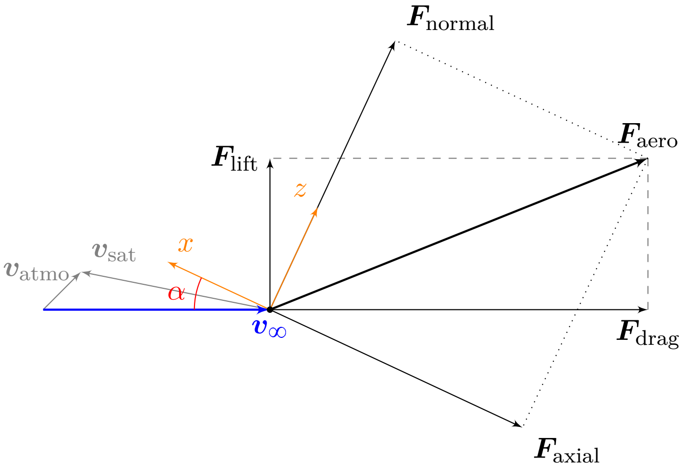

Figure 3.2.: The drag force $\boldsymbol{F}_{\text{drag}}$ is the projection of the aerodynamic force $\boldsymbol{F}_{\text{aero}}$ on the freestream velocity $\boldsymbol{v}_\infty$. The lift force is the component of the aerodynamic force perpendicular to the freestream velocity. The freestream velocity is the velocity of the atmosphere relative to the satellite, assuming the presence of satellite does not affect the atmosphere's motion. The axes of the satellite body frame are labeled with x and z. The normal and axial forces are the projections of the aerodynamic force on the x and z axes, respectively. The angle of attack is denoted by α.

the aerodynamic acceleration orthogonal to the drag (lift and side) can be neglected for satellites typically (e.g., King-Hele 1987, p. 21, Doornbos 2012, Section 3.2.1)

In addition, if there are forces not acting on the center of mass, turning moments arise. Besides aerodynamic torques also other torques caused, for example, by a gravity gradient or the Earth's magnetic field, influence the turning moment. Controlled satellites can neutralize those moments with control jets and fly without (large) rotations along the orbit. Uncontrolled objects, however, are destabilized by the moments and tumble in space (King-Hele, 1987, p.20).

Note that the inverse problem to Equation 3.5 (and the other projections) is ambiguous as one can find arbitrary combinations of drag coefficient, reference surface area, and free stream mass density explaining the aerodynamic force. Therefore, it is mandatory to consistently use combinations of q_∞, A, and C_D when any of them have been determined from observations of the drag force.

3.3. Gas-Surface Interaction for Rarefied Gas Dynamics

The fundamental assumption of rarefied gas dynamics is that particle-particle interactions can be neglected. Thus, aerodynamic forces can be derived from energy and momentum transfer between individual particles and the boundary, which is the satellite's surface in this context. Gas-surface interaction is typically described statistically employing the mapping between the distribution of the incident and reflected particle velocities (e.g., Wu, 2022, Chapter 2.6). Since it is challenging to determine this mapping, simplified empirical approaches employing *accommodation* and *reflection* coefficients are often employed.

It is assumed that a particle is not reflected instantly but "bounces around in the spaces between the molecules or atoms of the surface and then at some later time leaves the surface"

(Sentman, 1961, pp. 2–2). Thus, the thermal energy of the impinging particles is accommodated in the satellite. This is expressed via the *thermal accommodation coefficient* (e.g. Chambre and Schaaf 2017, Eq. 4-1 and introduced by Knudsen 1911; Smoluchowski von Smolan 1898)

$$\alpha = \frac{dE_i - dE_r}{dE_i - dE_w} \tag{3.9}$$

with incident energy flux dE_i and reflected energy flux dE_r. The flux dE_w denotes the energy that would be emitted if all incident particles were reflected following a Maxwellian distribution described by the temperature T_w of the reflecting surface (Chambre and Schaaf, 2017, p. 9). In the case $\alpha = 0$, the reflection is perfectly elastic, and the reflected flux is equal to the impinging flux. The case $\alpha = 1$ describes a perfect accommodation where the reflected energy flux is equal to the flux of a Maxwellian distribution associated with the temperature of the surface. Note that one can refine Equation 3.9 by introducing individual coefficients for each degree of freedom storing thermal energy (translation, rotation, vibration). The thermal accommodation depends on the properties of the surface material. Thermal accommodation factors for different materials are provided for example in Chambre and Schaaf (2017, Table H, 4a).

A frequently chosen approach for modeling the momentum transfer is to separate the reflected particle flux into a specular and a diffuse proportion (e.g.,Wu 2022, Chapter 2.6.1, Chambre and Schaaf 2017, Section H.4, or Sentman 1961, p. 2-3). In the case of specular reflection, the angle of incidence is equal to the angle of reflection. This is not the case for diffuse reflection, where the angle of reflection is not related to the angle of incidence. It is assumed that the velocity of the diffusely reflected particles follows a Maxwellian velocity distribution. A specularly reflected particle transfers momentum only along the normal to the surface, while a diffusely reflected particle also contributes to the momentum transfer tangential to the surface. Two separate reflection coefficients, one for the tangential moment transfer and one for the normal moment transfer, are used to describe the reflection. (e.g., Sentman 1961, p. 2-4 or Chambre and Schaaf 2017, p. 10).

The thermal accommodation and reflection coefficients are equal to zero for hypothetical materials solely reflecting specularly. For hypothetical materials solely reflecting diffusely, the coefficients are equal to one (Chambre and Schaaf, 2017, p. 10). The aerodynamic force acting on an infinitesimal surface element can be computed by Chambre and Schaaf (2017, Equations 7-6 and 7-7) and depends on the thermal accommodation and reflection coefficients. The aerodynamic force is obtained by integrating the force acting on a surface element over the surface under consideration. In Chambre and Schaaf (p. 19-20, 2017), the force integral was computed over planes, cylinders, and spheres, assuming either purely diffuse or secular reflection, and solved for the drag coefficient. For example, The drag coefficient of a sphere for diffuse reflection is (Chambre and Schaaf, 2017, Equation 8-6)

$$C_D = \frac{\exp\left(-\dfrac{S^2}{2}\right)}{\sqrt{\pi}S^3}(1 + 2S^2) + \frac{4S^4 + 4S^2 - 1}{2S^4}\operatorname{erf}(S) + \frac{2\sqrt{\pi}}{3S_w}. \tag{3.10}$$

Here erf is the error function and

$$S = \frac{|\boldsymbol{v}_\infty|}{\sqrt{\frac{2RT}{M}}} \tag{3.11}$$

is the dimensionless molecular speed ratio which is the quotient of the freestream velocity and the most probable random speed of the gas with molar mass M at temperature T and gas constant R. The most probable random speed corresponds to the velocity where the Maxwell Boltzmann distribution reaches its maximum (e.g., Gombosi, 1994, Section 2.5.1). A large molecular speed ratio indicates that the random motion of the gas is less important than the freestream velocity. The ratio S_w from Equation 3.10

$$S_w = \frac{|\boldsymbol{v}_\infty|}{\sqrt{\frac{2RT_w}{M}}} \tag{3.12}$$

depends on the temperature of the surface T_w. For the case that the surface temperature of the object is in thermal equilibrium with the freestream temperature ($T = T_w$ and $S = S_w$), Figure 3.3 shows the drag coefficient for a sphere and a cylinder, assuming diffuse reflection. In the case of hyperthermal flow $S \gg 1$, the random velocity of the gas particles does not play a role. As the molecular speed in Equation 3.10 approaches positive infinity, the drag coefficient becomes two, assuming thermal equilibrium of the gas and the surface.

Note that in Equation 3.11, a gas consisting of only a single constituent with molar mass M is assumed. As a consequence of the assumption that particles do not interact, one can compute the drag coefficient for a gas mixture from the individual contribution of each species weighted by the mass fraction (Doornbos, 2012, Equation 3.51)

$$C_D = \sum_{i=1}^{s} w_i C_{Di}. \tag{3.13}$$

Sentman (1961) provides the axial, normal, and turning coefficients for flat plates, cylinders, cones, and spherical segments, assuming a completely diffuse reflection of the incident particle flux and a constant temperature of the reflected particles.

In the case of free molecular flow, one can decompose satellites with complex shapes into simple geometries to compute the total aerodynamic coefficient because the flow is not disturbed by the satellite (Sentman, 1961, Section 3). The total aerodynamic coefficient is the sum of all individual coefficients, assuming there are no secondary reflections. There is an ongoing effort to improve the models of satellites. For example, the macro model of S. Bruinsma and Biancale (2003) consists of 15 panels, while the model of March (2020) published 17 years later consists of hundreds of panels.

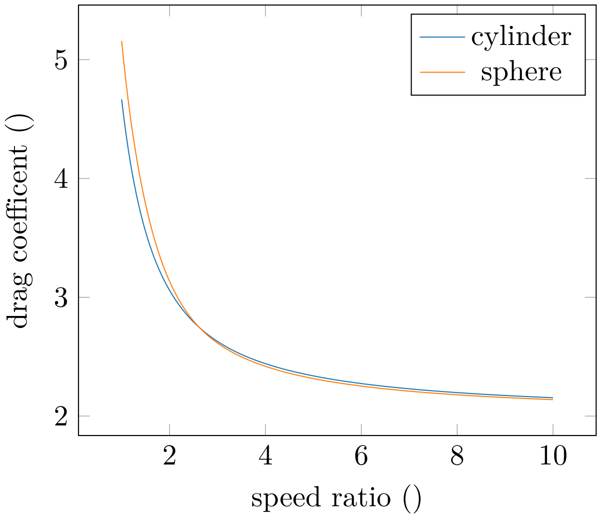

Figure 3.3.: Drag coefficient associated with a purely diffuse reflection for a sphere and cylinder (Chambre and Schaaf, 2017, Eq. 8-4 and 8-6) aligned to the free stream velocity. It is assumed that the surface has a uniform temperature equal to the freestream temperature ($S = S_w$). The reference surface area associated with the drag coefficient is the projection on a plane whose normal is the freestream velocity.

3.4. Satellite Lifetime and Re-Entry

The satellite lifetime (e.g., King-Hele 1987, Chapter 12 or Klinkrad et al. 2006, Chapter 6.3) depends on many factors like the mass and geometry of the satellite, its amount of propellant, the orbit, or space weather.

Assuming an idealized, constant, and spherical atmosphere and an idealized circular orbit the lifetime of an uncontrolled satellite can be approximated via (King-Hele, 1987, Equation 12.30)

$$T_L = \frac{H}{\sqrt{\mu_\oplus a}} \frac{b}{\rho F} \tag{3.14}$$

with the length of the semi-major axis a of the Kepler orbit and a correction factor F for the co-rotation of the atmosphere introduced by King-Hele (1987, Chapter 2.5). Here, H denotes the scale height of the mass density. The ballistic coefficient

$$b = \frac{1}{C_D} \frac{m}{A} \tag{3.15}$$

can be interpreted as a measure of a satellite's sensitivity to drag (e.g., Doornbos, 2012, pp. 55-56). When using Equation 3.15, one must make sure to use the reference surface area and drag coefficient that are assigned to each other. Figure 3.4 shows the dependence of the satellite lifetime on the semi-major axis according to Equation 3.14 using typical drag coefficients and mass-to-surface ratios. Although the illustration is highly idealized, it gives a general overview about the lifetime. A typical spherical satellite (solid line) survives less than a day at an altitude of around 150 km, a week at 200 km, and a year at 350 km.

As an object re-enters the atmosphere, its temperature rises. When the temperature reaches the melting point of the material the object is made of, it is ablated (Klinkrad et al., 2006,

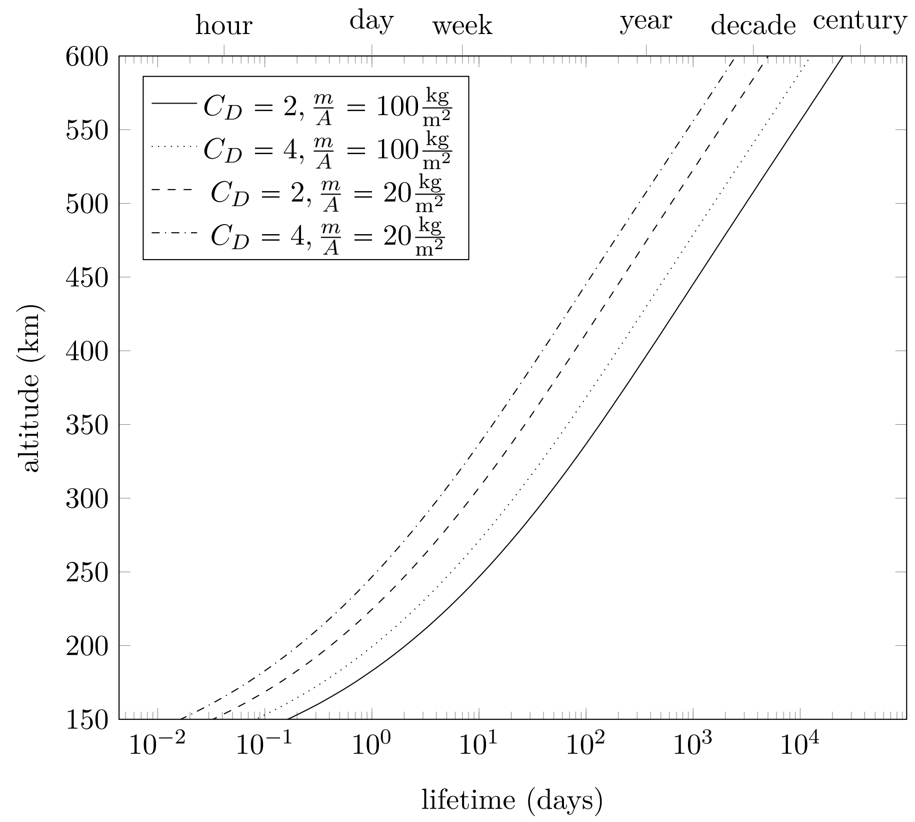

Figure 3.4.: Estimation of the lifetime of an uncontrolled satellite in a circular orbit derived from Equation 3.14, assuming a spherical, isotherm, and constant atmosphere. The co-rotation of the atmosphere is neglected ($F = 1$). The pressure scale height profile (close enough to density scale height at the plotted altitudes) and the mass density from the *USSA76* (1976) are used. This idealized equation only provides an approximate estimate and cannot accurately determine the actual lifespan of a satellite: orbits around Earth are never exactly circular, the mass density of the atmosphere underlies strong spatial and temporal variations, and the drag coefficient and mass-to-surface ratio are not constant.

Chapter 9.4). Depending on the properties of the object and the atmosphere, it disintegrates completely. There are two ways to survive the re-entry: First, effective re-radiation that prevents the material from reaching its melting point. Second, a sufficiently large heat storage for the incoming energy (Klinkrad et al., 2006, Chapter 9.4). Parts of the entry object, like solar arrays or antennas, break up when joints melt or when the aerodynamic forces exceed the stress limits. Klinkrad et al. (2006, Chapter 9.4). A finding of the Vehicle Atmospheric Survivability Project (Stern, 2008) in the 1970s was that objects break up at about 78 km altitude. However, these experiments only considered aluminum structures (Peddakotla et al., 2023). There are several software packages used for simulating re-entry (e.g., Lips and Fritsche, 2005).

4. Observations of the Upper Atmosphere

The instruments and their observations introduced in this chapter are the basis of the semi-empirical models described in Chapter 5. In addition, some of the observations have been used in data assimilation experiments in this thesis (Chapter 8) or in other studies referenced in Section 7.1 about related works.

In this chapter 'upper atmosphere' refers to all layers above the tropopause (see Figure 2.3). The instruments used to observe Earth's upper atmosphere are located on Earth's surface or carried by satellites, balloons or sounding rockets. Sounding rockets (e.g., Christe et al., 2016; Larsen, 2015) are used since the end of World War II to measure in-situ profiles of the upper atmosphere. They are invaluable for probing the atmosphere above the altitude balloons can reach ($\sim 40\,\mathrm{km}$) and below the altitude where LEO satellite orbits do not decay within a few days ($\sim 250\,\mathrm{km}$, see Figure 3.4). Sounding rockets can be equipped, for example, with mass spectrometers (see Section 4.3) to measure the density of the atmosphere or Langimur probes to measure the electron density.

The mass densities derived from space-born accelerometers are the primary observation of the assimilation experiments conducted in this thesis and are explained in Section 4.1. This section also includes a brief description of the satellite missions used in this thesis. The subsequent Section 4.2 explains how mass density can be derived from any tracked satellite from orbital decay analysis. Section 4.3 summarizes how mass spectrometers are used for observing atmospheres. Remote sensing observations of the atmosphere are conducted using incoherent scatter radar (see Section 4.4), radio occultation (see Section 4.5), spectrographic imagers (e.g., Eastes et al., 2017; Immel et al., 2017) or radiometers (e.g., Siegel, 2007).

4.1. Accelerometer-Derived Mass Densities

An accelerometer installed on a satellite's center of mass is in freefall and, therefore, solely responds to non-gravitational forces, excluding gravitational acceleration. After the calibration of the accelerometer (Vielberg, 2024, Section 3.1.5.3), the total observed acceleration is the superposition of aerodynamic acceleration $\boldsymbol{a}_{\text{aero}}$ (see Section 3.2), radiation pressure $\boldsymbol{a}_{\text{RP}}$, satellite-induced accelerations $\boldsymbol{a}_{\text{sat}}$ and noise ε (Vielberg, 2024, Chapter 4)

$$\boldsymbol{a} = \boldsymbol{a}_{\text{aero}} + \boldsymbol{a}_{\text{RP}} + \boldsymbol{a}_{\text{sat}} + \varepsilon. \tag{4.1}$$

Radiation pressure (e.g., Montenbruck and Gill 2000, Section 3.4 or Vielberg 2024, Section 4.2) is caused by photons hitting a surface transferring momentum. The momentum carried by a photon depends on its wavelength: the shorter the wavelength, the greater the momentum. Radiation pressure also depends on the surface area of the object, the angle of incidence, and the

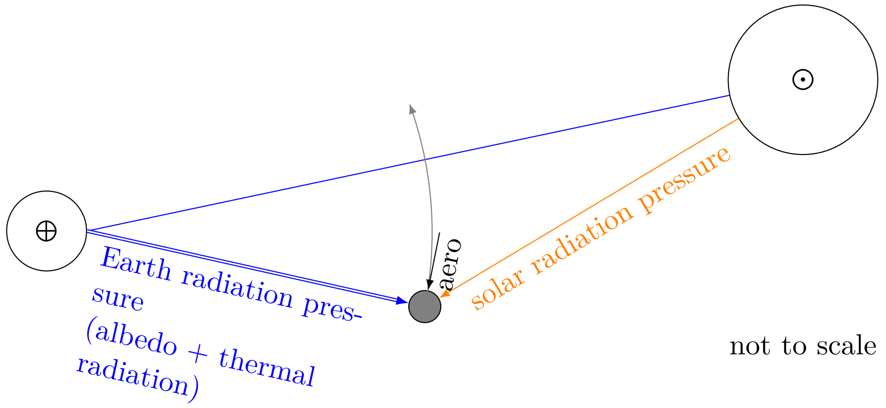

Figure 4.1.: Photons colliding with satellites transfer momentum and accelerate them. Solar radiation pressure is caused by photons emitted by the Sun that directly hit the satellite (orange arrow). Earth radiation pressure (blue arrows) has two components: photons emitted by the Sun that are reflected by Earth and hit the satellite (albedo), and thermal radiation emitted by Earth itself.

reflection properties of the surface. The radiative flux decreases quadratically with the distance to its source. Therefore, radiation pressure also decreases quadratically. Satellites orbiting Earth experience radiation pressure from the Sun, the Earth, and the Moon (see Figure 4.1). However, lunar radiation pressure is small compared with the other sources for LEO-satellites. The incident radiation also heats the satellite, which causes thermal re-radiation pressure (Vielberg, 2024, Section 4.2).

Solar radiation pressure is caused by photons that are emitted by the Sun hitting the satellite directly. Earth radiation pressure is the combination of radiation emitted by the Sun reflected towards satellites by Earth's surface (albedo) and the thermal radiation of Earth itself. While Earth's thermal radiation affects the satellite on both the day and the night-side, the solar radiation is only reflected on the day-side and does not affect satellites shadowed by Earth (see Vielberg, 2024, Figure 4.4).

The photons do not only transfer momentum, but also thermal energy when being absorbed by the surface. Therefore, the illuminated side of a satellite has a higher temperature than the rest of the satellite. Since the thermal emission depends on the temperature (Stefan-Boltzmann law), the radiation emitted on the illuminated surface has larger momentum, causing a net acceleration of the satellite that must be considered. Further, satellite-induced accelerations include twanks, thruster firings, antenna thrust, and accelerations caused by the Lorentz force (e.g., Vielberg, 2024, Section 4.3).

Provided that the radiation pressure and the satellite-induced accelerations can be modeled with sufficient accuracy, the aerodynamic acceleration can be calculated by solving Equation 4.1 for it:

$$\boldsymbol{a}_{\text{aero}} = \boldsymbol{a} - \boldsymbol{a}_{\text{RP}} - \boldsymbol{a}_{\text{sat}} - \varepsilon. \tag{4.2}$$

The accelerometer measures the three components with respect to the satellite body-fixed frame. Inserting the along-track component of the measured acceleration $a_{\text{aero},x}$ into Equation 3.7 and solving for the density (inserting Equation 3.4 for the dynamic pressure) yields the freestream mass density

$$\rho_\infty = 2\frac{m_{\text{sat}}}{A}\frac{a_{\text{aero},x}}{C_A|\boldsymbol{v}_\infty|^2}. \tag{4.3}$$

Since collisions of charged particles transfer momentum to a satellite ρ_∞ in Equation 4.3 also contains the contribution of charged particles. However, the mass fraction of ions is well below 1 % (see Figure 2.20 d), and the drag force is mainly due to neutral particles.

Accelerometer-derived densities have a temporal resolution of a few seconds. However, a very well calibrated and ultra precise accelerometer is required, which is only found on a few satellites. Moreover, there is limited information about the uncertainty of accelerometer-derived mass densities. The quality of the density computed from Equation 4.3 depends on the quality of all quantities on the right-hand side. This means accurate and precise estimates for

- the mass and shape of the satellite,
- the radiation pressure and satellite induced-accelerations,
- the axial force coefficient C_A and therefore the gas-surface interaction,
- and the velocity of the satellite and the atmosphere (wind) constituting the freestream velocity $\boldsymbol{v}_\infty$

are required. Thus, accelerometer-derived densities underlay many assumptions and “the main challenge lies in attributing how much of the orbital perturbation is the result of changes in the upper atmosphere versus changes in a satellite’s ballistic coefficient.” (Thayer et al., 2021).

4.1.1. Satellites Equipped with High-precision and High-accuracy Accelerometers

Over the years several LEO satellite missions were equipped with accelerometers sensitive enough to determine satellite drag: the Challenging Minisatellite Payload (CHAMP; Section 4.1.2) mission, the Gravity Recovery And Climate Experiment (GRACE; Section 4.1.3) missions, the Gravity field and steady-state ocean circulation explorer (GOCE, e.g., Brockmann et al. 2014), and the Swarm mission (e.g., Friis-Christensen et al., 2008). In this thesis mainly the accelerometer-derived mass densities from GRACE and CHAMP are used.

4.1.2. CHAMP

The Challenging Minisatellite Payload (CHAMP; Reigber et al. 2002) mission was launched on 15 July 2000 and re-entered on 19 September 2010, resulting in a mission duration of more than ten years. The initial altitude was 460 km on a circular orbit inclined by 87.3°. Its objective was to recover the global gravity field via satellite-to-satellite tracking in low-high mode[1] , to recover the magnetic field, and to profile the atmosphere and ionosphere with GPS. It carried a ’STAR’ accelerometer in the center of mass that was used to determine non-gravitational forces. The ’STAR’ accelerometer was a capacitive three-axis accelerometer with a resolution

---

[1] CHAMP was the low satellite while Global Positioning System (GPS) satellites were the high satellites (Hofmann-Wellenhof and Moritz, 2006, p. 277).

of $1 \times 10^{-9}\,\mathrm{m/s^2/\sqrt{Hz}}$ (e.g., Flury et al., 2008; Touboul et al., 2004) constructed by the Office National d'Etudes et de Recherches Aérospatiales (ONERA). In this thesis the CHAMP orbit computed by Prange (2010) at AIUB is used.

4.1.3. GRACE

The Gravity Recovery And Climate Experiment (GRACE; Tapley et al. 2004) consisted of two identical satellites on the same orbit separated along track by about 220 km. The primary objective of GRACE was to measure Earth's time variable gravity field using satellite-to-satellite tracking in low-low mode. The main product are monthly solutions of the Earth's gravity field. The GRACE mission was launched on 17 March 2002 and re-entered on 10 March 2018. The mission was almost 16 years in space. The initial altitude was 500 km, and the orbit was almost polar with an inclination of 89.5°. The follow-on mission GRACE-FO (Landerer et al., 2020) was launched on 22 May 2018 and is, at the time of the publication, still in orbit. Both GRACE satellites were equipped with a 'SuperSTAR' accelerometer (Flury et al., 2008), which is the successor of the accelerometer installed on CHAMP. It was designed for a resolution of $1 \times 10^{-10}\,\mathrm{m/s^2/\sqrt{Hz}}$ (e.g., Flury et al., 2008; Touboul et al., 2004). In this thesis only GRACE-A data is used. The orbit provided in the official GRACE release (Bettadpur, 2012) is used.

4.2. Determination of Mass Density from Satellite Orbits

The kinetic energy and angular momentum of orbits is reduced by atmospheric drag, leading to a decrease of the semi-major axis and eccentricity (Montenbruck and Gill, 2000). Since the drag acceleration and the associated orbital decay depend on the mass density, one can derive it from the orbit.

This approach only requires measuring the trajectory of a satellite and also works for passive satellites, for example, spherical Satellite Laser Ranging (SLR) satellites. Other techniques frequently applied for satellite tracking are radio (or optical) tracking, global navigation satellite system (GNSS), and Doppler Orbitography and Radiopositioning Integrated by Satellite (DORIS).

Orbital decay is not measured instantly, but determined over a certain time-span and therefore is an integrated quantity. Accordingly, densities derived from orbital decay are not instantaneous, but average values along the orbit.

The Staff of the royal aircraft establishment (1957) derived the mass density at the altitude of Sputnik 1 from the decay of its orbital period. The theory for this approach is described in King-Hele (1987, Chapter 10). Bowman et al. (2004) derive daily neutral mass density values from orbital energy dissipation rates (Storz, 2012).

It is also possible to co-estimate mass density within precise orbit determination. Precise orbit determination requires a force model (e.g. Montenbruck and Gill, 2000, Chapter 3) including atmospheric drag force. This allows the introduction of correction parameters for the drag force such as (temporarily resolved) bias or scale parameters. Zeitler et al. (2021) describe how co-estimation is implemented in two software packages. Mass densities derived within orbit determination are based on modeled densities, that are corrected with parameters that have typically a temporal resolution of hours to days. Moreover, when co-estimating a scale factor for the mass density, the complete right-hand side of Equation 4.3 is scaled, not only the mass density. This means the factor may be influenced by scales of the other variables, especially the axial force coefficient.

4.3. Mass Spectrometry

A mass spectrometer (Gross, 2017) is a type of instrument used to analyze the neutral and charged composition of the constituents in a sample. There are different constructions (e.g. Arevalo Jr et al., 2020; Gross, 2017), but the general principle is the same: first, the sample under consideration is ionized, then separated into its constituents by its mass-to-charge ratio, and finally, the individual constituents are detected.

There are many satellite missions equipped with mass spectrometers. They are used to examine solar wind, cosmic dust, planets, moons and comets (Arevalo Jr et al., 2020; P. V. Johnson et al., 2012; Mahaffy, 1999; Palmer and Limero, 2001; Vazquez et al., 2021).

> However, compared with state-of-the-art commercial systems, spaceflight instruments are necessarily constrained in analytical capability because of a trade-off in performance versus resource requirements; even the most advanced orbiters and landed platforms offer only limited SWaP [size, weight and power] for scientific instruments. (Arevalo Jr et al., 2020)

An early example of a satellite equipped with a spaceflight mass spectrometer is the third Sputnik mission, flying from 15 May 1958 until 6 April 1960 that measured the positive ion concentration of Earth's atmosphere (ISTOMIN, 1962). The neutral number concentration of N_2, N, O and H was measured by the Atmosphere Explorer missions (AE-C, AE-D, AE-E) from 1973 until 1978 and Dynamics Explorer 2 (DE-2) from 1981 until 1983 (Dandouras et al., 2020, Table 1). DE-2 carried a quadrupole mass spectrometer[1] that was designed to sample the abundances of neutral species with an accuracy of about 15 % (Carignan et al., 1981) every second. "The most contemporary QMS [quadrupole mass spectrometer] flown to date [...] achieve[d] an extended mass range of 2 to 535 u with a mass resolving power up to $m/\Delta m = 500$ (FWHM [full width at half maximum]) and 10^9 total dynamic range." (Arevalo Jr et al., 2020) Modern spaceflight mass spectrometers, like the mass spectrometer for planetary exploration (MASPEX, T. G. Brockwell et al. 2016) achieve a mass resolving power up to $m/\Delta m = 46\,000$ (full width at half maximum) (Arevalo Jr et al., 2020).

There is not any recent satellite mission equipped with a mass spectrometer to measure the mass density of Earth's upper atmosphere. To detect the major neutral species (H, He, N, O, N_2, NO) and the ionized counterparts (H^+, He^+, N^+, O^+, ${N_2}^+$, NO^+) the rejected Deadalus proposal intended an instrument with mass resolving power of $m/\Delta m = 30$, a mass range larger than 40 u, and dynamic range of 10^{10} with 16 Hz sampling (Sarris et al., 2020, Section 4.2.5). NASA's upcoming Geospace Dynamics Constellation (GDC) mission (e.g., Akbari et al., 2024) is intended to fly between 400 km and 350 km and to carry the Modular Spectrometer for

---

[1] Details on quadropole mass spectrometers can be found for example in Gross (2017, Section 4.4) and Arevalo Jr et al. (2020, Section 3.2).

Atmosphere and Ionosphere Characterization (MoSAIC) experiment. It is a quadrupole mass spectrometer with an intended cadence of 1-2 s, an accuracy of 10 % and a precision of 1 % (Dr. Mehdi Benna, personal communication).

4.4. Incoherent Scatter Radar

Incoherent scatter radars (e.g., Bilitza, 1991; Sulzer, 2015) are ground based instruments primarily used for probing the ionosphere. They measure the number density and temperature of electrons, and the temperature and velocity of ions in the atmosphere along the line of sight. Incoherent scatter radars emit electromagnetic radiation with high power (1 MW and more) in radio frequency range using antennas with large apertures of 30 m and larger (Sulzer, 2015). Most of the emitted radiation passes through the ionosphere, except for a small amount being reradiated by free electrons resulting in incoherent scatter returns. The ratio of transmitted power to scattered power is approximately 10^{-19} (Häggström, 2021). Thus, the signal received at the radars is very weak.

Incoherent scatter radars can reach altitudes up to 2000 km and a resolution of a few hundred meters. Currently, there are about ten incoherent scatter radars in the world (Häggström, 2021). Further processing of the measured profiles allows the derivation of many other parameters of the charged and neutral atmosphere (Häggström, 2021). For example, Nicolls et al. (2014) have demonstrated that multifrequency incoherent scatter radar measurements allow to infer the ion-neutral collision frequency, which can be used to scale mass density models.

4.5. Radio Occultation

Radio occultation (e.g., Leroy, 2015; Liou, 2010) is a remote sensing method originally developed for probing the atmosphere of planets. It requires at least two satellites, one of them sending a radio signal and the other receiving it. The signal does not travel on a straight line as it would in vacuum, but it is refracted (delayed and bend) by the atmosphere according to Snells' law. When the elevation of the transmitter as seen from the receiver is low or negative (that is the case during the rise and set of the sender), the way through the atmosphere is much longer compared with high elevations (e.g., when the sender is in the zenith of the receiver). In these receiver-sender constellations, the atmosphere *occults* the sender (see Figure 4.2).

The bending angle and refractivity of the signal depends on the electron density, pressure, temperature, and water vapor content (most of it is located in the troposphere) of the atmosphere (Ho et al., 2020), enabling the inversion of the received signals to these quantities. Depending on the constellation of transmitter and receiver, the signal travels through different heights so that large areas of the atmosphere can be probed. For Earth, it is convenient to use the already existing dense network of GNSS satellites as senders (e.g., Leroy, 2015; Limberger, 2015). Satellite missions equipped with antennas for GNSS radio occultation are for example CHAMP, GRACE, GRACE-FO, FORMOSAT-3/COSMIC (Ho et al., 2020), FORMOSAT-7/COSMIC-2 (Schreiner et al., 2020), or TerraSAR-X. Each of those missions covers the global atmosphere. For Earth, the vertical resolution is in the order of hundredths of meters and the horizontal resolution is in the range of several hundredths kilometers (Leroy, 2015). "GPS RO performs

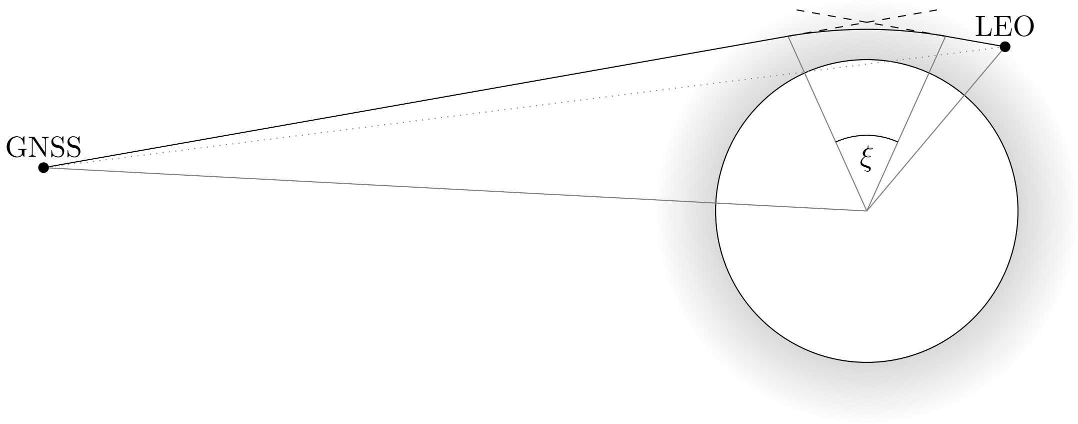

Figure 4.2.: Schematic illustration of radio occultation using GNSS satellites (see also Liou (2010, Figure 2.1.1) or Hajj et al. (2002, Figure 1)). The signal emitted by the GNSS satellite does not travel on a straight line (dotted line) but is bent by the atmosphere (solid black path). The bending angle is denoted by ξ.

best in the 8–30 km height region, where the refractivity N can be retrieved with a precision of 0.2 % and an accuracy that is an order of magnitude better.” (Leroy, 2015)

5. Models of the Upper Atmosphere

There are many models of the atmosphere with different simulation methods, altitude ranges, reference systems, and simulated state variables (e.g., Emmert, 2015, Section 3). I consider global models that can predict the mass density in the LEO regime as it is needed for atmospheric drag computation (see Section 3.2). Models that only consider the charged part of the atmosphere, like the Global Assimilative Ionosphere Model (GAIM, R. W. Schunk et al. 2004), are not discussed further here, as the primary goal is to enhance the mass density estimation.

Models can be divided into two types: (semi-)empirical models and numerical models. Empirical models are functions fitted to a large dataset of observations. Provided with position, time, and solar and geomagnetic activity they compute the state of the atmosphere for the given inputs. Empirical models approximate the state of the atmosphere at arbitrary position, time and space weather conditions, based on the underlying observation dataset. Numerical models forward an initial state based on physical principles like conservation of mass, energy and momentum. They are discretized in time and space using some grid structure. Numerical models that describe the global planetary scale motion of a fluid (including gases) are called *general circulation models*. (Semi-)empirical models can also incorporate some physics, for example, aerostatic equilibrium (Section 2.1.3), and are therefore often called semi-empirical models. On the other hand, numerical models also contain empirical parts, for example, an empirical EUV model.

While (semi-)empirical models can be limited to a single compartment like the neutral atmosphere, numerical models often simulate coupled compartments accounting for their mutual interaction. For example, in upper atmosphere models, the coupling between the neutral and charged part of the atmosphere is typically considered. This allows to self-consistently simulate both compartments.

A key difference between semi-empirical and numerical models is the runtime. Semi-empirical models can be solved instantly for a single position and time. In contrast, numerical models cannot: They must be forwarded globally–taking into account all grid cells–from an available initial state to the chosen point in time. The desired state variable is then obtained by interpolation from the model grid to the desired position.

With the beginning of the satellite era, the development of upper atmosphere models began. The timeline in Figure 5.1 gives an overview of the development and lists the associated publications. While the first empirical models date back to the early 60s, the first general circulation models were published in the 80s. A more recent development is the use of machine learning to construct empirical models (e.g., Pan et al., 2024; P. Wang et al., 2023; S. Wang et al., 2014).

Table 5.1 gives an overview of the inputs, outputs, and coordinate systems of some recent models. All listed models use the F10.7 index (Section 2.3.1.2) as a proxy for solar EUV radiation. The Drag Temperature Model-2020 (DTM-2020; S. Bruinsma and Boniface 2021)

Table 5.1.: This table summarizes the properties of selected models providing the mass density in the thermosphere.

(a) External forcing. SW: solar wind (velocity and density), IMF: interplanetary magnetic field flux density. See Section 2.3.1.2 and 2.3.2.2 for more details on solar and geomagnetic indices, respectively.

	solar forcing	geomagnetic forcing
JB08	F10.7, S_{10}, M_{10}, Y_{10}	Dst
MET 07	F10.7	Kp
NRLMSIS 2.0	F10.7	Kp
DTM-2020	F10.7 (or F30)	Kp (or Hpo)
TIE-GCM 2.0	F10.7	SW+IMF or Kp
CTIPe	F10.7	SW+IMF

(b) Quantities that are written by the models to the output files.

	ρ	T_N	T_E	C_{N_2}	C_{O_2}	C_O	C_{He}	C_{Ar}	C_H	C_N	C_{O^*}	$\overline{M}$
JB08	●	●	●	○	○	○	○	○	○	○	○	○
MET 07	●	●	●	●	●	●	●	●	●	○	○	●
NRLMSIS 2.0	●	●	●	●	●	●	●	●	●	●	●	○
DTM-2020	●	●	●	●	●	●	●	○	●	○	○	●
TIE-GCM 2.0	●	●	○	●	●	●	●	●	○	○	○	●
CTIPe	●	●	○	●	●	●	●	○	○	○	○	●

(c) Coordinate system used by the models. Unfortunately, the coordinate systems used are not documented for all models.

	coordinate system		vertical boundary	
	latitude	ellipsoid	lower(km)	upper (km)
JB08	geocentric	WGS84	175	1000
MET 07			90	2500
NRLMSIS 2.0	geodetic	WGS84	0	exosphere
DTM-2020			120	~1500
TIE-GCM 2.0	geocentric		97	~500
CTIPe			80	~500

also allows the F30 index as an alternative driver. The JB08 (Bowman et al., 2008a) does not rely on the F10.7 index alone for solar forcing but uses additional indices as drivers. The Kp index (Section 2.3.2.2) is a prominent choice as a geomagnetic activity proxy. The Naval Research Laboratory Mass Spectrometer and Incoherent Scatter radar 2.0 (NRLMSIS 2.0, Emmert et al. 2021) is the only model listed here whose lower vertical boundary coincides with the Earth's surface.

While Figure 5.1 gives a broad overview on models of the upper atmosphere, the only numerical model described in more detail in Section 5.1 is the Thermosphere Ionosphere Electrodynamics General Circulation Model 2.0 (TIE-GCM 2.0, Qian et al. 2014). In Section 5.2 some details of selected semi-empirical models are provided. An overview on studies about the accuracy of the models is given in Section 5.3.

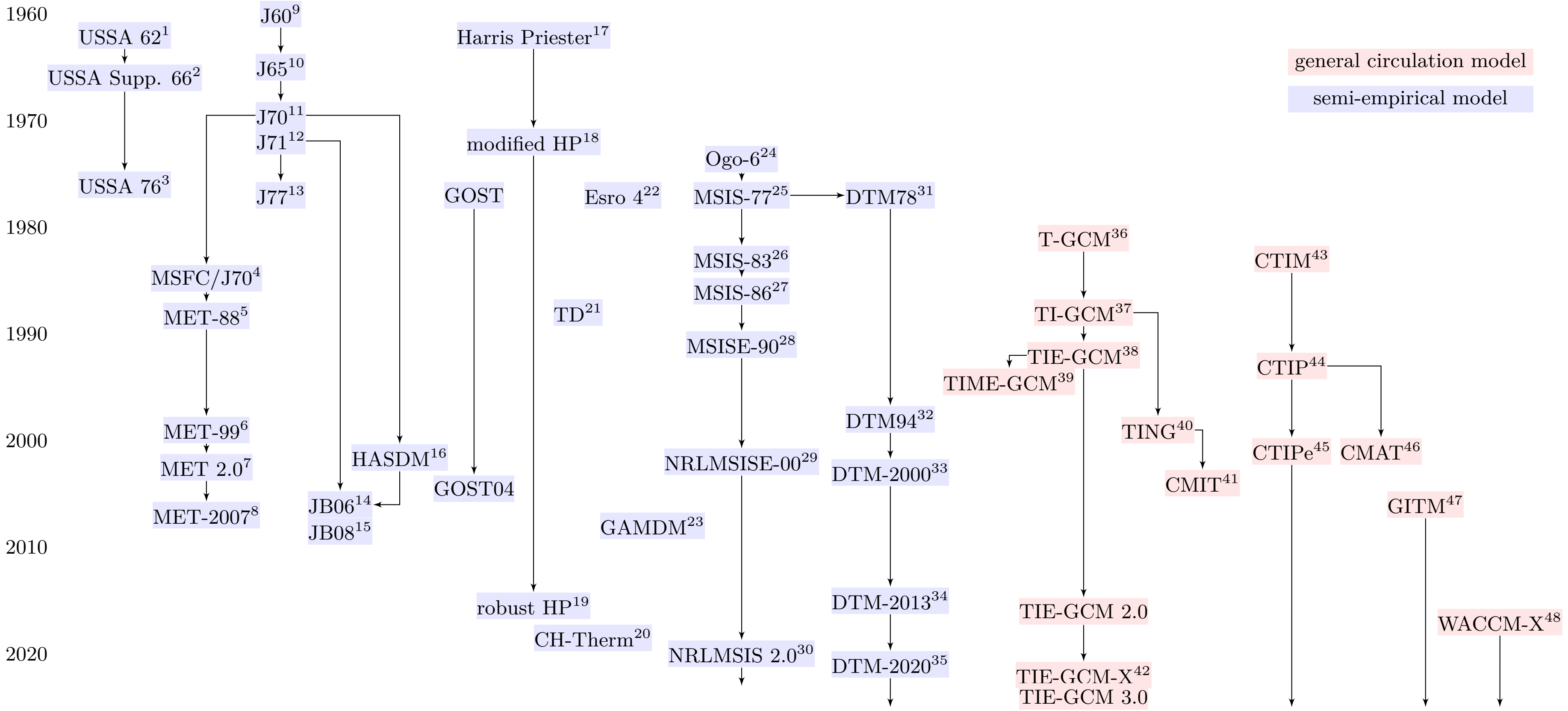

---

[1]*USSA62* 1962, [2]*USSA66* 1966, [3]*USSA76* 1976, [4]D. L. Johnson and R. E. Smith 1985, [5]Hickey, Michael Philip 1988, [6]R. E. Smith 1998, [7]Owens, J.K. 2002, [8]Suggs, R.J. and Suggs, R.M. 2007, [9]Jacchia 1960, [10]Jacchia 1965, [11]Jacchia 1970, [12]Jacchia 1971, [13]Jacchia 1977, [14]Bowman et al. 2008b, [15]Bowman et al. 2008a, [16]Storz et al. 2002, [17]I. Harris and Priester 1962, [18]Wagner and Velez 1972, [19]Hatten and Russell 2017, [20]Xiong et al. 2018, [21]Sehnal 1988, [22]von Zahn et al. 1977, [23]Emmert and Picone 2010, [24]Hedin et al. 1974, [25] Hedin et al. 1977, [26]Hedin 1983, [27]Hedin 1987, [28]Hedin 1991, [29]Picone et al. 2002, [30]Emmert et al. 2021, [31]Barlier, F. et al. 1978, [32]C. Berger et al. 1998, [33]S. Bruinsma et al. 2003, [34]S. Bruinsma 2015, [35]S. Bruinsma and Boniface 2021, [36]Dickinson et al. 1981,[37]Roble et al. 1988, [38]Richmond et al. 1992, [39]Roble and E. C. Ridley 1994, [40]W. Wang et al. 1999; W. Wang 1998, [41]Wiltberger et al. 2004, [42]Cai et al. 2022, [43]Fuller-Rowell,T.J. et al. 1996, [44]Millward, G.H. et al. 1996, [45]Millward et al. 2001, [46]M. J. Harris 2001, [47]A. J. Ridley et al. 2006, [48]H.-L. Liu et al. 2018

Figure 5.1.: Timeline of thermosphere mass density models. This overview is not complete. For example, there are many models derived from the Jacchia models not included. This figure is inspired by Vallado and Finkleman (2014, Fig. 3).

5.1. TIE-GCM

The Thermosphere Ionosphere Electrodynamics General Circulation Model (TIE-GCM; Qian et al. 2014) , is developed at the National Center for Atmospheric Research (NCAR) High Altitude Observatory (HAO). It was first released in 1981. The latest release is the TIE-GCM 3.0 (see Figure 5.1). For this thesis, the TIE-GCM 2.0 is used since it was the latest release when I integrated data assimilation. The TIE-GCM is written mostly in Fortran 77 (e.g., Kedward et al., 2022) and parallelized with the Message Passing Interface (MPI; Message Passing Interface Forum 2023) . The TIE-GCM 2.0 is a global model of the atmosphere from approximately 97 km to 500 km. The exact location of the upper boundary depends on the location since pressure is used internally as the vertical coordinate. It “self-consistently solves the fully coupled nonlinear, hydrodynamic, thermodynamic, and continuity equations of the neutral gas, the ion and electron energy and momentum equations, the ion continuity equation, and the neutral wind dynamo.” (Qian et al., 2014) While presenting all the equations in comprehensive detail would undoubtedly be cumbersome, they have been cataloged in (Qian et al., 2014, Table 1) and the model description[1].

5.1.1. State Variables

The TIE-GCM incorporates 17 prognostic state variables (see Table 5.3). For these state variables, initial values must be specified before starting the model. In addition, the TIE-GCM can compute many diagnostic state variables that are computed during the model forecast. An example of a diagnostic state variable is the neutral mass density. For some of the prognostic state variables, the temporal gradient is required. It is implicitly represented by including the corresponding state variable at the previous time step.

5.1.2. External Forcing and Lower Boundaries

Solar XUV and EUV radiation is the major energy input of the thermosphere (see Section 2.3.1.1). The TIE-GCM approximates the solar spectrum (Section 2.3.1) between 0.05 nm and 175 nm by proxy models that simulate binned solar energy flux densities (Equation 2.30) based on the F10.7 index (see Section 2.3.1.2). The spectrum between 175 nm and 105 nm is covered by the model of T. N. Woods and Rottman (2002). The wavelengths from 105 to 0.05 nm are simulated according to the approach from Solomon and Qian (2005), which relies mainly on the EUVAC (Richards et al., 1994) and HFG model (Hinteregger et al., 1981).

The ion convection/electric potential at the poles is either simulated by the Heelis (Heelis et al., 1982) or the Weimar model (Weimer, 2005). The Heelis model uses the Kp index (see Section 2.3.2.2). The Weimar model uses the IMF flux density and solar wind velocity and density from the high resolution OMNI data set (Papitashvili and King, 2020a).

To run the TIE-GCM, one must specify lower boundary conditions for the neutral temperature, the neutral horizontal wind velocity, and the geopotential height. The default setting assumes there is no wind, the neutral temperature is 181 K, and the geopotential height is 96.4 km. Instead of this flat lower boundary one can load zonal climatologies containing indi-

---

[1] `https://www.hao.ucar.edu/modeling/tgcm/doc/description/model_description.pdf`

Table 5.3.: This table contains all prognostic state variables of the TIE-GCM 2.0. The short name is used to label the variables in the output files of the TIE-GCM. If the last column $t-1$ is true, the corresponding state variable is also required at the previous time step to compute temporal gradients. To distinguish between the current and previous time step in the output files, the short name of the variable referring to the previous time step is appended by '_NM'.

name	symbol	short name	units	$t-1$
thermosphere				
mass fraction of atomic Oxygen	w_{O}	O1	-	yes
mass fraction of molecular Oxygen	$w_{\mathrm{O_2}}$	O2	-	yes
mass fraction of atomic Helium	w_{He}	HE	-	yes
mass fraction of atomic Argon	w_{Ar}	AR	-	yes
mass fraction of excited Nitrogen in ^4S atomic state	$w_{\mathrm{N}(^4S)}$	N4S	-	yes
mass fraction of excited Nitrogen in ^2D atomic state	$w_{\mathrm{N}(^2D)}$	N2D	-	no
mass fraction of nitric oxide	w_{NO}	NO	-	yes
neutral temperature	T_n	TN	K	yes
neutral zonal wind (in east direction)	u_n	UN	$\mathrm{cm\,s^{-1}}$	yes
neutral meridional wind (in north direction)	v_n	VN	$\mathrm{cm\,s^{-1}}$	yes
vertical motion[1]	ω_n	OMEGA	$\mathrm{s^{-1}}$	no
ionosphere				
number density of atomic Oxygen ions	$C_{\mathrm{O^+}}$	OP	$\mathrm{cm^{-3}}$	yes
number density of molecular Oxygen ions	$C_{\mathrm{O_2^+}}$	O2P	$\mathrm{cm^{-3}}$	no
ion temperature	T_i	TI	K	no
electron temperature	T_e	TE	K	no
electron number density	C_{e}	NE	$\mathrm{cm^{-3}}$	no
electro dynamics				
electric potential	U	POTEN	V	no

[1] Multiplying the vertical motion with the pressure scale height, which is defined in Equation 2.19, yields the neutral vertical wind velocity in $\mathrm{m\,s^{-1}}$.

vidual zonal conditions for each month of year and each hour of day. Those climatologies can be obtained for example from empirical models. Additionally, semi-diurnal and diurnal atmospheric tides simulated by the Global Scale Wave Model (GSWM; Hagan and Forbes 2002; X. Zhang et al. 2010) can be added to the lower boundary.

5.1.3. Parameters

The model parameters of the TIE-GCM control its dynamics. A few parameters can be controlled via the configuration file read by the TIE-GCM; the majority is hardcoded and requires recompilation of the code if changed. The sheer number of model parameters makes a comprehensive listing impractical. Thus, the following description is limed to the parameters required for the understanding of Chapters 7 and 8.

The Joule heating (see Section 2.3.2.1) computation in the TIE-GCM does not account for small-scale fluctuations in the electric field (M. V. Codrescu et al., 1995; Maute et al., 2021). To compensate for this, a scaling factor, the Joule heating factor, is used within the TIE-GCM for correcting the Joule heating. The default value is 1.5, increasing Joule heating by 50 %.

The momentum transfer collision frequency of O and O^+ in the TIE-GCM is modeled according to the Banks model (R. Schunk and Nagy 2009, Table 4.5, P. M. Banks and Kockarts 1973a, Table 9.13, P. Banks 1966, Table 10). The so-called Burnside factor is used within the TIE-GCM to correct the modeled collision frequency. Ieda (2021) figured that the Burnside factor was introduced due to a misunderstanding and recommends replacing the Banks model with the Stallcop model (Stallcop et al., 1991). For the moment, I ignore this and use the classical model. The default value for the Burnside factor in the TIE-GCM is 1.5.

The TIE-GCM parametrizes the energy distribution of polar rain electrons and cusp electrons with Maxwellian distributions using the distribution's peak[1] as form parameter (Rees and Luckey 1974, Equation 1, Ashrafi et al. 2005, Equation 6).

5.1.4. Discretization

The TIE-GCM is discretized in time and space. The temporal resolution is set individually for each model run and is constant over each run. Typically, the duration between subsequent model steps is chosen between 30 s to 60 s. During geomagnetic storms, higher resolutions, for example, 10 s, might be necessary for a stable model forward integration.

The TIE-GCM uses mostly polar coordinates with regular spacing for spatial coordinates. Some state variables are defined on geomagnetic coordinates employing modified magnetic apex latitude and longitude (see Appendix E.3). The following discussion only refers to the polar coordinates since all prognostic state variables and all other state variables relevant to this thesis are specified on those. Further details about the geomagnetic coordinates can be found in the model description (*Grid Structure and Resolution — TIEGCM 2.0 Documentation* 2024).

The angles of the polar coordinates are geocentric longitude and latitude. For the TIE-GCM 2.0, the horizontal resolution can be either 5° or 2.5°. The vertical component is specified in pressure levels (see Equation A.30). This enables a simplification of the continuity equation: When using pressure coordinates together with the aerostatic assumption (see Appendix A.1), the continuity equation is equivalent to that of an incompressible fluid (Emmert, 2015). The TIE-GCM 2.0 uses 0.5 or 0.25 pressure levels as vertical resolution when running with 5° or 2.5° resolution, respectively. The model covers pressure levels between $k = -7$ and $k = 7$ with reference pressure $p_0 = 5 \times 10^{-5}\,\mathrm{Pa}$ at $k = 0$. This corresponds to $5.5 \times 10^{-2}\,\mathrm{Pa}$ and $4.6 \times 10^{-8}\,\mathrm{Pa}$ at the lower and upper boundary.

While the horizontal coordinates always refer to the center of the cells, the vertical coordinates either correspond to the center of a cell or the interface between two cells. The coordinates at the interfaces are calculated via linear interpolation. Thus, state variables specified at the interfaces can be used directly as input for vertical integration at the cell centers using the trapezoidal rule.

5.1.5. Derivatives

The TIE-GCM calculates horizontal derivatives via fourth-order centered finite differences and vertical derivatives as well as temporal derivatives via second-order centered finite differences

---

[1] called 'characteristic Maxwellian energy' in TIE-GCM

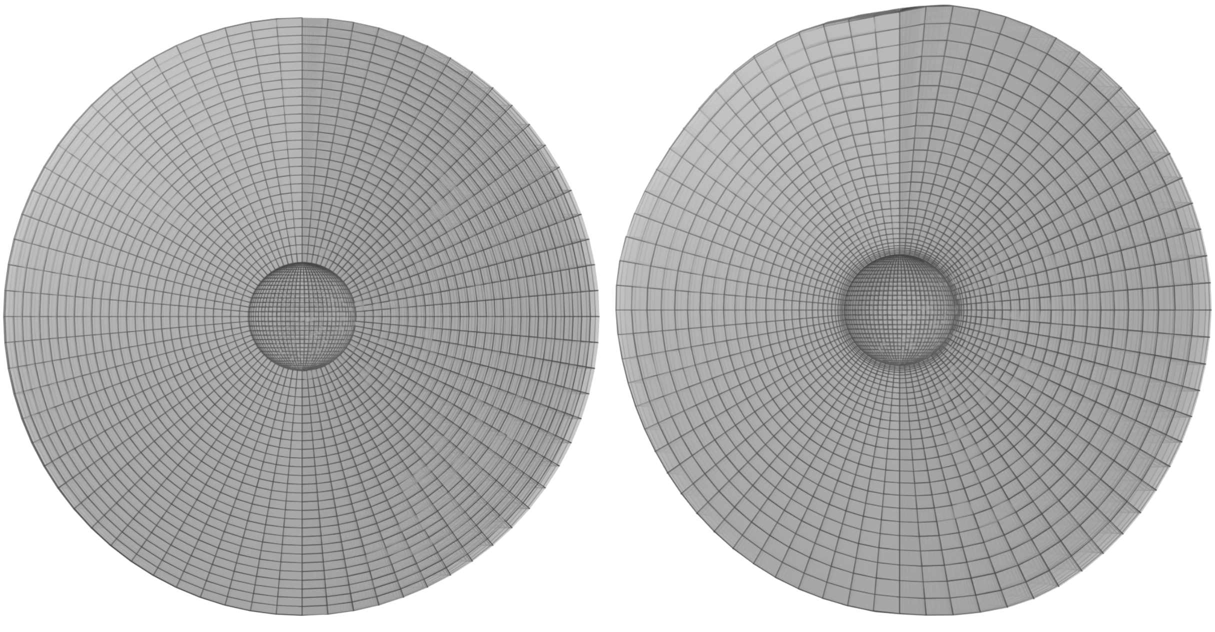

(a) pressure level is vertical coordinate (b) geometric height is vertical coordinate

Figure 5.2.: These cross-sections through a meridian of the TIE-GCM grid (5° version) illustrate the difference between pressure level and geometric height. While the pressure levels are constant, the geometric height is different for each cell and point in time.

(Qian et al., 2014). Those differencing schemes are known to cause a spurious growth of high-frequency waves over several model integration steps, making the calculations unstable (Shapiro, 1970). The TIE-GCM compensates this effect by smoothing all time-dependent fields with a Shapiro low-pass filter (Shapiro, 1970, 1975). Additionally, physically unrealistic high-frequency zonal waves at high latitudes are eliminated in the spectral domain which is accessed via fast Fourier transformation (Qian et al., 2014).

5.1.6. Interpolation

As described above, most of the state variables in the TIE-GCM are given on a three-dimensional grid at each time step that is regular in geocentric longitude, latitude, and pressure (see Figure 5.2a). However, many applications require geometric altitudes instead of pressure as a vertical coordinate. The pressure levels can be converted to geopotential altitude using Equation 2.26. This conversion requires the geoptential altitude at the lower boundary (Section 5.1.2). A subsequent conversion from geopotential to geometric altitude is possible via Equation 2.28. Within the TIE-GCM 2.0 a slightly more sophisticated approach for converting geopotential to geometric altitudes is employed that uses gravitational acceleration depending on latitude[1]. If not specified otherwise, the TIE-GCM assumes the lower boundary is located at 96.4 km. The resulting geometric altitudes depend heavily on space weather. The geometric altitude of the upper boundary varies about around 460 km and 820 km.

---

[1] The TIE-GCM 2.0 employs the approximation $g(\phi) = g_{45}(1 + a\cos(2\phi) + b\cos^2(2\phi))$ for calculating Earth's gravity. The gravity at 45° is chosen as $g_{45} = 9.806\,16\,\mathrm{m\,s^{-2}}$, which is closer to the actual value than the conventional value (List, 1951, p.4). The coefficient a is -0.002637 and the quadratic term is neglected ($b = 0$).

When transforming the original grid to geometric altitudes, one obtains a grid that is regular in longitude and latitude but not in altitude. Each cell has an individual altitude (see Figure 5.2b). By performing the interpolation on the irregular dimension (altitude) first, the remaining dimensions (longitude, and latitude) can be interpolated efficient by exploiting the resulting regular structure. An example of how the interpolation can be implemented is described later in Section 7.3.

5.2. Semi-Empirical Models

Semi-empirical upper atmosphere models are constructed by fitting extensive temperature, composition, and density observation datasets to parametric functions. The datasets are obtained, for example, from incoherent scatter radar (Section 4.4), mass spectrometers (Section 4.3), derived from accelerometers (Section 4.1), and derived from orbital decay (4.2). Semi-empirical models represent the average state of the upper atmosphere, parameterized by position, time, and solar and geomagnetic activity. The development history of empirical models dates back to the 1960s (see Figure 5.1). Today, the NRLMSIS, Jacchia-Bowman, and DTM semi-empirical models are frequently employed.

5.2.1. MSIS

The first model of the Mass Spectrometer Incoherent Scatter radar (MSIS) series dates back to 1977 (see Figure 5.1). The latest version is the Naval Research Laboratory Mass Spectrometer and Incoherent Scatter radar 2.0 (NRLMSIS 2.0, Emmert et al. 2021). As the name suggests, the original model is based on mass spectrometer (see Section 4.3) and incoherent scatter radar measurements (see Section 4.4). However, the underlying dataset of observations was drastically increased in later versions (Emmert et al., 2021, Table 1). The data sets cover altitudes from 0 km up to 575 km. 84 % of the observations are located between 0 km and 105 km.

The NRLMSIS 2.0 is a global model from the ground to the exosphere. Although one can sample the model with an arbitrary resolution, the actual horizontal resolution is limited by the choice of the parametric functions. The MSIS models use spherical harmonic functions up to degree six (Hedin 1987, Equation A22 and Emmert et al. 2021, Section 2.4 and text S2) to expand the vertical temperature and density profile parameters to the global atmosphere. Thus, the NRLMSIS 2.0 can resolve horizontal signal with wavelengths larger than $\frac{360°}{6} = 60°$.

The response to external forcing is limited by the resolution of the external forcings (Table 5.2a). The MSIS models uses the Kp and F10.7 index. Thus, the response to space weather is delayed up to three hours.

5.2.2. Jacchia-Bowman (JB)

The Jacchia-Bowman models (Bowman et al., 2008a,b) are based on the Jacchia models (see Figure 5.1). The latest version is the JB08. Its drivers (Table 5.2a) are explained in Tobiska et al. (2008a), and summarized in Section 2.3.1.2 and Section 2.3.2.2.

The JB08 model is constructed from four mass density datasets (Bowman et al., 2008a, Section II):

1. Air Force daily density data (Bowman et al., 2004) derived from orbital decay of satellites with perigee altitudes from 175 km to 1000 km and observed by radar and optical instruments (Space Surveillance Network),
2. Air Force High Accuracy Satellite Drag Model (HASDM Storz et al., 2002) constructed from satellite tracking observations (Space Surveillance Network) and tracking inactive payloads and debris with low perigrees,
3. accelerometer-derived densities from the CHAMP satellite,
4. and accelerometer-derived densities from the GRACE satellite.

The JB08 model reaches from 175 km to 1000 km altitude.

5.3. Model Performance

To compare neutral mass densities derived from models with observations, the ratio between modeled and observed densities–also called scale factor–is often considered. In case the mass density is not observed directly, but linked to atmospheric drag via aerodynamics (Section 4.1), the scale factor cannot be attributed to the mass density alone. Instead, it may also include errors of the aerodynamic and force models. One has to keep this in mind when interpreting comparisons based on scale factors.

Gaposchkin and Coster (1990) compared the atmospheric drag of three spherical satellites at different altitudes obtained from precise tracking data with simulated drag. They used different empirical density models (J71, DTM78, J77, MSIS83, MSIS86) for the atmospheric drag simulation and found that the simulated drag was not better than 15 % accurate at lower altitudes and worse at higher altitudes.

F. A. Marcos (1990) compared accelerometer-derived mass densities from different satellites from 150 to 250 km altitude within the period 1974-1982 with 15 empirical models (many versions of the Jaccia models and models derived from Jacchia models, many versions of the MSIS model series, and USSA62, USSA66). The mean of the scale factor exhibited a deviation of approximately ±10 % from 1, and the standard deviation of the scale factor was around 15 %.

F. Marcos et al. (2006) compared several empirical models (J70, MET 2.0, NRLMSISE-00, DTM-2000, JB06) with daily density values obtained by tracking 38 satellites. The comparison was made in terms of scale factors and focused on altitudes below 600 km. The mean scale factors of the models were found to be similar, but the JB06 model, which was the latest model at the study's publication, had a standard deviation of the scale factors up to 10 % lower.

S. L. Bruinsma et al. (2012) compared the DTM2000, DTM2009, NRLMSISE-00, and JB08 models with neutral mass densities derived from accelerometers, orbital decay/energy dissipation and thruster data of the drag-free GOCE satellite. The accuracy of the models was found to depend on the altitude. Using a metric that considered mean, root mean square error (RMSE) and correlation, the JB08 was the best model below 300 km, between 300-500 km JB08 and DTM2009 were best, and above 500 km DTM2009 and NRLMSISE-00 were the best performing models. From that, they concluded that the DTM2009 had the best overall performance.

S. L. Bruinsma et al. (2014) compared the NRLMSISE-00, JB08 and DTM2012 with data from the GOCE satellite over a ∼2.5 year lasting period and found that they match at the 10 % level.

C. He et al. (2018) reviewed twelve empirical density models (Jacchia, MSIS, DTM, and JB series), compared them with each other and with accelerometer-derived densities from the GRACE mission from different sources. The accelerometer-derived densities differed by 5 % among each other during high solar activity and 20 % during low activity. All twelve models overestimate the neutral mass density.

Zeitler et al. (2021) computed half-daily scale factors for SLR satellites, GRACE and CHAMP w.r.t. the NRLMSISE-00 model. They found that the model overestimates the density under low solar activity and underestimates the density at high activity. The half-daily scale factors, which indicate the discrepancy between the model and the observations, reached up to 30 % at low solar activity and up to 70 % at high solar activity. The mean value of the scale factors obtained from precise orbit determination using SLR observations indicated that the model underestimates the densities by 10 % to 12 % on average during high solar activity. During low solar activity, the density was overestimated by up to 4 % on average.

S. Bruinsma et al. (2023) compared recent mass density datasets. They emphasized that current density data sets are not consistent and need to be calibrated before combining or assimilating them.

J. He et al. (2023) investigated a moderate geomagnetic storm using semi-empirical models (NRLMSIS 2.0 and DTM2013), numerical models (MAGE (TIE-GCM), CTIPe, WAM-IPE and WACCM-X), and observations (Swarm-A, GRACE-FO). They found that the models captured the storm induced density enhancement but found discrepancies of up to 70 % between the models.

6. Data Assimilation

> Data assimilation (DA) is the science of combining observations of a system, including their uncertainty, with estimates of that system from a dynamical model, including its uncertainty, to obtain a new and more accurate description of the system including an uncertainty estimate of that description. (Vetra-Carvalho et al. 2018)

Data assimilation can be categorized into two branches: *statistical* and *variational* methods (see for example, Asch et al., 2016, Figure 1.5). Statistical data assimilation methods emanate from estimation theory and maximize the PDF of the state of the system (e.g., by seeking the state with the smallest variance). The basis for variational methods is optimal control theory. The name relates to the *calculus of variations*, which enables finding extrema of functionals. Variational data assimilation methods minimize a cost function to find the optimal state (Asch et al., 2016, Section 2.1), for example, using conjugate gradients methods. In certain instances, statistical and variational methods are identical, resulting in equivalent outcomes (Asch et al., 2016).

One has to distinguish between *filters* and *smoothers*. While filters correct the modeled state at a point in time using only observations given simultaneously, smoothers also consider future observations. Filters first forward the model state and then update the state by the given observations at that time. Both steps (forwarding and updating) are repeated sequentially.

This chapter provides an overview of statistical filters, with a detailed description of ensemble square root filters used in this thesis. The first Section 6.1 summarizes the stochastic fundamentals. The discussion of data assimilation begins in Section 6.2, where the relationship between models and observations is established. Section 6.3 introduces statistical data assimilation, ensemble (square root) filters, and especially the Error-Subspace Transform Kalman Filter (ESTKF). How to localize a filter is explained in Section 6.4 and how to co-estimate model dynamics in Section 6.5. I do not apply variational methods since this would explicitly require the variance covariance matrix (VCM) of the model. In addition, for variational data assimilation over a time window (4DVar), the gradient of the objective function is required, necessitating an adjoint model formulation (e.g., Errico, 1997) of the TIE-GCM in practice. Therefore, variational methods are not further discussed here. The interested reader may, for example, refer to Ide et al. (1997, Section 4), Asch et al. (2016) and Lahoz et al. (2010). In this chapter, I use the notation for data assimilation proposed by Ide et al. (1997) for vectors, matrices, and operators.

6.1. Stochastic Fundamentals

This section provides a concise overview of random variables, statistical moments, and normal distributions necessary for deriving statistical data assimilation.

6.1.1. Random Variables

A continuous random variable X has a cumulative distribution function (CDF) $F(x)$ and a probability density function (PDF) $f(x)$ related by (Koch, 1999, Definition 2.30)

$$F(x) = \int_{-\infty}^{x} f(t)dt = P(X < x). \tag{6.1}$$

The result of $F(x)$ is the probability that the corresponding random variable X is less than x and $f(x)$ is the probability that the random value has value x. The PDF has to satisfy the following conditions (Koch, 1999, Equation 2.35)

$$f(x) \geqslant 0, \tag{6.2}$$

$$\int_{-\infty}^{\infty} f(x)dx = 1, \tag{6.3}$$

that means probabilities are non-negative, and the combined probability of all possible outcomes is one. This is valid for arbitrary dimensions, i.e., x is a vector containing n random variables. The explicit multidimensional formulation of Equation 6.1 is (Koch, 1999, Definition 2.41)

$$F(x_1, \dots, x_n) = \int_{-\infty}^{x_n} \dots \int_{-\infty}^{x_1} f(t_1, \dots, t_n)\, dt_1 \dots dt_n = P(X_1 < x_1, \dots, X_n < x_n). \tag{6.4}$$

Analogous to the one-dimensional case, the conditions

$$f(x_1, \dots, x_n) \geqslant 0, \tag{6.5}$$

$$\int_{-\infty}^{\infty} \dots \int_{-\infty}^{\infty} f(x_1, \dots, x_n)\, dx_1 \dots dx_n = 1 \tag{6.6}$$

have to be fulfilled (Koch, 1999, Equation 2.45).

For $n > 1$, one can compute marginal and conditional PDFs. To obtain the marginal PDF (Koch, 1999, Section 2.2.6)

$$f(x_{i+1}, \dots, x_n) = \int_{-\infty}^{\infty} \dots \int_{-\infty}^{\infty} f(t_1, \dots, t_i, t_{i+1}, \dots, t_n)\, dt_1 \dots dt_i. \tag{6.7}$$

one has to integrate over the variables one wants to marginalize. The conditional PDF (Koch, 1999, Section 2.2.7)

$$f(x_1, \dots, x_i | x_{i+1}, \dots, x_n) = \frac{f(x_1, \dots, x_n)}{\int_{-\infty}^{\infty} \dots \int_{-\infty}^{\infty} f(t_1, \dots, t_n)\, dt_1 \dots dt_i} \tag{6.8}$$

is the cross-section along the conditional variables normalized by the corresponding marginal PDF. Equation 6.8 is called Bayes' law since the first known occurrence of this relation can be found in Bayes and Price (1763). An illustration of Bayes' law using a bivariate normal distribution is given in Figure 6.1.

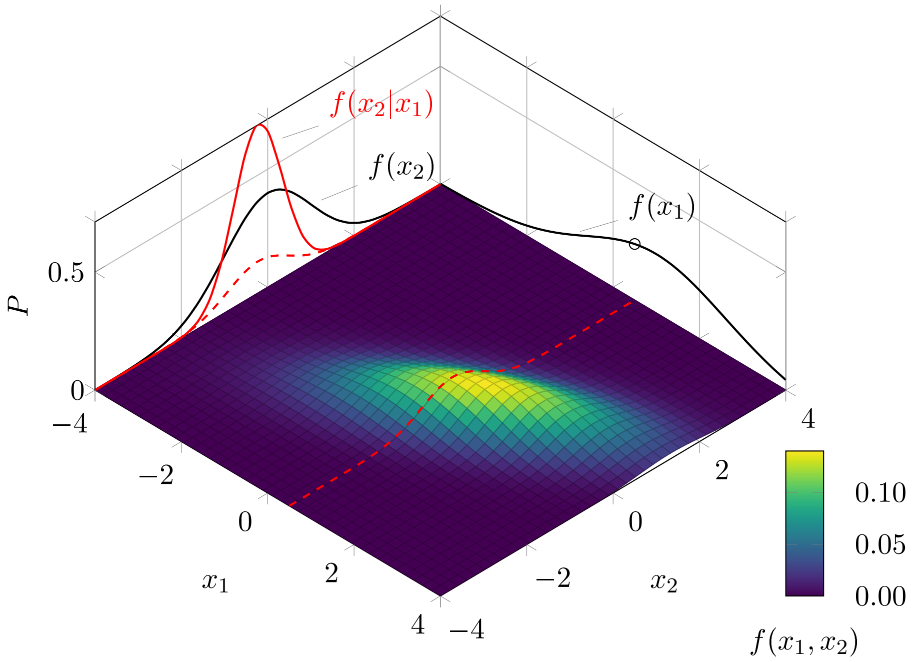

Figure 6.1.: This surface plot displays a bivariate normal distribution. The solid black lines are the corresponding marginal distributions. The red dashed line is a cross-section through the bivariate normal distribution. The solid red line is the conditional probability of x_2 given x_1. It is a scaled or normalized version of the cross-section.

In the following, a more condensed notation using vectors as function arguments is introduced. Subdividing the random vector $\boldsymbol{x}$ into two parts yields

$$\boldsymbol{x} = \begin{bmatrix} x_1 \\ \vdots \\ x_i \\ x_{i+1} \\ \vdots \\ x_n \end{bmatrix} \begin{matrix} \left.\vphantom{\begin{matrix} x_1 \\ \vdots \\ x_i \end{matrix}}\right\} \boldsymbol{x_1} \\ \left.\vphantom{\begin{matrix} x_{i+1} \\ \vdots \\ x_n \end{matrix}}\right\} \boldsymbol{x_2} \end{matrix} = \begin{bmatrix} \boldsymbol{x_1} \\ \boldsymbol{x_2} \end{bmatrix} \tag{6.9}$$

then Equation 6.8 can be written as

$$f(\boldsymbol{x_1}|\boldsymbol{x_2}) = \frac{f(\boldsymbol{x_1}, \boldsymbol{x_2})}{f(\boldsymbol{x_2})}. \tag{6.10}$$

An alternative formulation is

$$f(\boldsymbol{x_1}|\boldsymbol{x_2}) = \frac{f(\boldsymbol{x_2}|\boldsymbol{x_1}) f(\boldsymbol{x_1})}{f(\boldsymbol{x_2})}. \tag{6.11}$$

6.1.2. Moments

The k-th moment of a multivariate PDF is defined as (Koch, 1999, Definition 2.64)

$$\mu^{(k)}_{x_1,\cdots,x_n} = E(X_1^{k_1} \dots X_n^{k_n}) = \int_{-\infty}^{\infty} \cdots \int_{-\infty}^{\infty} x_1^{k_1} \dots x_n^{k_n} f(x_1, \dots, x_n)\, dx_1, \dots, dx_n \tag{6.12}$$

with order

$$k = \sum_{i=1}^{n} k_i, \quad k_i \in \mathbb{N} \tag{6.13}$$

that is the sum of natural powers applied to each component of the random variable. $E(X_i)$ denotes the expected value (Koch, 1999, Definition 2.60) of the random variable x_i. Accordingly, the k-th moment of a single variable is (Koch, 1999, Equation 2.65)

$$\mu^{(k)}_{x_i} = E(X_i^k) = \int_{-\infty}^{\infty} \cdots \int_{-\infty}^{\infty} x_i^k f(x_1, \dots, x_n)\, dx_1, \dots, dx_n \tag{6.14}$$

The first moment ($k = 1$) is the expected value or mean value and in the following denoted with μ_i. Because of Equation 6.3 the first moment of a PDF is equivalent to the center of mass of $f(x)$.

6.1.2.1. Central Moments

Moments that are reduced by the mean (Koch, 1999, Definition 2.67)

$$\bar{\mu}^{(k)}_{x_1,\cdots,x_n} = E\left((X_1 - \mu_1)^{k_1} \dots (X_n - \mu_n)^{k_n}\right) \tag{6.15}$$

are central moments. The second central moment ($k = 2$) is called *covariance* (Koch, 1999, Definition 2.68)

$$\sigma_{i,j} = E\left((X_i - \mu_i)(X_j - \mu_j)\right) = \int_{-\infty}^{\infty} \cdots \int_{-\infty}^{\infty} (x_i - \mu_i)(x_j - \mu_j) f(x_1, \dots, x_n)\, dx_1, \dots, dx_n. \tag{6.16}$$

The special case $i = j$ is called *variance* and is a measure for the scattering of the random variable. The variance covariance matrix (VCM)

$$\mathbf{\Sigma} = \begin{bmatrix} \sigma_{1,1} & \sigma_{1,2} & \cdots & \sigma_{1,n} \\ \sigma_{2,1} & \sigma_{2,2} & \cdots & \sigma_{2,n} \\ & \cdots & & \\ \sigma_{n,1} & \sigma_{n,2} & \cdots & \sigma_{n,n} \end{bmatrix} \tag{6.17}$$

contains all possible combinations of central second moments of a random vector. The diagonal elements are the variances, and the off-diagonal elements are the covariances. The square root of the variance is the *standard deviation*

$$\sigma_i := \sqrt{\sigma_{i,i}}. \tag{6.18}$$

Accordingly an alternative notation for the variance is $\sigma_i^2 = \sigma_{i,i}$.

The correlation is the covariance normalized by the product of the standard deviations (Koch, 1999, Definition 2.72)

$$\rho_{i,j} = \frac{\sigma_{i,j}}{\sigma_i \sigma_j} \tag{6.19}$$

The correlation matrix $\boldsymbol{R}$ is given by (Koch, 1999, Equation 2.81)

$$\boldsymbol{R} = \boldsymbol{F}\boldsymbol{\Sigma}\boldsymbol{F} \quad \text{with} \quad \boldsymbol{F} = \begin{bmatrix} \frac{1}{\sigma_1} & & \\ & \ddots & \\ & & \frac{1}{\sigma_n} \end{bmatrix} \tag{6.20}$$

and the VCM accordingly by

$$\boldsymbol{\Sigma} = \boldsymbol{F}^{-1}\boldsymbol{R}\boldsymbol{F}^{-1}. \tag{6.21}$$

The higher the order of a moment, the larger the number of permutations satisfying Equation 6.13. Two statistics of particular interest derived from a third and a fourth moment are skewness and kurtosis, respectively. The skewness is the univariate ($x_1{=}x_2{=}x_3$) third central moment ($k_1{=}k_2{=}k_3 = 1$) normalized by the standard deviation (e.g., Kokoska and Zwillinger, 2000, Equation 2.37)

$$\gamma_1(x) = \frac{E\left((X-\mu)^3\right)}{\sigma^3}. \tag{6.22}$$

It characterizes the asymmetry of a distribution. The kurtosis is the univariate ($x_1{=}x_2$) fourth central moment ($k_1{=}k_2 = 2$) normalized by the standard deviation (e.g., Kokoska and Zwillinger, 2000, Equation 2.42)

$$\beta_2(x) = \frac{E\left((X-\mu)^4\right)}{\sigma^4}. \tag{6.23}$$

6.1.2.2. Estimation of Moments from Samples

Given m samples of a multivariate PDF of dimension n one can collect all samples in a matrix

$$\boldsymbol{X} = \begin{bmatrix} x_{1,1} & x_{1,2} & x_{1,3} & \cdots & x_{1,m} \\ x_{2,1} & x_{2,2} & x_{2,3} & \cdots & x_{2,m} \\ & & \vdots & & \\ x_{n,1} & x_{n,2} & x_{n,3} & \cdots & x_{n,m} \end{bmatrix} \tag{6.24}$$

where the first index corresponds to the variable and the second index to the sample.

The sample mean of an element x_i of the random vector is

$$\mu_i \approx \hat{\mu}_i = \frac{1}{m}\sum_{u=1}^{m} x_{i,u}. \tag{6.25}$$

The sample covariance of the random variables x_i and x_j is

$$\sigma_{i,j} \approx \hat{\sigma}_{i,j} = \frac{1}{m-1} \sum_{u=1}^{m} \left(x_{i,u} - \hat{\mu}_i\right) \left(x_{j,u} - \hat{\mu}_j\right). \tag{6.26}$$

This is an unbiased estimator of the covariance, which considers that one degree of freedom was lost by the computation of the sample mean. The sample mean of the entire random vector can be computed by

$$\hat{\boldsymbol{\mu}} = \frac{1}{m} \boldsymbol{X} \boldsymbol{I} \tag{6.27}$$

and the sample VCM with

$$\hat{\boldsymbol{\Sigma}} = \frac{1}{m-1} \left(\boldsymbol{X} - \bar{\boldsymbol{X}}\right) \left(\boldsymbol{X} - \bar{\boldsymbol{X}}\right)^{\mathsf{T}} \quad \text{with} \quad \bar{\boldsymbol{X}} = \hat{\boldsymbol{\mu}} \boldsymbol{I}^{\mathsf{T}}. \tag{6.28}$$

The rank of the perturbation matrix $\boldsymbol{X} - \bar{\boldsymbol{X}}$ is at most $m-1$, as one degree of freedom is lost by the computation of the mean from $\boldsymbol{X}$. Accordingly, the dyadic product is divided by $m-1$. Note that the sample VCM $\hat{\boldsymbol{\Sigma}}$ is only invertible if $m > n$, that is the sample size is greater than the dimension of the random vector (e.g., Ledoit and Wolf, 2004).

The sample skewness of a variable x_i is (e.g., *skewness* 2025)

$$\hat{\gamma}_1(x_i) = \frac{m}{(m-1)(m-2)} \sum_{u=1}^{m} \left(\frac{x_{i,u} - \hat{\mu}_i}{\hat{\sigma}_i}\right)^3, \tag{6.29}$$

the sample kurtosis is (e.g., *kurtosis* 2025)

$$\hat{\beta}_2(x_i) = \frac{m(m+1)}{(m-1)(m-2)(m-3)} \sum_{u=1}^{m} \left(\frac{x_{i,u} - \hat{\mu}_i}{\hat{\sigma}_i}\right)^4, \tag{6.30}$$

and the sample excess kurtosis

$$\hat{\gamma}_2(x_i) = \hat{\beta}_2(x_i) - 3\frac{(m-1)^2}{(m-2)(m-3)}. \tag{6.31}$$

6.1.3. Normal Distribution

A random vector $\boldsymbol{x}$ of size n is normally distributed $\boldsymbol{x} \sim N(\boldsymbol{\mu}, \boldsymbol{\Sigma})$ if its associated PDF is given by (Koch, 1999, Definition 2.125)

$$f(x_1, \ldots, x_n) = f(\boldsymbol{x}) = \frac{1}{(2\pi)^{\frac{n}{2}} \left(\det \boldsymbol{\Sigma}\right)^{\frac{1}{2}}} \exp\left(\boldsymbol{x} - \boldsymbol{\mu}\right)^{\mathsf{T}} \boldsymbol{\Sigma}^{-1} \left(\boldsymbol{x} - \boldsymbol{\mu}\right) \tag{6.32}$$

and consequently fully defined by the mean vector $\boldsymbol{\mu}$ and the VCM $\boldsymbol{\Sigma}$.

When subdividing the mean vector and the VCM as in Equation 6.9 one gets

$$\boldsymbol{x} = \begin{bmatrix} \boldsymbol{x}_1 \\ \boldsymbol{x}_2 \end{bmatrix}, \quad \boldsymbol{\mu} = \begin{bmatrix} \boldsymbol{\mu}_1 \\ \boldsymbol{\mu}_2 \end{bmatrix} \quad \text{and} \quad \boldsymbol{\Sigma} = \begin{bmatrix} \boldsymbol{\Sigma}_{11} & \boldsymbol{\Sigma}_{12} \\ \boldsymbol{\Sigma}_{21} & \boldsymbol{\Sigma}_{22} \end{bmatrix}. \tag{6.33}$$

The marginal distribution of a normally distributed random vector is a normal distribution (Koch, 1999, Definition 2.136)

$$\boldsymbol{x}_1 \sim N(\boldsymbol{\mu}_1, \, \boldsymbol{\Sigma}_{11}). \tag{6.34}$$

The same holds for the conditional distribution of normal distributions (Koch, 1999, Theorem 2.137)

$$\boldsymbol{x_1}|\boldsymbol{x_2} \sim N\left(\boldsymbol{\mu}_1 + \boldsymbol{\Sigma}_{12}\boldsymbol{\Sigma}_{22}^{-1}(\boldsymbol{x}_2 - \boldsymbol{\mu}_2), \, \boldsymbol{\Sigma}_{11} - \boldsymbol{\Sigma}_{12}\boldsymbol{\Sigma}_{22}^{-1}\boldsymbol{\Sigma}_{21}\right). \tag{6.35}$$

This is also illustrated in Figure 6.1.

6.2. Modeling and Observing the State of a System

The state of a system, for example, a pendulum, a vehicle, the ocean, the atmosphere, or the solar system can be described with a set of time variable parameters. For instance, the state of the upper atmosphere may include temperature, wind velocity and composition.

"Systems whose future states evolve from their present states according to precise physical laws or mathematical equations are known as dynamical systems" (Lorenz, 1995, p. 2). In a *convergent system* "[...] rather similar initial states, each evolving according to the same laws, may become progressively more similar" (Lorenz, 1995, p. 3). In contrast, the future state of a *divergent system* strongly depends on the initial state, so that "[...] somewhat similar [initial] states become less and less similar" (Lorenz, 1995, p. 3). Divergent systems can exhibit chaotic behavior; however, divergence does not inherently imply chaos. "Chaos is aperiodic long-term behavior in a deterministic system that exhibits sensitive dependence on initial conditions" (Strogatz, 2019, p. 331). Examples of chaotic systems are double pendulums, weather in the lower atmosphere, or three-body systems[1]. A measure of sensitivity to initial conditions is provided by characteristic exponents (e.g., Eckmann and Ruelle, 1985).

A dynamic model is an approximation of a dynamic system describing its state with a set of state variables. In practice, the state is discretized in time and space, for example, using a grid or mesh. Given a parametrization using n_x state variables, the model operator $\mathcal{M} : \mathbb{R}^{n_x} \to \mathbb{R}^{n_x}$, which is also called forward operator, computes the state $\boldsymbol{x} \in \mathbb{R}^{n_x}$ at epoch t given a preceding state[2] at epoch s

$$\boldsymbol{x}(t) = \mathcal{M}_{s,t}(\boldsymbol{x}(s)) + \boldsymbol{\eta}(t) \tag{6.36}$$

with the model error $\boldsymbol{\eta} \in \mathbb{R}^{n_x}$, which represents imperfections in the model. The model operator can be a simple linear function, but also a non-linear complex program consisting of thousands lines of code. The model operator also may include external forcing and boundary conditions.

---

[1] An exception is restricted three-body systems (e.g., Frauenfelder and van Koert, 2018) which assume that the mass of the third body is virtually zero.

[2] Of course it is possible to construct models that can also propagate the state backward in time, i.e., compute the state at epoch t given a future state at epoch u.

An example of external forcing is the EUV radiation of the Sun heating and ionizing the upper atmosphere.

To run a model as specified in Equation 6.36, initial values for the state $\boldsymbol{x}^b$ are required. The initial state is also called the first guess or background state, hence the index 'b'. For a model discretized in time, the model operator forecasting the state from time step zero to step n is the composition

$$\mathcal{M}_{0,n}(\boldsymbol{x}_0) = (\mathcal{M}_{n-1,n} \circ \ldots \circ \mathcal{M}_{1,2} \circ \mathcal{M}_{0,1})(\boldsymbol{x}_0). \tag{6.37}$$

The observations $\boldsymbol{y} \in \mathbb{R}^{n_y}$ at epoch t are related to the state at the same epoch by the observation operator $\mathcal{H} : \mathbb{R}^{n_x} \to \mathbb{R}^{n_y}$

$$\boldsymbol{y}(t) = \mathcal{H}\left(\boldsymbol{x}(t)\right) + \boldsymbol{\varepsilon}(t) \tag{6.38}$$

with the observation error vector $\boldsymbol{\varepsilon}$. If the observations are not positioned at the same location as the state parameters, the observation operator incorporates an interpolation. The Jacobian matrix of the observation operator is

$$\boldsymbol{H}_t = \left.\frac{\partial \mathcal{H}(\boldsymbol{x})}{\partial \boldsymbol{x}}\right|_{\boldsymbol{x}=\boldsymbol{x}(t)} \tag{6.39}$$

and the Jacobian matrix of the model operator is

$$\boldsymbol{M}_{s,t} = \left.\frac{\partial \mathcal{M}_{s,t}(\boldsymbol{x})}{\partial \boldsymbol{x}}\right|_{\boldsymbol{x}=\boldsymbol{x}(s)}. \tag{6.40}$$

Using the Jacobian matrix introduced in Equation 6.39 one can approximate the observation operator in Equation 6.38 by a matrix vector product:

$$\boldsymbol{y}(t) = \boldsymbol{H}_t \boldsymbol{x}(t) + \boldsymbol{\varepsilon}(t). \tag{6.41}$$

For a linear observation operator, this equation is exact. Otherwise linearization errors are introduced. Similarly, using Equation 6.40, the model operators in Equation 6.37 can be approximated by matrix multiplications.

6.3. Statistical Filters

Statistical filter schemes update the state of a system sequentially at specific epochs by assimilating data at the same epochs. According to Bayes' law (Equation 6.11), the conditional PDF of the state $\boldsymbol{x}$ given the observations $\boldsymbol{y}$ is

$$f(\boldsymbol{x}|\boldsymbol{y}) = \frac{f(\boldsymbol{y}|\boldsymbol{x})f(\boldsymbol{x})}{f(\boldsymbol{y})}, \tag{6.42}$$

with the prior knowledge $f(\boldsymbol{y}|\boldsymbol{x})f(\boldsymbol{x})$, and the PDF of the observations $f(\boldsymbol{y})$ as normalization.

Statistical data assimilation filters seek at finding the state

$$\boldsymbol{x}^a = \arg\max_{\boldsymbol{x}} f(\boldsymbol{x}|\boldsymbol{y}) \tag{6.43}$$

maximizing the PDF of the state $\boldsymbol{x}$ given the observations $\boldsymbol{y}$.

Many statistical schemes are derivatives of the Kalman filter. For large-scale problems efficient ensemble-based methods have been developed.

6.3.1. Kalman Filter

The Kalman filter (Kalman and Bucy, 1961; Kalman, 1960) computes the optimal state that is the unbiased state with minimal variance if the following conditions are satisfied:

- all errors are unbiased (have zero mean) and are Gaussian (Equation 6.32)
  - observation error $\boldsymbol{\varepsilon} \sim N(\boldsymbol{0}, \boldsymbol{R})$
  - model error (system noise) $\boldsymbol{\eta} \sim N(\boldsymbol{0}, \boldsymbol{Q})$
  - (initial) state error $\boldsymbol{\xi} \sim N(\boldsymbol{0}, \boldsymbol{P})$
- some errors are uncorrelated
  - Model errors $\boldsymbol{\eta}$ and state errors $\boldsymbol{\xi}$ are uncorrelated (error propagation in Equation 6.45).
  - State errors $\boldsymbol{\xi}$ and observation errors $\boldsymbol{\varepsilon}$ are uncorrelated (error propagation in Equation 6.50).
- operators are linear
  - The mapping between the state and observations is linear i.e., the observation operator is exactly described by the matrix vector product $\mathcal{H}(\boldsymbol{x}) = \boldsymbol{H}\boldsymbol{x}$. This ensures the PDF of the computed observations are Gaussian.
  - The system is linear, i.e., the model operator is exactly described by the matrix vector product $\mathcal{M}(\boldsymbol{x}) = \boldsymbol{M}\boldsymbol{x}$. This ensures the PDF of the forecasted states are Gaussian.

If these conditions are violated the state estimated by the Kalman filter is not unbiased or not of minimal variance or both. The Kalman Filter consists of two steps, the forecast (prediction) and update (analysis) step. Both steps are repeated sequentially.

Forecast Step The forecasted state $\boldsymbol{x}_i^f$ and the associated VCM $\boldsymbol{P}_i^f$ are obtained by forwarding the model to the prediction time t_i, that is the point in time at which the next observations are available:

$$\boldsymbol{x}_i^f = \boldsymbol{M}_{i-1,i}\, \boldsymbol{x}_{i-1}^a + \boldsymbol{\eta}_i \tag{6.44}$$

$$\boldsymbol{P}_i^f = \boldsymbol{M}_{i-1,i}\, \boldsymbol{P}_{i-1}^a\, \boldsymbol{M}_{i-1,i}^{\mathsf{T}} + \boldsymbol{Q}_i \tag{6.45}$$

The inputs for that computation are the state $\boldsymbol{x}_{i-1}^a$ and the associated VCM $\boldsymbol{P}_{i-1}^a$ of the previous update step or the initial values in the case of the first forecast step. Equation 6.45 does not consider correlations between the model errors $\boldsymbol{\eta}_i$ and the errors $\boldsymbol{\xi}^a_{i-1}$ associated with the state $\boldsymbol{x}^a_{i-1}$.

Update Step The update step minimizes

$$\begin{aligned} J(\boldsymbol{x}) =& \frac{1}{2}\left(\boldsymbol{x}-\boldsymbol{x}^f_i\right)^{\mathsf{T}}\left(\boldsymbol{P}^f_i\right)^{-1}\left(\boldsymbol{x}-\boldsymbol{x}^f_i\right) \\ &+\frac{1}{2}\left(\boldsymbol{H}_i\,\boldsymbol{x}-\boldsymbol{y}^o_i\right)^{\mathsf{T}}\boldsymbol{R}_i^{-1}\left(\boldsymbol{H}_i\,\boldsymbol{x}-\boldsymbol{y}^o_i\right) \end{aligned} \tag{6.46}$$

(e.g., Lahoz et al., 2010), to compute the unbiased state with minimal variance, which is equivalent to the solution provided by Equation 6.43, given that all assumptions of the Kalman filter are satisfied (Asch et al., 2016, Section 3.4.4). $\boldsymbol{x}^f_i$ is the forecasted state and its VCM is $\boldsymbol{P}^f_i$. $\boldsymbol{y}^o_i$ contains the observations and the associated VCM is $\boldsymbol{R}_i$. The linear observation operator mapping the state to the observations is $\boldsymbol{H}_i$. An equivalent compact formulation is

$$J(\boldsymbol{x}) = \left\|\boldsymbol{x}-\boldsymbol{x}^f_i\right\|^2_{(\boldsymbol{P}^f_i)^{-1}} + \left\|\boldsymbol{H}_i\,\boldsymbol{x}-\boldsymbol{y}^o_i\right\|^2_{\boldsymbol{R}_i^{-1}} \tag{6.47}$$

with $\|\cdot\|_{\boldsymbol{M}}$ being the scalar product w.r.t. some metric $\boldsymbol{M}$.

The Kalman filter finds the optimal state in a least squares sense. The first term of Equation 6.47 penalizes the distance to the forecasted state, and the second term the distance to the observations. The minimum of Equation 6.47 is (see Appendix A.6.1 for a derivation)

$$\boldsymbol{x}^a_i = \boldsymbol{x}^f_i + \boldsymbol{K}_i\,\underbrace{(\boldsymbol{y}^o_i - \boldsymbol{H}_i\boldsymbol{x}^f_i)}_{\boldsymbol{d}_i} \tag{6.48}$$

with the Kalman matrix or gain matrix

$$\boldsymbol{K}_i = \boldsymbol{P}^f_i\boldsymbol{H}_i^{\mathsf{T}}(\boldsymbol{R}_i + \boldsymbol{H}_i\boldsymbol{P}^f_i\boldsymbol{H}_i^{\mathsf{T}})^{-1}. \tag{6.49}$$

The difference between observed and predicted observations $\boldsymbol{y}^o_i - \mathcal{H}(\boldsymbol{x}^f_i)$ is called innovation and denoted by $\boldsymbol{d}$. The entry in the u-th row and v-th column of $\boldsymbol{K}$ contains the influence of the v-th innovation on the u-th state. A zero element means that the u-th state is not influenced by the v-th observation. The VCM of the analyzed state $\boldsymbol{x}^a_i$ is (see Appendix A.6.1 for a derivation)

$$\boldsymbol{P}^a_i = (\mathbb{1} - \boldsymbol{K}_i\boldsymbol{H}_i)\boldsymbol{P}^f_i. \tag{6.50}$$

6.3.2. Extended Kalman Filter

The Extended Kalman Filter (EKF, e.g., Jazwinski, 1970, Theorem 8.1) is a variant of the Kalman filter that uses the actual operators instead of the linearized counterparts when possible and can handle non-linearities better than the original filter. The EKF uses the (non-linear) model operator to forecast the state (compare to Equation 6.44)

$$\boldsymbol{x}^f_i = \mathcal{M}_{i-1,i}(\boldsymbol{x}^a_{i-1}) + \boldsymbol{\eta}_i \tag{6.51}$$

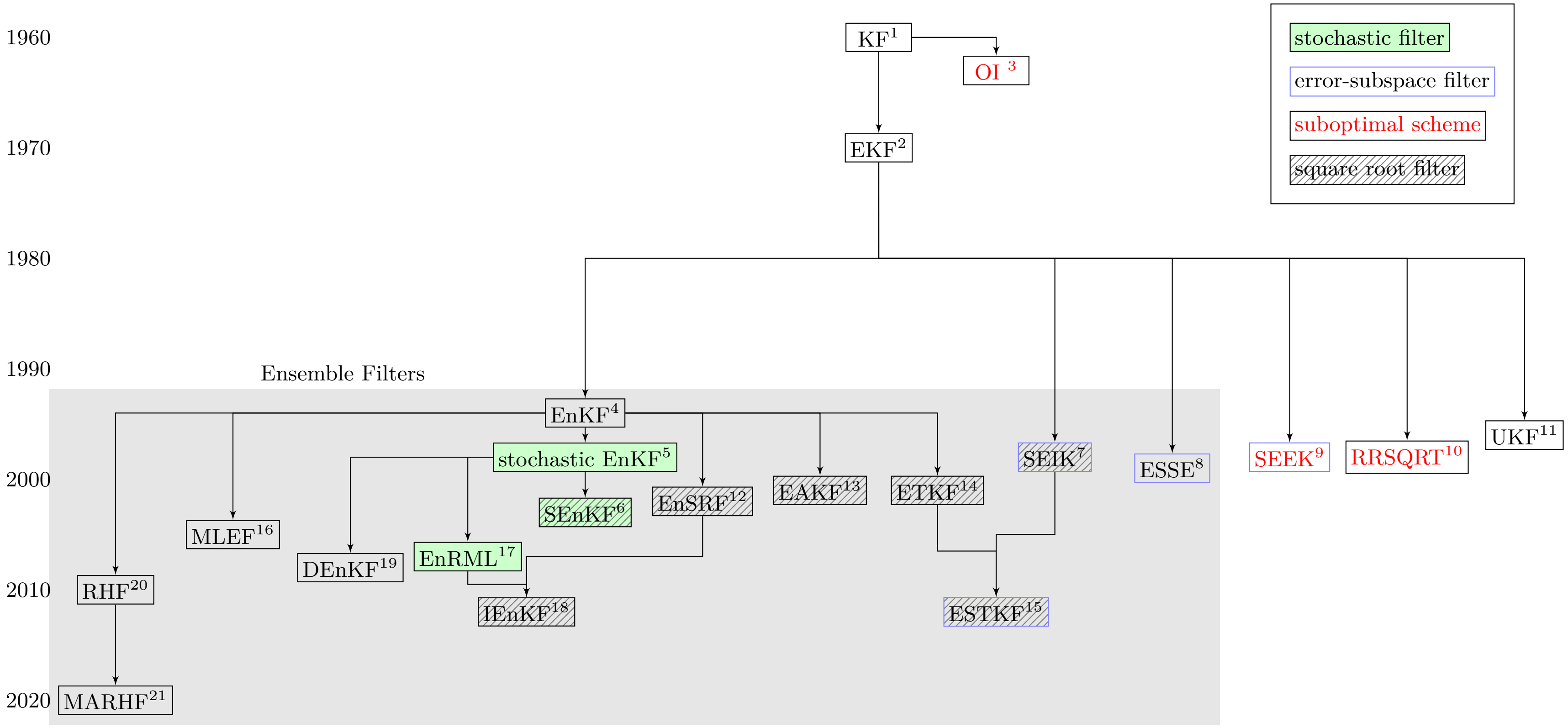

---

[1]Kalman filter (Kalman and Bucy, 1961; Kalman, 1960) [2]extended KF (Jazwinski, 1970; G. L. Smith et al., 1962) [3]optimal interpolation (Gandin, 1963) [4]ensemble KF (Evensen, 1994) [5]stochastic ensemble KF (Burgers et al., 1998; Houtekamer and Mitchell, 1998) [6]square root ensemble KF (Evensen, 2003) [7]singular evolutive interpolated KF (Pham et al., 1998) [8]error-subspace statistical estimation (Lermusiaux and Robinson, 1999) [9]singular evolutive extended KF (Tuan Pham et al., 1998) [10]Reduced Rank Square Root KF (Verlaan and Heemink, 1997) [11]Unscented KF (Julier and Uhlmann, 1997) [12]ensemble square root filter (Whitaker and Hamill, 2002) [13]ensemble adjustment KF (J. L. Anderson, 2001) [14] ensemble transform KF (Bishop et al., 2001) [15]error-subspace transform KF (Nerger et al., 2012b) [16]error-subspace transform KF (Zupanski, 2005; Zupanski et al., 2008) [17]ensemble randomized maximal likelihood KF (Gu and D. S. Oliver, 2007) [18]Iterative ensemble KF (Sakov et al., 2012) [19]deterministic ensemble KF (Sakov and Oke, 2008a) [20]rank histogram filter (J. L. Anderson, 2010) [21]marginal adjustment rank histogram filter (J. L. Anderson, 2020)

Figure 6.2.: Development time line of Kalman filters focusing on ensemble filters. This overview is incomplete. Stochastic filters use an ensemble of observations to represent the observation uncertainty. Error-subspace filters account for the rank deficiency in the state ensemble perturbation matrix and are slightly faster. Suboptimal filters further reduce the cost of the Kalman fitler, but are not optimal even for linear problems (Todling and Cohn, 1994). Tippett et al. (2003) classified filters using ensembles which are scaled matrix square roots of the state VCM as square root filters.

Table 6.1.: Dimensions of matrices used in the Kalman filter. n_y is the number of observations and n_x the number of state variables.

n_y	$n_y \times n_y$	n_x	$n_x \times n_x$	$n_y \times n_x$	$n_x \times n_y$
$\boldsymbol{y}^o$	$\boldsymbol{R}$	$\boldsymbol{x}^a$, $\boldsymbol{x}^f$	$\boldsymbol{P}^a$, $\boldsymbol{P}^f$, $\boldsymbol{M}$	$\boldsymbol{H}$	$\boldsymbol{H}^\intercal$, $\boldsymbol{K}$

but the linearized model operator to propagate the model uncertainties in Equation 6.45. Thus, the forecasted state is computed without linearization errors, but the representation of the uncertainty of the forecasted state is subject to linearization errors, for non-linear models. The innovation is computed with the (non-linear) observation operator (compare to Equation 6.48)

$$\boldsymbol{d}_i = \boldsymbol{y}_i^o - \mathcal{H}_i(\boldsymbol{x}_i^f) \tag{6.52}$$

but the linearized observation operator is used in Equation 6.49 and Equation 6.50. This introduces errors in the analyzed state and its VCM depending on the degree of non-linearity. As the uncertainty remains to represented by VCMs higher statistical moments are not represented by the EKF. Examples of applications of the EKF that lead to unstable results can be found in Evensen (1992, 1993) and Miller et al. (1994).

6.3.3. Ensemble Kalman Filters

Applying the (extended) Kalman Filter to large-scale models is extremely costly or even impossible. Since the dimension of the state vector is typically greater than the dimension of the observation vector $n_x \gg n_y$, the limiting factors are the matrices of size $n_x \times n_x$ (see Table 6.1). The memory required to store the VCM $\boldsymbol{P}$ of the state quadratically depends on the size of the state vector. For a state vector with five million elements[1] one needs 200 TB to save the corresponding VCM with double precision.

The propagation of the model error (Equation 6.45) within the (extended) Kalman Filter poses two challenges. First, the complexity of computing the matrix product of two quadratic matrices (without optimization) is $O(n^3)$, so the complexity for Equation 6.45 is $O({n_x}^3)$. Second, the linearized model operator is required. For models consisting of thousands of lines of complex code, calculating the partials may be difficult but can still be determined numerically. Another challenge is the determination of the VCM of the initial state. This information is typically not provided by the models.

Although the advances in the performance of computers are significant, the complexity of the models increases, too. Thus, there is a need for efficient algorithms. The representation of the uncertainty using ensembles is a popular approach. Another advantage of ensemble-based approaches is that they provide a natural way to obtain the VCM of the model forecast. However, one still needs to generate a realistic ensemble, which is often done by perturbing the model inputs.

---

[1] This is a realistic estimate for the state vector of the TIE-GCM with 2.5° resolution: a single field has $144 \times 72 \times 56$ entries. Thus, using four fields at the previous and current steps results in 4 644 864 elements.

The number of ensembles members is denoted by n_e. Each column of the ensemble matrix $\boldsymbol{X} \in \mathbb{R}^{n_x \times n_e}$ contains the state of the corresponding ensemble member

$$\boldsymbol{X} = \left[\boldsymbol{x}_0 \, \boldsymbol{x}_1 \, \ldots \, \boldsymbol{x}_{n_e}\right]. \tag{6.53}$$

The following derivation of ensemble Kalman filters follows Vetra-Carvalho et al. (2018). One can express the analyzed (updated) ensemble matrix

$$\boldsymbol{X}^a = \overline{\boldsymbol{X}}^a + \hat{\boldsymbol{X}}^a \tag{6.54}$$

as the sum of the analyzed ensemble mean $\overline{\boldsymbol{X}}^a$ and the analyzed ensemble perturbations $\hat{\boldsymbol{X}}^a$. All columns of $\overline{\boldsymbol{X}}^a$ contain the analyzed ensemble mean $\overline{\boldsymbol{x}}^a$. The analyzed ensemble mean and analyzed ensemble perturbations are computed from the forecasted counterparts using a linear transformation (Vetra-Carvalho et al., 2018, Eq.17-18):

$$\begin{aligned} \overline{\boldsymbol{x}}^a =& \overline{\boldsymbol{x}}^f + \hat{\boldsymbol{X}}^f \overline{\boldsymbol{w}} & (6.55) \\ \hat{\boldsymbol{X}}^a =& \hat{\boldsymbol{X}}^f \hat{\boldsymbol{W}} & (6.56) \end{aligned}$$

The ensemble Kalman filters covered in Vetra-Carvalho et al. (2018) differ in how the weights $\overline{\boldsymbol{w}}$ and $\hat{\boldsymbol{W}}$ are computed.

Figure 6.2 shows the development history of ensemble-based Kalman filters. The Ensemble Kalman Filter (EnKF), developed by Evensen (1994), constituted a pioneering contribution to the development of a variety of filters. As the original EnKF update step underestimates the spread of the state ensemble, Burgers et al. (1998) and Houtekamer and Mitchell (1998) independently introduced perturbations for each ensemble member that are added to the innovation. The resulting filter is the 'stochastic' EnKF. However, the addition of sampled perturbations to the innovation is an additional source of noise. Thus, deterministic filters were developed which avoid the use of perturbed innovations. These filters were classified as ensemble square root filters by Tippett et al. (2003), and are explained in great detail in the following.

Representing the VCM by an ensemble Given n_e samples of the PDF of the updated state (or analyzed state), one can approximate the corresponding VCM using Equation 6.28

$$\boldsymbol{P}^a \approx \frac{\left(\boldsymbol{X}^a - \overline{\boldsymbol{X}}^a\right)\left(\boldsymbol{X}^a - \overline{\boldsymbol{X}}^a\right)^\top}{n_e - 1} = \frac{\hat{\boldsymbol{X}}^a \left(\hat{\boldsymbol{X}}^a\right)^\top}{n_e - 1}. \tag{6.57}$$

The VCM is of low rank since n_e is much smaller than n_x in practice. Equating Equation 6.50 with Equation 6.57 yields (see Appendix A.6.4)

$$\hat{\boldsymbol{X}}^a \left(\hat{\boldsymbol{X}}^a\right)^\top = \hat{\boldsymbol{X}}^f \left(\mathbb{1}_{n_e} - \boldsymbol{S}^\top \boldsymbol{F}^{-1} \boldsymbol{S}\right) \left(\hat{\boldsymbol{X}}^f\right)^\top \tag{6.58}$$

with the forecast ensemble perturbation matrix in the observation space

$$\boldsymbol{S} = \boldsymbol{H} \hat{\boldsymbol{X}}^f \tag{6.59}$$

and the VCM of the innovation

$$\boldsymbol{F} = (n_e - 1)\boldsymbol{R} + \boldsymbol{S}\boldsymbol{S}^\mathsf{T}. \tag{6.60}$$

Solving Equation 6.58 for the analyzed state perturbations $\hat{\boldsymbol{X}}^a$ yields (see Appendix A.6.5)

$$\hat{\boldsymbol{X}}^a = \hat{\boldsymbol{X}}^f \boldsymbol{T} \tag{6.61}$$

with the transform matrix $\boldsymbol{T} \in \mathbb{R}^{n_e \times n_e}$ being a square root of

$$\boldsymbol{T}\boldsymbol{T}^\mathsf{T} = \left(\mathbb{1}_{n_e} - \boldsymbol{S}^\mathsf{T}\boldsymbol{F}^{-1}\boldsymbol{S}\right). \tag{6.62}$$

Equation 6.62 can be rewritten as (see Appendix A.6.6)

$$\boldsymbol{T}\boldsymbol{T}^\mathsf{T} = \left(\mathbb{1}_{n_e} + \frac{1}{n_e - 1}\boldsymbol{S}^\mathsf{T}\boldsymbol{R}^{-1}\boldsymbol{S}\right)^{-1}. \tag{6.63}$$

Note that the factorization $\boldsymbol{T}\boldsymbol{T}^\mathsf{T}$ is not unique. It has been shown that using a symmetric transformation matrix $\boldsymbol{T}$ preserves the ensemble mean during the transformation of the ensemble perturbations formulated in Equation 6.56 (e.g., Sakov and Oke, 2008b; X. Wang et al., 2004). Thus, in practice, the singular value decomposition is often employed to obtain the transformation matrix.

Inserting Equation 6.61 into 6.57 finally provides the VCM of the analyzed state computed from the forecasted ensemble perturbations:

$$\boldsymbol{P}^a = \frac{1}{n_e - 1}\hat{\boldsymbol{X}}^f \boldsymbol{T}\boldsymbol{T}^\mathsf{T} \left(\hat{\boldsymbol{X}}^f\right)^\mathsf{T} \tag{6.64}$$

Representing the updated state by an ensemble By expressing the gain matrix with the VCM of the analyzed state (see Appendix A.6.2) and inserting this into Equation 6.48 one obtains

$$\boldsymbol{x}^a = \boldsymbol{x}^f + \boldsymbol{P}^a \boldsymbol{H}^\mathsf{T}\boldsymbol{R}^{-1}\boldsymbol{d}. \tag{6.65}$$

Inserting Equation 6.64 gives

$$\boldsymbol{x}^a = \boldsymbol{x}^f + \frac{1}{n_e - 1}\hat{\boldsymbol{X}}^f \boldsymbol{T}\boldsymbol{T}^\mathsf{T} \left(\hat{\boldsymbol{X}}^f\right)^\mathsf{T} \boldsymbol{H}^\mathsf{T}\boldsymbol{R}^{-1}\boldsymbol{d}. \tag{6.66}$$

6.3.4. Ensemble Transform Kalman Filter

The Ensemble Transform Kalman Filter (ETKF) was developed by Bishop et al. (2001). The weights for the update step follow directly from the previous considerations. Comparing Equation 6.56 with Equation 6.61, yields

$$\hat{\boldsymbol{W}}_\text{ETKF} = \boldsymbol{T} \tag{6.67}$$

for the weight matrix of the ensemble perturbations. Comparing Equation 6.66 with Equation 6.55 gives

$$\overline{\boldsymbol{w}}_{\mathrm{ETKF}} = \frac{1}{n_e - 1}\boldsymbol{T}\boldsymbol{T}^{\mathsf{T}}\left(\boldsymbol{H}\hat{\boldsymbol{X}}^{f}\right)^{\mathsf{T}}\boldsymbol{R}^{-1}\boldsymbol{d}. \tag{6.68}$$

6.3.5. Error-Subspace Transform Kalman Filter

The ESTKF was developed by Nerger et al. (2012b) by combining the ETKF with the Singular Evolutive Interpolated Kalman (SEIK) filter (Pham et al., 1998).

The calculation of the ensemble perturbations in Equation 6.54 can be expressed as a matrix-matrix product

$$\hat{\boldsymbol{X}} = \boldsymbol{X} - \overline{\boldsymbol{X}} = \boldsymbol{X}\boldsymbol{A} \tag{6.69}$$

with

$$\boldsymbol{A} = \mathbb{1}_{n_e} - \boldsymbol{I}_{n_e \times n_e}\frac{1}{n_e} = \left[\underbrace{\begin{matrix} 1-\frac{1}{n_e} & -\frac{1}{n_e} & -\frac{1}{n_e} & \cdots \\ -\frac{1}{n_e} & 1-\frac{1}{n_e} & -\frac{1}{n_e} & \cdots \\ -\frac{1}{n_e} & -\frac{1}{n_e} & 1-\frac{1}{n_e} & \\ \vdots & \vdots & & \ddots \\ -\frac{1}{n_e} & -\frac{1}{n_e} & \cdots & -\frac{1}{n_e} \end{matrix}}_{\boldsymbol{A}_S} \begin{matrix} -\frac{1}{n_e} \\ -\frac{1}{n_e} \\ \\ \vdots \\ 1-\frac{1}{n_e} \end{matrix}\right]. \tag{6.70}$$

The rank of $\hat{\boldsymbol{X}}$ is at most $n_e - 1$ because one degree of freedom is required to calculate the ensemble mean. As a consequence the sum of each row of $\hat{\boldsymbol{X}}$ is zero.

The SEIK filter accounts for this rank deficiency by skipping the last column of matrix $\boldsymbol{A}$ (Nerger et al., 2012b, Eq. 15). Thus, the filter only operates on the first $n_e - 1$ ensemble perturbations contained in the matrix

$$\boldsymbol{L}_S = \boldsymbol{X}^f\boldsymbol{A}_S. \tag{6.71}$$

The matrix $\boldsymbol{L}_S$ contains the basis vectors of the error-subspace and has full rank (if the rank of $\hat{\boldsymbol{X}}$ is $n_e - 1$, which is typically the case).

The ESTKF uses a different approach to account for the rank deficiency in $\hat{\boldsymbol{X}}$. It uses a matrix $\boldsymbol{A}_E \in \mathbb{R}^{n_e \times n_e - 1}$ that subtracts the ensemble mean and additionally a fraction of the last column of $\boldsymbol{X}$ from all other columns (Nerger et al., 2012b, Eq. 24)

$$\boldsymbol{A}_E(i,j) = \begin{cases} 1 - \dfrac{1}{n_e}\dfrac{1}{\frac{1}{\sqrt{n_e}} + 1}, & i = j \wedge i < n_e \quad \text{(main diagonal)} \\ -\dfrac{1}{n_e}\dfrac{1}{\frac{1}{\sqrt{n_e}} + 1}, & i \neq j \wedge i < n_e \quad \text{(off diagonals)} \\ -\frac{1}{\sqrt{n_e}}, & i = n_e \quad \text{(last row)} \end{cases} . \tag{6.72}$$

Thus, unlike the SEIK filter, the ESTKF does not depend on the order of members in the ensemble matrix (Nerger et al., 2012b). The columns of $\boldsymbol{A}_E$ are orthonormal and orthogonal to

$\boldsymbol{I}$ and $\boldsymbol{A}_E^\mathsf{T}\boldsymbol{A}_E = \mathbb{1}_{(n_e-1)}$. The basis vectors $\boldsymbol{L}_E \in \mathbb{R}^{n_x \times n_e - 1}$ of the error-subspace are

$$\boldsymbol{L}_E = \boldsymbol{X}^f \boldsymbol{A}_E. \tag{6.73}$$

The ESTKF computes the transformation matrix

$$\boldsymbol{T}_E\boldsymbol{T}_E^\mathsf{T} = \left(\mathbb{1}_{(n_e-1)} + \frac{1}{n_e-1}(\boldsymbol{H}\boldsymbol{L}_E)^\mathsf{T}\boldsymbol{R}^{-1}(\boldsymbol{H}\boldsymbol{L}_E)\right)^{-1} \tag{6.74}$$

in the error-subspace (Vetra-Carvalho et al., 2018, Equation 77). The weight matrix

$$\hat{\boldsymbol{W}}_{\mathrm{ESTKF}} = \boldsymbol{A}_E\boldsymbol{T}_E\boldsymbol{A}_E^\mathsf{T} \tag{6.75}$$

necessary to calculate the ensemble perturbations is obtained by projecting the transformation matrix in the error-subspace back to the ensemble space (Vetra-Carvalho et al., 2018, Equation 79). The weight matrix of the ensemble mean is given by (Vetra-Carvalho et al., 2018, Equation 80)

$$\overline{\boldsymbol{w}}_{\mathrm{ESTKF}} = \frac{1}{\sqrt{n_e-1}}\boldsymbol{A}_E\boldsymbol{T}_E\boldsymbol{T}_E^\mathsf{T}(\boldsymbol{H}\boldsymbol{L}_E)^\mathsf{T}\boldsymbol{R}^{-1}\boldsymbol{d}. \tag{6.76}$$

Both $\boldsymbol{T}_E$ and $\boldsymbol{T}_E\boldsymbol{T}_E^\mathsf{T}$ are computed via eigenvalue decomposition of the right-hand side of Equation 6.74.

Compared with the ETKF, the ESTKF and SEIK filter have slightly lower computational costs since the matrix spanning the error-subspace $\boldsymbol{L}$ has one column less than the ensemble perturbation matrix $\hat{\boldsymbol{X}}^f$ (Nerger et al., 2012b, Section 5).

6.4. Localization

The state of a system often contains variables associated with a specific location, such as the center of a model grid cell. Observations are measured at specific points in space and time or refer to integrals over space and/or time. During the update step of the Kalman filter, the impact of an observation on an element of the state vector depends solely on the correlations encoded in the VCM of the state. The update step does not explicitly consider the distance between the location of the observations and states.

If there are spatial (long-range) correlations in the system and they are represented correctly in the forecasted state VCM, a single observation could theoretically improve the state estimate of the whole system. For example, a single in-situ mass density observation in the atmosphere could improve the density estimate of the atmosphere globally. If there is a correlation between mass density and temperature, both would be updated when assimilating mass density only.

For ensemble Kalman filters, the impact of an observation on an element of the state vector depends on the correlations encoded in the forecasted state ensemble. As the number of ensemble members is chosen to be much lower than the dimension of the state vector ($n_e \ll n_x$) to reduce computational costs, spurious correlations might arise in the ensemble. Especially over long distances, the random errors in the representation of the covariances are typically greater than

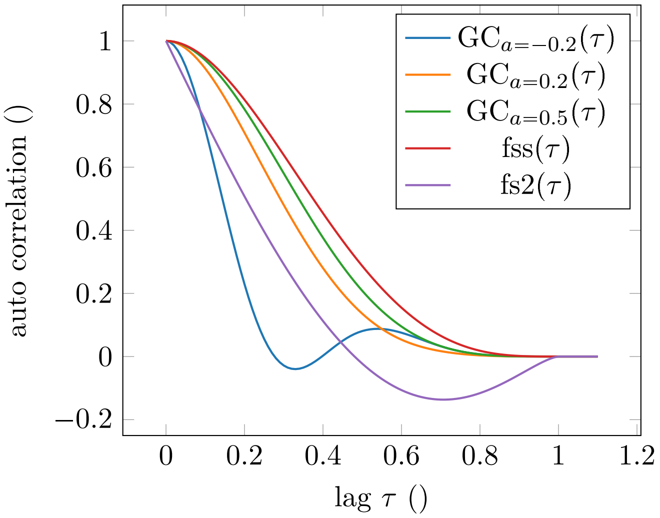

Figure 6.3.: Some finite analytical autocorrelation functions with local support in $[0, 1]$. The functions can be defined on arbitrary intervals. $\mathrm{GC}(\tau)$ has an additional form parameter a and is defined in Gaspari et al. (2006, Equation 33) and Moreaux (2008, Equation 41). The PDAF has implemented $\mathrm{GC}_{a=0.5}(\tau)$, which mimics a Gaussian and is explicitly formulated in Gaspari and Cohn (1999, Equation 4.10). $\mathrm{fss}(\tau)$ is defined in Schuh (2017, Equation 154) and $\mathrm{fs2}(\tau)$ in Schuh (2017, Equation 165). For covariance localization, the lag is the distance between two states. For observation localization, the lag is the distance between the subdomain and the observation.

the actual signal for small ensembles (Nerger et al., 2006, p. 640). As a result, spurious correlations (e.g., Hamill et al., 2001) and locally unrealistic estimates can occur (Nerger et al., 2006, p. 640).

To address this issue, long-range correlations are filtered out in the analysis step by applying a suited localization schema. Localization reduces or eliminates the impact of an observation on an entry in the state vector based on the distance between the state and the observations.

6.4.1. Covariance Localization

Covariance localization (Houtekamer and Mitchell, 1998, 2001) directly operates on the VCM of the forecasted state $\boldsymbol{P}^f$. Thus, it cannot be applied to filters that do not compute the VCM or its projection in the observation space explicitly (Janjić et al., 2011; Nerger et al., 2012a). This is the case for the ESTKF, so covariance localization cannot be applied to it. Covariance localization suppresses or dampens long-range covariances by an element-wise multiplication of the forecast VCM with a correlation matrix of compact support. This matrix is constructed from finite analytical correlation functions, for example, as described in Gaspari and Cohn (1999), Gaspari et al. (2006), and Moreaux (2008) or as plotted in Figure 6.3. To construct the correlation matrix, the distances between the individual pairs of states are calculated w.r.t a given metric and then fed into the finite correlation function.

6.4.2. Domain Localization

Domain localization (Hunt et al., 2007; Janjić et al., 2011; Nerger et al., 2006, 2012a; Ott et al., 2004; Testut et al., 2003) subdivides the model grid or mesh into subdomains and performs the

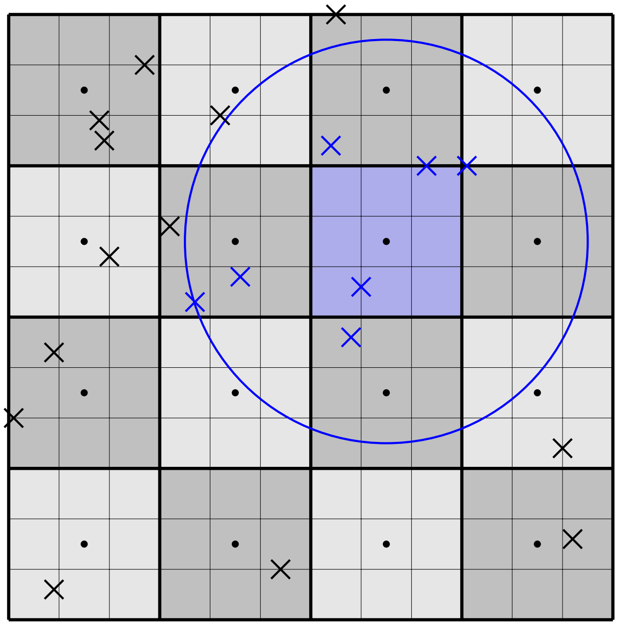

Figure 6.4.: Exemplary illustration of domain localization. A 12 × 12 regular grid is divided into 16 subdomains of size 3 × 3. The center of each subdomain is marked with a black dot. Observations are marked with crosses. For the subdomain highlighted with blue, the cutoff radius is illustrated with a blue circle. The update step for this subdomain only considers the observations within the circle (blue crosses).

analysis step separately on each subdomain, taking only observations within a specified cut-off distance into account.

An algorithm for domain localization for subspace error filters such as the ESTKF, or SEIK filter was developed by Nerger et al. (2006). It assumes disjoint subdomains and uses the distance between the centers of the subdomains and the location of the observations to determine which observations are included in a local analysis step (see Figure 6.4).

The analysis weights of the k-th subdomain are given by

$$\begin{aligned} \overline{\boldsymbol{x}}^a{}_\sigma &= \overline{\boldsymbol{x}}^f{}_\sigma + \hat{\boldsymbol{X}}_\sigma \overline{\boldsymbol{w}}_k && (6.77)\\ \hat{\boldsymbol{X}}^a_\sigma &= \hat{\boldsymbol{X}}^f_\sigma \hat{\boldsymbol{W}}_k && (6.78) \end{aligned}$$

where subscript σ denotes the application of a linear operator that selects only the rows of the state vector included in the k-th subdomain. In the analysis step all subdomains are updated according to those equations.

The analysis step of the k-th subdomain for the ESTKF is

$$\begin{aligned} \overline{\boldsymbol{w}}_k &= \frac{1}{\sqrt{n_e - 1}} \boldsymbol{A}_{E\sigma} \boldsymbol{T}_{E\delta} \boldsymbol{T}_{E\delta}^\mathsf{T} (\boldsymbol{H}_\delta \boldsymbol{L}_E)^\mathsf{T} \boldsymbol{R}_\delta^{-1} \boldsymbol{d}_\delta && (6.79)\\ \hat{\boldsymbol{W}}_k &= \boldsymbol{A}_{E\sigma} \boldsymbol{T}_{E\delta} \boldsymbol{A}_{E\sigma}^\mathsf{T} && (6.80)\\ \boldsymbol{T}_{E\delta} \boldsymbol{T}_{E\delta}^\mathsf{T} &= \left(\mathbb{1}_{n_\delta} + \frac{1}{n_e - 1} (\boldsymbol{H}_\delta \boldsymbol{L}_E)^\mathsf{T} \boldsymbol{R}_\delta^{-1} (\boldsymbol{H}_\delta \boldsymbol{L}_E) \right)^{-1} && (6.81) \end{aligned}$$

where subscript δ denotes the application of a linear operator that selects the rows of the observation vector associated with the k-th subdomain and n_δ is the number of observations used in the analysis of the k-th subdomain.

6.4.2.1. Observation Localization

Pure domain localization is binary, meaning that an observation is either included in the local analysis step or not. A continuous weighting of the observations can be obtained by observation localization (Hunt et al., 2007), which weights the observations associated with a subdomain additionally by their distance to the subdomain. Thus, it implies domain localization. The weighting is similar to the weighting of covariance localization (Section 6.4.1), but instead of the VCM of the forecast $\boldsymbol{P}^f$, all local VCMs of the observations $\boldsymbol{R}_\delta$ are weighted by their distance to the subdomain.

6.5. Co-estimation of Model Dynamics

Co-estimation of model dynamics can be seen as calibrating (constant) parameters of the model that determine how a state is forwarded. These parameters do not represent the state of the system but rather its dynamic behavior. For co-estimating model dynamics the state vector $\boldsymbol{x}$ is augumented by model parameters $\boldsymbol{c}$ (e.g., Bocquet et al., 2021). The augmented state vector is then given by

$$\boldsymbol{z} = \begin{bmatrix} \boldsymbol{x} \\ \boldsymbol{c} \end{bmatrix}. \tag{6.82}$$

General circulation models like the TIE-GCM consist of many hundredths model parameters and it is virtually impossible to co-estimate all simultaneously due to multicollinearity. Thus, a suited set of model parameters has to be determined. Analogous to the state the VCM of the model parameters is represented by an ensemble. The ensemble matrix of the augmented state vector is

$$\boldsymbol{Z} = \begin{bmatrix} \boldsymbol{X} \\ \boldsymbol{C} \end{bmatrix} \tag{6.83}$$

and the ensemble perturbations are

$$\hat{\boldsymbol{Z}} = \begin{bmatrix} \hat{\boldsymbol{X}} \\ \hat{\boldsymbol{C}} \end{bmatrix}. \tag{6.84}$$

During the analysis steps, the model parameters are updated based on their correlation with the state, which is implicitly contained in the ensemble. Those model parameters are not necessarily associated with a specific location. In this case applying a localized filter is not straightforward. Bocquet et al. (2021) describes an approach enabling the localization of the state and co-estimation of global model parameters. Here, the approach for domain localization is explained. First, the traditional localized filter is performed to update the state ensemble. In a post-processing step, the ensemble of the model parameters is calculated by linear regression with the state ensemble via (Bocquet et al., 2021, Equation 22)

$$\boldsymbol{C}^a = \boldsymbol{C}^f + \zeta \hat{\boldsymbol{C}}^f \underbrace{\left(\hat{\boldsymbol{X}}^f\right)^+ \left(\boldsymbol{X}^a - \boldsymbol{X}^f\right)}_{\hat{\boldsymbol{W}}_c}. \tag{6.85}$$

The weights $\hat{\boldsymbol{W}}_c$ can be found by solving the over-constrained linear system $\hat{\boldsymbol{C}}^f \hat{\boldsymbol{W}}_c = \boldsymbol{X}^a - \boldsymbol{X}^f$ using for example singular value decomposition to obtain the pseudo inverse. This approach requires finding a suitable value for the tapering coefficient ζ (Bocquet et al., 2021, Section 3.2.4).

7. Implementation of an Assimilative TIE-GCM Version

I use the Parallel Data Assimilation Framework (PDAF; Nerger 2024; Nerger and Hiller 2013; Nerger et al. 2005, 2020) developed at the Alfred Wegener Institute in Bremerhaven to implement an assimilative version of the Thermosphere Ionosphere Electrodynamics General Circulation Model (TIE-GCM; Qian et al. 2014) developed at the National Center for Atmospheric Research High Altitude Observatory in Boulder and described in Section 5.1. PDAF and the TIE-GCM are both open source software[1]. Although there are already assimilative TIE-GCM implementations (see Section 7.1), my assimilation system is the first employing a (fully-parallel online[2]) PDAF integration. Meaning, the assimilation system does not re-initialize the model after each analysis step ('online'), making it faster than implementations which require re-initialization. Additionally, my assimilation system forwards all ensemble members in parallel and the computations for each member are also computed in parallel ('fully-parallel'). Details on the parallelization concept are given in Appendix C.2. Each ensemble member is distributed to a maximum of eight physical processor cores to achieve good efficiency (see Appendix C.3). PDAF supports many ensemble Kalman filters (Section 6.3.3). However, I implemented only the Error-Subspace Transform Kalman Filter (ESTKF; Section 6.3.5) into the assimilation system for two reasons. First, it belongs to the class of square root filters that do not suffer from additional sampling noise introduced by the perturbation of observations (Section 6.3.3). Second, the analysis step is computed in the error-subspace, which slightly reduces the computational costs (Section 6.3.5), which is relevant as my assimilation system aims at high efficiency and low run time (see Hypothesis H 1).

The structure of the newly developed TIE-GCM data assimilation system is summarized in Figure 7.1. The first step is the generation of the ensemble (Section 7.2) by perturbing boundary conditions, external forcings, and model parameters (boxes in the upper left corner in Figure 7.1). After forwarding the model, the observation operator of the corresponding observation is used to map the forwarded state to the observation space (Section 7.3). Next, the ensemble is updated, possibly using a localization schema (Section 7.5) and/or co-estimating model dynamics in form of model parameters. Before the updated state can be forwarded, it must be constrained to maintain physically consistent values (Section 7.4). Section 7.6 describes a two-step approach, which first calibrates an empirical model using accelerometer-derived mass densities and then globally evaluates the model and assimilates it. Any observation assimilated into the TIE-GCM must be located in the same reference system. Thus, satellite orbits provided in the geocentric

---

[1] PDAF is published under the LGPL-3.0 license and TIE-GCM under the NCAR TIE-GCM open source academic research license.

[2] Additional information on the implementation concept are available online at `https://pdaf.awi.de/trac/wiki/ImplementationConceptOnline`

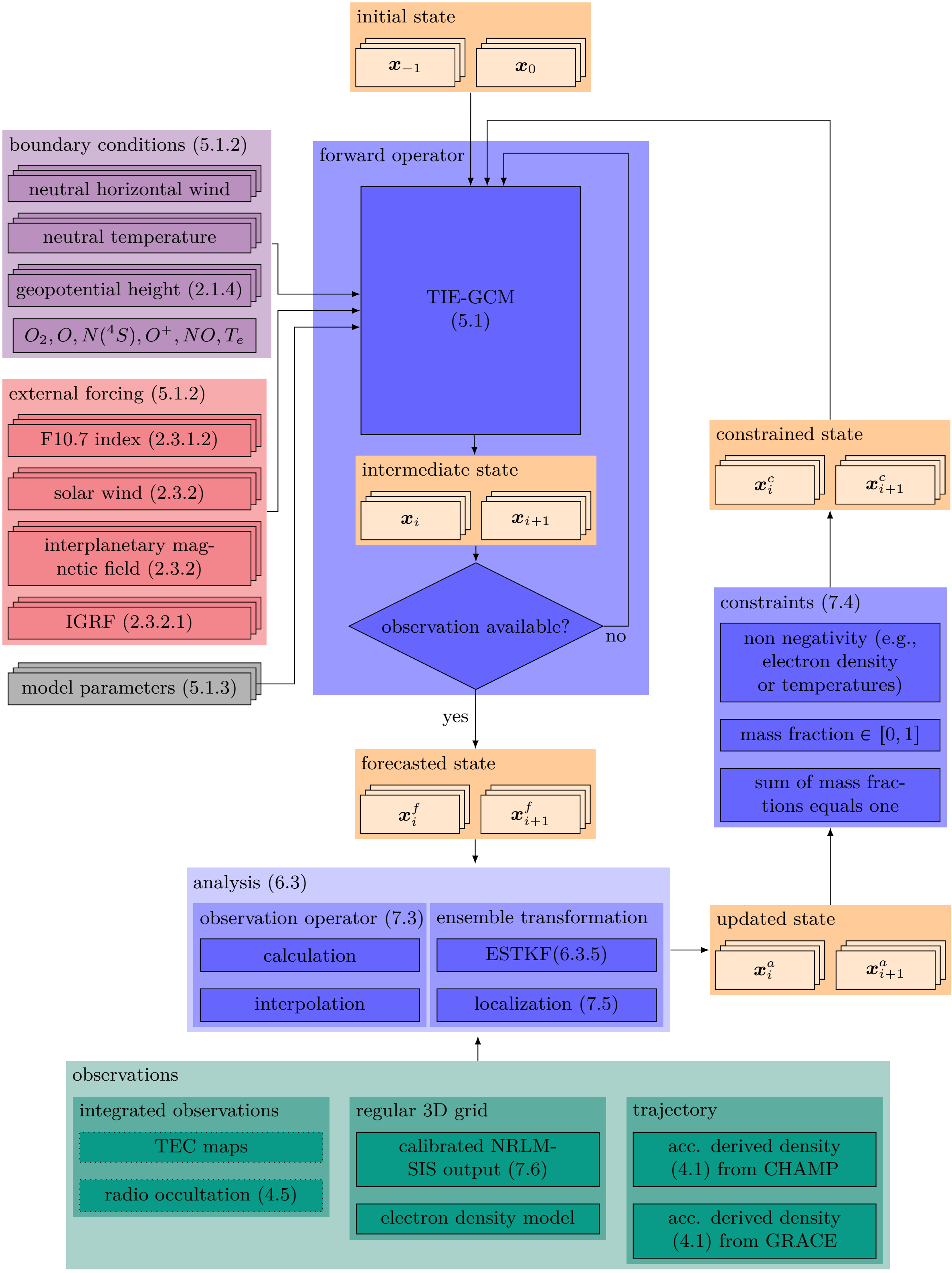

Figure 7.1.: Flow diagram of PDAF TIE-GCM. Nodes with a double shadow indicate that the corresponding quantity is given as an ensemble. The state ensemble is generated by perturbing the model inputs (see Section 7.2), which are located in the upper left corner of this diagram. References to sections of this thesis are provided in brackets. The state vector is colored yellow, external forcings with red, boundary conditions with purple, observations are colored green and steps of the Kalman filter with blue.

celestial reference system (GCRS) are rotated into the International Terrestrial Reference System (ITRS) as described in Appendix E.1 in a pre-processing step. Additionally, the orbits and observations are given in GPS time, while the TIE-GCM uses coordinated universal time (UTC). For data assimilation, one needs to use the same time scale for models and observations. The details about the necessary transformation are found, for example, in Müller (1999).

7.1. Related Works

Data assimilation of accelerometer-derived mass densities, electron number density profiles, and vertical TEC have been applied to numerical models of the upper atmosphere in several studies. Table 7.1 provides an overview of recent studies. Data assimilation within the TIE-GCM has been conducted with the use of the Data Assimilation Research Testbed (DART; J. Anderson et al. 2009) . DART is open source software[1]. It does not support 'online' assimilation, meaning the model is re-initialized after each analysis step. DART was also employed for an assimilation study using the Global Ionosphere Thermosphere Model (GITM; A. J. Ridley et al. 2006) . For the Coupled Thermosphere Ionosphere Plasmasphere Electrodynamics (CTIPe; Millward et al. 2001) model, the Thermosphere Ionosphere Data Assimilation (TIDA; S. M. Codrescu et al. 2018) software is employed in several studies. However, neither the CTIPe nor the TIDA software are publicly available. The studies employing ensemble-based Kalman filters investigate assimilation periods lasting between 1-5 days. A plausible reason for this duration is the computational cost. However, this is not discussed explicitly in the studies. The studies investigate either specific geomagnetic storms or periods with quiet geomagnetic conditions. Sutton (2018) almost covered an entire year including many different geomagnetic conditions at solar maximum conditions. However, it is also the only study using a variational data assimilation approach and it only estimates the model drivers. Matsuo et al. (2012) use an update method closely related to optimal interpolation to estimate the mass density at 400 km altitude for an entire year.

Most studies apply a localization schema to reduce the impact of spurious long-range correlations. When assimilating accelerometer-derived mass densities, localization limits the mass density improvement to the vicinity of the orbits (e.g., Matsuo et al., 2013). The TIDA software does not apply localization. This is justified on the grounds that "it becomes improbable for spurious correlations to arise when the size of the ensemble is an order of magnitude greater than the number of randomized elements" (S. M. Codrescu et al., 2018). M. V. Codrescu et al. (2022) and S. M. Codrescu et al. (2018) could improve the mass density estimation along the GRACE and CHAMP missions by assimilating accelerometer-derived densities from only one of the satellite missions.

Some of the studies (M. V. Codrescu et al., 2022; Matsuo et al., 2013; Morozov et al., 2013) co-estimated the external forcings used to drive the models. Matsuo et al. (2013) and Morozov et al. (2013) assimilated accelerometer-derived mass densities from CHAMP and co-estimated the F10.7 index. Morozov et al. (2013) demonstrated that the bias between the GITM and the accelerometer-derived mass densities along GRACE is reduced when co-estimating F10.7.

---

[1] Published under the Apache-2.0 license.

Table 7.1.: This table provides an overview of recent studies on data assimilation in numerical models of the upper atmosphere. This list is not intended to be complete. To save space in the column labeled 'observations', the following abbreviations are used here.
COSMIC profiles: Radio occultation Electron density profiles (Section 4.5) form Constellation Observing System for Meteorology, Ionosphere, and Climate/Formosa Satellite 3 (COSMIC/FORMOSAT-3); ADMD: accelerometer-derived mass densities (Section 4.1).
Additional information about the models can be found in Chapter 5. For more details about the filters see Chapter 6. The time between subsequent assimilation steps is denoted by Δ_t. The number of ensemble members is denoted by n_e. See Section 2.3.1.2 for the F10.7 index and Section 2.3.2.2 for the Kp index.

model	study	software	filter	n_e	Δ_t	observations	period	max Kp	median F10.7
TIE-GCM	Lee et al. 2012	DART	EnKF	90	1 h	COSMIC profiles	12 - 13 Apr 2008	3.3	68
	Matsuo et al. 2013	DART	EnKF	100	1.5 h	ADMD CHAMP	28 - 29 Mar 2002	3.3	174
				90	1 h	synthetic COSMIC profiles	8 - 9 Apr 2008	3.7	69
	Hsu et al. 2014	DART	EnKF	90	1 h	synthetic COSMIC profiles	8 Apr 2008	2.7	69
	Chartier et al. 2016	DART	EnKF	90	1 h	vertical TEC	10 Sep 2005	5.7	306
							21 Jan 2005	8.0	119
	Chen et al. 2016	DART	EnKF	90	10 min	GPS TEC	16 - 18 Mar 2015	7.7	116
	Sutton 2018		IRIDEA	9	3 h	ADMD CHAMP	21 Mar - 31 Dec 2003	9.0	123
	Kodikara et al. 2021	DART	EAKF	90	1 h	COSMIC profiles	4 - 8 Mar 2008	4.0	68
							2 - 6 Jun 2014	3.3	109
	Corbin and Kusche 2022	PDAF	ESTKF	100	1 h	calibrated NRLMSIS 2.0	27 Mar - 9 Apr 2010	7.7	78
CTIPe	Matsuo et al. 2012		OI		1.5 h	ADMD GRACE and CHAMP	2007	5.1	71
	S. M. Codrescu et al. 2018	TIDA	EnKF	75	10 min	ADMD CHAMP	20 Mar 2007	0.3	71
	M. V. Codrescu et al. 2022	TIDA	EnKF	75	30 min	ADMD GRACE and CHAMP	27 - 31 Oct 2003	9.0	86
							27 Sep - 2 Oct 2002	7.3	145
							26 Jul - 30 Jul 2004	8.7	113
	Fernandez-Gomez et al. 2022	TIDA	EnKF	75	10 min	ADMD GRACE	16 - 18 Mar 2015	7.7	116
GITM	Morozov et al. 2013	DART	EAKF	20	30 min	ADMD CHAMP	1 - 2 Dec 2002	3.7	146

The assimilation of COSMIC profiles improved ionospheric parameters, such as the height of the F2-layer's peak and the associated electron number density (Lee et al., 2012), the neutral mass density (Matsuo et al., 2013), and the electron number density (Hsu et al., 2014). While most studies assimilating mass densities seek to improve the mass density estimate itself, Fernandez-Gomez et al. (2022) investigates how the electron number density estimation can be improved by the assimilation of mass densities. They found that the electron number density along the orbit of GRACE simulated by the CTIPe was improved by 22 % when assimilating accelerometer-derived mass densities from the Swarm-A satellite during a geomagnetic storm.

Data assimilation is not limited to numerical models. Forootan et al. (2022) used data assimilation to correct the mass density prediction of the semi-empirical model NRLMSISE-00 and to simultaneously estimate its key parameters. For this, they employed the EnKF and mass density observations derived from the GRACE accelerometer. Note that, semi-empirical models are not dynamical as the prediction does not dependent on previous states. Consequently, the only method for correcting model predictions during periods not encompassed by the assimilation epochs is to estimate the model parameters.

So far, an efficient implementation that fully utilizes the high temporal resolution of a few seconds of the accelerometer-derived densities and runs over arbitrarily long periods has yet to be investigated.

7.2. State Ensemble Generation

The TIE-GCM is a highly driven model, which means that its long-term behavior does not depend on the initial state (convergent system) but is controlled by external forcings, model constants, and lower boundary conditions (see Figure 7.2). Consequently, the model does not behave chaotic (Section 6.2). Therefore, to obtain a realistic state ensemble spread over longer time spans, it is necessary to perturb these model inputs rather than the initial states alone. All perturbations applied to the model inputs are sampled for all ensemble members in advance of any model run, thus ensuring that any model run can be repeated with the exact same perturbations if necessary. To get the initial states for each ensemble member, one forwards some arbitrary initial state for each ensemble member using an OLS long enough for the model to adapt to the perturbed model inputs.

7.2.1. External forcing

The external forcings of the TIE-GCM (Section 5.1.2) are time-variable, and so is their variability. Consequently, time-variable perturbations are needed to represent the variability. The external forcings perturbations are sampled for each ensemble member and point in time. The ensemble of external forcings perturbations must reflect the variability for each epoch and its temporal dependence.

7.2.1.1. Sampling Procedure

Initially, it is assumed that for each external forcing parameter, the mean and standard deviation are given as time series, describing a Gaussian at each point in time. The perturbations are

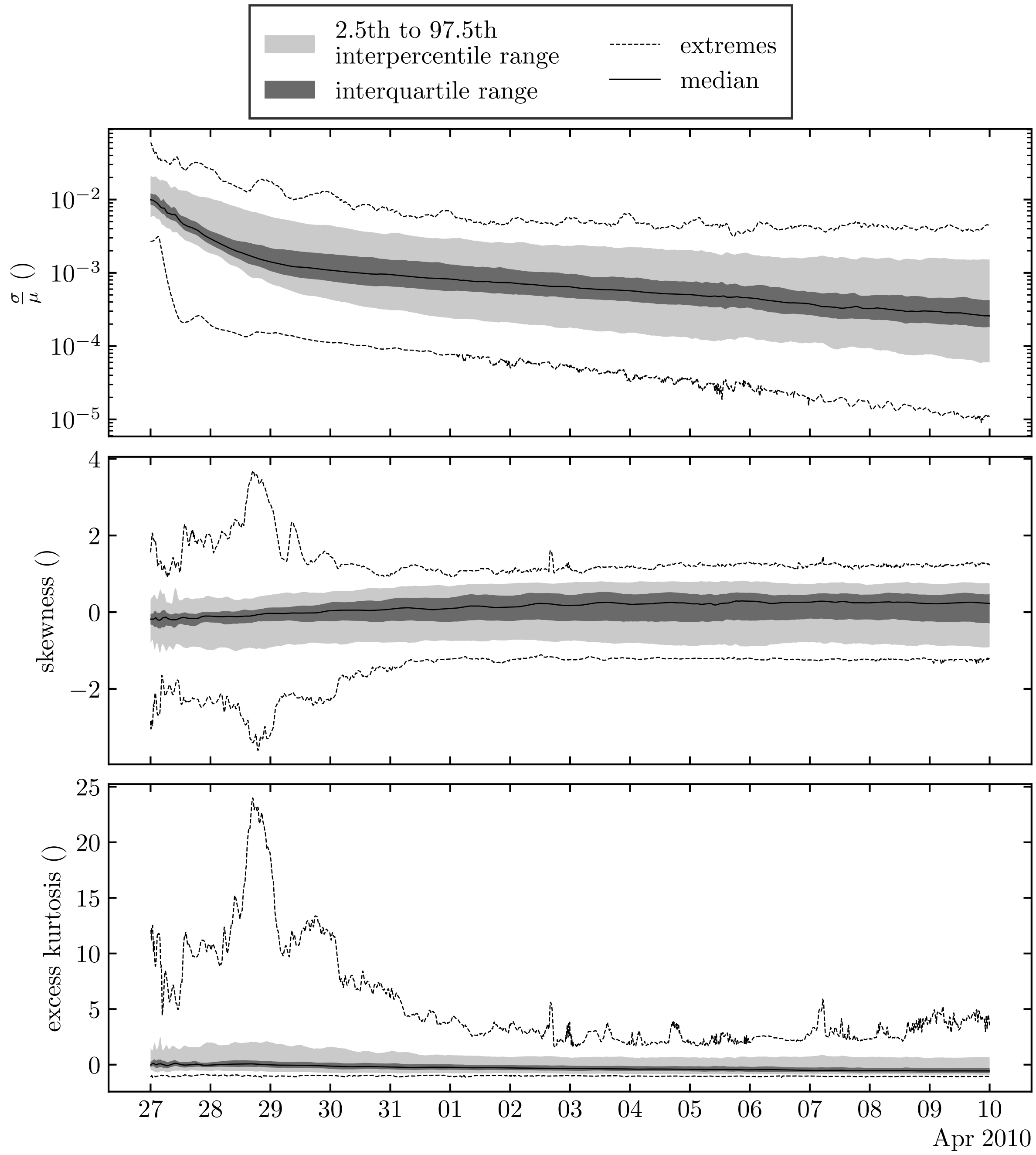

Figure 7.2.: An open loop simulation with 96 ensemble members of the TIE-GCM with perturbed initial states (the first 96 ensembles members of Setup 2) but without perturbing external forcings, boundary conditions or model parameters was conducted for this plot. The moments of the neutral density–represented by the ensemble–of all grid cells are aggregated in this plot. The solid black line is the median, taking into account all grid cells. The dark gray and light gray areas contain 50 % and 95 % of all values centered around the median, respectively. The extreme values are illustrated with dashed lines. The ensemble spread decreases rapidly. After about two days, the average standard deviation decreased from a hundredth to a thousandth of the mean mass density, and the model dynamics took control of the system's state. Thus, after two days, the dependence on the initial state is negligible for most grid cells and continues to drop. To account for the different volumes of the TIE-GCM cells, all percentiles were computed by weighting the contribution of each cell by its volume (see Appendix C.4).

then sampled from the time series of the standard deviations. The temporal dependence of the perturbations is also taken from the time series of the standard deviations. This procedure is described in detail in this section and used for all experiments in this thesis. However, in practice, the mean and standard deviation time series are computed from the same raw data. Thus, the spectrum of the standard deviation time series inherits frequencies of the mean time series, which are associated with long-term signals (e.g., the 27-day solar cycle) and should not be attributed to noise or short-term variability. Hence, in future experiments, one should directly operate on the raw time series: The trend can be separated by a lowpass filter, and the remaining signal could be used to sample a time series of perturbations using, for example, an auto-regressive moving average model.

The perturbation sampling procedure requires for each external forcing parameter an equidistant time series $\{x\}_{\Delta t}$ of the uncertainty/variability of the parameter with n samples and temporal resolution Δt. In the first step, the empirical autocorrelation function of $\{x\}_{\Delta t}$ is computed, which is approximated in the second step by an analytical autocorrelation function $\gamma(t)$ depending only on the lag t. It is required to choose functions that satisfy all the properties of autocorrelation functions (e.g. P. J. Brockwell and Davis, 1991, p. 26-28, Proposition 1.51 and Remark 3).

The correlation matrix $\boldsymbol{P}$ associated with an analytical autocorrelation function is a symmetric Toeplitz matrix since the covariance only depends on the lag t.

$$\boldsymbol{P} = \begin{bmatrix} \gamma(0) & \gamma(\Delta t) & \gamma(2\Delta t) & \cdots & \gamma((n-2)\Delta t) & \gamma((n-1)\Delta t) \\ \gamma(\Delta t) & \gamma(0) & \gamma(\Delta t) & \cdots & \gamma((n-3)\Delta t) & \gamma((n-2)\Delta t) \\ \gamma(2\Delta t) & \gamma(\Delta t) & \gamma(0) & \cdots & \gamma((n-4)\Delta t) & \gamma((n-3)\Delta t) \\ \vdots & & & & & \vdots \\ \gamma((n-2)\Delta t) & \gamma((n-3)\Delta t) & \gamma((n-4)\Delta t) & \cdots & \gamma(0) & \gamma(\Delta t) \\ \gamma((n-1)\Delta t) & \gamma((n-2)\Delta t) & \gamma((n-3)\Delta t) & \cdots & \gamma(\Delta t) & \gamma(0) \end{bmatrix} \tag{7.1}$$

The VCM of the perturbations is then given by Equation 6.21. An efficient way to sample an ensemble from a VCM is using its Cholesky factorization $\boldsymbol{R}$ (e.g., Vono et al. 2022, Algorithm 3.1; Alkhatib and Schuh 2007, Algorithem 1a)

$$\hat{\boldsymbol{X}}_{\text{Forcing}} = \boldsymbol{R}^{\mathrm{T}}\boldsymbol{N} \tag{7.2}$$

with $\boldsymbol{N}$ being a matrix of standard normal distributed random numbers with n rows and n_e columns. However, this algorithm cannot provide arbitrary long time series, as the computational cost would be too large[1]. The time series of external forcing perturbations sampled for this thesis are restricted to one year. To prevent unrealistic values from being sampled from the tails of the multivariate normal distribution, each value of each sampled time series is limited to the corresponding 5-sigma environment. This is necessary to prevent unrealistic forcings leading to model crashes. Due to the limits, the resulting time series are no longer normally distributed since all samples outside the 5-sigma environment are shifted to the boundaries. However, since

---

[1] This is true for dense VCMs. When constructing finite correlation functions, the sparsity of the VCM allows to considerably extend the period in which perturbations are sampled.

the probability of a single value being outside the 5-sigma environment is less than 0.0001 %, the deviation from a normal distribution is negligibly small. An alternative to this approach is to sample from a truncated normal distribution. However, sampling from a truncated normal distribution requires much more computational resources than sampling a normal distribution, especially for the case $n \gg 10$. The ensemble of the external forcing is obtained by adding the perturbations $\hat{\boldsymbol{X}}_{\text{Forcing}}$ to the external forcing parameter.

7.2.1.2. Application to TIE-GCM

When using the Weimer model (Section 5.1) there are five external forcing parameters that are summarized in Table 7.2. The standard deviation of the F10.7 index is computed from Tapping (2013, Paragraph 56). The standard deviation of the solar wind and IMF parameters is provided in the OMNI Hourly Data Set (Papitashvili and King, 2020c) and computed from all measurements within one hour. Figure 7.3 shows the ensemble representing the solar wind density as an example.

Figure 7.4 shows the auto correlation of $\{x\}_{\Delta t}$ for each parameter. Simple functions constructed from the exponential and cosine functions are employed to approximate the empirical autocorrelation function. They reproduce the main characteristics of the autocorrelation function but fail to reproduce the details, for example, small peaks associated with the solar rotation (see Figure 7.4). However, none of the assimilation experiments conducted in this thesis investigate periods longer than 26 days. Thus the correlation with lags larger than 26 days are not relevant. Instead of using the analytical function, one can also use the biased empirical correlation function (in Figure 7.4 the unbiased empirical autocorrelation function is shown), which is also positive definite. However, this restricts one to the sampling frequency of the empirical function.

To verify the sampling procedure, the given standard deviation of the external forcings is compared with the standard deviation computed from the ensemble of perturbations. As shown in Figure D.1, the deviation between given and sampled standard deviation are negligible.

For approximating the autocorrelation of the standard deviation time series of the solar wind density, a simple exponential function

$$\gamma_1(t) = \exp\left(-\frac{\ln(2)}{T}|t|\right) \tag{7.3}$$

parameterized by the half-life time T is sufficient. For the describing the autocorrelation of standard deviation time series of the solar wind velocity and the three IMF components, I add another exponential:

$$\gamma_2(t) = (1 - A_1)\exp\left(-\frac{\ln(2)}{T_0}|t|\right) + A_1 \exp\left(-\frac{\ln(2)}{T_1}|t|\right) \quad \text{with } 0 < A_1 \leqslant 1. \tag{7.4}$$

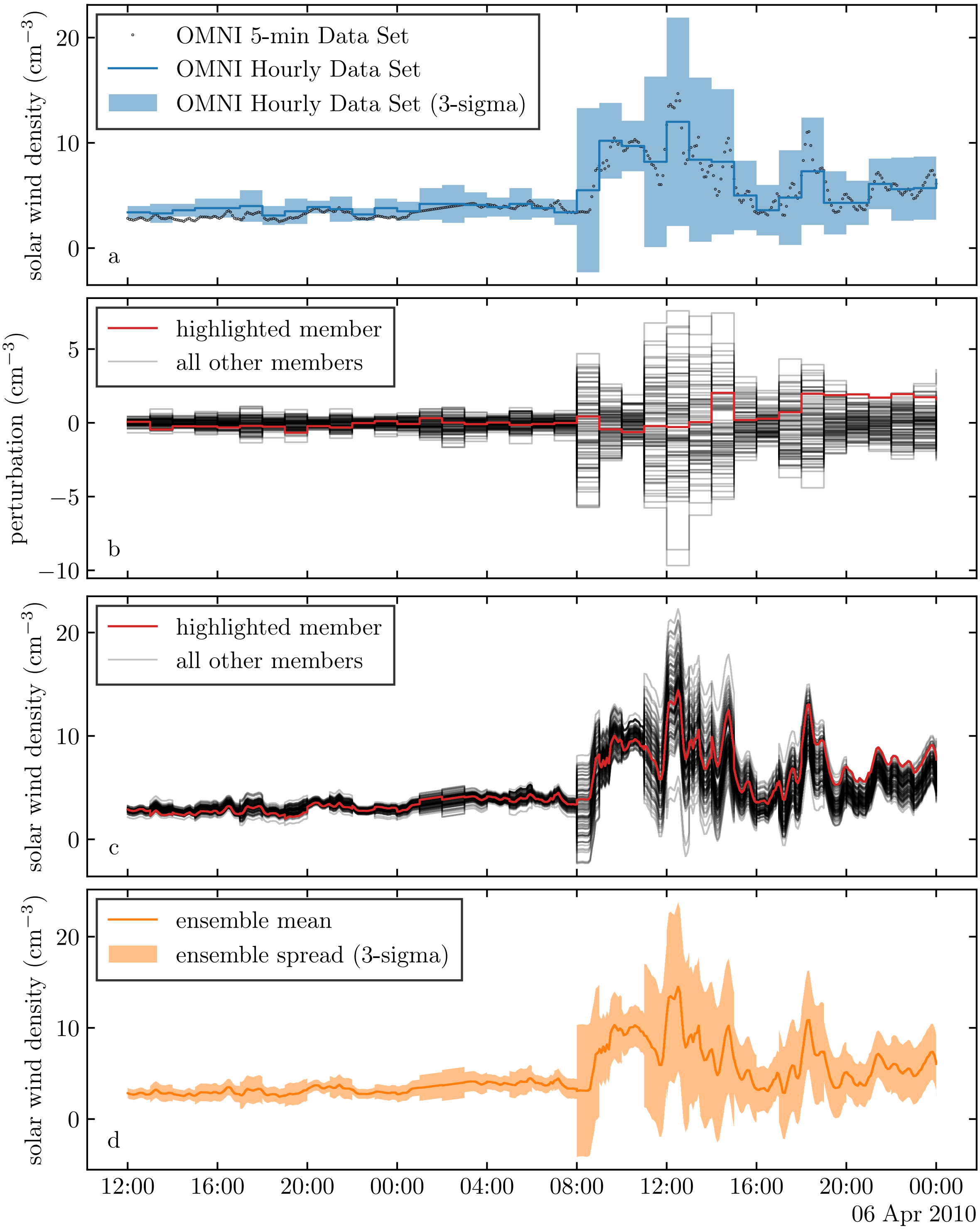

Figure 7.3.: The black dots in Panel a illustrate the solar wind density provided by the TIE-GCM and used to drive it (derived form the OMNI 5-min Data Set, Papitashvili and King 2020b). Superimposed is the solar wind density from the OMNI Hourly Data Set (solid blue line, Papitashvili and King 2020c, which also delivers the associated standard deviation (blue area). Panel b shows the ensemble of perturbations that was sampled to represent the standard deviation contained in the OMNI Hourly Data Set. A single ensemble member is highlighted with red, to show that temporal correlation is considered in the sampling procedure. Panel c shows the solar wind density of the OMNI 5-min Data Set perturbed by the ensemble shown in Panel b. Panel d shows the ensemble mean and the ensemble spread computed from the ensemble shown in Panel c.

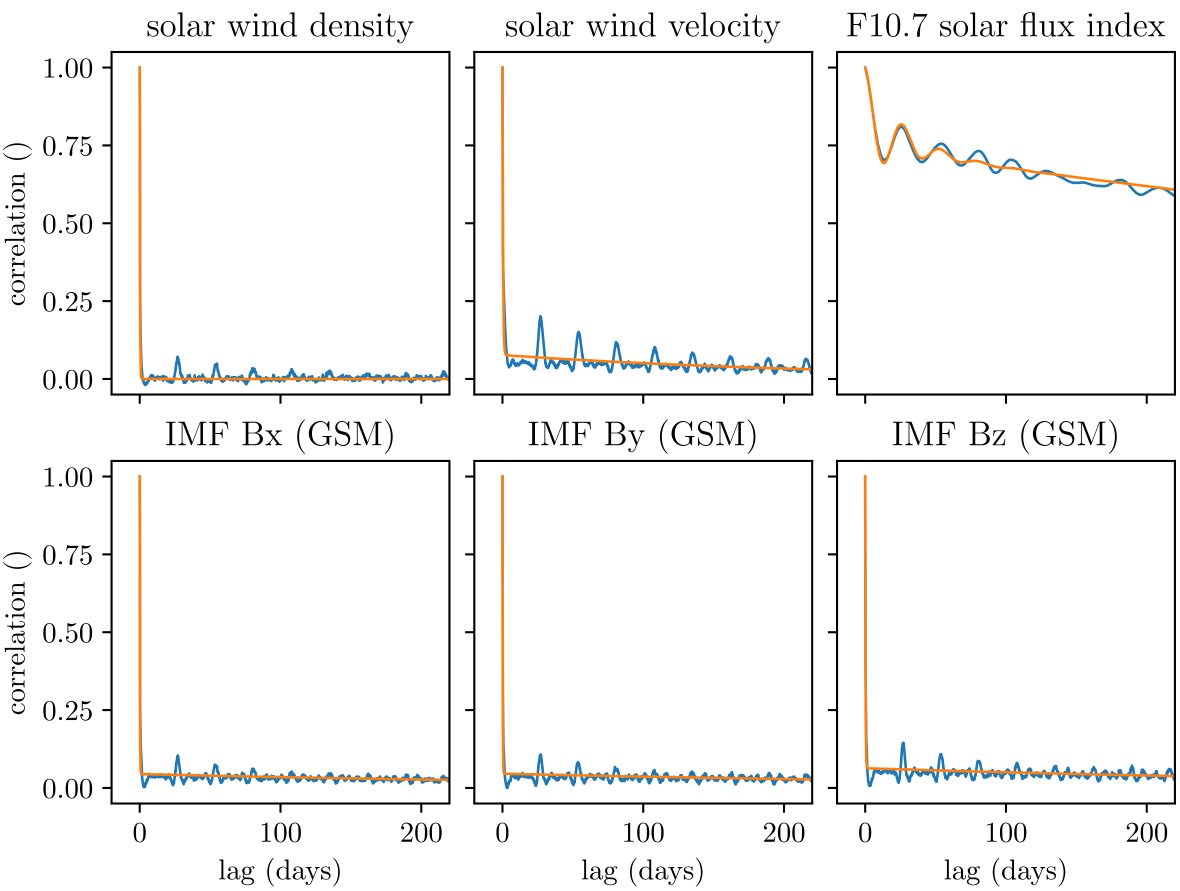

Figure 7.4.: Empirical (blue lines) and modeled autocorrelation function (orange lines) of the standard deviation of the external forcings. Only the first 200 days are shown here since I do not perform experiments with periods longer than some weeks. The x component of the IMF B_x is plotted here, although it is not an input of the TIE-GCM.

The analytical autocorrelation function for the uncertainty of the F10.7 index also contains cosine functions associated with the rotation of the Sun and the solar cycle:

$$\begin{aligned}\gamma_3(t) = (1 - A_1 - A_2) \exp\left(-\frac{\ln(2)}{T_0}|t|\right) \\ +A_1 \cos\left(2\pi\frac{t}{4530\,\mathrm{d}}\right) \exp\left(-\frac{\ln(2)}{T_1}|t|\right) \\ +A_2 \cos\left(2\pi\frac{t}{27\,\mathrm{d}}\right) \exp\left(-\frac{\ln(2)}{T_2}|t|\right)\end{aligned} \tag{7.5}$$

with the condition $0 < A_1 \leqslant 1 \wedge 0 < A_2 \leqslant 1 \wedge 0 < A_1 + A_2 \leqslant 1$. I use the period from 2000 until 2023 for the computation of the empirical autocorrelation functions. For fitting the functions to the empirical function, only the first 20 % of all values are used since the larger the lag, the larger the uncertainty.

The standard deviations of the components of the IMF flux in Papitashvili and King (2020c) are given in the GSE, but the TIE-GCM requires them in GSM. Thus, after the sampling, the sampled perturbations must be rotated accordingly (see Appendix E.2).

Table 7.2.: The column labeled with Δt, and $\gamma(t)$ contain the temporal resolution of the time series, and the autocorrelation function fitted to the empirical autocorrelation function, respectively. See Section 2.3.2 for further information about the solar wind and IMF, and Section 2.3.1.2 for the F10.7 index. The letters in the column σ indicate the source of the uncertainty of the corresponding parameter.

external forcing	σ	Δt	$\gamma(t)$	estimated parameters for $\gamma(t)$
solar wind density	[a]	1h	Eq. 7.3	$T = 3.36\,\mathrm{h}$
solar wind velocity			Eq. 7.4	$T_0 = 167\,\mathrm{d}$, $T_1 = 6.44\,\mathrm{h}$, $A_1 = 0.92$
y component of IMF flux in GSM			Eq. 7.4	$T_0 = 296\,\mathrm{d}$, $T_1 = 2.76\,\mathrm{h}$, $A_1 = 0.92$
z component of IMF flux in GSM			Eq. 7.4	$T_0 = 300\,\mathrm{d}$, $T_1 = 3.54\,\mathrm{h}$, $A_1 = 0.94$
F10.7 index	[b]	24 h	Eq. 7.5	$T_0 = 29\,\mathrm{d}$, $T_1 = 3.92\,\mathrm{year}$, $T_2 = 16\,\mathrm{d}$, $A_1 = 0.71$, $A_2 = 0.17$

[a] Papitashvili and King (2020c)
[b] Tapping (2013, Paragraph 56)

7.2.1.3. Earth Magnetic Field

In contrast to the previously discussed external forcings, the Earth's magnetic field is spatially resolved in the TIE-GCM 2.0. It is represented by the 12th release of the IGRF and is used to calculate the modified apex coordinates (Appendix E.3). The IGRF uses spherical harmonics up to degree thirteen and is updated every five years (Alken et al., 2021). There is no time series available to provide the uncertainty, but Beggan (2022) estimated the "large-scale time-invariant spatial uncertainty of the IGRF based on the globally averaged misfit of the model to ground-based measurements [...]" (Beggan, 2022). He provides the standard deviation of the east, north, and vertical components, as well as the standard deviation of the total field intensity, inclination, and declination.

Perturbing the east, north, and vertical components can cause instabilities in the model if a spatially constant perturbation is assumed for the corresponding component of the magnetic field. This is because the perturbation along a component can be much larger than the magnetic flux itself. Therefore, I perturb only the total field intensity with the standard deviation found by Beggan (2022) which is 178 nT. However, this standard deviation was computed for the magnetic field at the ground. Since Earth magnetic field is well approximated by a dipole field, the magnetic intensity gets smaller with increasing altitude and towards the equator. At 1000 km altitude, the total magnetic flux density is about 40 % lower than on the ground. Thus, using the same perturbation for all locations is likely to overestimate the uncertainty at high altitudes (see Figure C.3). This should be accounted for in a future implementation. Ideally, an ensemble of spherical harmonics coefficients would be used to represent the uncertainty of the IGRF.

7.2.2. Lower Boundary Conditions

To run the TIE-GCM one must specify the neutral temperature, the horizontal neutral wind velocity, and the geopotential height at the lowest pressure level (Section 5.1). In all experiments, the lower boundary conditions are constructed from zonal averages obtained from the NRLMSIS-

Table 7.3.: The perturbations for the lower boundary conditions listed in this table are sampled from truncated normal distributions with zero mean. The parameters of the distribution are taken from Corbin and Kusche (2022, Table 1)

		perturbation	
parameter	original value	standard deviation	limits
neutral temperature	from empirical model	3 K	± 9 K
neutral zonal wind		70 m	± 210 m
neutral meridional wind		$5\,\mathrm{m\,s^{-1}}$	$\pm\ 15\,\mathrm{m\,s^{-1}}$
geometric height		$6.5\,\mathrm{m\,s^{-1}}$	$\pm\ 19.5\,\mathrm{m\,s^{-1}}$

E00 and HWM 07 plus upward propagating atmospheric tides (Section 2.4) simulated by the Global Scale Wave Model (GSWM; Hagan and Forbes 2002; X. Zhang et al. 2010) .

A very simple approach for accounting for the uncertainty in the lower boundaries is adding a global offset as done in Corbin and Kusche (2022). This approach does not account for errors in the phases and amplitudes of the atmospheric tides, though. Offsetting the lower boundary conditions affects the neutral mass density in the lowest part of the TIE-GCM the most. The impact of external forcings on the neutral mass density in proximity to the lower boundary is much greater than for higher altitudes (see Appendix C.1). So, perturbing the lower boundary conditions is crucial for the ensemble spread of the lower model levels.

A better approach for the ensemble generation of the lower boundary conditions could running ensemble simulations of the NRLMSIS, Horizontal Wind Model (HWM), and GSWM with perturbed forcings. However, implementing this approach would require some additional effort. Thus, for now, I only perturb the offsets. The perturbations for the boundary conditions are sampled from truncated normal distributions using the parameters listed in Table 7.3.

7.2.3. Model Parameters

The parameters that are perturbed to generate the ensemble are listed in Table 7.4 and described in Section 5.1.3. A truncated normal distribution with zero mean is used to sample the perturbations. The standard deviation corresponds to 10 % of the unperturbed value. The limits are three times the standard deviation. For future experiments, it would be beneficial to expand the list to further increase the uncertainty of the model's forecast.

Table 7.4.: The perturbations for the model parameter listed in this table are sampled from truncated normal distributions with zero mean. The parameters of the distribution are taken from Corbin and Kusche (2022, Table 1). Although the Burnside factor is not listed in Corbin and Kusche (2022, Table 1), it is perturbed for the experiments in the paper nevertheless).

		perturbation	
parameter	original value	standard deviation	limits
Joule heating factor	1.5	0.15	± 0.45
Burnside factor	1.5	0.15	± 0.45
peak energy of cusp electrons	100 eV	10 eV	± 30 eV
peak energy of polar rain electrons	500 eV	50 eV	± 150 eV

7.3. Observation Operator for Neutral Mass and Electron Number Densities

In this implementation, the observation operator is the composition of two functions $\mathcal{H}(\boldsymbol{x}) = (\mathcal{I} \circ \mathcal{F})(\boldsymbol{x})$ that computes the observed quantity from the state vector via $\mathcal{F}(\boldsymbol{x})$ and interpolates it to the position of the observation using a suited interpolation function $\mathcal{I}$. The interpolation is always performed at the end so that interpolation errors do not affect the computation of the observed quantity. Only prognostic state variables (see Table 5.3) can be used in the state vector. Diagnostic state variables are not used to forward the model, therefore, updating them does not affect the model propagation at all.

To compute the neutral mass density from the prognostic variables of the TIE-GCM (Table 5.3), the state vector must include the individual mass fractions w_j of the neutral species and their temperature T. By inserting Equation 2.8 into Equation 2.15 an idealized expression for the mass density assuming an ideal gas is found:

$$\rho_{\text{neutral}} = \frac{p}{RT \sum\limits_{\text{species}} \frac{w_j}{M_j}} \quad \text{with species} = \{\mathrm{O_1}, \mathrm{O_2}, \mathrm{He}, \mathrm{N_2}\}. \tag{7.6}$$

The mass fraction of molecular nitrogen results from $w_{\mathrm{N_2}} = 1 - w_{\mathrm{O_1}} - w_{\mathrm{O_2}} - w_{\mathrm{He}}$. The molar masses M_j of the species are given in Table 2.2. Since the ion mass density is much lower than the neutral mass density (three orders of magnitude and more, Figure 2.20) one can approximate the total mass density with the neutral mass density.

The electron number density is a prognostic state variable and can be mapped directly to the observation. A unit conversion might still be necessary.

Before the actual interpolation can be applied, the pressure levels must be converted to geometric heights by applying a modified version of Equation 2.26 using a latitude and altitude-dependent value for the gravitational acceleration. The interpolation is performed first in the vertical direction. Since this is the only irregular dimension of the TIE-GCM grid, the intermediate result is given on a regular grid. The regular structure facilitates the subsequent interpolations in the remaining dimensions. The interpolation function $\mathcal{I}$ is constructed from B-splines (De Boor, 1978). The degree of the B-Splines can be chosen in the range from 1 (linear) to 5 (quintic). In the longitudinal direction, periodic splines are used. The value at the poles is computed as the mean from the surrounding cells. In case neutral mass density is computed, the vertical interpolation step is performed in logarithmic space. This reduces the interpolation error since in logarithmic space the neutral mass density profile is closer to a linear function.

7.4. Constraints on the Updated State

The Kalman filter does not consider any physics when updating the state. Thus, the updated state may violate physical laws or contain unrealistic estimates. As a consequence, one must check the state after each update and restore physical consistency if necessary. Otherwise, the model is likely to crash when further forwarded. Consistency is ensured by applying the limits listed in Table 7.5.

Additionally, the following constraints are applied after limiting the state variables according to Table 7.5.

(C 1) The sum of all neutral mass fractions must be one[1] (see Equation 2.3). For all grid cells not satisfying this constraint, the corresponding fractions are divided by the sum.

(C 2) The electron and ion temperature must be greater or equal to the neutral temperature. Ion or electron temperatures not satisfying this constraint are replaced by the neutral temperature.

Table 7.5.: This table lists the limits that are used to constrain the corresponding state variables after the update step. The reason why a condition is applied is indicated by letters.

state variable		limit	
name	units	lower	upper
any mass fraction		1×10^{-12} [e]	1
electron number density	cm^{-3}	3100 [a]	4.0×10^{6} [d]
neutral temperature	K	100 [a]	2800 [c]
ion temperature	K	100 [b]	4200 [d]
electron temperature	K	100 [b]	6100 [d]
O^+ number density	cm^{-3}	1×10^{-12} [e]	4.0×10^{6} [d]
$O_2{}^+$ number density	cm^{-3}	1×10^{-12} [e]	2.9×10^{5} [d]

[a] same limit as used in TIE-GCM 2.0
[b] follows from constraint C 2
[c] derived from the maximum in Figure 2.20 with some extra margin
[d] 1.2 times the maximum of Halloween storm simulation rounded to two significant figures
[e] limit is actually zero, but in practice a positive value close to zero is used to prevent invalid division by zero in model code

---

[1] In practice the sum is constrained to 1-1 × 10^{-12} since the mass fraction of N_2 is not part of the state vector and not part of the sum. This ensures it is not zero in the following calculations.

7.5. Localization

For domain localization (Section 6.4.2), one has to define a metric that is used for measuring the distance between observations and the center of the subdomains. PDAF offers different metrics. For spherical coordinates (longitude λ, latitude ϕ, altitude z) the distance is computed from the great circle distance d_{gc} and the vertical distance

$$d_{\mathrm{sph}} = \sqrt{d_{\mathrm{gc}}(\phi_1, \phi_2, \lambda_1, \lambda_2)^2 + (z_1 - z_2)^2}, \tag{7.7}$$

with d_{gc} computed by the haversine formula

$$d_{\mathrm{gc}} = 2R_{\oplus} \arcsin\left(\sqrt{\sin^2\left(\frac{\phi_2 - \phi_1}{2}\right) + \cos(\phi_1)\cos(\phi_2)\sin^2\left(\frac{\lambda_2 - \lambda_1}{2}\right)}\right). \tag{7.8}$$

In Corbin and Kusche (2022), the coordinates of the observations and the TIE-GCM grid cells were converted to the grid cell index, and the distance was computed as the Euclidean distance. This approach was chosen since grids with regular zonal and meridional spacing exhibit an increase in resolution towards the poles. By measuring the distance in grid cells, the number of included observations at the poles and the equator is more balanced. This approach is an implicit non-isotropic localization, since the geometric extent of a grid cell is much larger in the horizontal than in the vertical direction. The meridional extent of the grid cells is constant, but the zonal extent depends on latitude and altitude. For the TIE-GCM with 5° horizontal resolution, a cell located at the ring around the poles at 100 km has a zonal arc length of 49 km while a cell at the equator at 500 km altitude as an arc length of 600 km. The vertical extends increases with altitude by reason of the underlying pressure coordinates. For the 5° version the vertical extend is roughly 2.5 km and 30 km at the lower and upper layer, respectively.

PDAF supports non-isotropic localization since version 2.2 explicitly so that one can have different radii for vertical and horizontal distances. For observation localization PDAF supports two correlation functions: exponential decay and a finite 5-th order polynomial mimicking a Gaussian (defined in Gaspari and Cohn (1999, Equation 4.10) and illustrated in Figure 6.3 with the green line labeled with $\mathrm{GC}_{a=0.5}(\tau)$.)

7.6. Assimilation of Semi-Empirical Models via Two-Step Approach

Semi-empirical models are based on substantial records of observations from various instruments providing global mass density estimates (see Section 5.2). Assimilation of the mass density estimate of the semi-empirical model is considerably more straightforward than assimilating all of the datasets utilized in constructing the empirical model into numerical models since the data has already been harmonized and is globally available. However, the spatial and temporal resolution of the atmospheric signals captured by the empirical models is limited, and information contained in the original records is inevitably lost when the observations are fitted to the empirical model's representation of the atmosphere. Additionally, most of the recorded data is during geomagnetic quiet conditions, simply because this is the dominant state of the

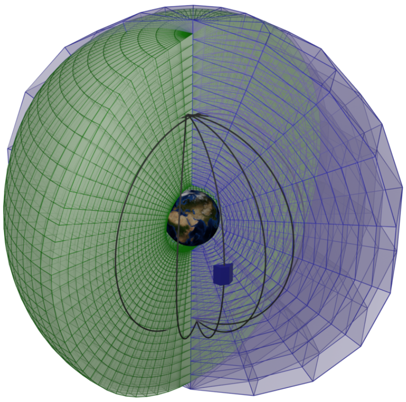

Figure 7.5.: The green lines represent the gird of TIE-GCM 2.0 with 5° horizontal resolution. The blue grid is the data grid at which the empirical model is evaluated. The black line is the orbit of the CHAMP satellite at about 300 km. The vertical direction is not to scale. The image of Earth is part of the 'Blue Marble' collection and was created by Reto Stöckli, NASA Earth Observatory.

geomagnetic activity (see Figure 2.17). Consequentially, empirical models perform exceptionally well during quiet conditions.

The two-step approach developed by Corbin and Kusche (2022) calibrates a semi-empirical model (NRLMSIS 2.0) with accelerometer-derived mass densities (from CHAMP) in the first step. Details about this first calibration step are explained in Section 7.6.1. In the second step, the model is evaluated globally, and the global and calibrated model output is assimilated into the numerical model. This can be interpreted as 'smart' interpolation of the accelerometer-derived mass densities. It allows to update the state of the numerical model globally and applying localization. However, it comes with a loss of temporal resolution compared to the original accelerometer-derived mass densities (Section 7.6.1).

The empirical model employed here is the NRLMSIS 2.0 (Section 5.2.1). It is evaluated on a 3D grid that is regular in longitude, latitude, and altitude. This grid is referenced as *data grid* in the following. The horizontal resolution of the data grid (see Figure 7.5) is adapted to the horizontal resolution of the semi-empirical model, which is limited by the maximal degree of the spherical harmonic coefficients used in the model formulation. The necessary transformation of the satellite orbit into the ITRS is summarized in Appendix E.1. The following aspects have changed since the publication of Corbin and Kusche (2022) in the implementation:

- Interpolation in observation operator:
  - Cubic B-spline interpolation is used instead of linear interpolation
  - Values at the poles ($\phi = \pm 90°$) are added to the knots of the splines and computed by averaging the surrounding cells.
- Additional physics-based constraints/limits are added to prevent invalid results:
  - Limits on ion and electron temperature (Table 7.5) and Constraint C 2
  - Limits on ion and electron number density (Table 7.5)
  - Positive hall conductivity in the TIE-GCM ion drag computation is enforced.

- The TIE-GCM routine computing the roots of a quartic equation (used to compute electron number density) captures negative arguments in square roots.

7.6.1. Calibration

The calibration of the empirical model is based on scale factors between the empirical model and the accelerometer-derived densities. The time series of scale factors is smoothed with a low-pass filter to eliminate the dependency of the orbital position. An example of this calibration is given in Figure 7.6 for the scale factor between mass densities derived from CHAMP's accelerometer and simulated by the NRLMSIS 2.0. The scale factor is greater than in most cases, indicating that the NRLMSIS 2.0 underestimates the mass density compared with the accelerometer-derived mass densities for the given period. During the 5 April geomagnetic storm the scale factor peaks with 1.5. A low-pass filter with a cut-off frequency of 3 h is applied to the time series of scale factors, which corresponds to two orbital revolutions of CHAMP. The scale factor's dependency on the argument of latitude is significantly reduced compared with the unfiltered data (compare panels b and e in Figure 7.6.) While this approach allows scaling the model globally, it has the disadvantage that the high temporal resolution of the accelerometer is lost to some extend.

The vertical extent of the data grid at which the empirical model is evaluated is aligned to the vertical extent of the TIE-GCM, and the spatial resolution is matched to the resolution of the empirical model. Corbin and Kusche (2022) used a regular grid with 20° horizontal resolution ranging from 100 km to 550 km with a vertical resolution of 25 km (see Figure 7.5).

7.6.2. Stochastic Model

In Corbin and Kusche (2022), correlations of the observations were neglected in the stochastic model. However, it is helpful to consider the correlations of the observations to prevent any unwarranted confidence in the observations. The empirical model has a horizontal resolution of 60° and is evaluated on a 20° grid that is assimilated into the TIE-GCM. Thus, mass densities located in grid cells close to each other have a large correlation by design. When not considering the correlations, increasing the localization radius has a similar effect as increasing the weight of the observations, since more (highly correlated) observations are included that are treated as they were uncorrelated. Thus, a decent stochastic model should provide the full VCM.

Unfortunately, information about the uncertainty of the modeled state variables is not included in the output of NRLMSIS 2.0. Thus, the VCM has to be constructed by other means. One approach is to create an ensemble of NRLMSIS 2.0 instances, where the external forcings of each instance are perturbed in a manner similar to that done in Section 7.2. The VCM can then be obtained for each time step from the ensemble using Equation 6.28. Although this is a promising approach, another much simpler approach based on literature standard deviations, weighting, and correlation functions is used for now.

The standard deviation of each grid cell of the data grid is obtained by multiplying the density from the uncalibrated model with a height depended factor (Corbin and Kusche, 2022, Equation 6). In addition it is weighted with a function depending on the Kp index representing geomagnetic activity (Corbin and Kusche, 2022, Equation 8), a function depending the spherical

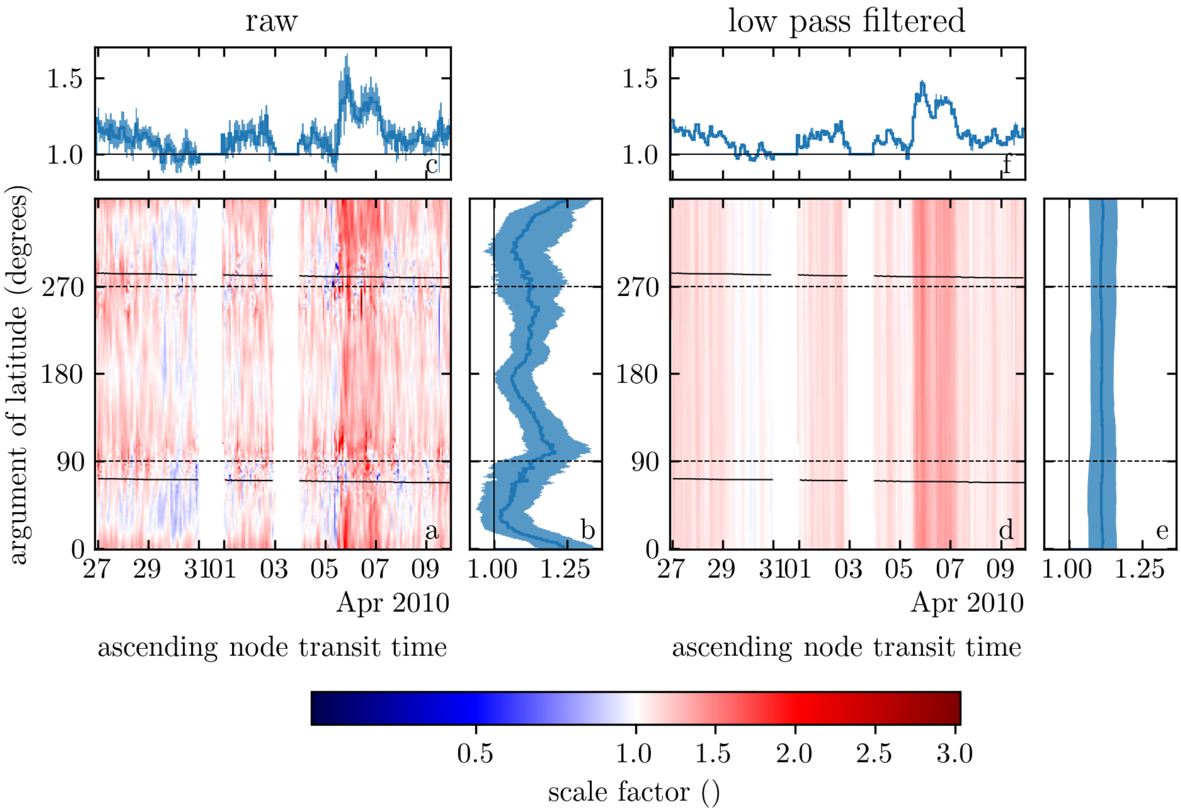

Figure 7.6.: This figure is a modified version originating from Corbin and Kusche (2022, Figure 3) with an improved colormap. It shows the scale factor between accelerometer-derived densities of the CHAMP satellite and the NRLMSIS 2.0. A scale factor greater than one indicates that the accelerometer-derived density is greater than the modeled density. The unprocessed scale factors are on the left (panels a, b, and c), and the filtered scale factors are on the right (panels d, e, and f). The argument of latitude is the angle between the ascending node and the position of the satellite, as measured in the orbital plane. The satellite passes the night-side and day-side equator at 0° and 180°, respectively. At 90° and 270° it is closest to the north and south pole, respectively. The solid black lines in panels a and d indicate the position of the solar terminator. The solid blue line in panel c and f is the median scale factor at each orbit. In panels b and e, the blue line is the median scale factor at each argument of latitude. The light blue area is the 25th to 75th interpercentile range.

and vertical geocentric distance to the satellite that was used for the calibration (Corbin and Kusche, 2022, Equation 9) and a constant weight factor p_0 which is set to one in this thesis.

Figure 7.7 shows an empirical autocorrelation function of the NRLMSIS 2.0 mass density depending on vertical distance and great circle distance. The autocorrelation decreases much faster the in vertical direction than in horizontal direction. To approximate the autocorrelation function with an analytical function the horizontal and vertical distance are combined using the Euclidean norm and a weight for the horizontal component. Fitting the weight and the

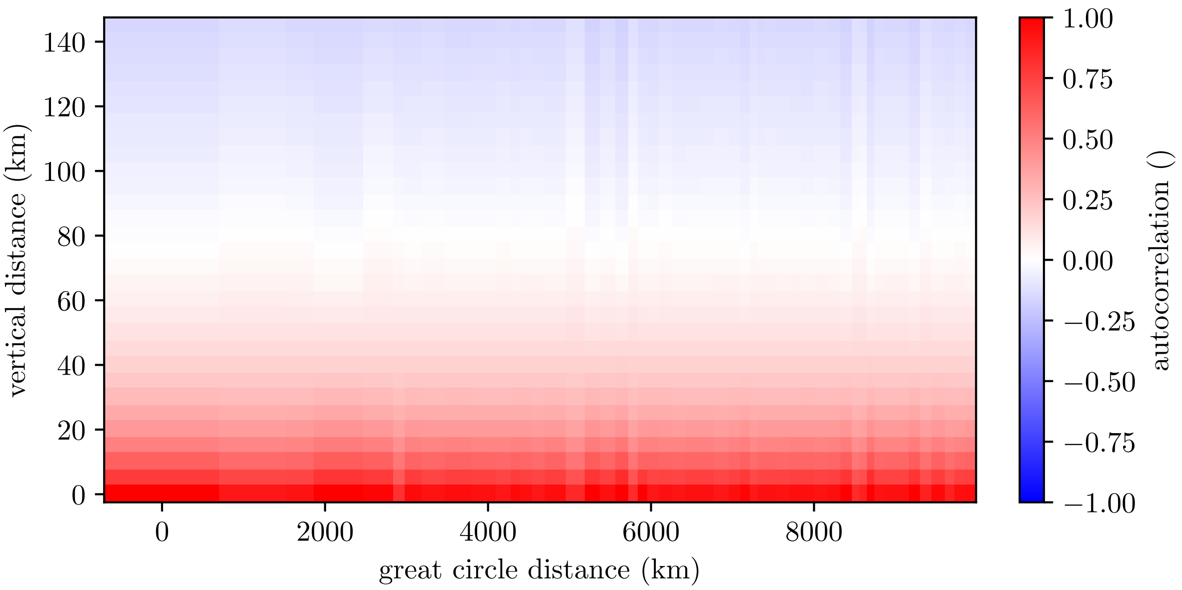

Figure 7.7.: The spatial correlation of neutral mass density of the NRLMSIS 2.0 was computed in dependence of vertical distance and great circle distance for 1 April 2010 00:00 UTC+0. The model was evaluated on a grid partitioned into cells of equal surface area and similar shape on a sphere using the algorithm developed by B. Beckers and P. Beckers (2012). For each altitude and hemisphere, 150 grid cells were evaluated. The correlations were computed using distance classes (50 for horizontal distance and 30 for vertical distance).

parameter of a simple exponential decay to the data in Figure 7.7 provides the approximation

$$c(\Delta_h, d_{\mathrm{gc}}) = \exp\left(-\frac{\sqrt{\left(\frac{d_{\mathrm{gc}}}{2670}\right)^2 + \Delta_h^2}}{20.5\,\mathrm{km}}\right) \tag{7.9}$$

with the vertical distance Δ_h and great circle distance d_{gc} in kilometers. Given the standard deviations of the observations, one can calculate the full VCM of the observations using Equation 6.21 where the correlations are computed from Equation 7.9.

8. Experiments

In Section 1.4, I formulated six hypotheses concerning overcoming challenges pertinent to data assimilation systems in the upper atmosphere. In this chapter I perform OLSs and data assimilation experiments to test those hypotheses. Since an efficient assimilation system is required, I investigate first how many ensemble members should be used, which requires balancing computational costs and representativeness of the state ensemble for the model errors (Section 8.1). In the following Section 8.2, the generation of the state ensemble with time-variable and static perturbations of the external forcings is compared. I demonstrate that compared with static external forcing perturbations, time-variable perturbations decrease spurious long-range correlations in the forecasted ensemble of the state. In Section 8.3, the neutral mass density simulated by TIE-GCM OLSs with 5° and 2.5° horizontal resolution are compared with accelerometer-derived densities and densities from empirical models. Data assimilation experiments where mass densities are assimilated are described in Section 8.4. The assimilation of electron densities from an empirical model is discussed in Section 8.5 and the co-estimation of Joule-heating in Section 8.6. Most experiments investigate the two-week long period from 27 March 2010 to 10 April 2010. Initially, the period represents quiet conditions, but it also includes a strong geomagnetic storm that hit Earth on 5 April 2010, allowing the assimilation to be tested under different conditions. In Section 8.7 additional periods are investigated to demonstrate that the assimilation system performs equally well for different solar and geomagnetic conditions.

There are three phases of a data assimilation experiment illustrated in Figure 8.1. In the first phase, a suited initial state is forwarded to the period of the experiment (dashed line in Figure 8.1). If the forecast duration is long enough (a few days), the exact choice of this initial state does not matter (see Figure 7.2). In a second phase, the state ensemble is initialized by applying perturbations to selected model inputs (see Section 7.2) over a suited period (spin-up phase, solid gray lines in Figure 8.1). In the third phase, using the states at the end of the spin-up phase (marked with black dots), one can either run an assimilation experiment or an OLS.

Setup 1: Default TIE-GCM setup for all experiments in this thesis

temporal resolution (step size)	15 s
lower boundary conditions	GSWM + climatology from HWM07 and NRLMSIS-E00
ion convection	Weimer (2005)
Burnside factor	1.5
Joule heating factor	1.5
external forcings	F10.7 index and solar wind from high resolution OMNI data set (Papitashvili and King, 2020a)

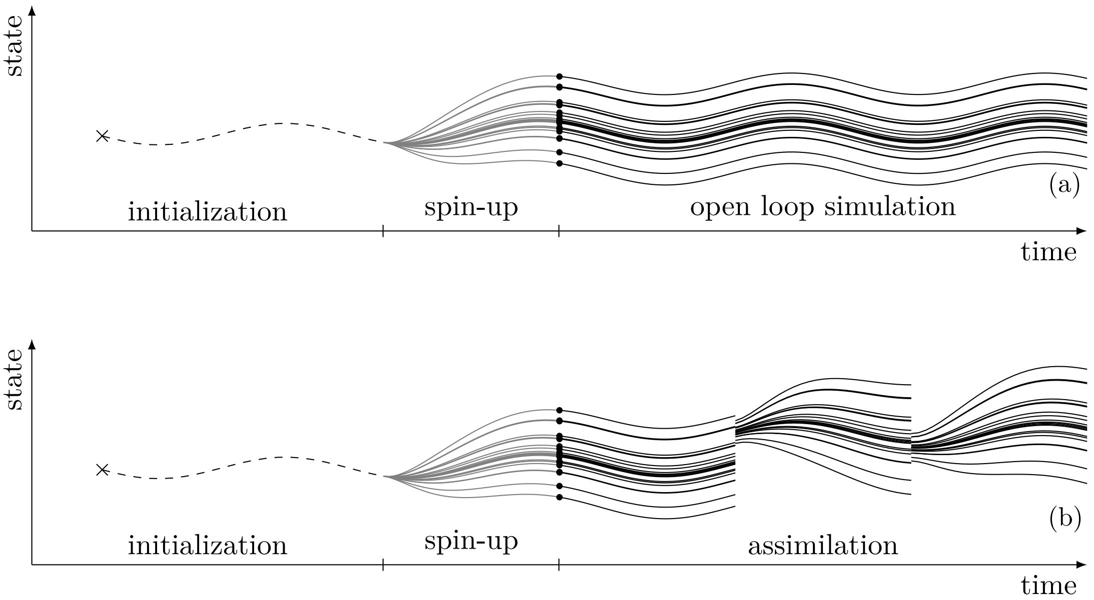

Figure 8.1.: This sketch illustrates the three phases of the open loop simulations (panel a) and assimilation experiments (panel b). The first and second phases are equivalent for both cases. In the first phase, a single model instance (dashed line) is forwarded from some initial state (marked with a black x) into the vicinity of the period in which observations are to be assimilated. Second, in the spin-up phase, the entire ensemble is forwarded from the last state of the initialization phase. Each solid line corresponds to an ensemble member. Because of the perturbations, the spread gradually increases. The resulting initial states for the subsequent assimilation phase are marked with black dots. As long as the ensemble generation approach is not changed, the same initial values are used for different assimilation setups or OLSs. Thus, computational resources are saved since the spin-up phase is computed only once for all experiments using the identical initial ensemble. The update step of the Kalman filter reduces the ensemble spread and causes jumps in the time series. Panel b illustrates both effects.

The default setup for TIE-GCM runs in open-loop mode or performing data assimilation is summarized in Setup 1. A previous investigation in Corbin and Kusche (2022, Table 3) indicated that the Weimer ion convection model provides better neutral mass density estimates than the Heelis model (the average difference to accelerometer-derived densities along the CHAMP orbit was reduced by 87 %). Additionally, using zonal mean climatology lower boundary conditions[1] gives better results than using a constant lower boundary (the average difference to accelerometer-derived densities along the CHAMP orbit was reduced by 22 %). I use a step size (temporal resolution) of 15 s for the TIE-GCM since longer step sizes as 30 s or 60 s caused model crashes more frequently.

---

[1] The TIE-GCM provides zonal and climatological lower boundary conditions (only depending on latitude, month, and hour) that are computed from the NRLMSISE-00 (temperature) and HWM 07 (meridional and zonal wind).

Setup 2: Spin-up

general

type	open loop
TIE-GCM setup	5°, Setup 1
start	17 Mar 2010 00:00 UTC+0
end	27 Mar 2010 00:00 UTC+0
writing frequency	every 10 minutes

ensemble

ensemble size	192
perturbations	time-variable (P 4, Table 8.1)

8.1. Determination of the Ensemble Size for all Experiments

Two conflicting objectives are minimized to determine the ensemble size: computational resources and sampling error. A large ensemble size reduces the sampling error of the VCM of the forecasted state but, at the same time, requires significant computational resources. To find a suited ensemble size, I forecast 192 ensemble members in the spin-up phase[1] (see Setup 2) and analyze subsets of different sizes. The subsets always incorporate the first n members of the total ensemble.

Figure 8.2 shows how the relative standard deviation (ratio of standard deviation and mean) of neutral mass density and electron number density depends on average on the vertical position (altitude or pressure) and ensemble size. The upper row shows the dependency on the pressure level, and the lower row shows the dependency on the geometric height. The relation between pressure level and geometric height is explained in Section 2.1.4. The average relative standard deviation of the neutral mass density is much larger when specified on geometric height instead of pressure levels. This is because the geometric height itself depends on the neutral mass density: The geopotential height and, therefore, the geometric height (Equation 2.28) depend on the lower boundary of the geopotential height and the vertically integrated reciprocal neutral mass density (see Equation A.29). Since each ensemble member has different neutral mass densities and lower boundary conditions, the geometric height of each member also has different values.

The height profiles corresponding to ensemble sizes of 32 and 64 members are clearly separated from the other height profiles corresponding to sizes greater than or equal to 96 (Figure 8.2). Using ensemble sizes greater than 96 affects the average relative standard deviation of neutral mass and electron number density only slightly.

So far, only the standard deviations (square root of the main diagonal of the VCM) of the model forecast have been considered. The correlation matrix of the forecasted state is explicitly computed for different ensemble sizes to analyze how the cross-correlations depend on the ensemble size. The correlation matrix computed from all 192 ensemble members is used as reference[2]. The reference correlation matrix is subtracted from the correlation matrices computed from a subset of the ensemble. The histograms of these differences are shown in Figure 8.3. The greater the number of ensemble members, the closer the cross-correlations align with the refer-

---

[1] The high-performance computing cluster *marvin* used for all computations in this thesis has 96 processor cores per node. The nodes are allocated exclusively to ensure that the computations and communication of other users on the cluster do not interfere with the assimilation runs. Ideally, when using four processor cores per ensemble member, the ensemble size is a multiple of 24 to use all processor cores on the allocated nodes.

[2] Note that although the reference matrix is computed from the ensemble with the most members, it remains underdetermined and singular because the number of ensemble members is less than the size of the state vector.

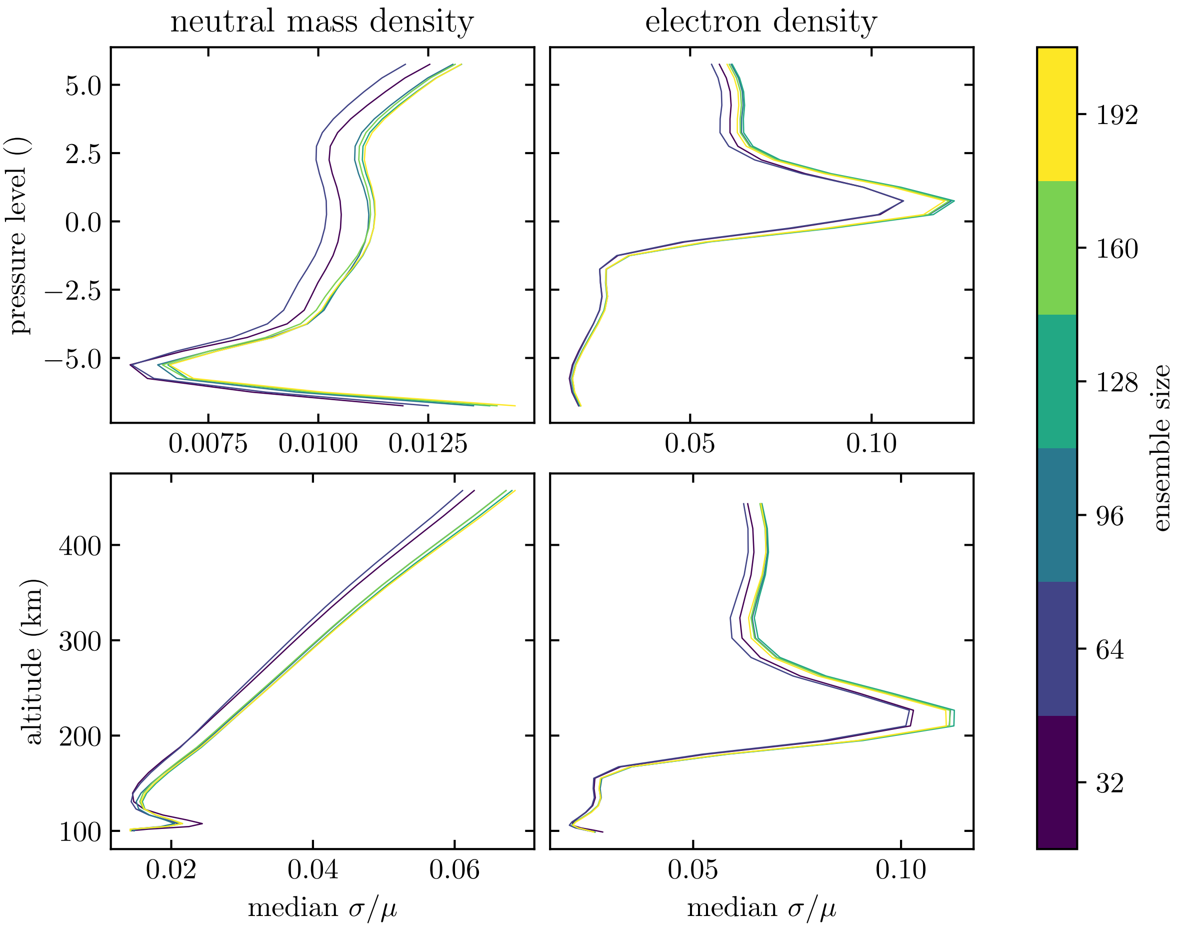

Figure 8.2.: The TIE-GCM (5° version) was forwarded ten days with the setup described in Setup 2. For all cells on the last day of the spin-up phase (from 26 Mar 2010 00:00 to 27 Mar 2010 00:00), the mean and standard deviation of neutral mass and electron number density were computed. In this figure, the ratio of standard deviation and mean is shown for different ensemble sizes, indicated by color. The data was reduced to height profiles by computing the horizontal and temporal median of the ratios for each ensemble size. The median was weighted using the surface area of each grid cell (see Appendix C.4). The densities were transformed to geometric height using linear interpolation to compute the height profiles in the lower row.

ence. Using the half of the full ensemble (96 members), 90 % of the cross-correlations differ by less than ±0.1 from the correlations computed from the reference ensemble with 192 members.

Since the standard deviations of neutral mass density and electron number density do not change a lot when using ensembles with more than 96 members and the cross-correlations largely agree within ±0.1 compared with the reference ensemble with 192 members, I use 96 ensemble members for all following experiments.

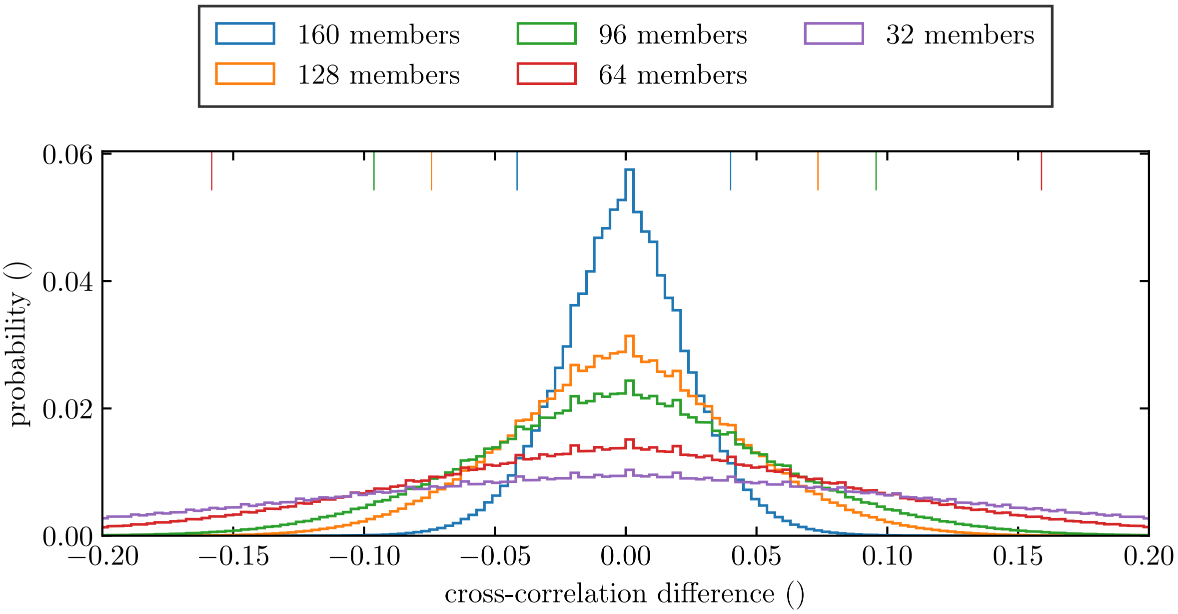

Figure 8.3.: For this plot, the correlation matrix was computed explicitly via Equation 6.28 and 6.20. However, only a subset was computed since the full correlation matrix requires too much memory. The subset includes all correlations of w_{O}, w_{O_2}, w_{He}, T_n, T_e, T_i, u_n, v_n, C_{O^+}, $C_{\mathrm{O}_2{}^+}$and ρ at two pressure levels located roughly at 282 km and 472 km. The correlation matrix was computed from the state ensemble at the end of the spin-up phase (27 March at 2010 00:00 UTC+0) described in Setup 2. The correlation matrix was computed for different ensemble sizes, taking only the first n ensemble members into account. The correlation matrix computed from the largest ensemble (192 members) is used as a reference. The reference matrix is subtracted from the correlation matrices, and the distribution of the corresponding differences is plotted here. The histogram is computed only from cross-correlations of the upper triangle so that symmetric correlations are not counted twice. The vertical ticks on the upper x-axis indicate the 5^{th} to 95^{th} interpercentile range. When interpreting these results, one has to consider that the reference correlation matrix does not contain the true correlations, but is subject to sampling errors.

8.2. Analysis of Correlations encoded in the Forecasted State Ensemble Matrix

The ensemble of forecasted states depends primarily on the perturbations applied to the external forcings, model parameters, and boundary conditions (see discussion in Section 7.2). Table 8.1 lists four different configurations of the perturbations. All configurations use the same static parametrization of the perturbations for lower boundary conditions and model parameters as described in Table 7.3 and Table 7.4, respectively. The parametrization for lower boundary constraints and model parameters is consistent to Corbin and Kusche (2022, Table 1).

The first configuration parameterizes the perturbations in the same way as in Corbin and Kusche (2022, Table 1). That is, all perturbations are static. The second configuration uses time-variable perturbations for the F10.7 index, solar wind density, and solar wind velocity as described in Section 7.2. The third configuration perturbs the IMF in addition to the second configuration. Finally, the fourth configuration perturbs the magnitude of Earth's magnetic field

Table 8.1.: Time-variable and static perturbations are sampled in advance for all ensemble members. 'static' means that the corresponding perturbation is constant for each ensemble member over the entire duration of the experiment. 'time-variable' indicates that a time series was sampled for each ensemble member, and the perturbation changes over time. The temporal resolution of the sampled external forcing perturbation time series is given in Table 7.2. The row indicated by P 1 corresponds to the perturbations in Corbin and Kusche (2022), the last row (P 4) to the complete set of perturbations described in Section 7.2.

	lower boundary	parameters	F10.7	solar wind	IMF	$\lvert B_\oplus \rvert$
P 1	static	static	static	static	none	none
P 2			time-variable	time-variable		
P 3					time-variable	
P 4						static

$|B_\oplus|$ in addition to the third configuration and corresponds to the complete set of perturbations described in Section 7.2.

First, I analyze the correlations of the forecasted state represented by the ensemble for the four configurations. For all configurations summarized in Table 8.1, Figures 8.4 and 8.5 illustrate the correlation matrix of the forecasted state that was explicitly computed from the ensemble at the end of the spin-up phase using Equations 6.28 and 6.20. For visual clarity, only two pressure levels are shown at approximately 282 km and 472 km altitudes. The matrices are sorted first by state variable (separated with solid black lines), followed by pressure level (indicated by alternating black and white stripes at the frame), latitude (slim black and white stripes at the frame), and longitude.

The static perturbations used in configuration P 1 (equivalent to the configuration in Corbin and Kusche (2022)) cause high correlations between the entries in the state vector (see Figure 8.5a). Both spatial correlations (correlations of the same state variable but at different grid cells) and correlations between different state variables are high. Especially, the negative correlations in the vast majority of all grid cells between neutral mass densities and neutral temperatures are striking.

The perturbations control spatial correlations and correlations between different state variables. While domain localization (Section 6.4.2) can account for spurious spatial long-range correlations, it cannot compensate for spurious inter-state variables correlations within the same sub-domain. Thus, to reduce spurious inter-state variable correlations, one must improve the realism of the perturbations. More realistic perturbations may reduce spurious spatial correlations and allow larger cut-off radii for localization. In an ideal scenario, observations could be assimilated without needing localization. However, it is unlikely that all spurious correlations can be eliminated.

When using time-variable perturbations instead of static perturbations for the solar wind and F10.7 index (compare Figure 8.5a and Figure 8.5b), the correlations between neutral mass density and the mass fractions of the neutral species are much lower. However, there are still substantial negative correlations between neutral mass density and the neutral, ion and electron temperatures. Since the neutral temperature stands in the denominator in Equation 7.6, neg-

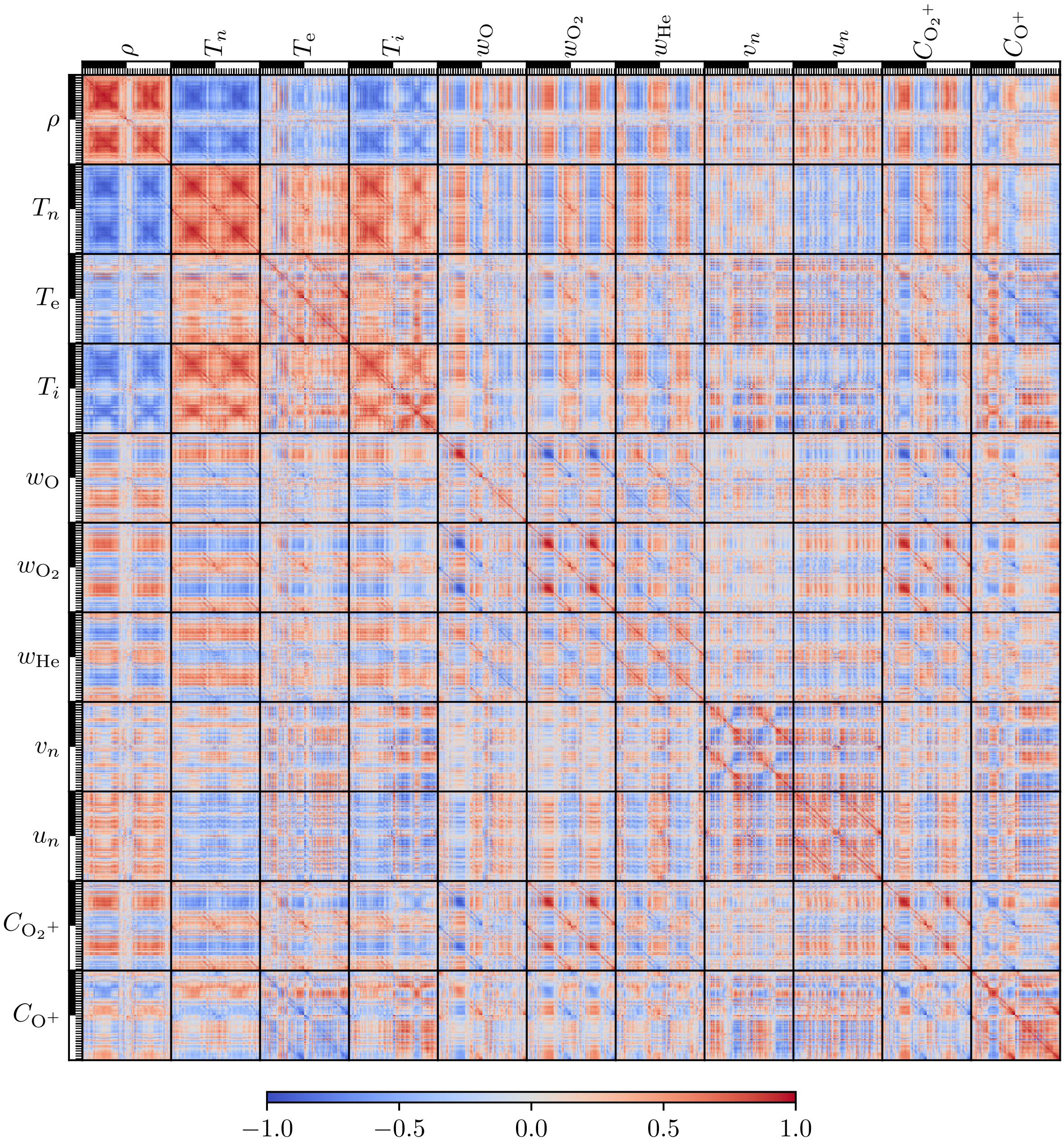

Figure 8.4.: This figure shows (a subset of) the correlation matrix of the forecasted state for the configurations P 4 (Table 8.1), which is the same configuration P 3, but Earth magnetic field is perturbed additionally. The matrix is explicitly computed from an ensemble with 96 members via Equations 6.28 and 6.20 at 27 March 2010 00:00 UTC+0 after forwarding the TIE-GCM 5° 10 days. The matrix is singular because $n_e \leqslant n_x$. The entries of the correlation matrix are first sorted by the state variables, which are separated by solid black lines in this figure. The labels are explained in Table 5.3. ρ indicates the total neutral mass density. T_n, T_e, and T_i stand for neutral, electron and ion temperature, respectively. w is the mass fraction, v_n and u_n are horizontal wind velocities and C is the number concentration. Each three-dimensional array holding a state variable was reshaped into a one-dimensional array where longitude changes fastest, followed by latitude and pressure level. The alternating black and white bars next to the labels indicate the pressure levels. Here, only the correlations of the cells at pressure level 2.25 and 6.25, corresponding roughly to 282 km, 472 km geometric altitude, are shown.

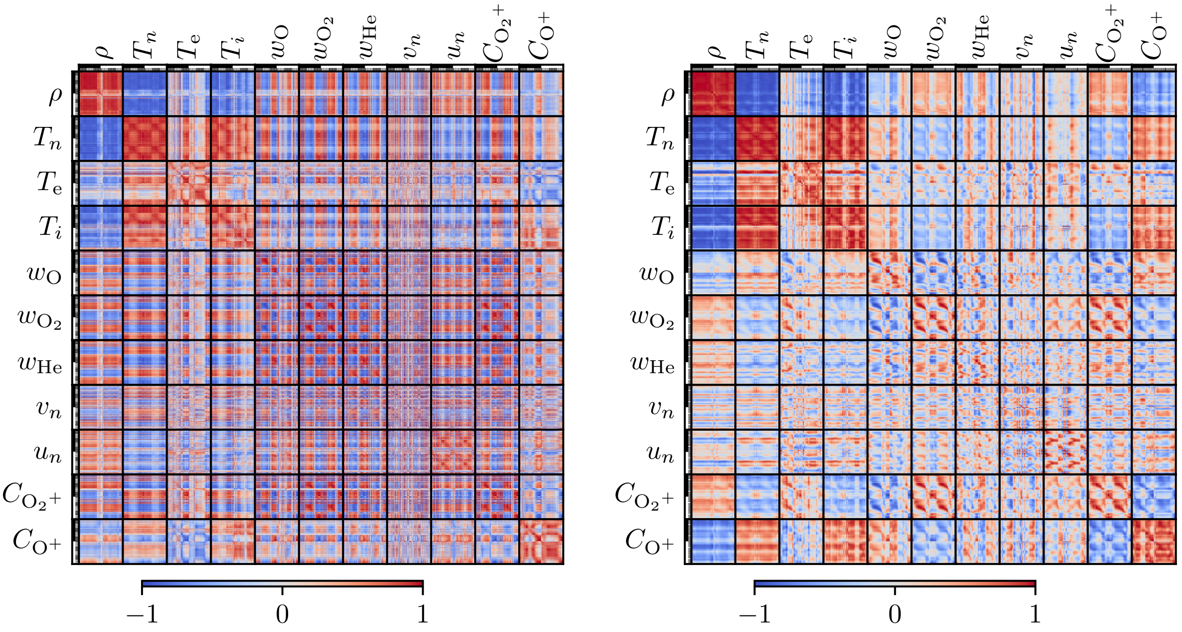

(a) P 1: Static perturbations as used in Corbin and Kusche (2022).

(b) P 2: Same as configuration P 1, but solar wind and F10.7 perturbations are time-variable.

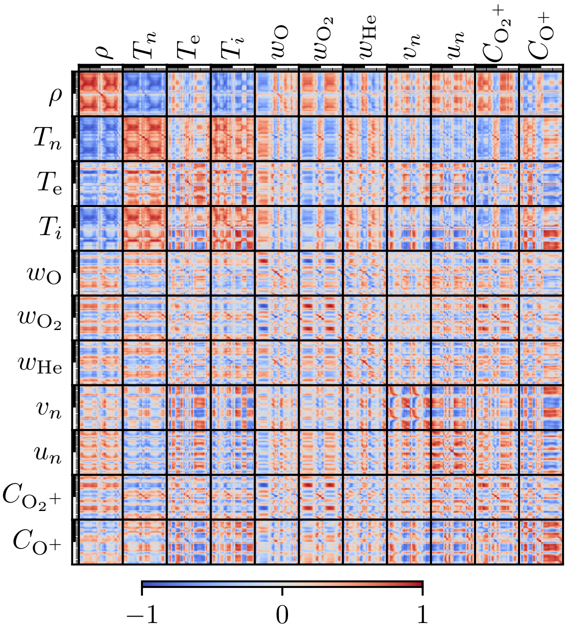

(c) P 3: Same as configuration P 2, but IMF parameters are perturbed additionally.

Figure 8.5.: This figure shows the correlation matrices of the forecasted state for the configurations P 1-P 3 listed in Table 8.1. More information on the illustration is provided in the caption of Figure 8.4.

ative correlations between neutral mass density and temperature are expected. However, the correlations are almost equal to negative ones for all grid cells in Figure 8.5b. The correlations between neutral mass density and the temperatures are reduced when using the complete set of perturbations (Figure 8.4, P 4), The correlation between neutral temperature and ion temperature is also significantly reduced. The static perturbation of $|B_\oplus|$ does not affect the considered correlation visibly (compare Figure 8.5c and Figure 8.4). However, it affects the standard deviation of the model forecast. For example, the neutral mass density is up to 20 % larger when perturbing Earth's magnetic field.

On the basis of these results, I use Configuration P 4 as the default choice for generating the perturbations in this thesis since it best reflects the forecasted state's uncertainty. For this configuration, the correlations between state variables at the same grid cell (diagonals of sub matrices in Figure 8.4) are illustrated with world maps in Figure D.2. The neutral temperature correlates negatively with the neutral mass density almost everywhere. At the pressure level around 472 km, the atomic oxygen mass fraction is highly correlated with the neutral mass density almost everywhere. This altitude is very close to the peak of atomic oxygen mass fraction (see Figure 2.5). The correlation is lower and partly negative at the lower pressure level located at 282 km. The correlation between electron number density and neutral mass density is almost identical to that between atomic oxygen ion number density and neutral mass density because of the assumption of a quasi-neutral atmosphere implemented in the TIE-GCM.

8.3. Open Loop Simulations

OLSs are conducted for analyzing the state ensemble without assimilating any data and for comparison with data assimilation results.

Figure 8.6 shows the external forcings driving the TIE-GCM and the corresponding standard deviations for two periods with different geomagnetic activity. In addition, the first four univariate central moments (see Section 6.1.2) of neutral mass density and electron number density computed from 96 ensemble members are shown. As expected, an elevated standard deviation in the external forcings also increases the standard deviation in the neutral mass and electron number densities. During the geomagnetic storm, skewness and excess kurtosis of neutral mass density deviate significantly from zero, especially at low latitudes, indicating a non-Gaussian distribution of the state during that period. The state vector must follow a Gaussian distribution for the Kalman filter to provide the optimal estimate. When the Kalman filter is applied to non-Gaussian states, the update step can still improve the state estimate; however, then the

Setup 3: Open loop simulation (OLS)

general

type	open loop
TIE-GCM setup	5°, Setup 1
start	27 Mar 2010 00:00 UTC+0
end	10 Apr 2010 00:00 UTC+0
writing frequency	every 10 minutes

ensemble

ensemble size	96
perturbations	time-variable (P 4, Table 8.1)

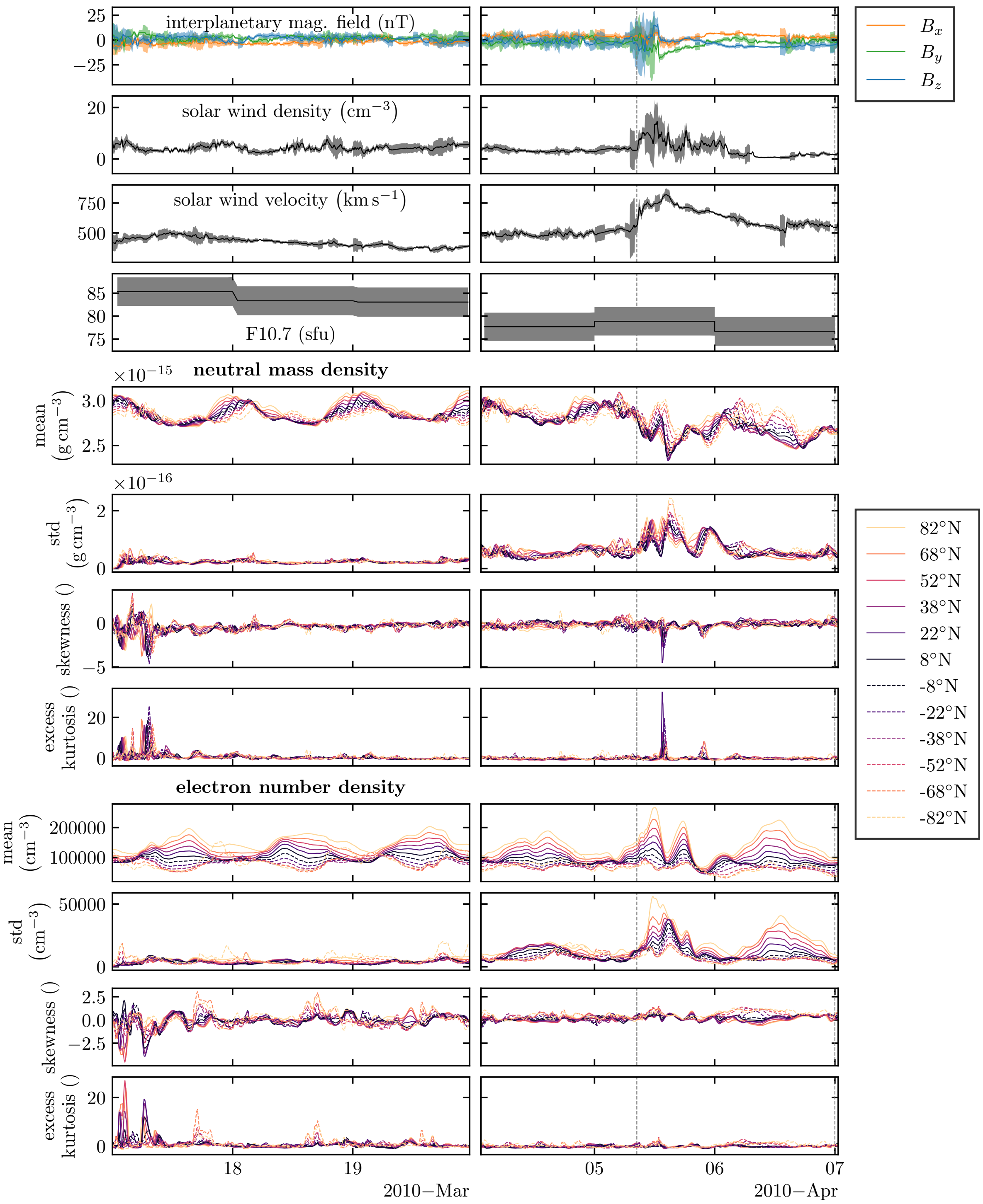

Figure 8.6.: The left column shows the first three days of the spin-up phase, and the right column three days of the OLS including the 5 April geomagnetic storm, indicated by dashed vertical lines. The first four rows contain the mean values and standard deviations of the sampled external forcings time series described in Section 7.2.1. The solid lines correspond to the mean value. The transparent areas correspond to the three sigma environment. The statistics about neutral mass density (rows 5-8) and electron number densities (rows 9-12) were computed from Setup 3 (96 members). The statistical moments plotted here are introduced in Section 6.1.2. For this plot, the densities at the Greenwich meridian at pressure level 3.5 (∼300 km) are shown. Different latitudes are indicated by color and line style (see legend).

updated state does not minimize Equation 6.47. Particle filters do not assume that the state vector follows a Gaussian distribution and hence may enable better state estimates for a state containing higher statistical moments. However, particle filters have sometimes reported to suffer from particle degeneracy (e.g., Kuptametee and Aunsri, 2022), especially for high dimensional problems. As particle filters are further developed to address high dimensional problems (e.g., van Leeuwen et al., 2019) they should be considered in future studies.

In Figure 8.7 different mass density time series along the orbits of CHAMP and GRACE are compared pairwise using 2D histograms. Both axes of each panel refer to the mass density of the corresponding time series, and the color indicates the frequency. Two time series would ideally agree if all data were on the diagonal cyan line. If the data in the bins is not symmetrical w.r.t. the diagonal line, there is a bias between both time series. In the following discussion, the median of the relative differences between two time series (median($\frac{\rho_1-\rho_2}{\rho_1}$)) is used to quantify the similarity of two time series.

Comparison of OLS and reference run The reference run is the single instance run of the TIE-GCM without any perturbation using Setup 1. The relative difference between the OLS and the reference run with 5° horizontal resolution are on average 2 % and 4 % for CHAMP and GRACE, respectively, indicating that the perturbations of the model inputs add a slight bias to the mass density simulation. This can also be seen in the corresponding histograms in panels e and m of Figure 8.7. The densities of the OLS are systematically larger than those of the reference run. Figure D.3 compares the OLS and reference run for different ensemble sizes. The results do not change significantly for ensembles with more than ten members. For an ensemble size of 96, the OLS to reference run ratio is on average 99.998 % for the neutral temperature and 102.6 % for the mass density.

Comparison of OLSs with $2.5°$ and $5.0°$ horizontal resolution For both satellites the TIE-GCM OLSs with 2.5° and 5° resolution produce similar results (histogram in panels f and n). For GRACE, the neutral mass densities of the 2.5° OLS are on average 3.6 % larger than the densities of the 5° OLS. The average relative difference between simulated and accelerometer-derived densities is reduced from −17 % to −13 %, when using 2.5° OLS instead of 5° OLS. For CHAMP, the neutral mass densities of the 2.5° OLS are on average 1 % larger than the densities of the 5° OLS. The average relative difference between simulated and accelerometer-derived densities is increased from 0.6 % to 2 % when using 2.5° OLS instead of 5° OLS. This effect is barely visible when comparing panels a and b.

Comparison of NRLMSIS 2.0 with accelerometer-derived densities Comparing the calibrated (Section 7.6.1) and uncalibrated NRLMSIS 2.0 with the accelerometer-derived densities, it becomes visible that the calibration reduces the bias for CHAMP (compare panels c and d). The effect of the calibration for the GRACE satellite is not as effective (compare panels k and l). For GRACE, panels i, j, and k show that the mass densities of the TIE-GCM and NRLMSIS 2.0 are systematically lower than the accelerometer-derived densities. Since both models are similarly affected, there might be a bias in the GRACE accelerometer-derived densities. This is in accordance with S. M. Codrescu et al. (2018) and Matsuo et al. (2012) who also report a

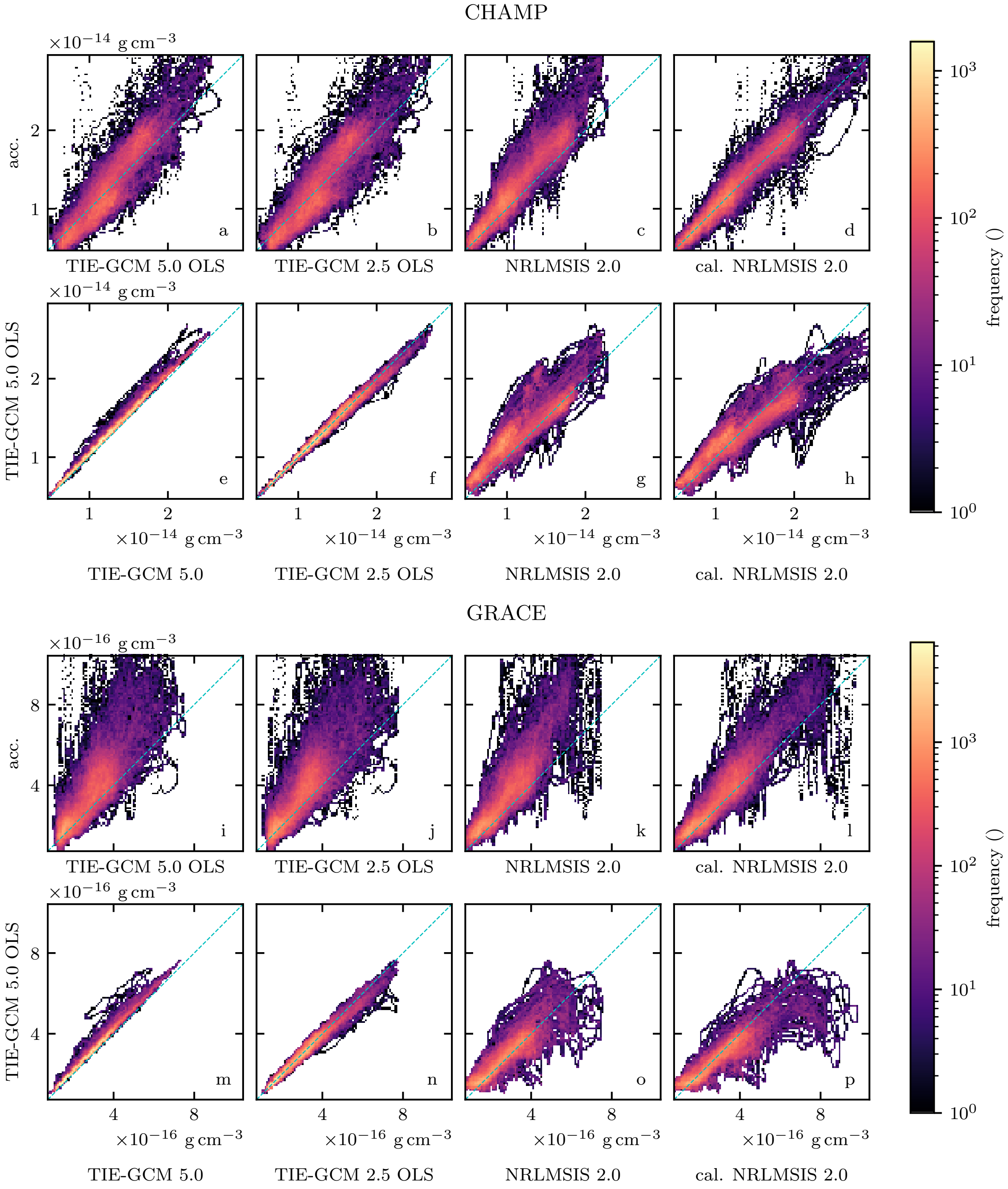

Figure 8.7.: Comparison of neutral mass densities from models and observations along the orbit of CHAMP (a-h) and GRACE (i-p) from 27 March 2010 00:00 UTC+0 to 10 April 2010 00:00 UTC+0. The OLS was performed according to Setup 3 for both model resolutions. The reference TIE-GCM run employed Setup 1. The TIE-GCM densities were written every 10 minutes and interpolated to the temporally higher resolved accelerometer-derived densities. The NRLMSIS was calibrated following Section 7.6. The mass densities were derived from the accelerometers as summarized in Section 4.1. The pairs of time series in each panel would agree ideally if all data were on the dashed cyan line.

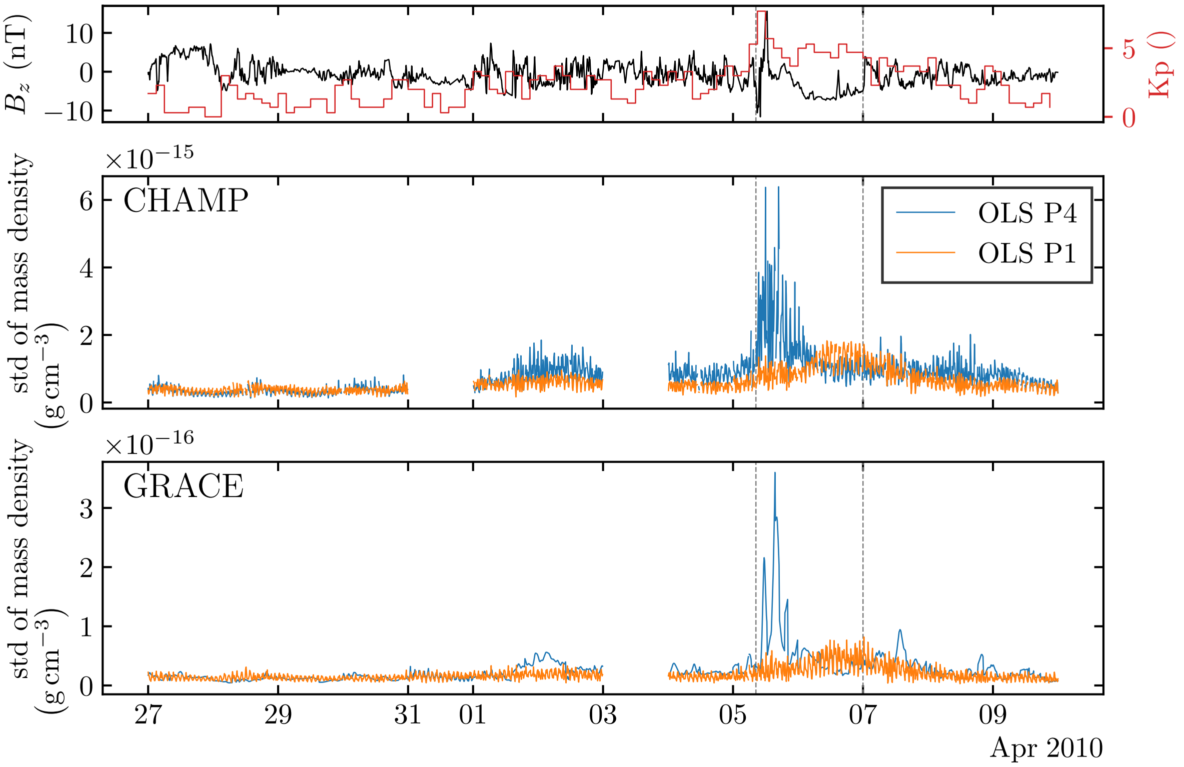

Figure 8.8.: The ensemble spread of the mass density characterized by the standard deviation is shown for CHAMP and GRACE. I suspect that the smoother GRACE time series is related to the B-spline extrapolation from the model grid to the position of the satellite. The z-component of the IMF in GSM frame and Kp time series are given in the upper panel to indicate the geomagnetic activity. The left dashed vertical line indicates the onset of the 5 April 2010 geomagnetic storm, and the right line indicates the beginning of the recovery phase according to Sheng et al. (2017).

bias between GRACE and CHAMP. Additionally, the model was only calibrated using neutral mass densities from CHAMP and not from GRACE. From this follows the expectation that the assimilation of calibrated data within the two-step approach works better for CHAMP than GRACE.

Comparison of OLS with static and time-variable perturbations The standard deviations of the modeled mass density–indicating the ensemble spread–of the OLSs employing static and time-variable perturbations are plotted in Figure 8.8 along the orbits of GRACE and CHAMP. The upper panel in Figure 8.8 shows the Kp index and z-component of the IMF in GSM frame to indicate the geomagnetic activity. The onset and end of the 5 April 2010 geomagnetic storm are marked with vertical dashed lines. The characteristics of the standard deviations are similar for both satellites. Three days before the geomagnetic storm, during the first half of the storm, and the recovery phase, the standard deviation of the TIE-GCM is underestimated by the static setup (orange line) when compared with the time-variable setup (blue line). The delay between the storm's onset and the peak of the standard deviation is small for the time-variable setup. In contrast, the static setup reaches the highest ensemble spread during the second half of the storm.

Setup 4: Direct Assimilation of Mass Densities (D 01)

general

type	assimilation run
TIE-GCM setup	5°, Setup 1
start	27 Mar 2010 00:00 UTC+0
end	10 Apr 2010 00:00 UTC+0
writing frequency	every 60 seconds

ensemble

initial state	Setup 2
ensemble size	96
perturbations	time-variable (P 4, Table 8.1)
state vector	w_{O}, $w_{\mathrm{O_2}}$, w_{He}, T_n, u_n, v_n, $w_{\mathrm{O}}{}'$, $w_{\mathrm{O_2}}{}'$, $w_{\mathrm{He}}{}'$, $T_n{}'$, $u_n{}'$, $v_n{}'$

filter

filter	localized ESTKF
forget factor	1.0
forecast duration	60 s

localization

sub-domain size	3x3x3 cells
horizontal localization radius	5000 km
vertical localization radius	500 km
weight function	$\mathrm{GC}_{a=0.5}(\tau)$

observation

domain	satellite orbit of CHAMP
quantity	neutral mass density
uncertainty	5 % of neutral density
interpolation	cubic B-Spline

8.4. Assimilation of Accelerometer-Derived Mass Densities

Two methods for the assimilation of accelerometer-derived mass densities into numerical models are discussed. First, the direct assimilation of along-track densities (Section 4.1). Second, the two-step approach (Section 7.6). It uses the along-track densities to calibrate a (semi-)empirical model, which is globally evaluated and then assimilated into the numerical model. In this section, the accelerometer-derived mass densities along the orbits of CHAMP and GRACE from an updated version of Vielberg et al. (2021)[1] are used.

8.4.1. Direct Assimilation

The reference setup for direct assimilation of mass densities is summarized in Setup 4. Some settings were varied and are listed in Table 8.2. However, a multidimensional grid search for tuning the assimilation setup is computationally expensive. Therefore, only one setting of Setup 4 is varied at once, while all others are fixed.

Table 8.2 provides for each experiment the median of the difference between the accelerometer-derived mass densities ρ^{acc} and the densities ρ^{assim} estimated by the assimilation run along the orbit of CHAMP and GRACE. The table also provides the RMSE of modeled and observed mass densities computed as

$$\mathrm{RMSE} = \sqrt{\frac{1}{n}\sum_{i=1}^{n}\left(\rho_i^{\mathrm{assim}} - \rho_i^{\mathrm{acc}}\right)^2}, \tag{8.1}$$

with n along track observations.

---

[1] The dataset contains only NaNs for CHAMP during March 2010. This gap was closed in the new version.

Table 8.2.: The reference setup is given in Setup 4 and corresponds to the experiment in the first row. Settings that differ from the reference setup are highlighted by a light gray background. σ denotes the standard deviation of the observations in percent of the neutral mass density. The computation of $\rho^{\text{assim}} - \rho^{\text{acc}}$ uses the TIE-GCM output with a resolution of one minute. The RMSE is computed from Equation 8.1. The perturbation setups are summarized in Table 8.1 and are used for the spin-up and assimilation phase.
The values in each column containing statistics on the differences are mapped to color values to visualize them. The colors can only be used to compare values within the same column. For columns containing the median difference, a white cell indicates that the differences are zero on average. The bluer the cell, the greater the observed mass density relative to the simulated density. The redder the cell, the greater the simulated mass density relative to the observed density. The cell with the corresponding column's smallest RMSE is also white. The more orange the cell, the greater the RMSE.

								$\rho^{\text{assim}} - \rho^{\text{acc}}$			
	TIE-GCM	localization radius						median $(\mathrm{g\,cm^{-3}})$		RMSE $(\mathrm{g\,cm^{-3}})$	
ID	resolution	horizontal	vertical	satellites	σ	perturbations	wind	CHAMP	GRACE	CHAMP	GRACE
D 01	5.0°	5000 km	500 km	CHAMP	5 %	P 4	yes	-2.4e-17	-5.1e-17	1.5e-15	1.3e-16
D 02	5.0°	5000 km	500 km	CHAMP	10 %	P 4	yes	-9.2e-17	-5.3e-17	1.8e-15	1.3e-16
D 03	5.0°	5000 km	500 km	CHAMP	15 %	P 4	yes	-1.0e-16	-5.2e-17	2.0e-15	1.3e-16
D 04	5.0°	5000 km	500 km	CHAMP	2 %	P 4	yes	6.0e-17	-4.3e-17	1.1e-15	1.2e-16
D 05	5.0°	5000 km	125 km	CHAMP	5 %	P 4	yes	3.7e-17	-4.5e-17	1.9e-15	1.2e-16
D 06	5.0°	5000 km	250 km	CHAMP	5 %	P 4	yes	-5.1e-18	-4.9e-17	1.6e-15	1.3e-16
D 07	5.0°	5000 km	750 km	CHAMP	5 %	P 4	yes	-2.0e-17	-5.1e-17	1.5e-15	1.3e-16
D 08	5.0°	2500 km	500 km	CHAMP	5 %	P 4	yes	-3.1e-17	-5.2e-17	1.6e-15	1.3e-16
D 09	5.0°	10 000 km	500 km	CHAMP	5 %	P 4	yes	-4.6e-18	-4.5e-17	1.5e-15	1.2e-16
D 10	5.0°	global		CHAMP	5 %	P 4	yes	-2.3e-16	-3.4e-17	1.8e-15	9.6e-17
D 11	5.0°	5000 km	500 km	GRACE	5 %	P 4	yes	1.0e-15	-7.3e-18	2.5e-15	6.9e-17
D 12	5.0°	5000 km	500 km	CHAMP+GRACE	5 %	P 4	yes	1.3e-16	-2.7e-17	1.6e-15	8.7e-17
D 13	5.0°	5000 km	500 km	CHAMP	5 %	P 1	yes	-1.5e-16	-5.8e-17	1.7e-15	1.4e-16
D 14	5.0°	5000 km	500 km	CHAMP	5 %	P 4	no	-5.3e-17	-5.3e-17	1.5e-15	1.2e-16
D 15	2.5°	5000 km	500 km	CHAMP	5 %	P 4	yes	-4.9e-18	-4.7e-17	1.5e-15	1.2e-16
D 16	5.0°	global		CHAMP	5 %	P 1	yes	-2.6e-16	-4.3e-17	1.9e-15	1.1e-16
OLS	5.0°					P 4		7.0e-17	-4.1e-17	2.3e-15	1.3e-16

Figure 8.9 shows how the differences between accelerometer-derived mass densities and mass densities from assimilation experiments along the orbits of CHAMP and GRACE are distributed. Each panel contains experiments in which the same setting was varied. The OLS and reference experiment D 01 are shown in all panels.

Specifying the uncertainty of the observations is crucial for data assimilation. The Kalman filter represents the uncertainty of the observations by a VCM. However, many accelerometer-derived density data sets do not provide the corresponding standard deviations and correlations. Recently, Siemes et al. (2024) developed an error propagation method for accelerometer-derived mass densities and applied it to GRACE. They found that the standard deviations obtained from error propagation are 5 % - 20 % of the density for GRACE during low solar activity and about 4 %-4.5 % of the density for high solar activity. Unfortunately the error propagation has not been applied to the CHAMP mission, yet. However, an earlier study by S. Bruinsma and Biancale (2003) found 15 % - 25 % for the accelerometer-derived mass densities from CHAMP by comparing them with an semi-empirical model. Here, I use a fixed percentage for the assimilation specified for each experiment in the column denoted with σ in Table 8.2. However, if available, data sets that provide uncertainty at every time step should be used for future experiments. Considering the experiments with varying uncertainty of the accelerometer-derived mass densities (experiments D 01 - D 04, Table 8.2), the experiment with the lowest RMSE (Equation 8.1) for CHAMP is the one assuming the lowest standard deviation for the densities derived from the CHAMP accelerometer (see also Figure 8.9a). However, one cannot use the observation uncertainty to tune the filter: When the standard deviation of the observations is decreased until the update step reproduces the observations perfectly, data assimilation becomes obsolete. In this case, one can use the observations directly without all the effort data assimilation requires. Ideally, the observations are provided with realistic uncertainties. By reason of the localization, the modeled neutral mass densities along the orbit of GRACE are less influenced by the update step and not well suited for assessing filter's performance. Still, meaningful comparisons can be conducted for experiments if they use the same standard deviations for the observations. I use a somewhat optimistic value of 5 % for the standard deviation of the accelerometer-derived mass density for the remaining experiments.

The choice of the vertical localization radius greatly influences the assimilation results (Figure 8.9b). While the difference between a vertical localization radius of 750 km (D 07) and 500 km (D 01) is barely visible, shorter vertical radii (D 05 and D 06) perform worse along the orbit of CHAMP (more considerable bias and RMSE). Within the investigated range between 2500 km (D 08) and 10 000 km (D 09), a larger horizontal localization radius leads to a lower bias along the orbit of CHAMP. The RMSE is barely affected.

The experiment employing the global ESTKF (no localization is applied, D 10) has a lower RMSE than the OLS along the orbit of CHAMP. However, it cannot reach the improvements of the localized version along CHAMP's orbit (Figure 8.9c). During the experiment, GRACE flies about 200 km above CHAMP, and the localization restricts updates of model cells this far from CHAMP. In contrast to the localized filter (D 01), the global filter (D 10) corrects the densities along the orbit of GRACE and performs better than the OLS. Over the entire duration of the experiment, the RMSE along the orbit of GRACE is reduced by 26 % compared with the

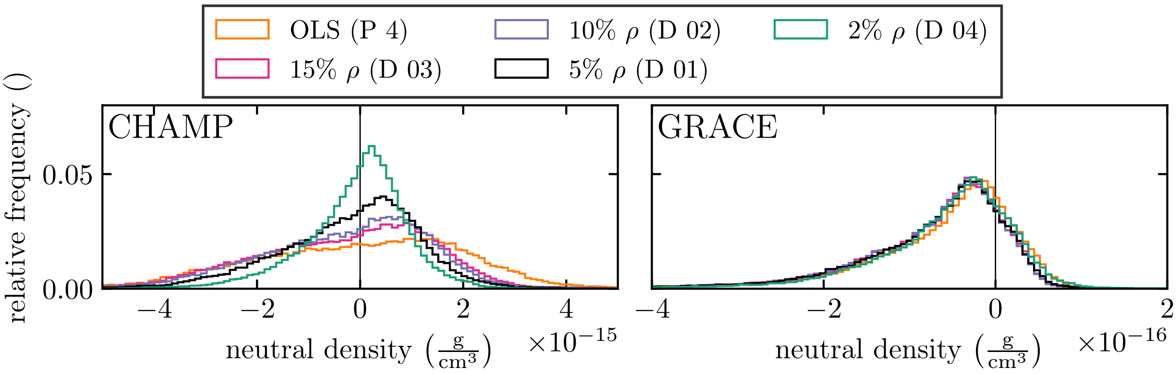

(a) Comparison of different standard deviations for observations.

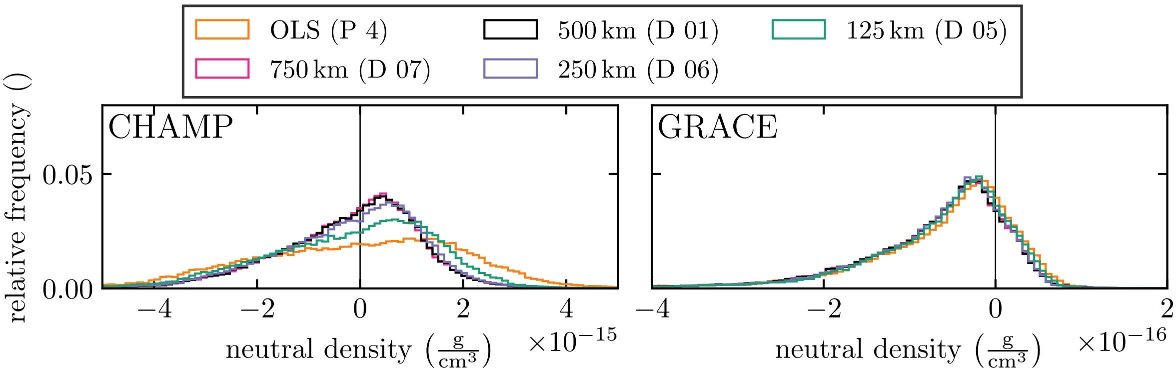

(b) Comparison of different vertical localization radii.

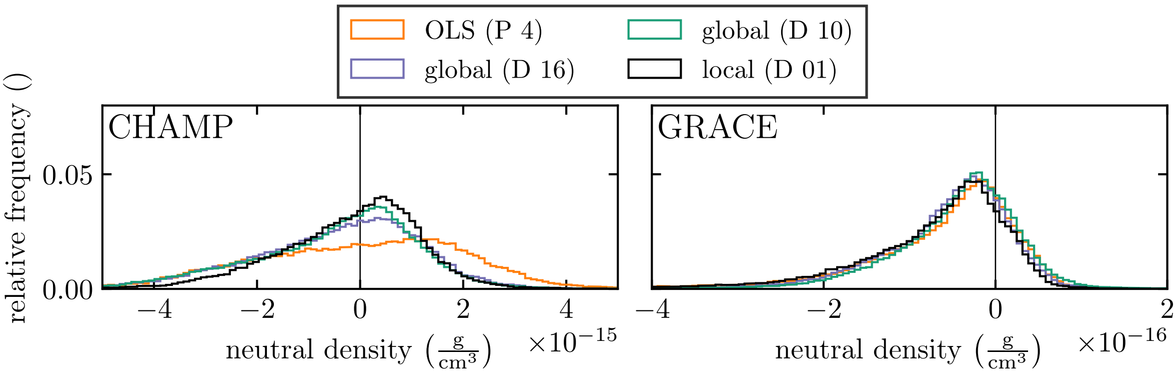

(c) Comparison of global and localized filter.

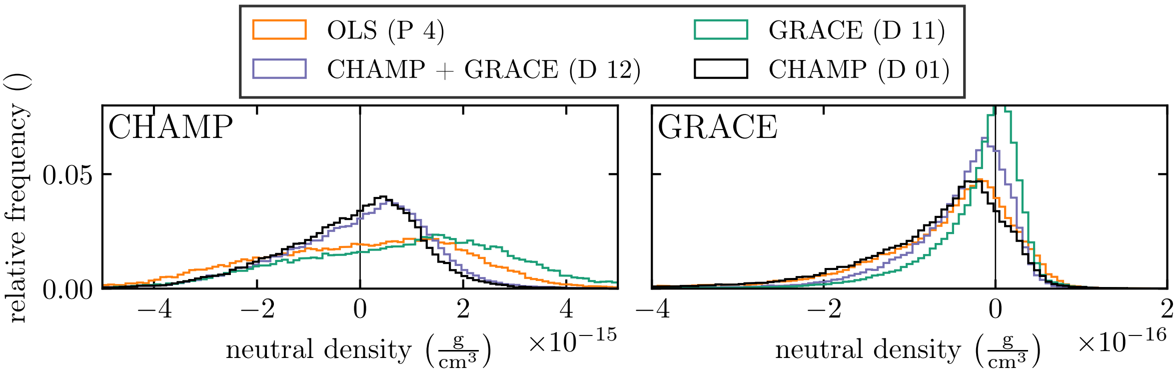

(d) Comparison of assimilated satellite missions.

Figure 8.9.: Histograms of mass density differences between TIE-GCM runs and derived from accelerometers. OLS (orange line) was computed according to Setup 3. The number in brackets corresponds to the experiments listed in Table 8.2. The reference assimilation run (D 01) is the black line in all panels.

reference D 01. The median difference between observations and simulations is reduced by 33 % when comparing with the reference D 01. During the storm, the mass density simulations of the global filter (D 10) are much closer to observations than the OLS (Figure 8.11), especially along the orbit of GRACE. There are some pronounced peaks in the GRACE time series of the global filter that do not occur (so elevated) in the observations, the localized filter (D 01) or the OLS, for example, at 7:55, 8:50, 10:30, or 12:15. At these points in time, GRACE flies above one of the poles.

Although spatial long-range spurious correlation in the forecasted ensemble matrix could be significantly reduced by introducing time-variable external forcing perturbations (Section 8.2), it is unlikely all have been eliminated. In Figure 8.10, the global ESTKF (D 10) is compared with its localized counterpart (D 01). The difference between the mass density of the corresponding experiment and the OLS at about 350 km altitude are shown side-by-side. While some regions show comparable behavior, the global filter has regions that seem incredible when compared with the localized filter, for example, in the south of Africa at 4:30 or North America at 9:00. Despite these effects visible in the world maps, the global filter produced convincing updates when looking at the density time series along the orbit of GRACE, especially during the geomagnetic storm (Figure 8.11).

Both CHAMP and GRACE fly in almost polar orbits. But in April 2010 GRACE flies about 175 km above CHAMP (Figure 8.11) and the right ascensions of the ascending nodes are wrapped by about 129° during the period of the experiment. The horizontal distances between both satellites projected on Earth's surface are plotted in Figure 8.11 c.

In experiment D 11 accelerometer-derived mass densities from GRACE are assimilated instead of accelerometer-derived mass densities from CHAMP. In experiment D 12 the accelerometer-derived mass densities from CHAMP and GRACE are assimilated simultaneously. Figure 8.9d compares the simultaneous assimilation with the assimilation of only one satellite mission. When assimilating only one satellite mission (D 01, D 11) the mass densities along the other mission are barely influenced due to localization. However, the differences along the orbit of the mission that is not assimilated have a larger bias than the OLS run (see Figure 8.9d). When both satellite missions are assimilated simultaneously (D 12), the differences to the observations for both satellites are much lower than for the OLS. When the satellites are considered in isolation, the assimilation run in which only the corresponding satellite was assimilated outperforms the simultaneous assimilation experiment, especially in the case of GRACE. Compared with the OLS the RMSE is reduced by 35 % for CHAMP (D 01) and 47 % for GRACE (D 11) when assimilated alone. Figure 8.11 shows the mass density along the orbits of CHAMP and GRACE from the simultaneous assimilation experiment (D 12) during a geomagnetic storm. It is close to the accelerometer-derived densities but does not follow every peak of the observations, for example, at 13:30 for GRACE. It would be interesting to find out whether the observations are erroneous and the model more accurately predicts the atmosphere in these situations or whether the model fails to account for specific effects captured by the accelerometer-derived mass densities.

For the assimilation of mass densities the minimal configuration of the state vector includes the neutral composition and the neutral temperature (see also Section 7.3). However, one can

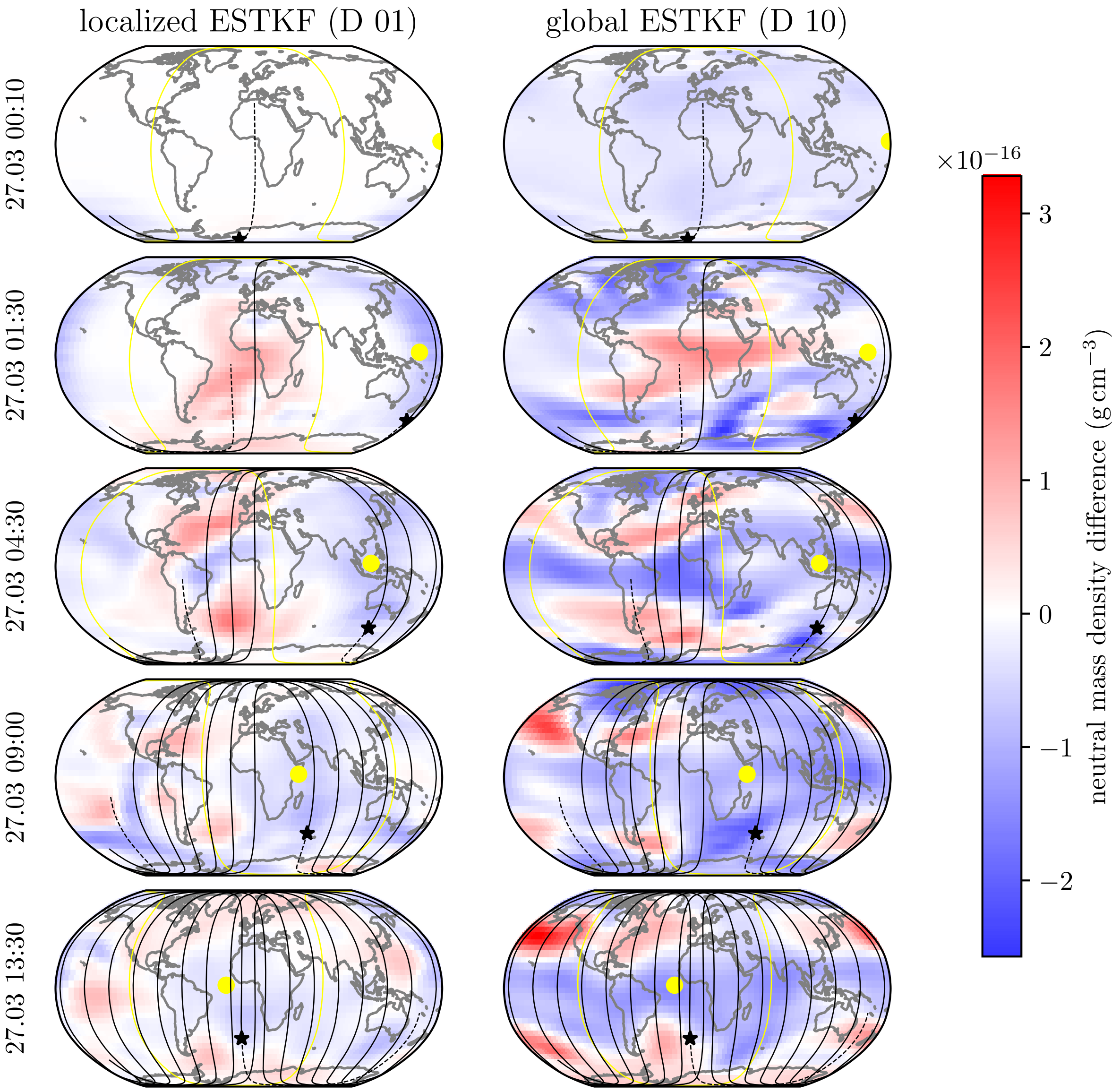

Figure 8.10.: Comparison of a local filter (experiment D 01 in Table 8.2) and a global filter (experiment D 10 in Table 8.2). All maps show the difference between the corresponding assimilation run and the OLS (Setup 3) at pressure level 3.75 (~350 km). The black star marks the position of CHAMP. The solid black line is the ground track of CHAMP since the first analysis step. The dashed line is the future orbit. The yellow dot shows the position of the Sun, and the solid yellow line is the solar terminator.

append the state vector by additional prognostic state variables (see Table 5.3) that are not required in the observation operator but are updated based on the correlations encoded in the forecasted ensemble, nevertheless. The horizontal components of the neutral wind velocity are included in the state vector for all but one experiment listed in Table 8.2. This is done as not including the horizontal wind velocities (D 14) in the state vector doubles the bias along the orbit of CHAMP (compare D 01 and D 14 in Table 8.2). The RMSE is barely affected when the wind velocity is not included.

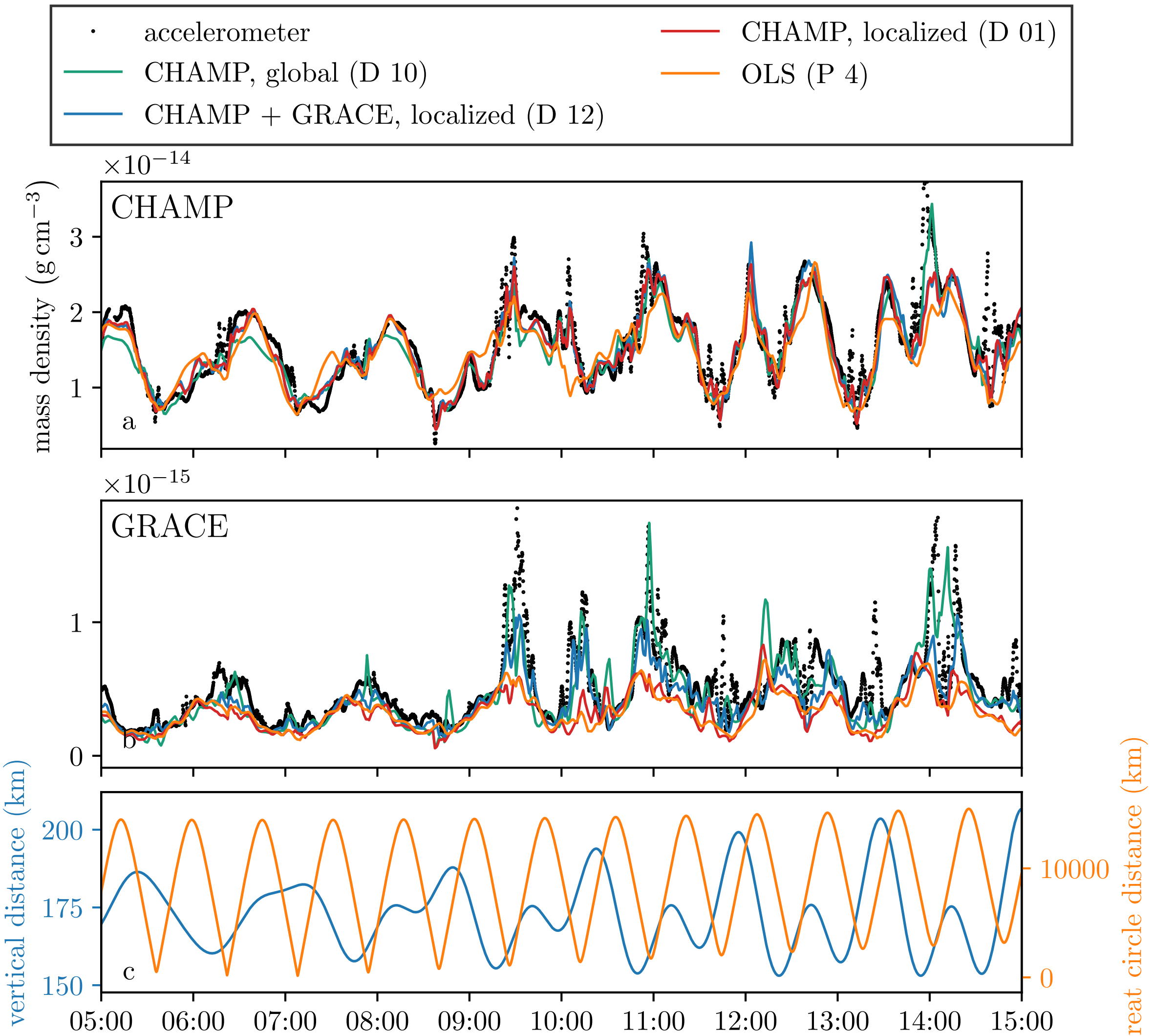

Figure 8.11.: This figure shows time series of mass density along the orbit of CHAMP and GRACE. The solid lines correspond to TIE-GCM runs (Table 8.2). Black dots correspond to densities derived from accelerometers. Panel c shows the vertical and great circle distance on Earth's surface between CHAMP and GRACE. The temporal resolution of the model runs is one minute.

Using the TIE-GCM with 2.5° resolution and eight processor cores per ensemble requires about five times longer than the 5.0° version using four processor cores per ensemble. The bias to the observations along the orbit of CHAMP (D 01 vs D 15) is reduced by a fifth while the RMSE is not affected significantly. Still, I recommend using the 5° version, given the much longer run time of the 2.5° version.

A direct comparison of the density estimates using static and time-variable perturbations can be conducted but does not provide any insights. Since the static perturbations lead to a lower ensemble spread (Figure 8.8), the Kalman filter gives less weight to the observations. Accordingly, experiment D 13 has a larger bias and RMSE than the assimilation run using time-variable perturbations (D 01) for CHAMP and GRACE.

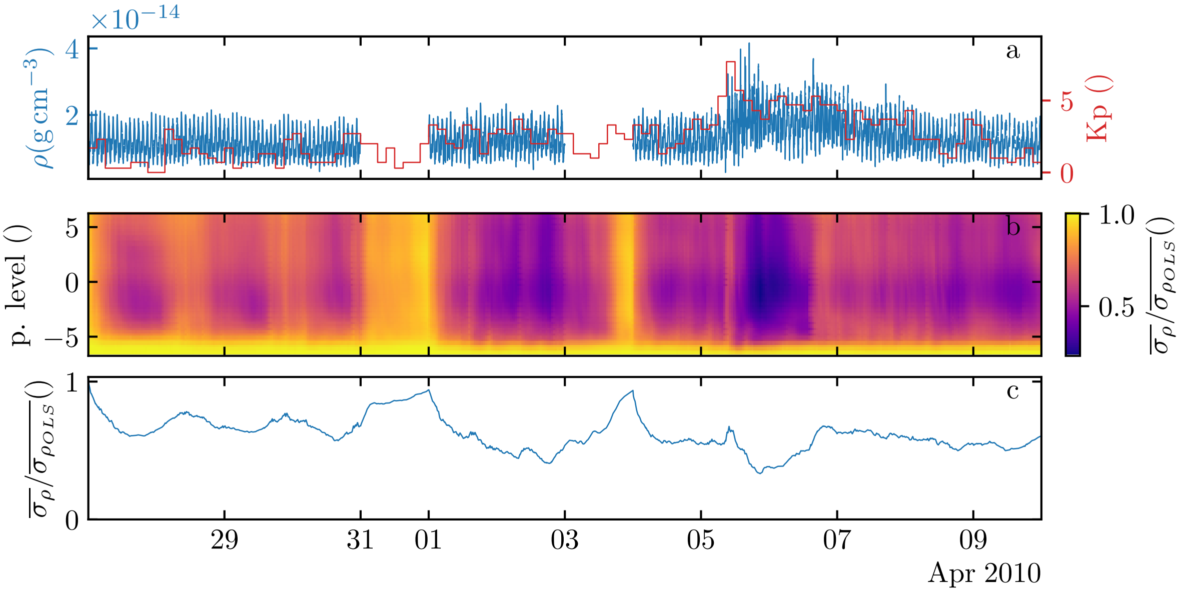

Figure 8.12.: The upper panel shows the mass density derived from CHAMP's accelerometer (blue line) and the Kp index (red line). Each column in panel b is a height profile of the ratio of the average standard deviation of the neutral mass density for experiment D 01 (Setup 4) and the OLS (Setup 3). The average standard deviation at each pressure level is weighted according to Appendix C.4. Panel c shows the median of the average ratio for each point in time.

To ensure that the results do not suffer from filter divergence[1], the ensemble spread of the assimilation run (D 01) is compared with the ensemble spread of the OLS. Figure 8.12 shows in panel a the Kp value to indicate the geomagnetic activity and the accelerometer-derived mass density of CHAMP as its standard deviation is a percentage of itself. For each pressure level and point in time, Panel b shows the averaged mass density standard deviation of experiment D 01 divided by the corresponding averaged mass density standard deviation of the OLS. This illustration shows that the pressure level-wise average standard deviation of the first direct assimilation experiment (D 01) is, at most altitudes, lower than the corresponding standard deviation of the OLS. During data gaps where no data is assimilated (31 March and 3 April), the standard deviation of the assimilation run approaches the standard deviation of the OLS. In the lower horizontal layers, the standard deviations are almost similar. The vertical localization effectively limits the influence of the update step at this altitudes. During the storm, the average standard deviation of the assimilation run is about 50 % of the standard deviation of the OLS. After the geomagnetic storm, the standard deviation increases. Thus, filter divergence is not an issue in the investigated period when using 96 ensemble members.

---

[1] Filter divergence (e.g., Asch et al., 2016, Section 6.5.2) is the consequence of the ensemble size being too small, leading to a (persistent and escalating) underestimation of the forecasted model error covariance. Consequently, the ensemble spread diminishes at each analysis step, while the observations have almost no influence on the state. This can lead to a divergence between the filtered and observed states since the model is almost unconstrained by the observations.

Setup 5: Two-Step approach (T 04)

general

type	assimilation run
TIE-GCM setup	5°, Setup 1
start	27 Mar 2010 00:00 UTC+0
end	10 Apr 2010 00:00 UTC+0
writing frequency	every 10 minutes

ensemble

initial state	Setup 2
ensemble size	96
perturbations	time-variable (P 4, Table 8.1)
state vector	w_{O}, w_{O_2}, w_{He}, T_n, u_n, v_n, $w_{\mathrm{O}}{}'$, $w_{\mathrm{O}_2}{}'$, $w_{\mathrm{He}}{}'$, $T_n{}'$, $u_n{}'$, $v_n{}'$

filter

filter	localized ESTKF
forget factor	1.0
forecast duration	1 h

localization

sub-domain size	3x3x3 cells
horizontal localization radius	5000 km
vertical localization radius	500 km
weight function	uniform

observation

domain	regular grid (Section 7.6)
quantity	neutral mass density from calibrated NRLMSIS 2.0
uncertainty	Corbin and Kusche (2022, Equation 7)
interpolation	cubic B-Spline
weight	1
half-life horizontal weights	∞
half-life vertical weights	500 km

8.4.2. Two-Step Approach

The two-step approach assimilates neutral mass densities located on a global grid that are derived from a calibrated empirical model (NRLMSIS 2.0) and is described in Section 7.6. The grid on which the NRLMSIS 2.0 is evaluated is referred to as *data grid* (a visualization of the grid is provided by Figure 7.5). The reference setup (T 04) is summarized in Setup 5. Table 8.3 summarizes the differences to the reference setup for all two-step assimilation experiments. Since semi-empirical models represent a spatio-temporal average state of the upper atmosphere and the calibration approach (Section 7.6.1) uses a 3 h low pass filter, the two-step approach can only improve the average behavior of the model.

As explained in Section 7.6.2, the data from the empirical model being assimilated is highly correlated. Ignoring these correlations using only a diagonal VCM may lead to too large confidence in the observations. In the event that the observations are highly correlated and the correlations are not taken into account, tuning settings that affect the number of observations considered by the subdomains may lead to unwanted results. This is because including additional observations that are highly correlated with the observations that have already been considered is effectively equivalent to increasing the weights of the observations that have already been included. Examples of these settings are the localization radius and the metric used to measure the distance between observations and subdomains.

The stochastic model for the observations proposed in Section 7.6.2 relies on metric distances and cannot be determined by using the number of cells as a metric. A disadvantage of this metric is that the closer a subdomain is located at one of Earth's poles, the more observations

Table 8.3.: The reference setup is given in Setup 5 and corresponds to the experiment in the first row. Light gray highlights the settings that differ from the reference setup. The color schema applied to illustrate the differences is described in Table 8.2. A uniform weighting means observation localization is not applied. The computation of $\rho^{\text{assim}} - \rho^{\text{acc}}$ uses the TIE-GCM output with a resolution of 10 minutes. The RMSE is computed from Equation 8.1.

			$\rho^{\text{assim}} - \rho^{\text{acc}}$			
			median ($\mathrm{g\,cm^{-3}}$)		RMSE ($\mathrm{g\,cm^{-3}}$)	
ID	weight	$\boldsymbol{R}$	CHAMP	GRACE	CHAMP	GRACE
T 04	uniform	diagonal	2.3e-16	-2.4e-17	1.8e-15	8.7e-17
T 05	$\mathrm{GC}_{a=0.5}(\tau)$	diagonal	-5.0e-16	-4.8e-17	2.1e-15	1.1e-16
T 06	uniform	full	-2.8e-15	-1.3e-16	4.5e-15	2.2e-16
T 07	$\mathrm{GC}_{a=0.5}(\tau)$	full	-1.9e-16	-3.9e-17	1.9e-15	9.9e-17
OLS			7.0e-17	-4.1e-17	2.3e-15	1.3e-16

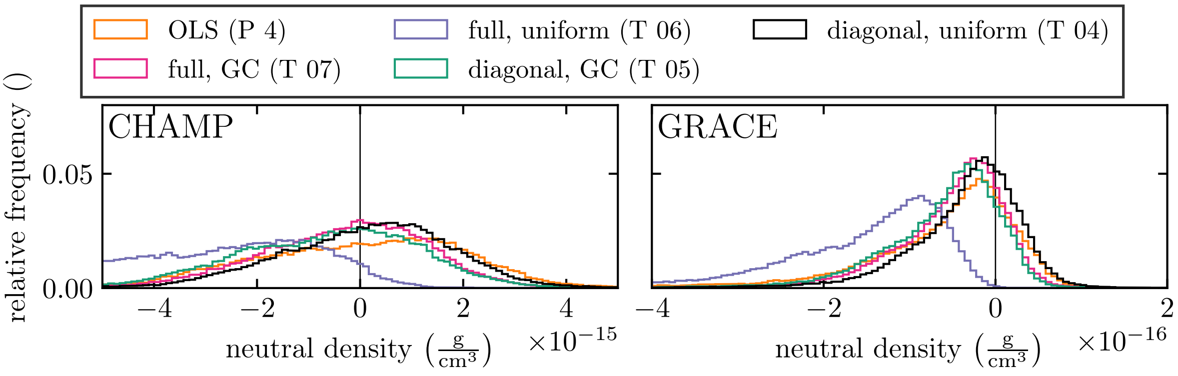

Figure 8.13.: Histograms of differences between TIE-GCM runs and accelerometer-derived neutral densities. The OLS (orange line) was computed according to Setup 3. The identifiers in brackets in the legend correspond to the experiments listed in Table 8.3.

are included. However, at the same time, the stochastic model considers the correlations between the observations, which accounts for this effect.

Figure 8.13 compares assimilation runs with full and diagonal VCM of the observation, denoted by $\boldsymbol{R}$, along the orbit of CHAMP and GRACE. Experiments T 04 and T 05 both use a diagonal VCM $\boldsymbol{R}$. However, experiment T 05 employs observation localization while experiment T 04 uses a uniform weight (no observation localization). When using a diagonal VCM $\boldsymbol{R}$, the median and RMSE of the differences between the assimilation run and the accelerometer-derived densities are larger when applying observation localization (compare T 04 and T 05). This is because observation localization downweights observations, and the filter gives more trust to the model estimate. Using the full VCM $\boldsymbol{R}$ without observation localization (T 06) leads to a large offset between the mass densities from the assimilation run and the accelerometer-derived mass densities (see Figure 8.13). This is likely caused by a flawed inversion: Domain localization (Section 6.4.2) requires for each sub domain the local part of the inverse of $\boldsymbol{R}$ associated with the sub domain. In the implementation, the local part of $\boldsymbol{R}$ is inverted, which is not

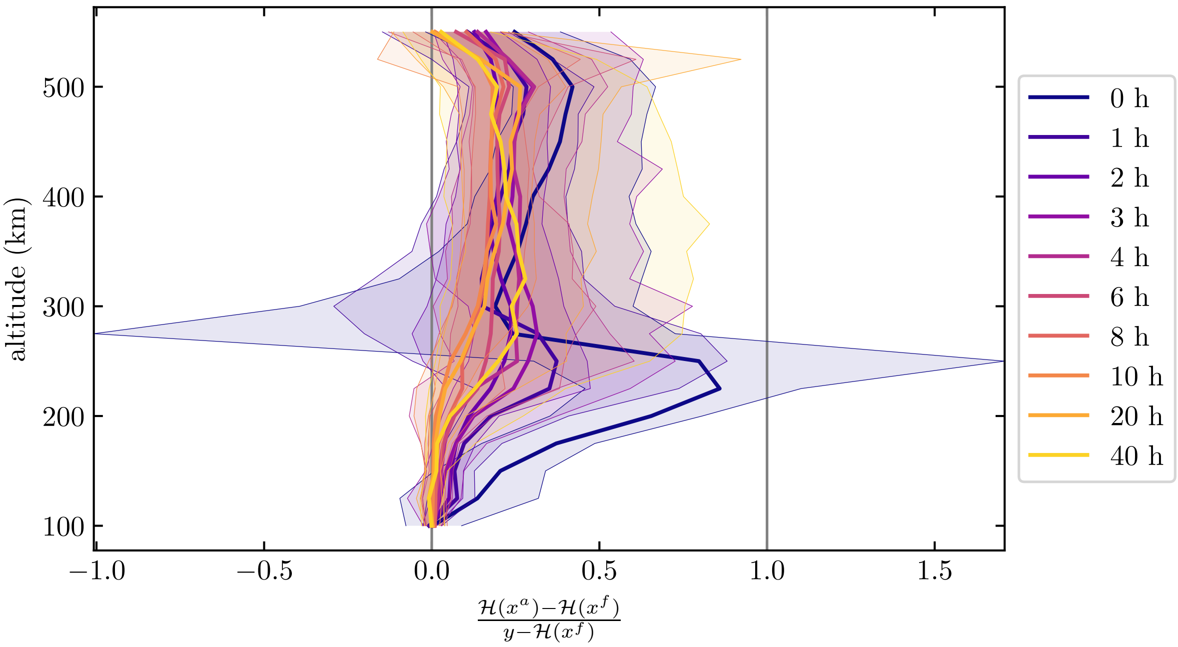

Figure 8.14.: The x-axis shows the innovation update ratio, which is the ratio of the state update in the observation space to the innovation. It measures how much of the innovation is applied in the update step. A value of one indicates that the innovation is fully applied to the forecast. In this case, the state in the observation space is equal to the observation itself. A value greater than one indicates that the update corrects the state beyond the observation. A value of zero indicates that the state is not updated at all. Negative values imply that the update pulls the state further away from the observations. The solid bold line is the median computed over all layers of the data grid at the corresponding color-coded analysis step. The shaded area marks the interval between the 25th and 75th percentile. This figure shows the innovation update ratio for experiment T 07.

equivalent to inverting the complete matrix and then extracting the local part. This error is mitigated by observation localization. Comparing the experiments using observation localization (T 05 and T 07), the experiment using the full VCM $\boldsymbol{R}$ has a lower bias and RMSE w.r.t. the accelerometer-derived densities.

In the following, the experiment using observation localization and the full VCM $\boldsymbol{R}$ is analyzed in more detail. Figure 8.14 shows the innovation update ratio

$$\frac{\mathcal{H}(\boldsymbol{x}^a) - \mathcal{H}(\boldsymbol{x}^f)}{\boldsymbol{y} - \mathcal{H}(\boldsymbol{x}^f)}, \tag{8.2}$$

which measures how much of the innovation is applied to the state for an update step. A ratio of zero indicates that the corresponding state is not updated at all. A ratio of one means that the complete innovation is applied to the forecasted state in the update step. Ratios greater than one indicate overshooting, meaning the update corrects the state beyond the observation. For negative ratios, the state is pushed further away from the observation. For experiment D01, the ratios are between 0 and 1 for most cases, indicating that the update neither overshoots nor

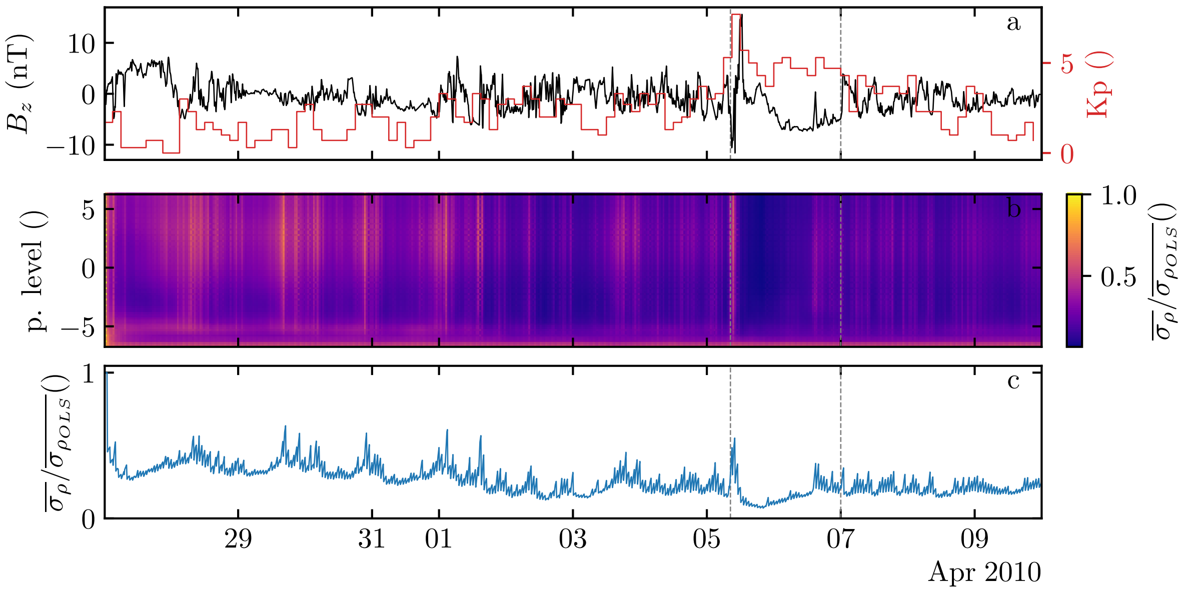

Figure 8.15.: The z-component of the IMF in GSM frame and Kp time series are given in the upper panel to indicate the geomagnetic activity. The left dashed vertical line indicates the onset of the storm, and the right line indicates the beginning of the recovery phase according to Sheng et al. (2017). Each column in panel b is a height profile of the ratio of the average standard deviation of the neutral mass density for experiment T 07 $\overline{\sigma_\rho}$ (Table 8.3) and the OLS $\overline{\sigma_{\rho_{\mathrm{OLS}}}}$ (Setup 3). The average standard deviation at each pressure level is weighted according to Appendix C.4. Panel c shows the median of the average ratio for each point in time.

pulls the state further away from the observations. The ratio is largest for the first update step, especially around 220 km altitude. In the following steps, the ratio becomes lower.

To ensure the experiments do not suffer from filter divergence, the standard deviation of neutral mass density is compared for experiment T 07 and the OLS in Figure 8.15. The ratio of the standard deviation drops instantly after the first analysis step. During the 1-hourly forecast phases the ratio increases. After the onset of the geomagnetic storm indicated by the left vertical dashed line, the ratio first increases rapidly and then decreases again, reaching the minimum value. With decreasing geomagnetic activity, the ratio increases again. Filter divergence is not an issue for the investigated period. However, if the negative trend continues, one should consider increasing the ensemble spread after each update step using a constant inflation factor.

Figure 8.16 compares neutral mass density for selected points in the atmosphere for the first two days of the assimilation phase with quiet conditions. The figure shows the mass densities obtained from the OLS, the assimilation experiment T 07, and the calibrated, and the original NRLMSIS 2.0. Figure D.4 shows the same for the period of the geomagnetic storm hitting Earth on 5 April 2010. After each analysis step, the mass density gradually approaches the OLS. This is explained by the model dynamics, which tend to restore the OLS (see also Figure 7.2). Accordingly, each assimilation step introduces a discontinuity when the state is updated. At the poles, the mass density approaches the OLS more quickly, and the jumps at the update steps (green dots) are particularly large (see panels a-d, q, and r in Figure 8.16). This motivates the co-estimation of model dynamics, as it potentially can reduce those jumps.

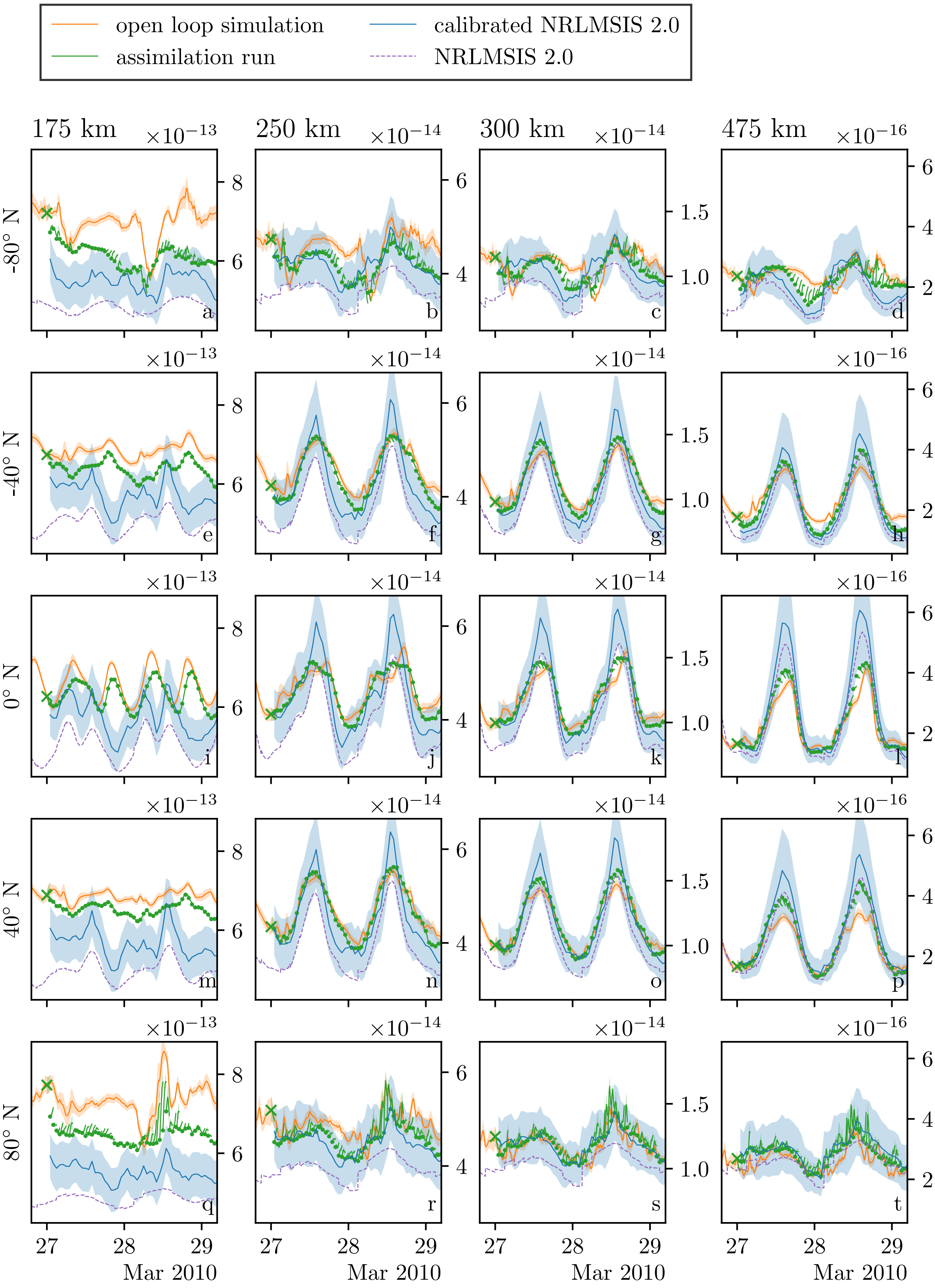

Figure 8.16.: Each panel contains time series of mass density (g cm^{-3}) for different cells of the data grid. Each row corresponds to a geocentric latitude and each column to an ellipsoidal height. The longitude is always 0°E. The panels of each column share the same y-axis. The error bands show the standard deviation. The orange line shows the OLS mass density, the blue line the calibrated NRLMSIS 2.0 mass density (Section 7.6.1) that was assimilated and the green line is the assimilation run.

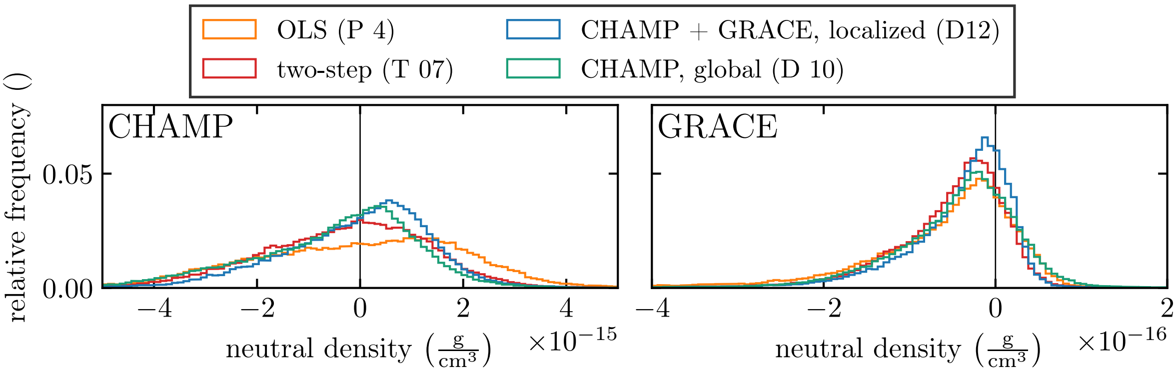

Figure 8.17.: Histograms of differences between TIE-GCM runs and accelerometer-derived neutral densities. The OLS (orange line) was computed according to Setup 3. The identifiers in brackets in the legend correspond to the experiments listed in Table 8.3.

As already explained in Section 8.3, the calibrated NRLMSIS 2.0 has an offset to the mass densities derived from GRACE's accelerometer. Thus, the improvements for the corresponding along track densities are small (Table 8.3).

While the accelerometer derived mass densities do not enter the assimilation direclty as they are used for calibartion of the model, the direct approch useses them direclty without any intermediate steps.

In the two-step approach (Section 7.6), the accelerometer-derived mass densities do not enter the assimilation process directly. Instead, they are used to calibrate the NRLMSIS 2.0, which is subsequently evaluated globally and assimilated. Conversely, the direct approach assimilates the accelerometer-derived mass densities without intermediate steps. In Figure 8.17, the mass density estimates of the two-step and direct assimilation approach along the orbits of GRACE and CHAMP are compared with the corresponding accelerometer-derived mass densities. All selected assimilation runs perform better than the OLS. The simultaneous direct assimilation of both satellites using localization has the smallest spread. However, the localization restricts the updates to the vicinity of the orbits. The two-step approach reliably corrects the model over the two weeks. Considering the entire two-week period, the two-step approach performs better than the global assimilation for GRACE but worse for CHAMP. However, it cannot compete against the direct assimilation approaches (global and localized) during the geomagnetic storm, as shown in Figure 8.18, since the calibrated empirical model has a much lower temporal resolution. Since the two-step approach performs the analysis step less frequently than the direct assimilation (every hour vs every minute), it runs about 40 % faster.

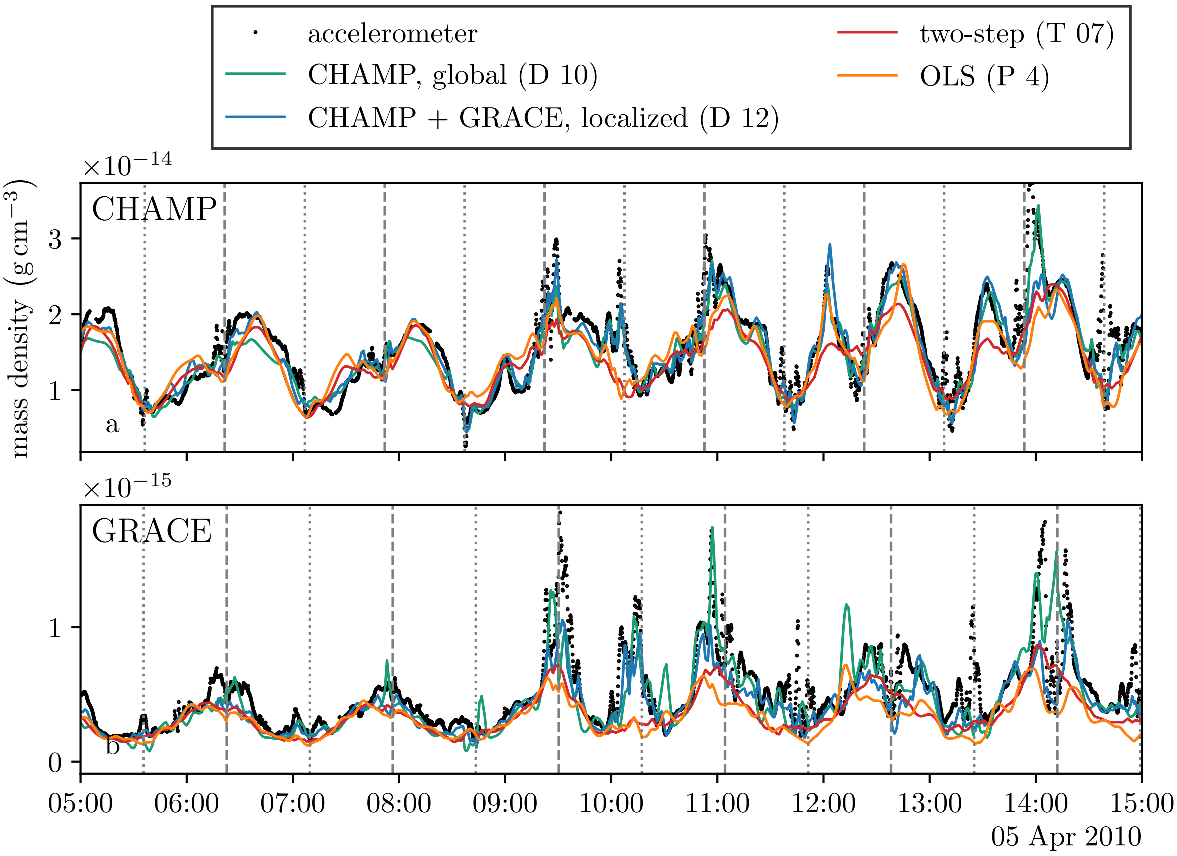

Figure 8.18.: This figure shows time series of mass density along the orbits of CHAMP and GRACE from TIE-GCM runs (solid lines) and derived from accelerometers (black dots). The dashed vertical lines indicate the satellite's passage above the north pole, and the dotted vertical lines mark the passage above the south pole. The temporal resolution of the model runs is one minute, except for the two-step assimilation, which wrote the density only every 10 minutes to file.

8.5. Assimilation of Electron Densities

The high resolution global electron density model (HRGEM) developed at DGFI-TUM (Lalgudi Gopalakrishnan and Schmidt, 2022) provides the electron number density and standard deviation for positions in the ionosphere that can be chosen arbitrarily. The standard deviations are obtained from a Monte-Carlo approach. HRGEM is a semi-empirical model using a multi-layer Chapman representation: The total electron number density is the superposition of the electron densities associated with the D-, E-, F1-, and F2-layer (Section 2.2.4) and the plasmasphere (Section 2.3.2.1). The ionospheric layers are described by a Chapman function (see Figure 2.11 for an example of the shape of a vertical Chapman function profile) parameterized by the peak electron density, the height of this peak and a scale height parameter. The electron number density in the plasmasphere is represented by exponential decay. The parameters of all layers and the plasmasphere are expanded by B-splines to the globe and are subject to equality and inequality constraints, to prevent nonphysical profiles. The parameters are fitted to IRI-2012 model simulations and radio occultation (see Section 4.5) measurements (GRACE, GRACE-

Setup 6: 3D Electron Density (E 03)

general

type	assimilation run
TIE-GCM setup	5°, Setup 1
start	27 Mar 2010 00:00 UTC+0
end	31 Mar 2010 00:00 UTC+0
writing frequency	every 10 minutes

ensemble

initial state	Setup 2
ensemble size	96
perturbations	time-variable (P 4, Table 8.1)
state vector	$w_{\mathrm{O}},\ w_{\mathrm{O}_2},\ w_{\mathrm{He}},\ T_n,\ C_{\mathrm{e}},\ C_{\mathrm{O}_2{}^+},$ $C_{\mathrm{O}^+} w_{\mathrm{O}}{}',\ w_{\mathrm{O}_2}{}',\ w_{\mathrm{He}}{}',\ T_n{}',\ C_{\mathrm{O}^+}{}'$

filter

filter	localized ESTKF
forget factor	1.0
forecast duration	1 h

localization

sub-domain size	1x1x1 cells
horizontal localization radius	1.5 cells
vertical localization radius	5 cells
weight function	$\mathrm{GC}_{a=0.5}(\tau)$

observation

domain	global 5° × 5° × 40 km grid, between 200 km-440 km altitude
quantity	electron number density from Lalgudi Gopalakrishnan and Schmidt (2022)
interpolation	linear

FO and Formosat-3/COSMIC), and GNSS observations. The model has been tested against incoherent scatter radar measurements (Section 4.4) and ionosonde data.

For this experiment, the model was evaluated on a grid with 5° horizontal resolution and 40 km vertical resolution between 200 km and 450 km altitude. The period between 27 March 2010 and 30 March 2010 is investigated. The setup for the assimilation experiment is summarized in Setup 6.

Figure 8.19 compares the electron number densities for the TIE-GCM and HRGEM at different altitudes for one point in time, which is characteristic of the investigated period. In most regions, the TIE-GCM underestimates the electron number density. This behavior has been also observed by Kodikara et al. (2021). On the night-side the differences are lower than on the day-side. At 320 km and 440 km around the subsolar point the HRGEM estimates a much denser electron number density than the TIE-GCM.

The HRGEM does not provide correlations. Consequently, the localization radius is chosen to be very small so that the missing correlations do not disrupt the update. Since each element of the state vector is updated individually, the runtime of the update step is about 20 times longer than for the two-step approach, where subdomains of 3 × 3 × 3 are updated.

In the previous experiments, the state vector only contained state variables associated with the neutral atmosphere. For the assimilation of electron densities, the electron number density itself and the ion number densities must be included (Hsu et al., 2014). Only adding the electron number density to the state vector is not sufficient since the TIE-GCM assumes a quasi-neutral atmosphere. This assumption recovers the forecasted electron density immediately after the update when the ion density is not updated. Thus, the prognostic ion number densities ($\mathrm{O_1}^+$,$\mathrm{O_2}^+$) must be included in the state vector for an enduring update of the electron density. The neutral state variables are kept in the state vector. As neutral state variables are correlated

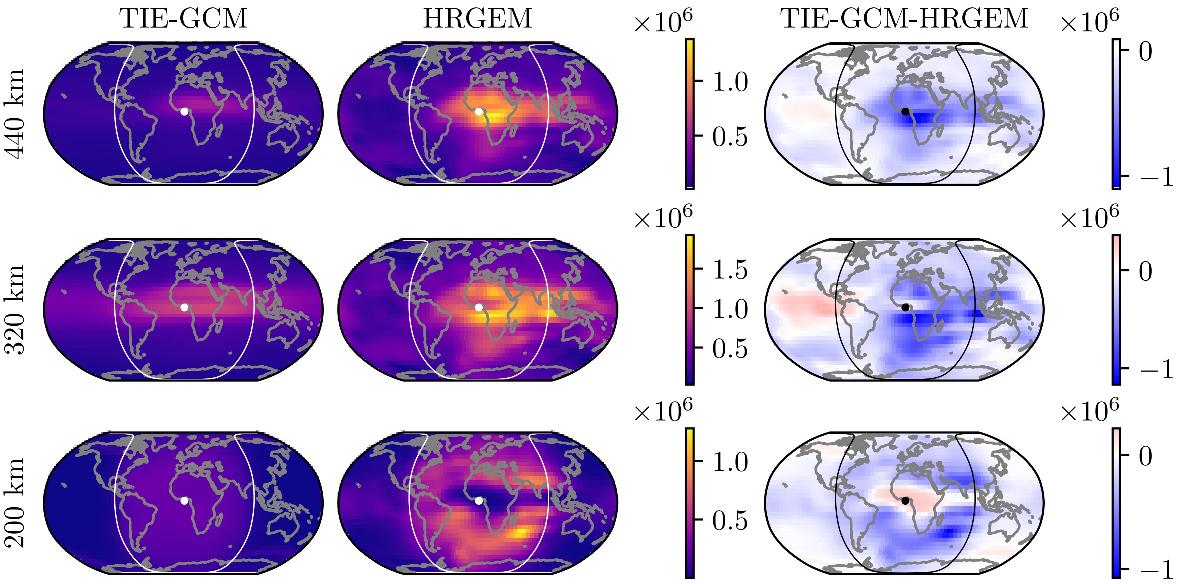

Figure 8.19.: The maps show the electron number density (difference) in cm^{-3} for 27 March 2010 12:00 UTC. Each row corresponds to an altitude. The left column contains the electron number densities from the OLS (P4). The white dot indicates the position of the subsolar point, and the white line represents the solar terminator.

with the density of charged particles (see Figure 8.5), this allows updating the neutral state variables by assimilation of electron densities.

It turned out that using cubic B-splines for the vertical interpolation can cause negative electron densities along the height profile in some cases (small electron densities and large vertical gradients). This is obviously nonphysical and causes model crashes. Thus, linear interpolation is used for all experiments where electron densities are assimilated. An alternative way, which might be considered in future studies, is constraining the B-splines.

The electron densities and their standard deviation provided by the HRGEM require the following preprocessing. Some of the HRGEM electron densities are less than the lower limit of the TIE-GCM, which limits the electron density to $3100\,\mathrm{cm}^{-3}$ (see Table 7.5). Thus, it is useless to assimilate electron densities below this threshold. Consequently, observations below this value are set to the limit and are down-weighted. Additionally, some of the standard deviations of the HRGEM electron densities are very small, especially on the night-side. The minimal HRGEM electron density standard deviation is set to $100\,\mathrm{cm}^{-3}$ to prevent filter failures caused by too-high confidence in those observations. This limit affects less than 0.1 % of the HRGEM electron densities.

Figure 8.20 compares the electron densities from the HRGEM with those from the OLS and the assimilation run (E 03) for different altitudes and longitudes. The electron number densities predicted by the TIE-GCM assimilating HRGEM electron densities (E 03) are much closer to the electron densities from the HRGEM than the OLS. Similarly to the two-step approach (see Figure 8.16), the assimilation run has large jumps as it gradually approaches the OLS after each update step. The jumps are enormous in the auroral region (−82°N), where the update is large, and at the same time, the model approaches the OLS fast. In the second row the electron

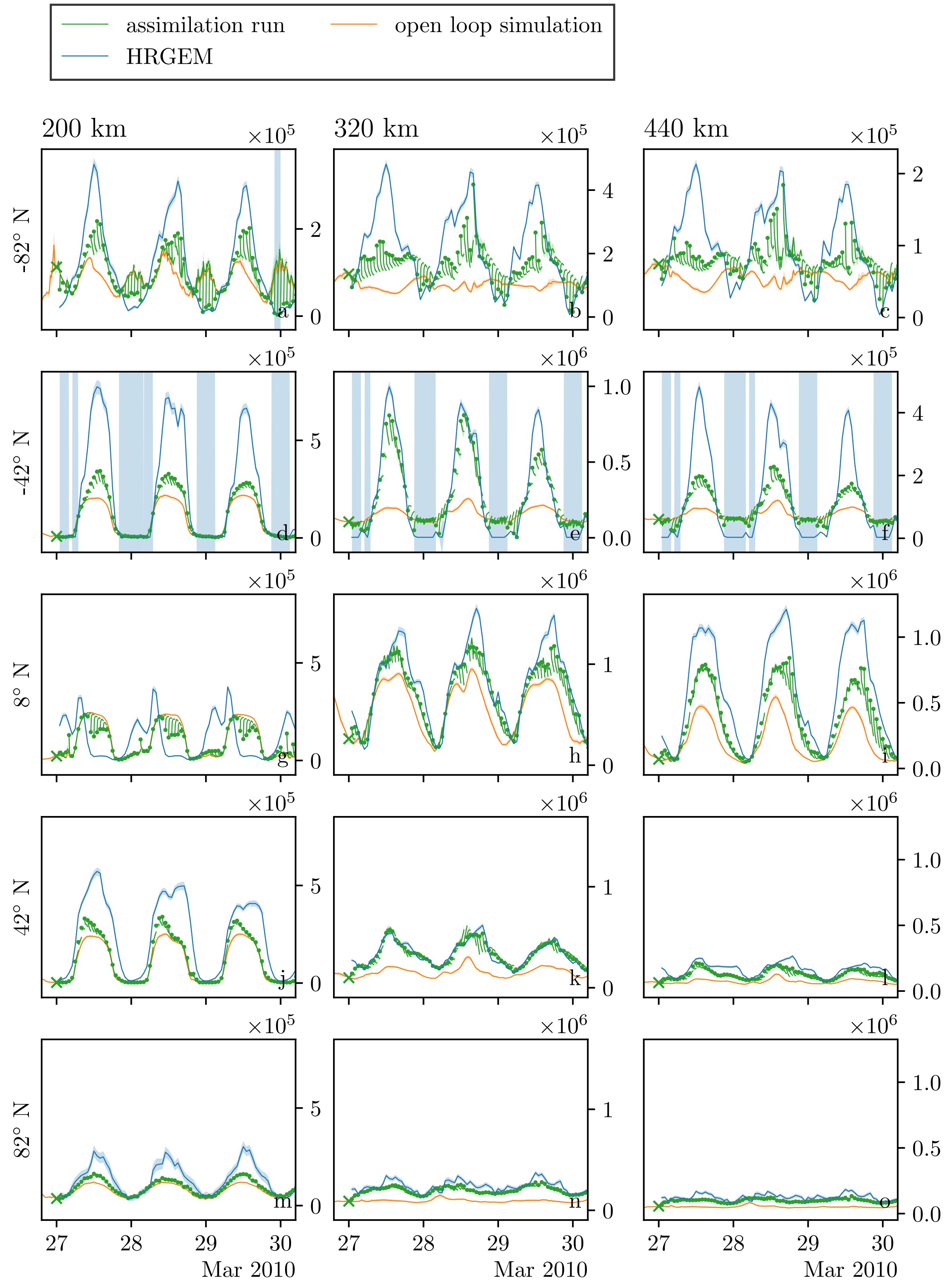

Figure 8.20.: Each panel contains time series of electron number density (cm^{-3}) for different cells of the HRGEM grid. Linear interpolation was used to interpolate the data on the TIE-GCM to the HRGEM grid. Each row corresponds to a geocentric latitude and each column to an ellipsoidal height. The longitude is always 0°E. The panels of each column share the same y-axis. The error bands show the standard deviation. The orange line is the OLS (P 4), the blue line the HRGEM data that was assimilated and the green line is the assimilation run.

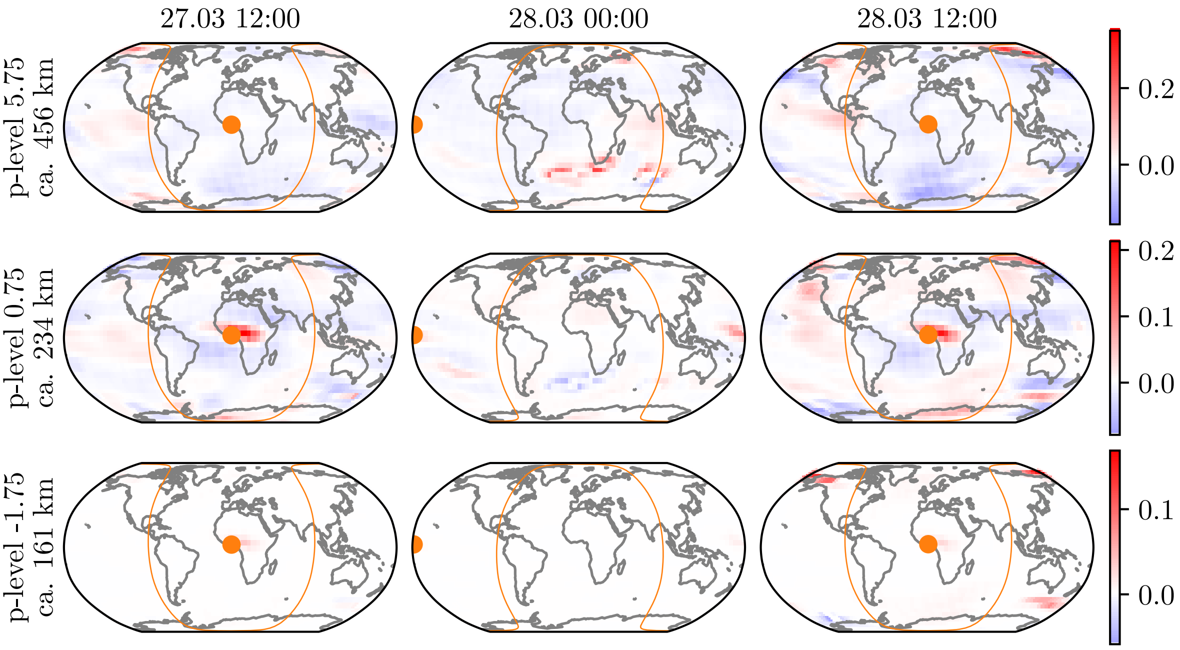

Figure 8.21.: Each row shows maps for the same pressure level and each column maps for the same analysis step (Setup E 3). The color indicates the mass density update divided by the mass density predicted by the OLS at the corresponding cell. A positive value indicates an increase of the mass density compared to the forecasted state.

densities on the night-side fall below the limit of 3100 cm^{-3}, so that they are associated with a very high uncertainty.

The assimilation of electron number density (Setup 6) has almost a negligible impact on the neutral mass density averaged over a pressure level, with a maximum effect of ±2 % compared to the OLS (Figure D.5). However, when looking at individual pressure levels and analysis steps, mass density updates of up to 35 % of the OLS mass density are revealed (see Figure 8.21). However, those effects occur mainly at poles. Large areas get only very small mass density updates. At higher altitudes the maximum relative mass density update is larger. For large areas the state update is small. The assimilation does not enhance the mass density estimate when compared with the accelerometer-derived densities of GRACE and CHAMP during the investigated period (see Figure 8.22). The update of the mass densities in the update step is based on the correlations encoded in the forecasted ensemble. Thus, it may be necessary to revisit the ensemble generation strategy and adjust it to the scenario in which the electron density is assimilated to improve the mass density estimate. Unfortunately, this period does not include a geomagnetic storm. This should be considered in future studies.

Instead of assimilating the three-dimensional electron density, one could also assimilate two-dimensional data derived from the vertical electron density profiles. Examples of such quantities are the vertical TEC or the height where the peak of the F2 layer (Section 2.2.4) is located (hmF2). For vertical TEC assimilation, the observation operator is the sum of all electron densities over a vertical column. When using a vertical TEC map matching the horizontal

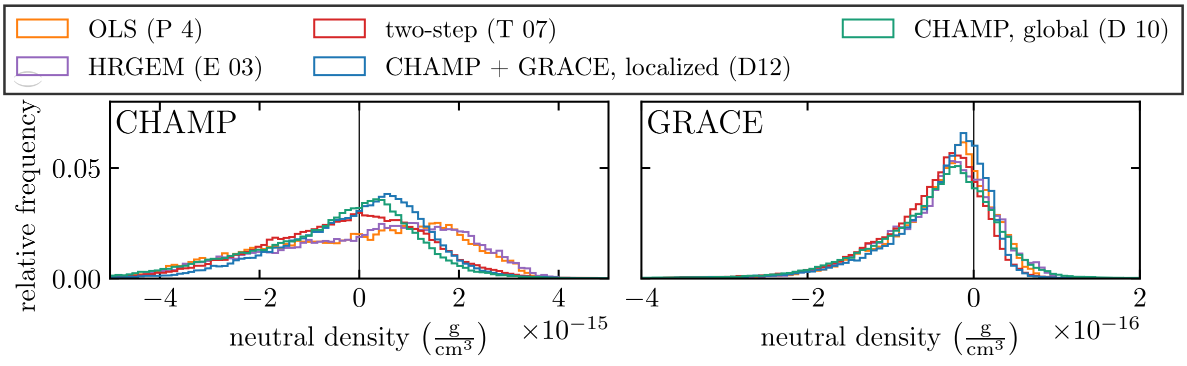

Figure 8.22.: Histograms of differences between TIE-GCM runs and accelerometer-derived neutral densities. The OLS (orange line) was computed according to Setup 3. The period from which this diagram was computed is only four days long. So, it cannot be compared directly with the other histograms shown so far.

grid layout of the TIE-GCM, interpolation is unnecessary. Additionally, compared with the 3D electron densities, such a map results in a smaller observation vector, decreasing the run time.

8.6. Co-Estimation of Model Dynamics

First, it is necessary to determine which model parameters are calibrated. External forcings, such as the F10.7 index, have been co-estimated, for example, in Matsuo et al. (2013, Section 3.2). However, this does not update the dynamics of the model; rather, it distorts the (measured) external forcings so that they fit the model more closely. Instead of external forcing, it would be preferable to co-estimate the model parameters that actually control the model dynamics.

Figure C.2 illustrates the influence of model parameters on the mass density. The Joule heating factor and the Burnside factor (Section 5.1.3) have a significant impact on the neutral mass density. For future studies, collaboration with model developers would be helpful in identifying further uncertain parameters that would benefit from co-estimation.

The model parameters considered here are global, meaning they do not depend on the position. Thus, when using global filters, one can simply augment the state vector. The parameters are then updated based on the correlations with the other entries of the state vector. However, when using localization, different approaches are required to estimate global model parameters (Section 6.5).

In the following, the co-estimation of model parameters using direct assimilation of accelerometer-derived mass densities is investigated. The model dynamics are only updated every 20th assimilation step. This is done for two reasons: First, the state has some time to adapt to the updated parameter. Second, the runtime for the localized filter is reduced.

It is necessary to perturb the co-estimated model parameters in the initial augmented state vector for each ensemble member. Otherwise, these parameters will not be updated by the Kalman filter, as their variance is zero. In case the spread of a model parameter is decreased by the update step, the variance of the state will also be reduced in the subsequent forecast phase.

Setup 7: Calibration (Y 01)

general

type	assimilation and calibration
TIE-GCM setup	5°, Setup 1
start	27 Mar 2010 00:00 UTC+0
end	22 Apr 2010 00:00 UTC+0
writing frequency	every 60 s

ensemble

initial state	Setup 2
ensemble size	96
perturbations	time-variable (P 4, Table 8.1)
state vector	$w_{\mathrm{O}},\ w_{\mathrm{O}_2},\ w_{\mathrm{He}},\ T_n,\ w_{\mathrm{O}}',\ w_{\mathrm{O}_2}',\ w_{\mathrm{He}}',\ T_n'$

filter

filter	localized ESTKF
forget factor	1.0
forecast duration	60 s

localization

sub-domain size	3x3x3 cells
horizontal localization radius	5000 km
vertical localization radius	500 km
weight function	$\mathrm{GC}_{a=0.5}(\tau)$

observation

domain	satellite orbit of CHAMP
quantity	neutral mass density
uncertainty	5 % of neutral density
interpolation	cubic B-Spline

calibration

co-estimated parameters	Joule heating factor
estimation frequency	every 20 min

Table 8.4.: Overview of assimilation setups that co-estimate Joule heating. The reference setup is summarized in Setup 7 and corresponds to the experiment in the first row. Settings that differ from the reference setup are highlighted with light gray.

	localization radius		
ID	horizontal	vertical	satellites
Y 01	5000 km	500 km	CHAMP
Y 02	5000 km	500 km	CHAMP+GRACE
Y 03	global		CHAMP

Table 8.4 contains the assimilation experiments that co-estimate the Joule heating factor. For the co-estimation runs, the period is extended by twelve days compared with the direct assimilation runs (Table 8.2), so the long-term behavior of the co-estimated Joule heating factor can be better investigated. The time series of ensemble mean and ensemble standard deviation of the Joule heating factor co-estimated in the experiments Y 01-Y 03 are plotted in Figure 8.23. While the variance gradually decreases for the global filter, it gradually increases when employing localization. In the original Kalman filter, the variance of the (augmented) state decreases after each analysis step (Equation 6.50). In the case of the global filter, the global model parameters are updated together with the model state in the analysis step of the Kalman filter. In contrast, the localized filter updates the global model parameters after applying the Kalman filter, employing a linear regression of the state update (Section 6.5). The increase in ensemble spread suggests that the combination of localization and co-estimation of Joule heating is not functioning as intended. In Malartic et al. (2022, Section 2.3.2) an update method for global parameters after a localized Kalman update with increased accuracy is proposed that might improve the results for these experiments.

After the geomagnetic storm, the ensemble mean returns almost to the initial value for all experiments. The largest difference to the initial value at the end has experiment Y 02 (0.05, 4 %). This has only a small impact on the mass density ($\sim 1\,\%$ at 400 km altitude, see Figure C.2), indicating that the default value for the Joule heating factor is at least for quiet conditions well suited. In fact, when applying any of the co-estimated ensemble mean Joule heating factor time series to a single instance TIE-GCM run, the density estimation does not perform better than the OLS when compared with CHAMP and GRACE accelerometer derived mass densities.

The co-estimation of Joule heating factor could not improve the mass density estimation of the TIE-GCM in the investigated period. The estimated Joule heating factor suggests that the default value of 1.5 already fits well with the observations. Here, a 26-day long period has been examined. For future experiments, longer periods should be considered to exclude the possibility that this is just a coincidence. The computational cost for the co-estimation runs applying localization is especially large. Global filters are much faster, as no post-processing step is required, as the model parameter is estimated during the update step. Moreover, other model parameters should be considered for future co-estimation experiments. Hard-coded chemical reaction rates of atmospheric constituents are possible candidate parameters.

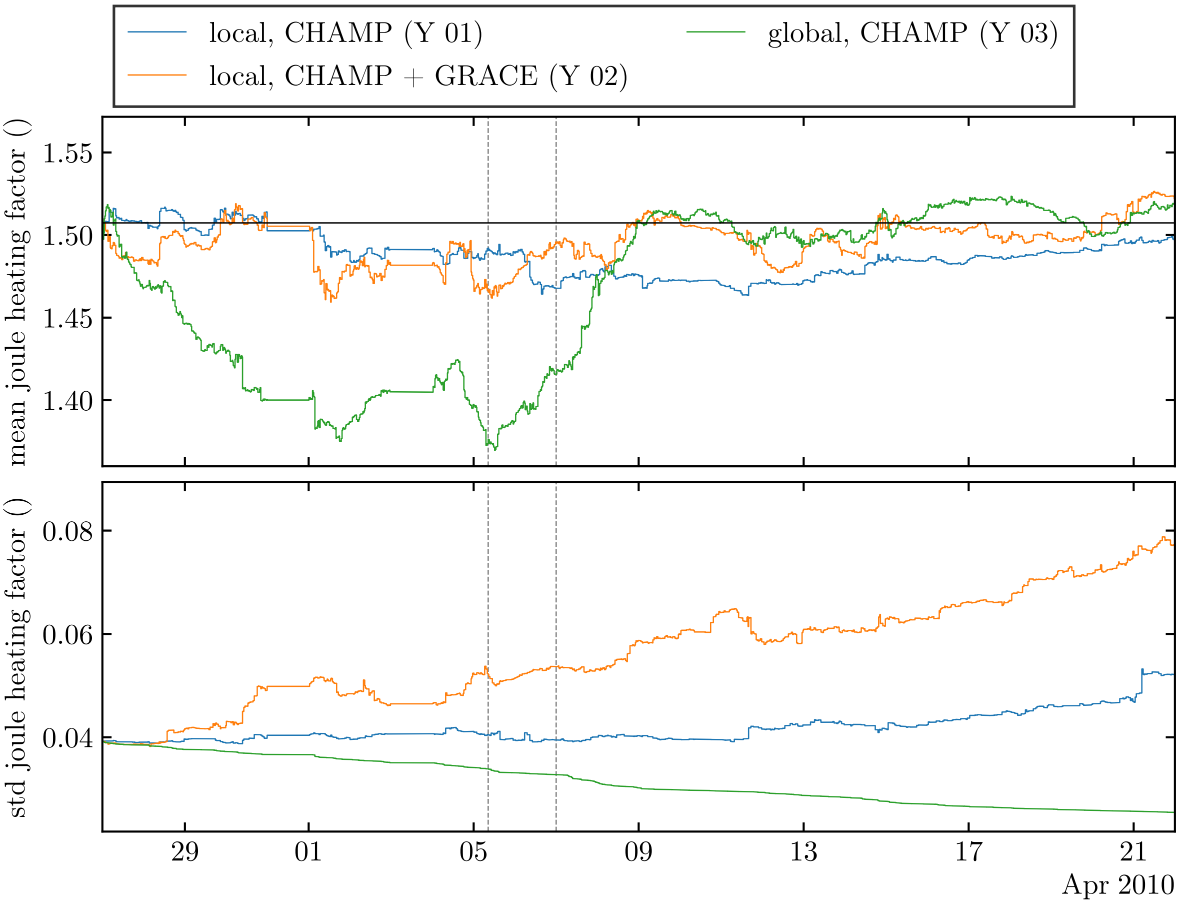

Figure 8.23.: The upper panel contains the ensemble mean of the Joule heating factor co-estimated in the experiments listed in Table 8.4. The lower panel contains the associated standard deviations. The black solid horizontal line is the initial mean. The vertical dashed lines mark the beginning and end of the 5 April 2010 geomagnetic storm.

8.7. Transferability to Other Periods

So far, the experiments have been conducted in March and April 2010. This period covers only a small range of solar and geomagnetic activity. Therefore, the following two additional periods also containing geomagnetic storms are investigated: the period around the Halloween 2003 storm (Denig et al., 2018; Lopez et al., 2004) and the 2015 June solstice[1] storm (e.g., Astafyeva et al., 2016; Augusto et al., 2018; Y. D. Liu et al., 2015). Table 8.5 provides an overview of all three geomagnetic storms investigated in this thesis. The experiments also cover the period well before and after the storm so that also quiet conditions are included in the analysis.

For the Halloween 2003 geomagnetic storm, the accelerometer-derived mass densities along the orbit of CHAMP are assimilated using a local (D 101) and a global filter (D 102). Figure 8.24 compares the accelerometer-derived mass densities with the local and global filter and the OLS. When comparing the observed densities to the densities simulated in the assimilation runs, the local (D 101) and the global (D 102) filters outperform the OLS, which drastically underestimates

---

[1] The storm is often called ’summer solstice storm’. However, this term is ambiguous. Therefore, I here refer to it as ’June solstice storm’.

Table 8.5.: In this thesis three periods containing geomagnetic storms of different intensity are investigated. This table gives the corresponding solar activity (F10.7) and information about the storm for each period. The class of a storm depends on its Kp value (see Figure 2.17).

	F10.7			storm		
experiment's period	median	min	max	name	period	class
25 Oct - 06 Nov 2003	241.6	110.0	307.3	Halloween 2003	29-31 Oct	extreme (G5)
27 Mar - 10 Apr 2010	77.8	75.5	85.5	April 2010	05 Apr	strong (G3)
15 Jun - 29 Jun 2015	132.9	100.1	174.0	June Solstice 2015	22-23 Jun	severe (G4)

Table 8.6.: Some previously conducted experiments are repeated for different periods. The settings are the same as in the column 'setup', except for the period and the satellite. The RMSE is computed from Equation 8.1. The color schema applied to illustrate the differences is described in Table 8.2.

					$\rho^{\text{assim}} - \rho^{\text{acc}}$			
					median ($\mathrm{g\,cm^{-3}}$)		RMSE ($\mathrm{g\,cm^{-3}}$)	
period ID		obervations	filter	setup	CHAMP	GRACE	CHAMP	GRACE
25 Oct 2003 - 06 Nov 2003	D 101	CHAMP	local	D 01	-2.9e-16	-8.5e-18	1.7e-15	6.7e-16
	D 102		global	D 10	-4.5e-17	1.1e-16	1.4e-15	5.4e-16
	OLS				-1.0e-15	-2.2e-16	3.1e-15	1.0e-15
					Swarm-C	GRACE	Swarm-C	GRACE
15 Jun 2015 - 29 Jun 2015	D 201	GRACE	local	D 01	2.9e-16	4.5e-18	4.5e-16	3.7e-16
	D 202		global	D 10	3.1e-16	5.7e-18	4.5e-16	4.1e-16
	OLS				2.7e-16	-2.2e-17	4.1e-16	6.4e-16

the mass density. The median mass density difference along the orbit of CHAMP and GRACE is two orders of magnitude lower for the local filter (D 101) than for the OLS. The median difference to the accelerometer-derived mass densities along the orbit of CHAMP is an order of magnitude lower when the global filter is used instead of the local filter (Table 8.6). During the Halloween 2003 geomagnetic storm, the vertical separation between GRACE and CHAMP is approximately 100 km shorter in comparison to the previously investigated period (compare panel c in and Figure 8.24 and 8.11). Accordingly, the impact of the localized filter on the mass density along the orbit of GRACE is much stronger than during the April 2010 storm (compare panel b in and Figure 8.24 and 8.11). Still, in the shown snapshot, the global filter is closer to the accelerometer-derived mass densities of the GRACE satellite than the local filter.

For the June solstice 2015 storm, the accelerometer-derived mass densities along the orbit of GRACE are assimilated since CHAMP re-entered in 2010. There is a data gap in the accelerometer-derived mass densities for GRACE, so the first update step is on 23 June 2015. Again, a local filter (D 201) and a global filter (D 202) are employed. Figure 8.25 compares the observed and modeled mass densities along the orbits of the GRACE and the Swarm-C satellite. As expected, the assimilation runs are much closer to the observations than the OLS for GRACE. The local filter performs slightly better than the global filter. However, for Swarm-C the OLS is closer to the observations than the assimilation runs. This does not necessarily

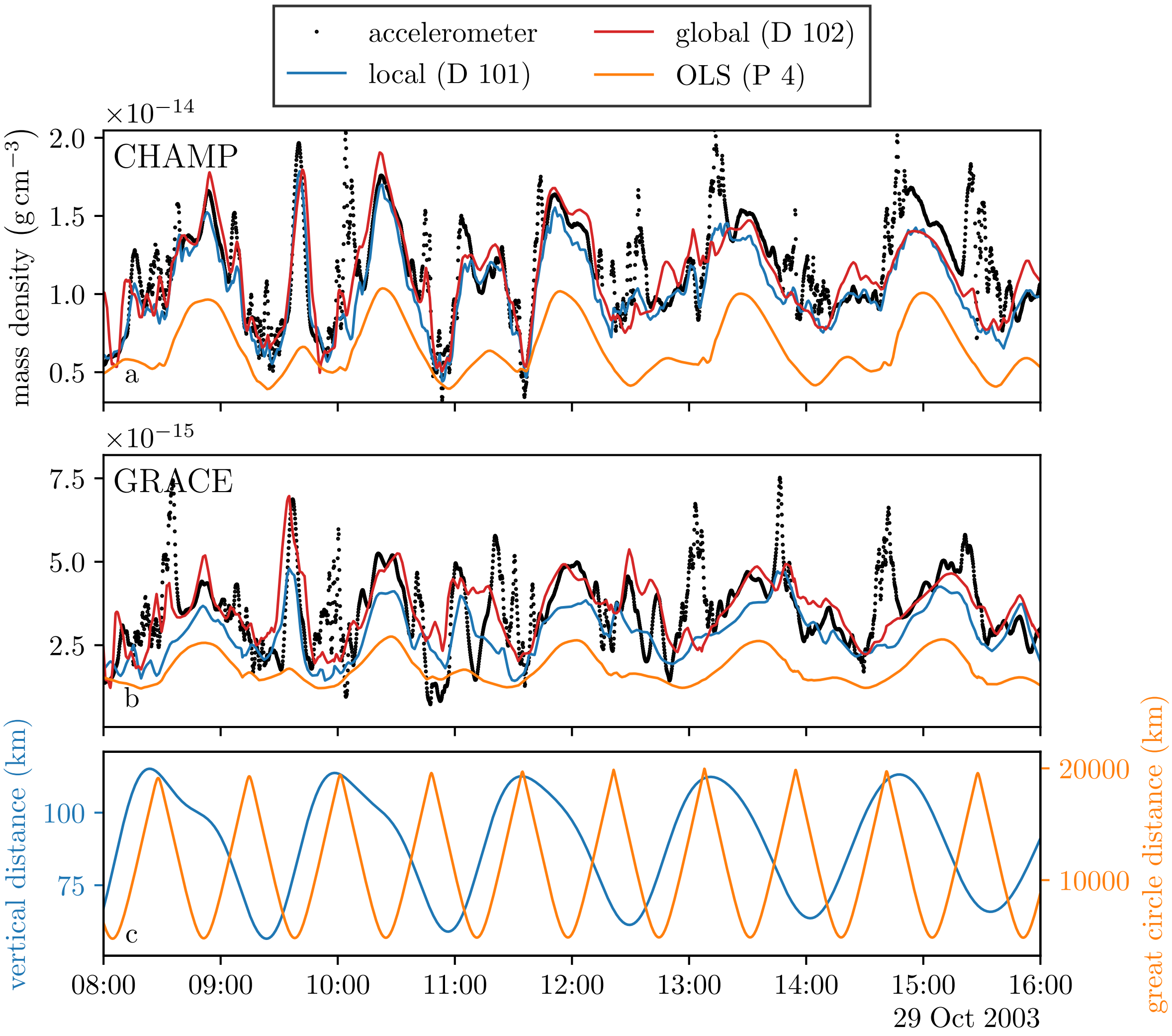

Figure 8.24.: The two upper panels show time series of mass density during the Halloween storm 2003 along the orbit of CHAMP and GRACE from TIE-GCM runs (solid lines) and derived from accelerometers (black dots). The temporal resolution of the model runs is one minute, except for the OLS, which was saved only every 10 minutes. Panel c shows the vertical and great circle distance on Earth's surface between CHAMP and GRACE.

mean that the assimilation has failed. Instead, there may be a bias in accelerometer-derived densities of the Swarm-C satellite. In fact, the Swarm accelerometers are known to "suffer from a variety of disturbances, the most prominent being slow temperature-induced bias variations and sudden bias changes" (Siemes et al., 2016). Since Swarm-C flies only about 60 km higher than GRACE, one would expect that the OLS for both satellites to perform comparably well. However, for Swarm-C the observations fit the OLS much worse than GRACE, indicating a bias in the observations.

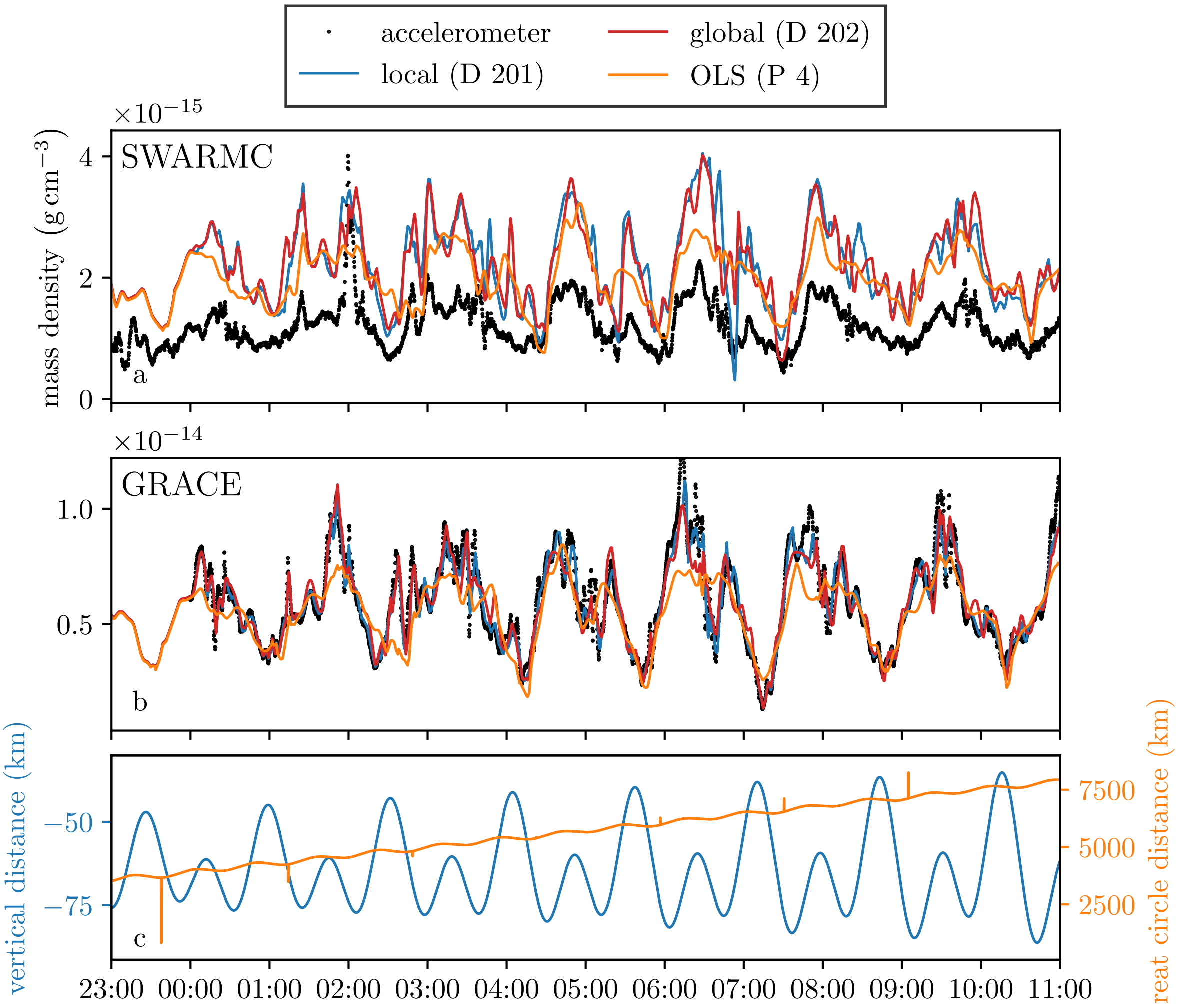

Figure 8.25.: The two upper panels show time series of mass density during the June solstice 2015 storm along the orbit of CHAMP and GRACE from TIE-GCM runs (solid lines) and derived from accelerometers (black dots). The temporal resolution of the model runs is one minute, except for OLS, which was saved only every 10 minutes. Panel c shows the vertical and great circle distance on Earth's surface between Swarm-C and GRACE.

9. Conclusions

A new data assimilation system employing the TIE-GCM 2.0 has been developed to overcome the limitations of data assimilation systems formulated in Section 1.3 and to enhance the TIE-GCM's mass density estimation skills. For this purpose, different data assimilation approaches have been developed, implemented, and tested. First, accelerometer-derived mass densities from the CHAMP and GRACE missions were assimilated directly into the TIE-GCM using localized and global filters. Second, within a two-step approach, the global density estimation of a calibrated semi-empirical model has been assimilated. Third, the assimilation of global 3D electron number densities has been implemented and investigated. Finally, the Joule heating factor has been co-estimated.

9.1. Evaluation of the Hypotheses

In Section 1.4 six hypotheses have been formulated which are evaluated based on the experiments conducted in Chapter 8.

9.1.1. Runtime of the Assimilation System

Since the PDAF is directly implemented into the TIE-GCM 2.0, it is only initialized once, making it much faster than implementations that must re-initialize the model after each analysis step. The ensemble size and the number of physical processor cores per ensemble member were tuned to save computational resources and enable short runtimes while ensuring adequate model state updates. A good balance is provided by an ensemble of 96 members and four physical processor cores per ensemble member for the TIE-GCM 2.0 with 5° horizontal resolution. Additionally, the choice of the ESTKF slightly decreases the run time as it operates on the error-subspace. These aspects allow for assimilation experiments covering 14 days, with assimilation steps every minute in a reasonable runtime of ~14 h per assimilation experiment when using localization and ~10 h without localization[1]. This corresponds to 384 core hours per day when using localization. Accordingly a data assimilation experiment covering a year would require 140 160 core hours. This can be easily provided by even small high performance clusters. Thus, Hypothesis H 1 can be accepted.

Using the TIE-GCM with 2.5° horizontal resolution increases the runtime by about a factor of 10, while the differences in the mass density forecast to the TIE-GCM with 5° resolution are comparably minor. Thus, I recommend using the version with the lower resolution for data assimilation experiments.

---

[1] Domain localization (Section 6.4.2) is computationally more expensive as the update step has to be computed for each subdomain individually.

9.1.2. Space Weather Dependent Ensemble Generation

Figure 8.8 shows that the model forecast uncertainty fits better to the actual space weather conditions when using time-variable perturbations and perturbing the magnetic field for the ensemble generation in an OLS. In an actual assimilation experiment, the offset between the simulated and accelerometer-derived mass density was an order of magnitude larger for static perturbations compared with time-variable perturbations (Experiment D 01 vs Experiment D 13). This, supports Hypothesis H 2.

9.1.3. Spurious Correlations in the Forecasted Model Errors

The success of data assimilation heavily depends on realistic stochastic models for the observation and model errors. For the ESTKF, a VCM explicitly represents the observation uncertainty, while an ensemble of states implicitly represents the model uncertainty. The stochastic models control how much confidence is placed in the observations and the model. Moreover, the correlations encoded in the forecasted state ensemble determine how the forecasted state is updated by the filter. Since spurious long-range correlations that produce unrealistic updates are often present in the forecasted state ensemble, localized filters are often employed. While they compensate for unwanted unrealistic state updates far away from the observations, they also limit the region affected by the assimilation. I could reduce spurious long-range correlations in the model forecast errors by introducing time-variable perturbations of external forcings (see Figure 8.5). The global assimilation of accelerometer-derived mass densities from CHAMP (Experiment D 10) significantly improved the mass density estimation along the orbit of GRACE, which flew about 175 km above CHAMP. The offset and RMSE along the GRACE orbit were reduced by 17 % and 26 %, respectively, when comparing to the OLS. Nevertheless, Figure 8.10 indicates that some spurious long-range correlations might still exist. When using static perturbations and not perturbing the IMF and Earth magnetic field, the global filter had a 26 % larger offset and 15 % greater RMSE along the GRACE orbit compared with the assimilation run with time-variable perturbations and perturbations of the magnetic fields (Experiment D 10 vs Experiment D 16). These findings support Hypothesis H 3.

9.1.4. Improved Mass Density Prediction Skills

The localized assimilation of along-track mass densities significantly improves the model forecast. For a two-week period in 2010, including a geomagnetic storm, the bias between the modeled mass densities and the accelerometer-derived mass densities along the orbit of CHAMP was on average reduced by two thirds compared with the OLS when applying a localized filter (Experiment D 01). For the same experiment the RMSE of the observed and simulated mass densities was reduced by one thirds. The simultaneous localized assimilation of GRACE and CHAMP (Experiment D 12) improved the density in the vicinity of both satellites. The RMSE of observed and simulated mass densities was reduced by 47 % and 30 % along the orbits of GRACE and CHAMP, respectively, for a two-week long period in 2010. The direct assimilation of accelerometer-derived mass densities was tested under different geomagnetic conditions in different years. The assimilation successfully improved the density estimation for all periods (Table 8.6).

Unfortunately, we do not have independent mass density observations for the investigated periods against which to compare the different models. Determining the mass densities from accelerometers (Section 4.1) involves many assumptions, and the observations have systematic and random errors. The ambiguity between ballistic coefficients and mass density (see Section 3.2) affects observations derived from orbital decay and accelerometers. No recent LEO satellite mission is equipped with a mass spectrometer that could measure the density without assumptions on the ballistic coefficients.

However, numerical models have a finer spatial resolution than empirical models. While the TIE-GCM's lowest possible horizontal resolution is 5°, the NRLMSIS 2.0 represents horizontal mass density variations of up to 60°. The temporal resolution of the external forcings limits the temporal resolution of all models. Thus, in the worst case, the NRLMSIS 2.0 has a three-hour delay to the onset of a geomagnetic storm as it depends on the Kp index. In contrast, the TIE-GCM can react much faster as it uses the IMF and solar wind with a high temporal resolution to drive the high latitude convection. Further the assimilation of mass-derived mass densities with high temporal resolution generates model forecasts that fit well to the corresponding observations. The data assimilation system thus provides the basis for outperforming semi-empirical models. However, hypothesis H 4 cannot be validated since there is no suitable observation independent on the ballistic coefficients for the investigated periods.

9.1.5. Assimilation of (Semi-)Empirical Models

The two-step approach enables global assimilation by assimilating the mass density estimate of a semi-empirical model. In this thesis, the NRLMSIS 2.0 was calibrated by accelerometer-derived mass densities. However, the two-step approach does not use the high temporal resolution of the accelerometers due to a low pass filter. During the 5 April 2010 geomagnetic storms, it performed inferior to the direct global assimilation of CHAMP data (e.g., Figure 8.18). However, during quiet conditions, the estimation was successfully improved. In the two-week long period including the storm, the RMSE of observed and simulated mass densities along the orbits of GRACE and CHAMP was reduced by 24 % and 17 %, respectively, compared with the OLS. Thus, Hypothesis H 5 is valid. However, the approach chosen in this thesis limits the temporal resolution of the assimilated data.

The assimilation of the electron densities provided by the DGFI-TUM corrected the electron density estimation but did not improve the mass density estimation when comparing to accelerometer-derived mass densities. Whether this is also the case during geomagnetic storms with increased electron densities has yet to be investigated. Moreover, cubic B-splines are not suited for vertical interpolation of electron densities in the observation operator, as they do not ensure non-negative electron density profiles.

9.1.6. Co-Estimation of Model Dynamics

The co-estimation of model dynamics is motivated by two reasons. First, the TIE-GCM is a convergent model highly driven by external forcings (Figure 7.2). Thus, the state gradually approaches the OLS after each analysis step. Estimating model parameters controlling the dynamics may achieve a permanent correction. Second, co-estimating global model parameters may improve density estimation globally, even when using localization. However, only the Joule heating factor has been co-estimated here since localized co-estimation experiments are computationally expensive. The experiments conducted (Table 8.4) indicate that the default Joule heating factor is already well-chosen. However, longer time periods need to be investigated to make sure this is not a coincidence. Additionally, other uncertain model parameters should be identified and co-estimated in future investigations. Thus, Hypothesis H 6 cannot be accepted.

9.2. Outlook

Although the ensemble generation was significantly improved, there is still potential for further improvements. For example, the perturbation of the lower boundary conditions could be derived by perturbing the inputs of the models that are used to calculate the lower boundary conditions: the corresponding models are the GSWM, NRLMSIS and HWM. Moreover, the upper boundary conditions could be perturbed in addition to the lower boundary conditions, for example, the oxygen ion flux as suggested by Lee et al. (2012). Additionally, quite simple analytical covariance functions have been employed so far to model the temporal dependency of the uncertainty of the time-variable external forcings. Alternatively one could use the empirical covariance, or auto-regressive processes.

The uncertainty of the accelerometer-derived mass density observations must be better represented than by a percentage of the density itself. Recent progress in specifying this uncertainty (e.g., Siemes et al., 2024) should be incorporated in the future. The stochastic model used to represent the uncertainty of the empirical model used for the two-step approach (Section 7.6.2) is highly dependent on a percentage of the density. An alternative to this rather simple approach is to run an ensemble of the empirical model with perturbed inputs.

Theoretically, one could also improve the state forecast of upper atmosphere numerical models globally by assimilating data from many well-distributed satellites. However, the simultaneous assimilation of data from different sources requires compensating for possible biases between them. As semi-empirical models also face this problem, they might provide valuable information for bias correction.

Future research should consider longer periods for the assimilation experiments, covering multiple years or even decades. This could help to understand long-term effects, such as the observed long-term cooling of the upper atmosphere discussed in Section 2.5. The assimilation run has the potential to function as a ”true state,” thereby enabling a comparative analysis with TIE-GCM simulations employing varying levels of CO_2. This setup allows for the attribution of the rise in CO_2 concentration to the observed cooling of the upper atmosphere.

Some aspects may further improve the performance of the TIE-GCM 2.0. First, the Burnside factor could be replaced (Ieda, 2021). Second, the climatological zonal lower boundary could be derived from the latest versions of the HWM and NRLMSIS. Third, there is a newer version of the IGRF that could replace the old one. The TIE-GCM 3.0 has already updated the IGRF. Many other aspects have been updated as well. Higher resolutions are possible. However, resolutions even higher than 2.5° will likely increase the runtime drastically if not compensated by more or faster processor cores. Also, the model is extended to higher altitudes so that, for example, the observation operator never needs to extrapolate the mass density to the orbit of GRACE. Despite the new TIE-GCM version, the here developed assimilative TIE-GCM 2.0 can be used for future studies. The higher resolution of the new version cannot be used for long periods without extraordinary computational costs. Doubling the TIE-GCM 2.0 resolution (5.0° to 2.5°) increased the run time already by a factor of ten. Still, potential runtime improvements in the TIE-GCM 3.0 need to be analyzed. However, the number of cells increases by a factor of eight when doubling the resolution which increases computational costs accordingly. Besides, the update to version 3 has not changed the model dynamics drastically, so that one can expect comparable model forecasts for both versions. Still, comparisons between the TIE-GCM 2.0 and TIE-GCM 3.0 should be conducted in the future to determine in which situation the here developed assimilative TIE-GCM could benefit from an upgrade to the latest release.

Apart from the assimilation approaches, two aspects are desirable for further advances. First, the assimilation would benefit from observations of the mass density that do not rely on an accurate and precise simulation of the gas surface interaction to rule out the ambiguity between mass density and ballistic coefficients. Fortunately, the upcoming NASA Geospace Dynamics Constellation (GDC) in 2030 or the ESA earth explorer candidate 'keystone' may deliver such observations in the future. Second, a decent uncertainty quantification of accelerometer-derived mass densities and semi-empirical models would immensely enhance the realism of the assimilated mass densities. The MAGIC mission, preceding GRACE-FO, consists of two GRACE-like pairs in a bender constellation and is already approved. Although the ambiguity with ballistic coefficients affects the accelerometer-derived mass density of the MAGIC mission, it ensures mass densities with high temporal resolution for future assimilation systems.

Bibliography

Akbari, H., D. Rowland, A. Coleman, A. Buynovskiy, and J. Thayer (2024). “Gradient Calculation Techniques for Multi-Point Ionosphere/Thermosphere Measurements from GDC”. In: *Frontiers in Astronomy and Space Sciences* 11. ISSN: 2296-987X. DOI: `10.3389/fspas.2024.1231840`.

Alken, P., E. Thébault, C. D. Beggan, H. Amit, J. Aubert, J. Baerenzung, T. N. Bondar, et al. (2021). “International Geomagnetic Reference Field: The Thirteenth Generation”. In: *Earth, Planets and Space* 73.1, p. 49. ISSN: 1880-5981. DOI: `10.1186/s40623-020-01288-x`.

Alkhatib, H. and W.-D. Schuh (2007). “Integration of the Monte Carlo Covariance Estimation Strategy into Tailored Solution Procedures for Large-Scale Least Squares Problems”. In: *Journal of Geodesy* 81.1, pp. 53–66. ISSN: 1432-1394. DOI: `10.1007/s00190-006-0034-z`.

Amdahl, G. M. (1967). “Validity of the Single Processor Approach to Achieving Large Scale Computing Capabilities”. In: *Proceedings of the April 18-20, 1967, Spring Joint Computer Conference.* AFIPS ’67 (Spring). New York, NY, USA: Association for Computing Machinery, pp. 483–485. ISBN: 978-1-4503-7895-6. DOI: `10.1145/1465482.1465560`.

Anderson, J., T. Hoar, K. Raeder, H. Liu, N. Collins, R. Torn, and A. Avellano (2009). “The Data Assimilation Research Testbed: A Community Facility”. In: *Bulletin of the American Meteorological Society* 90.9, pp. 1283–1296. ISSN: 0003-0007, 1520-0477. DOI: `10.1175/2009BAMS2618.1`.

Anderson, J. L. (2001). “An Ensemble Adjustment Kalman Filter for Data Assimilation”. In: *Monthly Weather Review* 129.12, pp. 2884–2903. ISSN: 1520-0493, 0027-0644. DOI: `10.1175/1520-0493(2001)129<2884:AEAKFF>2.0.CO;2`.

– (2010). “A Non-Gaussian Ensemble Filter Update for Data Assimilation”. In: *Monthly Weather Review* 138.11, pp. 4186–4198. ISSN: 1520-0493, 0027-0644. DOI: `10.1175/2010MWR3253.1`.

– (2020). “A Marginal Adjustment Rank Histogram Filter for Non-Gaussian Ensemble Data Assimilation”. In: *Monthly Weather Review* 148.8, pp. 3361–3378. ISSN: 1520-0493, 0027-0644. DOI: `10.1175/MWR-D-19-0307.1`.

Anderson, John D. and Cadou, Christopher P. (2023). *Fundamentals of Aerodynamics.* 7th ed. Mc Graw Hill. ISBN: 978-1-264-15192-9. URL: `https://www.mheducation.com/highered/product/fundamentals-aerodynamics-anderson/M9781264151929.html` (visited on 09/28/2023).

Arevalo Jr, R., Z. Ni, and R. M. Danell (2020). “Mass Spectrometry and Planetary Exploration: A Brief Review and Future Projection”. In: *Journal of Mass Spectrometry* 55.1. ISSN: 1096-9888. DOI: `10.1002/jms.4454`.

Asch, M., M. Bocquet, and M. Nodet (2016). *Data Assimilation.* Philadelphia, PA: Society for Industrial and Applied Mathematics. DOI: `10.1137/1.9781611974546`.

Aschwanden, M. J. (2014). “Chapter 11 - the Sun”. In: *Encyclopedia of the Solar System.* Ed. by T. Spohn, D. Breuer, and T. V. Johnson. 3rd ed. Boston: Elsevier, pp. 235–259. ISBN: 978-0-12-415845-0. DOI: `10.1016/B978-0-12-415845-0.00011-6`.

Ashrafi, M., M. J. Kosch, and F. Honary (2005). “Comparison of the Characteristic Energy of Precipitating Electrons Derived from Ground-Based and DMSP Satellite Data”. In: *Annales Geophysicae* 23.1, pp. 135–145. ISSN: 0992-7689. DOI: `10.5194/angeo-23-135-2005`.

Astafyeva, E., I. Zakharenkova, and P. Alken (2016). “Prompt Penetration Electric Fields and the Extreme Topside Ionospheric Response to the June 22–23, 2015 Geomagnetic Storm as Seen by the Swarm Constellation”. In: *Earth, Planets and Space* 68.1, p. 152. ISSN: 1880-5981. DOI: `10.1186/s40623-016-0526-x`.

Augusto, C. R. A., C. E. Navia, M. N. de Oliveira, A. A. Nepomuceno, J. P. Raulin, E. Tueros, R. R. S. de Mendonça, et al. (2018). “The 2015 Summer Solstice Storm: One of the Major Geomagnetic Storms of Solar Cycle 24 Observed at Ground Level”. In: *Solar Physics* 293.5, p. 84. ISSN: 1573-093X. DOI: `10.1007/s11207-018-1303-8`.

Baker, D. (1998). “What Is Space Weather?” In: *Advances in Space Research* 22.1, pp. 7–16. ISSN: 0273-1177. DOI: `10.1016/S0273-1177(97)01095-8`.

Balogh, A. and R. A. Treumann (2013). *Physics of Collisionless Shocks: Space Plasma Shock Waves.* New York, NY: Springer. ISBN: 978-1-4614-6098-5 978-1-4614-6099-2. DOI: `10.1007/978-1-4614-6099-2`.

Banks, P. (1966). “Collision Frequencies and Energy Transfer Ions”. In: *Planetary and Space Science* 14.11, pp. 1105–1122. ISSN: 0032-0633. DOI: `10.1016/0032-0633(66)90025-0`.

Banks, P. M. and G. Kockarts (1973a). *Aeronomy Part A.* 1st ed. New York and London: Academic Press. ISBN: 978-0-12-077801-0. DOI: `10.1016/C2013-0-10328-5`.

– (1973b). *Aeronomy Part B.* 1st ed. New York and London: Academic Press. ISBN: 978-0-12-077802-7. DOI: `10.1016/C2013-0-10329-7`.

Barlier, F., Berger, C., Falin, J.L., Kockarts, G., and Thuillier, G. (1978). “A Thermospheric Model Based on Satellite Drag Data”. In: *Annales de Geophysique* 34, pp. 9–24. URL: `https://orfeo.belnet.be/bitstream/handle/internal/6210/Barlier(1978a).pdf?sequence=1&isAllowed=y`.

Bartels, J. (1949). “The Standardized Index Ks, and the Planetary Index Kp, IATME Bull., 12 (b), 97, IUGG Publ”. In: *Office, Paris.*

Bartels, J., N. H. Heck, and H. F. Johnston (1939). “The Three-Hour-Range Index Measuring Geomagnetic Activity”. In: *Terrestrial Magnetism and Atmospheric Electricity* 44.4, pp. 411–454. DOI: `10.1029/TE044i004p00411`.

Bauer, S. J. and H. Lammer (2004). *Planetary Aeronomy.* Physics of Earth and Space Environments. Berlin, Heidelberg: Springer. ISBN: 978-3-642-05990-2 978-3-662-09362-7. DOI: `10.1007/978-3-662-09362-7`.

Baumjohann, W. (2012). *Basic Space Plasma Physics.* Ed. by R. A. Treumann. Rev. ed. New Jersey: World Scientific. xvi+479. ISBN: 978-1-84816-894-7. DOI: `10.1142/p850`.

Bayes, T. and R. Price (1763). “An Essay towards Solving a Problem in the Doctrine of Chances. By the Late Rev. Mr. Bayes, F. R. S. Communicated by Mr. Price, in a Letter to John Canton, A. M. F. R. S.” In: *Philosophical Transactions (1683-1775)* 53, pp. 370–418. ISSN: 02607085. URL: `http://www.jstor.org/stable/105741`.

Beckers, B. and P. Beckers (2012). “A General Rule for Disk and Hemisphere Partition into Equal-Area Cells”. In: *Computational Geometry* 45.7, pp. 275–283. ISSN: 0925-7721. DOI: `10.1016/j.comgeo.2012.01.011`.

Beggan, C. D. (2022). “Evidence-Based Uncertainty Estimates for the International Geomagnetic Reference Field”. In: *Earth, Planets and Space* 74.1, p. 17. ISSN: 1880-5981. DOI: `10.1186/s40623-022-01572-y`.

Berdermann, J., V. Bothmer, K. Börger, B. Görres, B. Heber, N. Jakowski, G. Reitz, et al. (2015). “Empfehlungen für die Stärkung nationaler Aktivitäten zum Thema Weltraumwetter”. In: 4. Nationalen Weltraumwetterworkshop. DLR Neustrelitz.

Berger, C., R. Biancale, M. Ill, and F. Barlier (1998). “Improvement of the Empirical Thermospheric Model DTM: DTM94 – a Comparative Review of Various Temporal Variations and Prospects in Space Geodesy Applications”. In: *Journal of Geodesy* 72.3, pp. 161–178. ISSN: 1432-1394. DOI: `10.1007/s001900050158`.

Berger, T. E., M. J. Holzinger, E. K. Sutton, and J. P. Thayer (2020). “Flying Through Uncertainty”. In: *Space Weather* 18.1, e2019SW002373. ISSN: 1542-7390. DOI: `10.1029/2019SW002373`.

Bettadpur, S. (2012). *GRACE Product Specification Document.* CSR-GR-03-02. Austin: University of Texas, Center for Space Research.

Bilitza, D. (1991). “Electron and Ion Temperature Data for Ionospheric Modelling”. In: *Advances in Space Research* 11.10, pp. 139–148. ISSN: 0273-1177. DOI: `10.1016/0273-1177(91)90336-I`.

Bilitza, D., M. Pezzopane, V. Truhlik, D. Altadill, B. W. Reinisch, and A. Pignalberi (2022). “The International Reference Ionosphere Model: A Review and Description of an Ionospheric Benchmark”. In: *Reviews of Geophysics* 60.4. ISSN: 1944-9208. DOI: `10.1029/2022RG000792`.

Birkland, K. (1908). *The Norwegian Aurora Polaris Expedition, 1902-1903.* Christiania: H. Aschelhoug. DOI: `10.5962/bhl.title.17857`.

Bishop, C. H., B. J. Etherton, and S. J. Majumdar (2001). “Adaptive Sampling with the Ensemble Transform Kalman Filter. Part I: Theoretical Aspects”. In: *Monthly Weather Review* 129.3, pp. 420–436. ISSN: 1520-0493, 0027-0644. DOI: `10.1175/1520-0493(2001)129<0420:ASWTET>2.0.CO;2`.

Bizouard, C., S. Lambert, C. Gattano, O. Becker, and J.-Y. Richard (2019). “The IERS EOP 14C04 Solution for Earth Orientation Parameters Consistent with ITRF 2014”. In: *Journal of Geodesy* 93.5, pp. 621–633. ISSN: 1432-1394. DOI: `10.1007/s00190-018-1186-3`.

Bocquet, M. and A. Farchi (2024). *Introduction to the Principles and Methods of Data Assimilation in the Geosciences.* 0.50. URL: `https://cerea.enpc.fr/HomePages/bocquet/teaching/assim-mb-en.pdf` (visited on 05/28/2024).

Bocquet, M., A. Farchi, and Q. Malartic (2021). “Online Learning of Both State and Dynamics Using Ensemble Kalman Filters”. In: *Foundations of Data Science* 3.3, pp. 305–330. DOI: `http://dx.doi.org/10.3934/fods.2020015`.

Bowman, B. R., F. A. Marcos, and M. J. Kendra (2004). “A Method For Computing Accurate Daily Atmospheric Density Values From Satellite Drag Data”. In: 14th AAS/AIAA Space Flight Mechanics Conference. San Diego: AAS Publications Office. URL: `https://spacewx.com/wp-content/uploads/2020/11/AAS_04-173_EDR_Method.pdf`.

Bowman, B. R., W. K. Tobiska, F. A. Marcos, C. Huang, C. Lin, and W. Burke (2008a). “A New Empirical Thermospheric Density Model JB2008 Using New Solar and Geomagnetic Indices”. In: *AIAA/AAS Astrodynamics Specialist Conference and Exhibit.* DOI: `10.2514/6.2008-6438`.

Bowman, B. R., W. K. Tobiska, F. A. Marcos, and C. Valladares (2008b). “The JB2006 Empirical Thermospheric Density Model”. In: *Journal of Atmospheric and Solar-Terrestrial Physics* 70.5, pp. 774–793. ISSN: 1364-6826. DOI: `10.1016/j.jastp.2007.10.002`.

Brockmann, J. M., N. Zehentner, E. Höck, R. Pail, I. Loth, T. Mayer-Gürr, and W.-D. Schuh (2014). “EGM_TIM_RL05: An Independent Geoid with Centimeter Accuracy Purely Based on the GOCE Mission”. In: *Geophysical Research Letters* 41.22, pp. 8089–8099. ISSN: 1944-8007. DOI: `10.1002/2014GL061904`.

Brockwell, P. J. and R. A. Davis (1991). *Time Series: Theory and Methods.* Springer Series in Statistics. New York, NY: Springer. ISBN: 978-1-4419-0319-8. DOI: `10.1007/978-1-4419-0320-4`.

Brockwell, T. G., K. J. Meech, K. Pickens, J. H. Waite, G. Miller, J. Roberts, J. I. Lunine, et al. (2016). “The Mass Spectrometer for Planetary Exploration (MASPEX)”. In: *2016 IEEE Aerospace Conference.* 2016 IEEE Aerospace Conference, pp. 1–17. DOI: `10.1109/AERO.2016.7500777`.

Bruinsma, S. L., E. Doornbos, and B. R. Bowman (2014). “Validation of GOCE Densities and Evaluation of Thermosphere Models”. In: *Advances in Space Research* 54.4, pp. 576–585. ISSN: 0273-1177. DOI: `10.1016/j.asr.2014.04.008`.

Bruinsma, S. (2015). “The DTM-2013 Thermosphere Model”. In: *Journal of Space Weather and Space Climate* 5, A1. ISSN: 2115-7251. DOI: `10.1051/swsc/2015001`.

Bruinsma, S. and R. Biancale (2003). “Total Densities Derived from Accelerometer Data”. In: *Journal of Spacecraft and Rockets* 40.2, pp. 230–236. ISSN: 0022-4650. DOI: `10.2514/2.3937`.

Bruinsma, S. and C. Boniface (2021). “The Operational and Research DTM-2020 Thermosphere Models”. In: *Journal of Space Weather and Space Climate* 11, p. 47. ISSN: 2115-7251. DOI: `10.1051/swsc/2021032`.

Bruinsma, S., C. Siemes, J. T. Emmert, and M. G. Mlynczak (2023). “Description and Comparison of 21st Century Thermosphere Data”. In: *Advances in Space Research.* COSPAR Space Weather Roadmap 2022: Scientific Research and Applications 72.12, pp. 5476–5489. ISSN: 0273-1177. DOI: `10.1016/j.asr.2022.09.038`.

Bruinsma, S., G. Thuillier, and F. Barlier (2003). “The DTM-2000 Empirical Thermosphere Model with New Data Assimilation and Constraints at Lower Boundary: Accuracy and Properties”. In: *Journal of Atmospheric and Solar-Terrestrial Physics* 65.9, pp. 1053–1070. ISSN: 1364-6826. DOI: `10.1016/S1364-6826(03)00137-8`.

Bruinsma, S. L., N. Sánchez-Ortiz, E. Olmedo, and N. Guijarro (2012). “Evaluation of the DTM-2009 Thermosphere Model for Benchmarking Purposes”. In: *Journal of Space Weather and Space Climate* 2, A04. ISSN: 2115-7251. DOI: `10.1051/swsc/2012005`.

Burgers, G., P. J. van Leeuwen, and G. Evensen (1998). “Analysis Scheme in the Ensemble Kalman Filter”. In: *Monthly Weather Review* 126.6, pp. 1719–1724. ISSN: 1520-0493, 0027-0644. DOI: `10.1175/1520-0493(1998)126<1719:ASITEK>2.0.CO;2`.

Cai, Y., X. Yue, W. Wang, S.-R. Zhang, H. Liu, D. Lin, H. Wu, et al. (2022). “Altitude Extension of the NCAR-TIEGCM (TIEGCM-X) and Evaluation”. In: *Space Weather* 20.11. ISSN: 1542-7390. DOI: `10.1029/2022SW003227`.

Carignan, G. R., B. P. Block, J. C. Maurer, A. E. Hedin, C. A. Reber, and N. W. Spencer (1981). “The Neutral Mass Spectrometer on Dynamics Explorer B”. In: *Space Science Instrumentation* 5. URL: `https://ntrs.nasa.gov/citations/19820032902` (visited on 02/05/2025).

Carrington, R. C. (1859). “Description of a Singular Appearance Seen in the Sun on September 1, 1859”. In: *Monthly Notices of the Royal Astronomical Society* 20.1, pp. 13–15. ISSN: 0035-8711. DOI: `10.1093/mnras/20.1.13`.

Chambre, P. A. and S. A. Schaaf (2017). “Flow of Rarefied Gases”. In: *Flow of Rarefied Gases.* Princeton University Press. ISBN: 978-1-4008-8580-0. DOI: `10.1515/9781400885800`.

Chapman, S. C., S. W. McIntosh, R. J. Leamon, and N. W. Watkins (2020). “Quantifying the Solar Cycle Modulation of Extreme Space Weather”. In: *Geophysical Research Letters* 47.11. ISSN: 1944-8007. DOI: `10.1029/2020GL087795`.

Chapman, S. (1970). *The Mathematical Theory of Non Uniform Gases an Account of the Kinetic Theory of Viscosity, Thermal Conduction and Diffusion in Gases.* Ed. by T. G. Cowling. 3rd ed. Cambridge: Univ. Press. xxiv+423. ISBN: 978-0-521-07577-0.

Chartier, A. T., T. Matsuo, J. L. Anderson, N. Collins, T. J. Hoar, G. Lu, C. N. Mitchell, et al. (2016). “Ionospheric Data Assimilation and Forecasting during Storms”. In: *Journal of Geophysical Research: Space Physics* 121.1, pp. 764–778. ISSN: 2169-9402. DOI: `10.1002/2014JA020799`.

Chassaing, P. (2022). “The Fundamental Balances of a Fluid Motion”. In: *Fundamentals of Fluid Mechanics: For Scientists and Engineers.* Ed. by P. Chassaing. Cham: Springer International Publishing, pp. 103–146. ISBN: 978-3-031-10086-4. DOI: `10.1007/978-3-031-10086-4_3`.

Chen, C. H., C. H. Lin, T. Matsuo, and W. H. Chen (2016). “Ionosphere Data Assimilation Modeling of 2015 St. Patrick’s Day Geomagnetic Storm”. In: *Journal of Geophysical Research: Space Physics* 121.11, pp. 11, 549–11, 559. ISSN: 2169-9402. DOI: `10.1002/2016JA023346`.

Christe, S., B. Zeiger, R. Pfaff, and M. Garcia (2016). “Introduction to the Special Issue on Sounding Rockets and Instrumentation”. In: *Journal of Astronomical Instrumentation* 05.01, p. 1602001. ISSN: 2251-1717. DOI: `10.1142/S2251171716020013`.

Cliver, E. W., C. J. Schrijver, K. Shibata, and I. G. Usoskin (2022). “Extreme Solar Events”. In: *Living Reviews in Solar Physics* 19.1, p. 2. ISSN: 1614-4961. DOI: `10.1007/s41116-022-00033-8`.

Cnossen, I. (2020). “Analysis and Attribution of Climate Change in the Upper Atmosphere From 1950 to 2015 Simulated by WACCM-X”. In: *Journal of Geophysical Research: Space Physics* 125.12, e2020JA028623. ISSN: 2169-9402. DOI: `10.1029/2020JA028623`.

Coddington, O., J. L. Lean, P. Pilewskie, M. Snow, and D. Lindholm (2016). “A Solar Irradiance Climate Data Record”. In: *Bulletin of the American Meteorological Society* 97.7, pp. 1265–1282. ISSN: 0003-0007, 1520-0477. DOI: `10.1175/BAMS-D-14-00265.1`.

Codrescu, M. V., T. J. Fuller-Rowell, and J. C. Foster (1995). “On the Importance of E-field Variability for Joule Heating in the High-Latitude Thermosphere”. In: *Geophysical Research Letters* 22.17, pp. 2393–2396. ISSN: 1944-8007. DOI: `10.1029/95GL01909`.

Codrescu, M. V., S. M. Codrescu, and M. Fedrizzi (2022). “Storm Time Neutral Density Assimilation in the Thermosphere Ionosphere with TIDA”. In: *Journal of Space Weather and Space Climate* 12, p. 16. ISSN: 2115-7251. DOI: `10.1051/swsc/2022011`.

Codrescu, S. M., M. V. Codrescu, and M. Fedrizzi (2018). “An Ensemble Kalman Filter for the Thermosphere-Ionosphere”. In: *Space Weather* 16.1, pp. 57–68. ISSN: 1542-7390. DOI: `10.1002/2017SW001752`.

Corbin, A. and J. Kusche (2022). “Improving the Estimation of Thermospheric Neutral Density via Two-Step Assimilation of in Situ Neutral Density into a Numerical Model”. In: *Earth, Planets and Space* 74.1, p. 183. ISSN: 1880-5981. DOI: `10.1186/s40623-022-01733-z`.

Cvitas, T. (1996). “Quantities Describing Compositions of Mixtures”. In: *Metrologia* 33.1, p. 35. ISSN: 0026-1394. DOI: `10.1088/0026-1394/33/1/5`.

Dandouras, I., M. Blanc, L. Fossati, M. Gerasimov, E. W. Guenther, K. G. Kislyakova, H. Lammer, et al. (2020). “Future Missions Related to the Determination of the Elemental and Isotopic Composition of Earth, Moon and the Terrestrial Planets”. In: *Space Science Reviews* 216.8, pp. 1–49. ISSN: 1572-9672. DOI: `10.1007/s11214-020-00736-0`.

Davies, K. (1990). *Ionospheric Radio*. IET Digital Library. ISBN: 978-1-84919-387-0. DOI: `10.1049/PBEW031E`.

De Boor, C. (1978). *A Practical Guide to Splines*. 3rd ed. Applied Mathematical Sciences 27. New York: Springer. ISBN: 978-0-387-90356-9. URL: `https://link.springer.com/book/9780387953663`.

Dehant, V. and P. M. Mathews (2015). *Precession, Nutation and Wobble of the Earth*. Cambridge: Cambridge University Press. ISBN: 978-1-107-09254-9. DOI: `10.1017/CBO9781316136133`.

Denig, W. F., D. Wilkinson, and R. J. Redmon (2018). “Chapter 12 - Extreme Space Weather Events: A GOES Perspective”. In: *Extreme Events in Geospace*. Ed. by N. Buzulukova. Elsevier, pp. 283–347. ISBN: 978-0-12-812700-1. DOI: `10.1016/B978-0-12-812700-1.00012-1`.

De Wit, T. D. and S. Bruinsma (2017). “The 30 Cm Radio Flux as a Solar Proxy for Thermosphere Density Modelling”. In: *Journal of Space Weather and Space Climate* 7, A9. ISSN: 2115-7251. DOI: `10.1051/swsc/2017008`.

De Wit, T. D., S. Bruinsma, and K. Shibasaki (2014). “Synoptic Radio Observations as Proxies for Upper Atmosphere Modelling”. In: *Journal of Space Weather and Space Climate* 4, A06. ISSN: 2115-7251. DOI: `10.1051/swsc/2014003`.

Dhadly, M. S., J. T. Emmert, D. P. Drob, J. P. McCormack, and R. J. Niciejewski (2018). “Short-Term and Interannual Variations of Migrating Diurnal and Semidiurnal Tides in the Mesosphere and Lower Thermosphere”. In: *Journal of Geophysical Research: Space Physics* 123.8, pp. 7106–7123. ISSN: 2169-9402. DOI: `10.1029/2018JA025748`.

Dickinson, R. E., E. C. Ridley, and R. G. Roble (1981). “A Three-Dimensional General Circulation Model of the Thermosphere”. In: *Journal of Geophysical Research: Space Physics* 86.A3, pp. 1499–1512. ISSN: 2156-2202. DOI: `10.1029/JA086iA03p01499`.

Domingo, V., B. Fleck, and A. I. Poland (1995). “The SOHO Mission: An Overview”. In: *Solar Physics* 162.1, pp. 1–37. ISSN: 1573-093X. DOI: `10.1007/BF00733425`.

Donaldson, J. K., T. J. Wellman, and W. L. Oliver (2010). “Long-Term Change in Thermospheric Temperature above Saint Santin”. In: *Journal of Geophysical Research: Space Physics* 115.A11. ISSN: 2156-2202. DOI: `10.1029/2010JA015346`.

Doornbos, E. (2012). *Thermospheric Density and Wind Determination from Satellite Dynamics*. Springer Theses. Berlin, Heidelberg: Springer Berlin Heidelberg. ISBN: 978-3-642-44264-3. DOI: `10.1007/978-3-642-25129-0`.

Dungey, J. W. (1961). “Interplanetary Magnetic Field and the Auroral Zones”. In: *Physical Review Letters* 6.2, pp. 47–48. DOI: `10.1103/PhysRevLett.6.47`.

Eastes, R. W., W. E. McClintock, A. G. Burns, D. N. Anderson, L. Andersson, M. Codrescu, J. T. Correira, et al. (2017). “The Global-Scale Observations of the Limb and Disk (GOLD) Mission”. In: *Space Science Reviews* 212.1, pp. 383–408. ISSN: 1572-9672. DOI: `10.1007/s11214-017-0392-2`.

Eckmann, J.-P. and D. Ruelle (1985). “Ergodic Theory of Chaos and Strange Attractors”. In: *Reviews of Modern Physics* 57.3, pp. 617–656. ISSN: 0034-6861. DOI: `10.1103/RevModPhys.57.617`.

Emmert, J. T. (2015). “Thermospheric Mass Density: A Review”. In: *Advances in Space Research* 56.5, pp. 773–824. ISSN: 0273-1177. DOI: `10.1016/j.asr.2015.05.038`.

Emmert, J. T., D. P. Drob, J. M. Picone, D. E. Siskind, M. Jones Jr., M. G. Mlynczak, P. F. Bernath, et al. (2021). “NRLMSIS 2.0: A Whole-Atmosphere Empirical Model of Temperature and Neutral Species Densities”. In: *Earth and Space Science* 8.3. ISSN: 2333-5084. DOI: `10.1029/2020EA001321`.

Emmert, J. T. and J. M. Picone (2010). “Climatology of Globally Averaged Thermospheric Mass Density”. In: *Journal of Geophysical Research: Space Physics* 115.A9. ISSN: 2156-2202. DOI: `10.1029/2010JA015298`.

Errico, R. M. (1997). “What Is an Adjoint Model?” In: *Bulletin of the American Meteorological Society* 78.11, pp. 2577–2591. ISSN: 0003-0007. URL: `https://www.jstor.org/stable/26215022` (visited on 04/22/2024).

Evensen, G. (1992). “Using the Extended Kalman Filter with a Multilayer Quasi-Geostrophic Ocean Model”. In: *Journal of Geophysical Research: Oceans* 97.C11, pp. 17905–17924. DOI: `10.1029/92JC01972`.

– (1993). “Open Boundary Conditions for the Extended Kalman Filter with a Quasi-Geostrophic Ocean Model”. In: *Journal of Geophysical Research: Oceans* 98.C9, pp. 16529–16546. DOI: `10.1029/93JC01365`.

– (1994). “Sequential Data Assimilation with a Nonlinear Quasi-Geostrophic Model Using Monte Carlo Methods to Forecast Error Statistics”. In: *Journal of Geophysical Research: Oceans* 99.C5, pp. 10143–10162. ISSN: 2156-2202. DOI: `10.1029/94JC00572`.

– (2003). “The Ensemble Kalman Filter: Theoretical Formulation and Practical Implementation”. In: *Ocean Dynamics* 53.4, pp. 343–367. ISSN: 1616-7228. DOI: `10.1007/s10236-003-0036-9`.

Evensen, G., F. C. Vossepoel, and P. J. Van Leeuwen (2022). *Data Assimilation Fundamentals: A Unified Formulation of the State and Parameter Estimation Problem.* Springer Textbooks in Earth Sciences, Geography and Environment. Cham: Springer International Publishing. ISBN: 978-3-030-96708-6 978-3-030-96709-3. DOI: `10.1007/978-3-030-96709-3`.

Fernandez-Gomez, I., T. Kodikara, C. Borries, E. Forootan, A. Goss, M. Schmidt, and M. V. Codrescu (2022). “Improving Estimates of the Ionosphere during Geomagnetic Storm Conditions through Assimilation of Thermospheric Mass Density”. In: *Earth, Planets and Space* 74.1, p. 121. ISSN: 1880-5981. DOI: `10.1186/s40623-022-01678-3`.

Flury, J., S. Bettadpur, and B. D. Tapley (2008). “Precise Accelerometry Onboard the GRACE Gravity Field Satellite Mission”. In: *Advances in Space Research* 42.8, pp. 1414–1423. ISSN: 0273-1177. DOI: `10.1016/j.asr.2008.05.004`.

Forootan, E., M. Kosary, S. Farzaneh, T. Kodikara, K. Vielberg, I. Fernandez-Gomez, C. Borries, et al. (2022). “Forecasting Global and Multi-Level Thermospheric Neutral Density and Ionospheric Electron Content by Tuning Models against Satellite-Based Accelerometer Measurements”. In: *Scientific Reports* 12.1, p. 2095. ISSN: 2045-2322. DOI: `10.1038/s41598-022-05952-y`.

Frauenfelder, U. and O. van Koert (2018). “The Restricted Three-Body Problem”. In: *The Restricted Three-Body Problem and Holomorphic Curves.* Ed. by U. Frauenfelder and O. van Koert. Cham: Springer International Publishing, pp. 57–84. ISBN: 978-3-319-72278-8. DOI: `10.1007/978-3-319-72278-8_5`.

Friis-Christensen, E., H. Lühr, D. Knudsen, and R. Haagmans (2008). “Swarm-An Earth Observation Mission Investigating Geospace”. In: *Advances in Space Research* 41.1, pp. 210–216. ISSN: 0273-1177. DOI: `10.1016/j.asr.2006.10.008`.

Fuller-Rowell,T.J., Rees, D., Quegan, S., Moffett, R.J., Codrescu, M.V., and Millward, G.H. (1996). “A Coupled Thermosphere-Ionosphere Model (CTIM)”. In: *Solar-Terrestrial Energy Program: Handbook of Ionospheric Models.* Ed. by R. W. Schunk. Logan, UT: Center for Atmospheric and Space Sciences, pp. 217–238. URL: `https://www.bc.edu/content/dam/bc1/offices/ISR/SCOSTEP/Multimedia/other/ionospheric-models.pdf`.

Gabrielse, C., S. R. Kaeppler, G. Lu, C.-P. Wang, and Y. Yu (2022). “Chapter 4 - Energetic Particle Dynamics, Precipitation, and Conductivity”. In: *Cross-Scale Coupling and Energy Transfer in the Magnetosphere-Ionosphere-Thermosphere System.* Ed. by Y. Nishimura, O. Verkhoglyadova, Y. Deng, and S.-R. Zhang. Elsevier, pp. 217–300. ISBN: 978-0-12-821366-7. DOI: `10.1016/B978-0-12-821366-7.00002-0`.

Gaffney, J. S. and N. A. Marley (2018). “Chapter 6 - Properties of Gases”. In: *General Chemistry for Engineers.* Ed. by J. S. Gaffney and N. A. Marley. Elsevier, pp. 181–212. ISBN: 978-0-12-810425-5. DOI: `10.1016/B978-0-12-810425-5.00006-0`.

Gandin, L. S. (1963). “Objective Analysis of Meteorological Fields”. In: Israel Program for Scientific Translations, 242 pp. URL: `https://www.semanticscholar.org/paper/Objective-Analysis-of-Meteorological-Fields-Gandin/54ea08011a74d7dfba009352f30be12defcb286d` (visited on 02/02/2023).

Gaposchkin, E. M. and A. J. Coster (1990). “Evaluation of Thermospheric Models and the Precipitation Index for Satellite Drag”. In: *Advances in Space Research* 10.3, pp. 303–309. ISSN: 0273-1177. DOI: `10.1016/0273-1177(90)90360-C`.

Garcia, R. F., E. Doornbos, S. Bruinsma, and H. Hebert (2014). “Atmospheric Gravity Waves Due to the Tohoku-Oki Tsunami Observed in the Thermosphere by GOCE”. In: *Journal of Geophysical Research: Atmospheres* 119.8, pp. 4498–4506. ISSN: 2169-8996. DOI: `10.1002/2013JD021120`.

Gaspari, G. and S. E. Cohn (1999). “Construction of Correlation Functions in Two and Three Dimensions”. In: *Quarterly Journal of the Royal Meteorological Society* 125.554, pp. 723–757. ISSN: 1477-870X. DOI: `10.1002/qj.49712555417`.

Gaspari, G., S. E. Cohn, J. Guo, and S. Pawson (2006). “Construction and Application of Covariance Functions with Variable Length-Fields”. In: *Quarterly Journal of the Royal Meteorological Society* 132.619, pp. 1815–1838. ISSN: 1477-870X. DOI: `10.1256/qj.05.08`.

Gold, T. (1959). “Motions in the Magnetosphere of the Earth”. In: *Journal of Geophysical Research (1896-1977)* 64.9, pp. 1219–1224. ISSN: 2156-2202. DOI: `10.1029/JZ064i009p01219`.

Gombosi, T. I. (1994). *Gaskinetic Theory.* Cambridge Atmospheric and Space Science Series. Cambridge: Cambridge University Press. ISBN: 978-0-521-43966-4. DOI: `10.1017/CBO9780511524943`.

Gosling, J. T. (2014). “Chapter 12 - The Solar Wind”. In: *Encyclopedia of the Solar System (Third Edition).* Ed. by T. Spohn, D. Breuer, and T. V. Johnson. Boston: Elsevier, pp. 261–279. ISBN: 978-0-12-415845-0. DOI: `10.1016/B978-0-12-415845-0.00012-8`.

Gosling, J. T. and V. J. Pizzo (1999). “Formation and Evolution of Corotating Interaction Regions and Their Three Dimensional Structure”. In: *Space Science Reviews* 89.1, pp. 21–52. ISSN: 1572-9672. DOI: `10.1023/A:1005291711900`.

Grid Structure and Resolution — TIEGCM 2.0 Documentation (2024). URL: `http://www.hao.ucar.edu/modeling/tgcm/tiegcm2.0/userguide/html/grid.html#altitude-coordinates-in-the-ncar-tie-gcm-and-time-gcm` (visited on 02/13/2024).

Gross, J. H. (2017). *Mass Spectrometry a Textbook.* 3rd ed. Cham: Springer. ISBN: 978-3-319-54397-0. DOI: `10.1007/978-3-319-54398-7`.

Gu, Y. and D. S. Oliver (2007). “An Iterative Ensemble Kalman Filter for Multiphase Fluid Flow Data Assimilation”. In: *SPE Journal* 12.04, pp. 438–446. ISSN: 1086-055X. DOI: `10.2118/108438-PA`.

Gustafson, J. L. (2011). “Amdahl’s Law”. In: *Encyclopedia of Parallel Computing.* Ed. by D. Padua. Boston, MA: Springer US, pp. 53–60. ISBN: 978-0-387-09766-4. DOI: `10.1007/978-0-387-09766-4_77`.

Hagan, M. E. and J. M. Forbes (2002). “Migrating and Nonmigrating Diurnal Tides in the Middle and Upper Atmosphere Excited by Tropospheric Latent Heat Release”. In: *Journal of Geophysical Research: Atmospheres* 107.D24, ACL 6-1-ACL 6–15. ISSN: 2156-2202. DOI: `10.1029/2001JD001236`.

Häggström, I. (2021). “3.8. Incoherent and Coherent Scatter Radars”. In: *3.8. Incoherent and Coherent Scatter Radars.* EDP Sciences, pp. 117–126. ISBN: 978-2-7598-1949-2. DOI: `10.1051/978-2-7598-1949-2.c012`.

Hajj, G. A., E. R. Kursinski, L. J. Romans, W. I. Bertiger, and S. S. Leroy (2002). “A Technical Description of Atmospheric Sounding by GPS Occultation”. In: *Journal of Atmospheric and Solar-Terrestrial Physics* 64.4, pp. 451–469. ISSN: 1364-6826. DOI: `10.1016/S1364-6826(01)00114-6`.

Hamill, T. M., J. S. Whitaker, and C. Snyder (2001). “Distance-Dependent Filtering of Background Error Covariance Estimates in an Ensemble Kalman Filter”. In: *Monthly Weather Review* 129.11, pp. 2776–2790. ISSN: 1520-0493, 0027-0644. DOI: `10.1175/1520-0493(2001)129<2776:DDFOBE>2.0.CO;2`.

Hapgood, M. A. (1992). “Space Physics Coordinate Transformations: A User Guide”. In: *Planetary and Space Science* 40.5, pp. 711–717. ISSN: 0032-0633. DOI: `10.1016/0032-0633(92)90012-D`.

Hapgood, M. (2019). “Technological Impacts of Space Weather”. In: *Geomagnetism, Aeronomy and Space Weather: A Journey from the Earth’s Core to the Sun.* Ed. by A. Yau, E. Petrovsky, M. Mandea, and M. Korte. Special Publications of the International Union of Geodesy and Geophysics. Cambridge: Cambridge University Press, pp. 251–264. ISBN: 978-1-108-41848-5. DOI: `10.1017/9781108290135.017`.

Hapgood, M., H. Liu, and N. Lugaz (2022). “SpaceX—Sailing Close to the Space Weather?” In: *Space weather : the international journal of research & applications* 20.3. ISSN: 1542-7390. DOI: `10.1029/2022SW003074`.

Harris, I. and W. Priester (1962). “Time-Dependent Structure of the Upper Atmosphere”. In: *Journal of the Atmospheric Sciences* 19.4, pp. 286–301. ISSN: 0022-4928, 1520-0469. DOI: `10.1175/1520-0469(1962)019<0286:TDSOTU>2.0.CO;2`.

Harris, M. J. (2001). “A New Coupled Middle Atmosphere and Thermosphere General Circulation Model: Studies of Dynamic, Energetic and Photochemical Coupling in the Middle and Upper Atmosphere”. Doctoral. UCL (University College London). 293 pp. URL: `https://discovery.ucl.ac.uk/id/eprint/10097965/` (visited on 11/17/2022).

Hathaway, D. H. (2015). “The Solar Cycle”. In: *Living Reviews in Solar Physics* 12.1, p. 227. DOI: `10.1007/lrsp-2015-4`.

Hatten, N. and R. P. Russell (2017). “A Smooth and Robust Harris-Priester Atmospheric Density Model for Low Earth Orbit Applications”. In: *Advances in Space Research* 59.2, pp. 571–586. ISSN: 0273-1177. DOI: `10.1016/j.asr.2016.10.015`.

Hayakawa, H., E. W. Cliver, F. Clette, Y. Ebihara, S. Toriumi, I. Ermolli, T. Chatzistergos, et al. (2023). “The Extreme Space Weather Event of 1872 February: Sunspots, Magnetic Disturbance, and Auroral Displays”. In: *The Astrophysical Journal* 959.1, p. 23. ISSN: 0004-637X. DOI: `10.3847/1538-4357/acc6cc`.

He, C., Y. Yang, B. Carter, E. Kerr, S. Wu, F. Deleflie, H. Cai, et al. (2018). “Review and Comparison of Empirical Thermospheric Mass Density Models”. In: *Progress in Aerospace Sciences* 103, pp. 31–51. ISSN: 0376-0421. DOI: `10.1016/j.paerosci.2018.10.003`.

He, J., E. Astafyeva, X. Yue, N. M. Pedatella, D. Lin, T. J. Fuller-Rowell, M. Fedrizzi, et al. (2023). “Comparison of Empirical and Theoretical Models of the Thermospheric Density Enhancement During the 3–4 February 2022 Geomagnetic Storm”. In: *Space weather : the international journal of research & applications* 21.9. ISSN: 1542-7390. DOI: `10.1029/2023SW003521`.

Heath, D. F. and B. M. Schlesinger (1986). “The Mg 280-Nm Doublet as a Monitor of Changes in Solar Ultraviolet Irradiance”. In: *Journal of Geophysical Research: Atmospheres* 91.D8, pp. 8672–8682. ISSN: 2156-2202. DOI: `10.1029/JD091iD08p08672`.

Hedin, A. E. (1983). “A Revised Thermospheric Model Based on Mass Spectrometer and Incoherent Scatter Data: MSIS-83”. In: *Journal of Geophysical Research: Space Physics* 88.A12, pp. 10170–10188. ISSN: 2156-2202. DOI: `10.1029/JA088iA12p10170`.

– (1987). “MSIS-86 Thermospheric Model”. In: *Journal of Geophysical Research: Space Physics* 92.A5, pp. 4649–4662. ISSN: 2156-2202. DOI: `10.1029/JA092iA05p04649`.

– (1991). “Extension of the MSIS Thermosphere Model into the Middle and Lower Atmosphere”. In: *Journal of Geophysical Research: Space Physics* 96.A2, pp. 1159–1172. ISSN: 2156-2202. DOI: `10.1029/90JA02125`.

Hedin, A. E., H. G. Mayr, C. A. Reber, N. W. Spencer, and G. R. Carignan (1974). “Empirical Model of Global Thermospheric Temperature and Composition Based on Data from the Ogo 6 Quadrupole Mass Spectrometer”. In: *Journal of Geophysical Research (1896-1977)* 79.1, pp. 215–225. ISSN: 2156-2202. DOI: `10.1029/JA079i001p00215`.

Hedin, A. E., J. E. Salah, J. V. Evans, C. A. Reber, G. P. Newton, N. W. Spencer, D. C. Kayser, et al. (1977). “A Global Thermospheric Model Based on Mass Spectrometer and Incoherent Scatter Data MSIS, 1. N2 Density and Temperature”. In: *Journal of Geophysical Research (1896-1977)* 82.16, pp. 2139–2147. ISSN: 2156-2202. DOI: `10.1029/JA082i016p02139`.

Heelis, R. A., J. K. Lowell, and R. W. Spiro (1982). “A Model of the High-Latitude Ionospheric Convection Pattern”. In: *Journal of Geophysical Research: Space Physics* 87.A8, pp. 6339–6345. ISSN: 2156-2202. DOI: `10.1029/JA087iA08p06339`.

Hickey, Michael Philip (1988). *THE NASA MARSHALL ENGINEERING THERMOSPHERE MODEL*. Contractor Report NASA CR - 179359. Alabama: Marshall Space Flight Center. URL: `https://ntrs.nasa.gov/api/citations/19880017376/downloads/19880017376.pdf`.

Hinteregger, H. E., K. Fukui, and B. R. Gilson (1981). “Observational, Reference and Model Data on Solar EUV, from Measurements on AE-E”. In: *Geophysical Research Letters* 8.11, pp. 1147–1150. ISSN: 1944-8007. DOI: `10.1029/GL008i011p01147`.

Ho, S.-p., R. A. Anthes, C. O. Ao, S. Healy, A. Horanyi, D. Hunt, A. J. Mannucci, et al. (2020). “The COSMIC/FORMOSAT-3 Radio Occultation Mission after 12 Years: Accomplishments, Remaining Challenges, and Potential Impacts of COSMIC-2”. In: *Bulletin of the American Meteorological Society* 101.7, E1107–E1136. ISSN: 0003-0007, 1520-0477. DOI: `10.1175/BAMS-D-18-0290.1`.

Hodgson, R. (1859). “On a Curious Appearance Seen in the Sun”. In: *Monthly Notices of the Royal Astronomical Society* 20.1, pp. 15–16. ISSN: 0035-8711. DOI: `10.1093/mnras/20.1.15`.

Hofmann-Wellenhof, B. and H. Moritz (2006). *Physical Geodesy*. 2nd ed. Springer Wien New York. ISBN: 978-3-211-33544-4. DOI: `10.1007/978-3-211-33545-1`.

Holt, J. M. and S. R. Zhang (2008). “Long-Term Temperature Trends in the Ionosphere above Millstone Hill”. In: *Geophysical Research Letters* 35.5. ISSN: 1944-8007. DOI: `10.1029/2007GL031148`.

Houtekamer, P. L. and H. L. Mitchell (1998). “Data Assimilation Using an Ensemble Kalman Filter Technique”. In: *Monthly Weather Review* 126.3, pp. 796–811. ISSN: 1520-0493, 0027-0644. DOI: `10.1175/1520-0493(1998)126<0796:DAUAEK>2.0.CO;2`.

– (2001). “A Sequential Ensemble Kalman Filter for Atmospheric Data Assimilation”. In: *Monthly Weather Review* 129.1, pp. 123–137. ISSN: 1520-0493, 0027-0644. DOI: `10.1175/1520-0493(2001)129<0123:ASEKFF>2.0.CO;2`.

Hsu, C.-T., T. Matsuo, W. Wang, and J.-Y. Liu (2014). “Effects of Inferring Unobserved Thermospheric and Ionospheric State Variables by Using an Ensemble Kalman Filter on Global Ionospheric Specification and Forecasting”. In: *Journal of Geophysical Research: Space Physics* 119.11, pp. 9256–9267. ISSN: 2169-9402. DOI: `10.1002/2014JA020390`.

Hunt, B. R., E. J. Kostelich, and I. Szunyogh (2007). “Efficient Data Assimilation for Spatiotemporal Chaos: A Local Ensemble Transform Kalman Filter”. In: *Physica D: Nonlinear Phenomena*. Data Assimilation 230.1, pp. 112–126. ISSN: 0167-2789. DOI: `10.1016/j.physd.2006.11.008`.

Ide, K., P. Courtier, M. Ghil, and A. C. Lorenc (1997). “Unified Notation for Data Assimilation : Operational, Sequential and Variational (Special Issue Data Assimilation in Meteology and Oceanography: Theory and Practice)”. In: *Journal of the Meteorological Society of Japan. Ser. II* 75 (1B), pp. 181–189. DOI: `10.2151/jmsj1965.75.1B_181`.

Ieda, A. (2021). “Atomic Oxygen Ion-Neutral Collision Frequency Models at Ionospheric Temperatures”. In: *Journal of Geophysical Research: Space Physics* 126.1. ISSN: 2169-9402. DOI: `10.1029/2020JA028441`.

IERS Conventions (2010). IERS Technical Note No. 36. Frankfurt am Main: Verlag des Bundesamts für Kartographie und Geodäsie. URL: `https://www.iers.org/SharedDocs/Publikationen/EN/IERS/Publications/tn/TechnNote36/tn36.pdf?__blob=publicationFile&v=1`.

Iijima, T. and T. A. Potemra (1978). “Large-Scale Characteristics of Field-Aligned Currents Associated with Substorms”. In: *Journal of Geophysical Research: Space Physics* 83.A2, pp. 599–615. ISSN: 2156-2202. DOI: `10.1029/JA083iA02p00599`.

Immel, T. J., S. L. England, S. B. Mende, R. A. Heelis, C. R. Englert, J. Edelstein, H. U. Frey, et al. (2017). “The Ionospheric Connection Explorer Mission: Mission Goals and Design”. In: *Space Science Reviews* 214.1, p. 13. ISSN: 1572-9672. DOI: `10.1007/s11214-017-0449-2`.

ISTOMIN, V. G. (1962). “Altitude Variations of Positive Ion Concetrations According to Mass Spectrometer Data From the Third Sputnik”. In: *ARS Journal* 32.7, pp. 1159–1161. DOI: `10.2514/8.6220`.

Jacchia, L. G. (1959a). “Corpuscular Radiation and the Acceleration of Artificial Satellites”. In: *Nature* 183.4676, pp. 1662–1663. ISSN: 1476-4687. DOI: `10.1038/1831662a0`.

– (1959b). “Two Atmospheric Effects in the Orbital Acceleration of Artificial Satellites”. In: *Nature* 183.4660, pp. 526–527. ISSN: 1476-4687. DOI: `10.1038/183526a0`.

– (1960). “A Variable Atmospheric-Density Model from Satellite Accelerations”. In: *Journal of Geophysical Research (1896-1977)* 65.9, pp. 2775–2782. ISSN: 2156-2202. DOI: `10.1029/JZ065i009p02775`.

Jacchia, L. G. (1965). “Static Diffusion Models of the Upper Atmosphere with Empirical Temperature Profiles”. In: *Smithsonian Contributions to Astrophysics; Vol.8, no.9.* ISSN: 0081-0231. URL: `http://repository.si.edu/xmlui/handle/10088/6621` (visited on 11/14/2022).

– (1970). “New Static Models of the Thermosphere and Exosphere with Empirical Temperature Profiles”. In: *SAO Special Report* 313. ISSN: 0081-0320. URL: `https://ui.adsabs.harvard.edu/abs/1970SAOSR.313.....J` (visited on 11/14/2022).

– (1971). “Revised Static Models of the Thermosphere and Exosphere with Empirical Temperature Profiles”. In: *SAO Special Report* 332. ISSN: 0081-0320. URL: `https://ui.adsabs.harvard.edu/abs/1971SAOSR.332.....J` (visited on 11/14/2022).

– (1977). *Thermospheric Temperature, Density, and Composition: New Models.* SAO-SPECIAL-REPT-375. URL: `https://ntrs.nasa.gov/citations/19770016704` (visited on 11/14/2022).

Janjić, T., L. Nerger, A. Albertella, J. Schröter, and S. Skachko (2011). “On Domain Localization in Ensemble-Based Kalman Filter Algorithms”. In: *Monthly Weather Review* 139.7, pp. 2046–2060. ISSN: 1520-0493, 0027-0644. DOI: `10.1175/2011MWR3552.1`.

“8 Applications of Linear Theory” (1970). In: *Stochastic Processes and Filtering Theory.* Ed. by A. H. Jazwinski. Vol. 64. Mathematics in Science and Engineering. Elsevier, pp. 266–331. DOI: `10.1016/S0076-5392(09)60377-5`.

Johnson, D. L. and R. E. Smith (1985). *The MSFC/J70 Orbital Atmosphere Model and the Data Bases for the MSFC Solar Activity Prediction Technique.* NAS 1.15:86522. URL: `https://ntrs.nasa.gov/citations/19860012552` (visited on 11/16/2022).

Johnson, P. V., L. W. Beegle, and I. Kanik (2012). “Mass Spectrometry in Solar System Exploration”. In: *Mass Spectrometry Handbook.* John Wiley & Sons, Ltd, pp. 389–405. ISBN: 978-1-118-18073-0. DOI: `10.1002/9781118180730.ch17`.

Julier, S. J. and J. K. Uhlmann (1997). “New Extension of the Kalman Filter to Nonlinear Systems”. In: *Signal Processing, Sensor Fusion, and Target Recognition VI.* Signal Processing, Sensor Fusion, and Target Recognition VI. Vol. 3068. SPIE, pp. 182–193. DOI: `10.1117/12.280797`.

Kalman, R. E. and R. S. Bucy (1961). “New Results in Linear Filtering and Prediction Theory”. In: *Journal of Basic Engineering* 83.1, pp. 95–108. ISSN: 0021-9223. DOI: `10.1115/1.3658902`.

Kalman, R. E. (1960). “A New Approach to Linear Filtering and Prediction Problems”. In: *Transactions of the ASME–Journal of Basic Engineering* 82 (Series D), pp. 35–45. URL: `https://www.cs.unc.edu/~welch/kalman/media/pdf/Kalman1960.pdf`.

Kedward, L. J., B. Aradi, O. Čertík, M. Curcic, S. Ehlert, P. Engel, R. Goswami, et al. (2022). “The State of Fortran”. In: *Computing in Science & Engineering* 24.2, pp. 63–72. ISSN: 1558-366X. DOI: `10.1109/MCSE.2022.3159862`.

Keith, W. and W. Heikkila (2020). *Earth’s Magnetosphere: Formed by the Low-Latitude Boundary Layer.* 2nd ed. San Diego: Elsevier Science & Technology. ISBN: 978-0-12-818160-7. DOI: `10.1016/C2017-0-04309-4`.

Kelley, Michael C. (2009). *The Earth’s Ionosphere - Plasma Physics and Electrodynamics.* 2nd ed. Vol. 96. International Geophysics. Academic Press. ISBN: 978-0-12-088425-4. DOI: `10.1016/S0074-6142(08)X0004-X`.

King-Hele, D. G. (1987). *Satellite Orbits in an Atmosphere: Theory and Applications.* Glagow and London: Blackie. ISBN: 978-0-216-92252-5.

Klinkrad, H., B. Fritsche, T. Lips, and G. Koppenwallner (2006). “Re-Entry Prediction and On-Ground Risk Estimation”. In: *Space Debris: Models and Risk Analysis.* Ed. by H. Klinkrad. Berlin, Heidelberg: Springer, pp. 241–288. ISBN: 978-3-540-37674-3. DOI: `10.1007/3-540-37674-7_9`.

Knudsen, M. (1911). “Die Molekulare Wärmeleitung Der Gase Und Der Akkommodationskoeffizient”. In: *Annalen der Physik* 339.4, pp. 593–656. ISSN: 1521-3889. DOI: `10.1002/andp.19113390402`.

Koch, K.-R. (1999). *Parameter Estimation and Hypothesis Testing in Linear Models.* 2nd ed. Springer-Verlag Berlin Heidelberg. DOI: `10.1007/978-3-662-03976-2`.

Kodikara, T., K. Zhang, N. M. Pedatella, and C. Borries (2021). “The Impact of Solar Activity on Forecasting the Upper Atmosphere via Assimilation of Electron Density Data”. In: *Space Weather* 19.5, e2020SW002660. ISSN: 1542-7390. DOI: `10.1029/2020SW002660`.

Kokoska, S. and D. Zwillinger (2000). *CRC Standard Probability and Statistics Tables and Formulae, Student Edition.* Boca Raton: CRC Press. 200 pp. ISBN: 978-0-429-18146-7. DOI: `10.1201/b16923`.

Kuptametee, C. and N. Aunsri (2022). “A Review of Resampling Techniques in Particle Filtering Framework”. In: *Measurement* 193, p. 110836. ISSN: 0263-2241. DOI: `10.1016/j.measurement.2022.110836`.

kurtosis (2025). URL: `https://de.mathworks.com/help/stats/kurtosis.html#f4975293` (visited on 04/14/2025).

Lahoz, W., B. Khattatov, and R. Menard, eds. (2010). *Data Assimilation: Making Sense of Observations.* Berlin Heidelberg: Springer-Verlag. ISBN: 978-3-540-74702-4. DOI: `10.1007/978-3-540-74703-1`.

Lalgudi Gopalakrishnan, G. and M. Schmidt (2022). “Ionospheric Electron Density Modelling Using B-splines and Constraint Optimization”. In: *Earth, Planets and Space* 74.1, p. 143. ISSN: 1880-5981. DOI: `10.1186/s40623-022-01693-4`.

Landerer, F. W., F. M. Flechtner, H. Save, F. H. Webb, T. Bandikova, W. I. Bertiger, S. V. Bettadpur, et al. (2020). “Extending the Global Mass Change Data Record: GRACE Follow-On Instrument and Science Data Performance”. In: *Geophysical Research Letters* 47.12. ISSN: 1944-8007. DOI: `10.1029/2020GL088306`.

Larsen, M. F. (2015). “OBSERVATIONS PLATFORMS | Rockets”. In: *Encyclopedia of Atmospheric Sciences (Second Edition)*. Ed. by G. R. North, J. Pyle, and F. Zhang. Oxford: Academic Press, pp. 285–289. ISBN: 978-0-12-382225-3. DOI: `10.1016/B978-0-12-382225-3.00258-9`.

Laundal, K. M. and A. D. Richmond (2017). “Magnetic Coordinate Systems”. In: *Space Science Reviews* 206.1, pp. 27–59. ISSN: 1572-9672. DOI: `10.1007/s11214-016-0275-y`.

Ledoit, O. and M. Wolf (2004). “A Well-Conditioned Estimator for Large-Dimensional Covariance Matrices”. In: *Journal of Multivariate Analysis* 88.2, pp. 365–411. ISSN: 0047-259X. DOI: `10.1016/S0047-259X(03)00096-4`.

Lee, I. T., T. Matsuo, A. D. Richmond, J. Y. Liu, W. Wang, C. H. Lin, J. L. Anderson, et al. (2012). “Assimilation of FORMOSAT-3/COSMIC Electron Density Profiles into a Coupled Thermosphere/Ionosphere Model Using Ensemble Kalman Filtering”. In: *Journal of Geophysical Research: Space Physics* 117.A10. ISSN: 2156-2202. DOI: `10.1029/2012JA017700`.

Lermusiaux, P. F. J. and A. R. Robinson (1999). “Data Assimilation via Error Subspace Statistical Estimation.Part I: Theory and Schemes”. In: *Monthly Weather Review* 127.7, pp. 1385–1407. ISSN: 1520-0493, 0027-0644. DOI: `10.1175/1520-0493(1999)127<1385:DAVESS>2.0.CO;2`.

Leroy, S. S. (2015). “SATELLITES AND SATELLITE REMOTE SENSING | GPS Meteorology”. In: *Encyclopedia of Atmospheric Sciences (Second Edition)*. Ed. by G. R. North, J. Pyle, and F. Zhang. Oxford: Academic Press, pp. 77–86. ISBN: 978-0-12-382225-3. DOI: `10.1016/B978-0-12-382225-3.00350-9`.

Lhotka, C. and Y. Narita (2019). “Kinematic Models of the Interplanetary Magnetic Field”. In: *Annales Geophysicae* 37.3, pp. 299–314. ISSN: 0992-7689. DOI: `10.5194/angeo-37-299-2019`.

Li, R., J. Lei, J. Kusche, T. Dang, F. Huang, X. Luan, S.-R. Zhang, et al. (2023). “Large-Scale Disturbances in the Upper Thermosphere Induced by the 2022 Tonga Volcanic Eruption”. In: *Geophysical Research Letters* 50.3. ISSN: 1944-8007. DOI: `10.1029/2022GL102265`.

Liddle, A. and J. Loveday (2008). “Lyman Alpha”. In: *The Oxford Companion to Cosmology*. Oxford University Press. ISBN: 978-0-19-860858-5. URL: `https://www.oxfordreference.com/display/10.1093/acref/9780198608585.001.0001/acref-9780198608585-e-237` (visited on 05/28/2024).

Limberger, M. (2015). “Ionosphere Modeling from GPS Radio Occultations and Complementary Data Based on B-splines”. Technische Universität München. URL: `https://mediatum.ub.tum.de/1254715` (visited on 01/18/2024).

Liou, Y. (2010). *Radio Occultation Method for Remote Sensing of the Atmosphere and Ionosphere*. IntechOpen. ISBN: 978-953-7619-60-2. DOI: `10.5772/151`.

Lips, T. and B. Fritsche (2005). “A Comparison of Commonly Used Re-Entry Analysis Tools”. In: *Acta Astronautica*. Infinite Possibilities Global Realities, Selected Proceedings of the 55th International Astronautical Federation Congress, Vancouver, Canada, 4-8 October 2004 57.2, pp. 312–323. ISSN: 0094-5765. DOI: `10.1016/j.actaastro.2005.03.010`.

List, R. J. (1951). *Smithsonian Meteorological Tables*. 6th ed. Vol. 114. Smithsonian Miscellaneous Collections. Washington: Smithsonian institution press. URL: `http://repository.si.edu/xmlui/handle/10088/23746` (visited on 02/10/2025).

Liu, H.-L. (2016). “Variability and Predictability of the Space Environment as Related to Lower Atmosphere Forcing”. In: *Space weather : the international journal of research & applications* 14.9, pp. 634–658. ISSN: 1542-7390. DOI: `10.1002/2016SW001450`.

Liu, H.-L., C. G. Bardeen, B. T. Foster, P. Lauritzen, J. Liu, G. Lu, D. R. Marsh, et al. (2018). “Development and Validation of the Whole Atmosphere Community Climate Model With Thermosphere and Ionosphere Extension (WACCM-X 2.0)”. In: *Journal of Advances in Modeling Earth Systems* 10.2, pp. 381–402. ISSN: 1942-2466. DOI: `10.1002/2017MS001232`.

Liu, Y. D., H. Hu, R. Wang, Z. Yang, B. Zhu, Y. A. Liu, J. G. Luhmann, et al. (2015). “Plasma And Magnetic Field Characteristics Of Solar Coronal Mass Ejections In Relation To Geomagnetic Storm Intensity And Variability”. In: *The Astrophysical Journal Letters* 809.2, p. L34. ISSN: 2041-8205. DOI: `10.1088/2041-8205/809/2/L34`.

Lopez, R. E., D. N. Baker, and J. Allen (2004). “Sun Unleashes Halloween Storm”. In: *Eos, Transactions American Geophysical Union* 85.11, pp. 105–108. ISSN: 2324-9250. DOI: `10.1029/2004EO110002`.

Lorenz, E. (1995). “Predictability: A Problem Partly Solved”. In: *Seminar on Predictability, 4-8 September 1995*. Vol. 1. Shinfield Park, Reading: ECMWF / ECMWF, pp. 1–18. URL: `https://www.ecmwf.int/node/10829`.

Love, J. J., H. Hayakawa, and E. W. Cliver (2019). “Intensity and Impact of the New York Railroad Superstorm of May 1921”. In: *Space weather : the international journal of research & applications* 17.8, pp. 1281–1292. ISSN: 1542-7390. DOI: `10.1029/2019SW002250`.

Love, J. J. and K. J. Remick (2007). “Magnetic Indices”. In: *Encyclopedia of Geomagnetism and Paleomagnetism*. Ed. by D. Gubbins and E. Herrero-Bervera. Dordrecht: Springer Netherlands, pp. 509–512. ISBN: 978-1-4020-4423-6. DOI: `10.1007/978-1-4020-4423-6_178`.

Luhmann, J. and S. C. Solomon (2014). “Chapter 22 - Space Weather”. In: *Encyclopedia of the Solar System*. Ed. by T. Spohn, D. Breuer, and T. V. Johnson. 3rd ed. Boston: Elsevier, pp. 479–492. ISBN: 978-0-12-415845-0. DOI: `10.1016/B978-0-12-415845-0.00022-0`.

Lyman, T. (1906). “The Spectrum of Hydrogen in the Region of Extremely Short Wave-Lengths”. In: *The Astrophysical Journal* 23, p. 181. ISSN: 0004-637X. DOI: `10.1086/141330`.

Mahaffy, P. (1999). "Mass Spectrometers Developed for Planetary Missions". In: *Laboratory Astrophysics and Space Research*. Ed. by P. Ehrenfreund, C. Krafft, H. Kochan, and V. Pirronello. Astrophysics and Space Science Library. Dordrecht: Springer Netherlands, pp. 355–376. ISBN: 978-94-011-4728-6. DOI: `10.1007/978-94-011-4728-6_13`.

Maini, A. K. and V. Agrawal (2014). *Satellite Technology: Principles and Applications, 3rd Edition*. 3rd ed. United Kingdom: John Wiley & Sons Ltd. ISBN: 978-1-118-63637-4. URL: `https://www.wiley.com/en-us/Satellite+Technology%3A+Principles+and+Applications%2C+3rd+Edition-p-9781118636374` (visited on 01/27/2025).

Malartic, Q., A. Farchi, and M. Bocquet (2022). "State, Global, and Local Parameter Estimation Using Local Ensemble Kalman Filters: Applications to Online Machine Learning of Chaotic Dynamics". In: *Quarterly Journal of the Royal Meteorological Society* 148.746, pp. 2167–2193. ISSN: 1477-870X. DOI: `10.1002/qj.4297`.

March, G. (2020). "Consistent Thermosphere Density and Wind Data from Satellite Observations: A Study of Satellite Aerodynamics and Thermospheric Products". DOI: `10.4233/uuid:862e11b6-4018-4f63-8332-8f88066b0c5c`.

March, G., J. van den IJssel, C. Siemes, P. N. A. M. Visser, E. N. Doornbos, and M. Pilinski (2021). "Gas-Surface Interactions Modelling Influence on Satellite Aerodynamics and Thermosphere Mass Density". In: *Journal of Space Weather and Space Climate* 11, p. 54. ISSN: 2115-7251. DOI: `10.1051/swsc/2021035`.

Marchaudon, A. (2019). "New Insights in Far-Space Measurements: Large-Scale Structures and Processes in the Solar Wind and Terrestrial Magnetosphere". In: *Geomagnetism, Aeronomy and Space Weather: A Journey from the Earth's Core to the Sun*. Ed. by A. Yau, E. Petrovsky, M. Mandea, and M. Korte. Special Publications of the International Union of Geodesy and Geophysics. Cambridge: Cambridge University Press, pp. 98–112. ISBN: 978-1-108-41848-5. DOI: `10.1017/9781108290135.009`.

Marcos, F., B. Bowman, and R. Sheehan (2006). "Accuracy of Earth's Thermospheric Neutral Density Models". In: *AIAA/AAS Astrodynamics Specialist Conference and Exhibit*. Guidance, Navigation, and Control and Co-located Conferences. American Institute of Aeronautics and Astronautics. DOI: `10.2514/6.2006-6167`.

Marcos, F. A. (1990). "Accuracy of Atmospheric Drag Models at Low Satellite Altitudes". In: *Advances in Space Research* 10.3, pp. 417–422. ISSN: 0273-1177. DOI: `10.1016/0273-1177(90)90381-9`.

Matsuo, T., M. Fedrizzi, T. J. Fuller-Rowell, and M. V. Codrescu (2012). "Data Assimilation of Thermospheric Mass Density". In: *Space Weather* 10.5. ISSN: 1542-7390. DOI: `10.1029/2012SW000773`.

Matsuo, T., I.-T. Lee, and J. L. Anderson (2013). "Thermospheric Mass Density Specification Using an Ensemble Kalman Filter". In: *Journal of Geophysical Research: Space Physics* 118.3, pp. 1339–1350. ISSN: 2169-9402. DOI: `10.1002/jgra.50162`.

Matzka, J., C. Stolle, Y. Yamazaki, O. Bronkalla, and A. Morschhauser (2021a). "The Geomagnetic Kp Index and Derived Indices of Geomagnetic Activity". In: *Space weather : the international journal of research & applications* n/a.n/a. DOI: `10.1029/2020SW002641`.

Matzka, J., O. Bronkalla, K. Tornow, K. Elger, and C. Stolle (2021b). *Geomagnetic Kp Index*. Version 1.0. GFZ Data Services. DOI: `10.5880/KP.0001`.

Maute, A., A. D. Richmond, G. Lu, D. J. Knipp, Y. Shi, and B. Anderson (2021). "Magnetosphere-Ionosphere Coupling via Prescribed Field-Aligned Current Simulated by the TIEGCM". In: *Journal of Geophysical Research: Space Physics* 126.1. ISSN: 2169-9402. DOI: `10.1029/2020JA028665`.

McDowell, J. C. (2025). *General Catalog of Artificial Space Objects*. Version 1.6.1. URL: `https://planet4589.org/space/gcat` (visited on 02/17/2025).

Message Passing Interface Forum (2023). *MPI: A Message-Passing Interface Standard Version 4.1*. manual. URL: `https://www.mpi-forum.org/docs/mpi-4.1/mpi41-report.pdf`.

Milan, S. E. (2009). "Both Solar Wind-Magnetosphere Coupling and Ring Current Intensity Control of the Size of the Auroral Oval". In: *Geophysical Research Letters* 36.18. ISSN: 1944-8007. DOI: `10.1029/2009GL039997`.

Milan, S. E. and A. Grocott (2021). "High Latitude Ionospheric Convection". In: *Ionosphere Dynamics and Applications*. American Geophysical Union (AGU), pp. 21–47. ISBN: 978-1-119-81561-7. DOI: `10.1002/9781119815617.ch2`.

Miller, R. N., M. Ghil, and F. Gauthiez (1994). "Advanced Data Assimilation in Strongly Nonlinear Dynamical Systems". In: *Journal of Atmospheric Sciences* 51.8, pp. 1037–1056. DOI: `10.1175/1520-0469(1994)051<1037:ADAISN>2.0.CO;2`.

Millward, G. H., I. C. F. Müller-Wodarg, A. D. Aylward, T. J. Fuller-Rowell, A. D. Richmond, and R. J. Moffett (2001). "An Investigation into the Influence of Tidal Forcing on F Region Equatorial Vertical Ion Drift Using a Global Ionosphere-Thermosphere Model with Coupled Electrodynamics". In: *Journal of Geophysical Research: Space Physics* 106.A11, pp. 24733–24744. ISSN: 2156-2202. DOI: `10.1029/2000JA000342`.

Millward, G.H., Moffett, R.J., Quegan, S., and Fuller-Rowell,T.J. (1996). "A Coupled Thermosphere-Ionosphere-PlasmasphereModel (CTIP)". In: *Solar-Terrestrial Energy Program: Handbook of Ionospheric Models*. Ed. by R. W. Schunk. Logan, UT: Center for Atmospheric and Space Sciences, pp. 239–279. URL: `https://www.bc.edu/content/dam/bc1/offices/ISR/SCOSTEP/Multimedia/other/ionospheric-models.pdf`.

Minzner, R. A., C. A. Reber, L. G. Jacchia, F. T. Huang, A. E. Cole, A. J. Kantor, T. J. Keneshea, et al. (1976). *Defining Constants, Equations, and Abbreviated Tables of the 1975 US Standard Atmosphere*. 19760017709. National Aeronautics and Space Administration. URL: `https://ntrs.nasa.gov/citations/19760017709`.

Montenbruck, O. and E. Gill (2000). *Satellite Orbits: Models, Methods and Applications.* Corr., 3.print. Berlin u.a.: Springer. ISBN: 978-3-642-63547-2. DOI: `10.1007/978-3-642-58351-3`.

Moreaux, G. (2008). "Compactly Supported Radial Covariance Functions". In: *Journal of Geodesy* 82.7, pp. 431–443. ISSN: 1432-1394. DOI: `10.1007/s00190-007-0195-4`.

Morozov, A. V., A. J. Ridley, D. S. Bernstein, N. Collins, T. J. Hoar, and J. L. Anderson (2013). "Data Assimilation and Driver Estimation for the Global Ionosphere–Thermosphere Model Using the Ensemble Adjustment Kalman Filter". In: *Journal of Atmospheric and Solar-Terrestrial Physics* 104, pp. 126–136. ISSN: 1364-6826. DOI: `10.1016/j.jastp.2013.08.016`.

Müller Jürgen, J. (1999). "Zeitskalen". In: *3. DFG-Rundgespräch zum Thema Bezugssysteme.* Ed. by M. Schneider. Vol. 5. Mitteilungen des Bundesamtes für Kartographie und Geodäsie 5. Frankfurt am Main: Bkg, pp. 77–83. ISBN: 978-3-88648-079-1.

Nerger, L. (2024). *PDAF (Parallel Data Assimilation Framework).* Zenodo. DOI: `10.5281/ZENODO.13789628`.

Nerger, L., S. Danilov, W. Hiller, and J. Schröter (2006). "Using Sea-Level Data to Constrain a Finite-Element Primitive-Equation Ocean Model with a Local SEIK Filter". In: *Ocean Dynamics* 56.5, pp. 634–649. ISSN: 1616-7228. DOI: `10.1007/s10236-006-0083-0`.

Nerger, L. and W. Hiller (2013). "Software for Ensemble-Based Data Assimilation Systems—Implementation Strategies and Scalability". In: *Computers & Geosciences.* Ensemble Kalman Filter for Data Assimilation 55, pp. 110–118. ISSN: 0098-3004. DOI: `10.1016/j.cageo.2012.03.026`.

Nerger, L., W. Hiller, and J. Schröter (2005). "PDAF-the Parallel Data Assimilation Framework: Experiences with Kalman Filtering". In: *Use of High Performance Computing in Meteorology.* World Scientific, pp. 63–83. DOI: `10.1142/9789812701831_0006`.

Nerger, L., T. Janjić, J. Schröter, and W. Hiller (2012a). "A Regulated Localization Scheme for Ensemble-Based Kalman Filters". In: *Quarterly Journal of the Royal Meteorological Society* 138.664, pp. 802–812. ISSN: 1477-870X. DOI: `10.1002/qj.945`.

– (2012b). "A Unification of Ensemble Square Root Kalman Filters". In: *Monthly Weather Review* 140.7, pp. 2335–2345. DOI: `10.1175/MWR-D-11-00102.1`.

Nerger, L., Q. Tang, and L. Mu (2020). "Efficient Ensemble Data Assimilation for Coupled Models with the Parallel Data Assimilation Framework: Example of AWI-CM (AWI-CM-PDAF 1.0)". In: *Geoscientific Model Development* 13.9, pp. 4305–4321. ISSN: 1991-959X. DOI: `10.5194/gmd-13-4305-2020`.

Nicolls, M. J., H. Bahcivan, I. Häggström, and M. Rietveld (2014). "Direct Measurement of Lower Thermospheric Neutral Density Using Multifrequency Incoherent Scattering". In: *Geophysical Research Letters* 41.23, pp. 8147–8154. ISSN: 1944-8007. DOI: `10.1002/2014GL062204`.

NOAA (2023). *NOAA Space Weather Scales.* URL: `https://www.swpc.noaa.gov/sites/default/files/images/NOAAscales.pdf` (visited on 03/28/2025).

Oberheide, J., M. E. Hagan, A. D. Richmond, and J. M. Forbes (2015). "DYNAMICAL METEOROLOGY | Atmospheric Tides". In: *Encyclopedia of Atmospheric Sciences (Second Edition).* Ed. by G. R. North, J. Pyle, and F. Zhang. Oxford: Academic Press, pp. 287–297. ISBN: 978-0-12-382225-3. DOI: `10.1016/B978-0-12-382225-3.00409-6`.

Oliver, W. L., S.-R. Zhang, and L. P. Goncharenko (2013). "Is Thermospheric Global Cooling Caused by Gravity Waves?" In: *Journal of Geophysical Research: Space Physics* 118.6, pp. 3898–3908. ISSN: 2169-9402. DOI: `10.1002/jgra.50370`.

Ott, E., B. R. Hunt, I. Szunyogh, A. V. Zimin, E. J. Kos ich, M. Corazza, E. Kalnay, et al. (2004). "A Local Ensemble Kalman Filter for Atmospheric Data Assimilation". In: *Tellus Series A-dynamic Meteorology and Oceanography* 56.5, pp. 415–428. ISSN: 1600-0870. DOI: `10.1111/j.1600-0870.2004.00076.x`.

Owens, M. J., N. U. Crooker, and M. Lockwood (2011). "How Is Open Solar Magnetic Flux Lost over the Solar Cycle?" In: *Journal of Geophysical Research: Space Physics* 116.A4. ISSN: 2156-2202. DOI: `10.1029/2010JA016039`.

Owens, J.K. (2002). *NASA Marshall Engineering Model-Version 2.0 Thermosphere.* NASA / TM–2002-211786. Alabama: Marshall Space Flight Center. URL: `https://ntrs.nasa.gov/api/citations/20020052422/downloads/20020052422.pdf`.

Paetzold, H. K. and H. Zschorner (1961). *The Structure of the Upper Atmosphere and Its Variations after Satellite Observations*, p. 958. URL: `https://ui.adsabs.harvard.edu/abs/1961spre.conf..958P` (visited on 02/16/2024).

Palmer, P. T. and T. F. Limero (2001). "Mass Spectrometry in the U.S. Space Program: Past, Present, and Future". In: *Journal of the American Society for Mass Spectrometry* 12.6, pp. 656–675. DOI: `10.1016/S1044-0305(01)00249-5`.

Palmroth, M., M. Grandin, T. Sarris, E. Doornbos, S. Tourgaidis, A. Aikio, S. Buchert, et al. (2021). "Lower-Thermosphere–Ionosphere (LTI) Quantities: Current Status of Measuring Techniques and Models". In: *Annales Geophysicae* 39.1, pp. 189–237. ISSN: 0992-7689. DOI: `10.5194/angeo-39-189-2021`.

Pan, Q., C. Xiong, H. Lühr, A. Smirnov, Y. Huang, C. Xu, X. Yang, et al. (2024). "Machine Learning Based Modeling of Thermospheric Mass Density". In: *Space Weather* 22.5. ISSN: 1542-7390. DOI: `10.1029/2023SW003844`.

Papitashvili, N. E. and J. H. King (2020a). *OMNI 1-Min Data Set.* NASA Space Physics Data Facility. DOI: `10.48322/45BB-8792`.

– (2020b). *OMNI 5-Min Data Set.* NASA Space Physics Data Facility. DOI: `10.48322/GBPG-5R77`.

– (2020c). *OMNI Hourly Data Set.* NASA Space Physics Data Facility. DOI: `10.48322/1SHR-HT18`.

Parker, E. N. (1958). "Dynamics of the Interplanetary Gas and Magnetic Fields." In: *The Astrophysical Journal* 128, p. 664. ISSN: 0004-637X. DOI: `10.1086/146579`.

Parker, W. E., M. K. Brown, and R. Linares (2025). "Greenhouse Gases Reduce the Satellite Carrying Capacity of Low Earth Orbit". In: *Nature Sustainability*, pp. 1–10. ISSN: 2398-9629. DOI: `10.1038/s41893-025-01512-0`.

Parks, G. K. (2015). "Magnetosphere". In: *Encyclopedia of Atmospheric Sciences (Second Edition).* Ed. by G. R. North, J. Pyle, and F. Zhang. Oxford: Academic Press, pp. 309–315. ISBN: 978-0-12-382225-3. DOI: `10.1016/B978-0-12-382225-3.00211-5`.

Payne, C. H. (1925). *Stellar Atmospheres: A Contribution to the Observational Study of High Temperature in the Reversing Layers of Stars.* Harvard Observatory Monographs. Harlow Shapley, Editor.No. 1. Cambridge, Mass.: The Observatory. 215 pp. URL: `https://articles.adsabs.harvard.edu/pdf/1925HarMo...1.....P`.

Peddakotla, S. A., J. Yuan, E. Minisci, M. Vasile, and M. Fossati (2023). "A Numerical Approach to Evaluate Temperature-Dependent Peridynamics Damage Model for Destructive Atmospheric Entry of Spacecraft". In: *The Aeronautical Journal* 127.1309, pp. 398–427. ISSN: 0001-9240, 2059-6464. DOI: `10.1017/aer.2022.69`.

Pham, D. T., J. Verron, and L. Gourdeau (1998). "Singular evolutive Kalman filters for data assimilation in oceanography". In: *Comptes Rendus de l'Academie des Sciences Series IIA Earth and Planetary Science* 4.326, pp. 255–260. ISSN: 1251-8050. URL: `https://www.infona.pl//resource/bwmeta1.element.elsevier-55754e63-0d65-35da-a1c0-e08ef0b79731` (visited on 02/02/2023).

Picone, J. M., A. E. Hedin, D. P. Drob, and A. C. Aikin (2002). "NRLMSISE-00 Empirical Model of the Atmosphere: Statistical Comparisons and Scientific Issues". In: *Journal of Geophysical Research: Space Physics* 107.A12, SIA 15-1-SIA 15–16. ISSN: 2156-2202. DOI: `10.1029/2002JA009430`.

Pizzo, V. (1978). "A Three-Dimensional Model of Corotating Streams in the Solar Wind, 1. Theoretical Foundations". In: *Journal of Geophysical Research: Space Physics* 83.A12, pp. 5563–5572. ISSN: 2156-2202. DOI: `10.1029/JA083iA12p05563`.

Prange, L. (2010). *Global Gravity Field Determination Using the GPS Measurements Made Onboard the Low Earth Orbiting Satellite CHAMP.* Vol. 81. Zürich: Schweizerische Geodätische Kommission / Swiss Geodetic Commission, p. 232. URL: `http://www.sgc.ethz.ch/sgc-volumes/sgk-81.pdf` (visited on 02/25/2025).

Prölss, G. W. (2004). *Physics of the Earth's Space Environment.* Berlin, Heidelberg: Springer Berlin Heidelberg. ISBN: 978-3-642-05979-7. DOI: `10.1007/978-3-642-97123-5`.

– (2011). "Density Perturbations in the Upper Atmosphere Caused by the Dissipation of Solar Wind Energy". In: *Surveys in Geophysics* 32.2, pp. 101–195. ISSN: 1573-0956. DOI: `10.1007/s10712-010-9104-0`.

Prša, A., P. Harmanec, G. Torres, E. Mamajek, M. Asplund, N. Capitaine, J. Christensen-Dalsgaard, et al. (2016). "Nominal Values for Selected Solar and Planetary Quantities: IAU 2015 Resolution B3". In: *The Astronomical Journal* 152, p. 41. ISSN: 0004-6256. DOI: `10.3847/0004-6256/152/2/41`.

Qian, L., A. G. Burns, B. A. Emery, B. Foster, G. Lu, A. Maute, A. D. Richmond, et al. (2014). "The NCAR TIE-GCM: A Community Model of the Coupled Thermosphere/Ionosphere System". In: *Modeling the Ionosphere–Thermosphere System.* Ed. by J. Huba, R. Schunk, and K. George. 1st ed. Geophysical Monograph Series. American Geophysical Union (AGU), pp. 73–83. DOI: `10.1002/9781118704417`.

Qian, L. and S. C. Solomon (2012). "Thermospheric Density: An Overview of Temporal and Spatial Variations". In: *Space Science Reviews* 168.1, pp. 147–173. ISSN: 1572-9672. DOI: `10.1007/s11214-011-9810-z`.

Reentry of International Space Station (ISS) Batteries into Earth's Atmosphere (2024). URL: `https://www.esa.int/Space_Safety/Space_Debris/Reentry_of_International_Space_Station_ISS_batteries_into_Earth_s_atmosphere` (visited on 10/18/2024).

Rees, M. H. and D. Luckey (1974). "Auroral Electron Energy Derived from Ratio of Spectroscopic Emissions 1. Model Computations". In: *Journal of Geophysical Research (1896-1977)* 79.34, pp. 5181–5186. ISSN: 2156-2202. DOI: `10.1029/JA079i034p05181`.

Reigber, Ch., H. Lühr, and P. Schwintzer (2002). "CHAMP Mission Status". In: *Advances in Space Research* 30.2, pp. 129–134. ISSN: 0273-1177. DOI: `10.1016/S0273-1177(02)00276-4`.

Renner, T. (2007). "Tables of Physical Quantities". In: *Quantities, Units and Symbols in Physical Chemistry.* Ed. by E. R. Cohen, T. Cvitas, J. G. Frey, B. Holström, K. Kuchitsu, R. Marquardt, I. Mills, et al. 3rd ed. The Royal Society of Chemistry. ISBN: 978-0-85404-433-7. DOI: `10.1039/9781847557889-00011`.

Richards, P. G., J. A. Fennelly, and D. G. Torr (1994). "EUVAC: A Solar EUV Flux Model for Aeronomic Calculations". In: *Journal of Geophysical Research: Space Physics* 99.A5, pp. 8981–8992. ISSN: 2156-2202. DOI: `10.1029/94JA00518`.

Richmond, A. D. (1995). "Ionospheric Electrodynamics Using Magnetic Apex Coordinates". In: *Journal of geomagnetism and geoelectricity* 47. DOI: `10.5636/jgg.47.191`.

– (2021). "Joule Heating in the Thermosphere". In: *Upper Atmosphere Dynamics and Energetics.* American Geophysical Union (AGU), pp. 1–18. ISBN: 978-1-119-81563-1. DOI: `10.1002/9781119815631.ch1`.

Richmond, A. D., E. C. Ridley, and R. G. Roble (1992). “A Thermosphere/Ionosphere General Circulation Model with Coupled Electrodynamics”. In: *Geophysical Research Letters* 19.6, pp. 601–604. ISSN: 1944-8007. DOI: `10.1029/92GL00401`.

Ridley, A. J., Y. Deng, and G. Tóth (2006). “The Global Ionosphere–Thermosphere Model”. In: *Journal of Atmospheric and Solar-Terrestrial Physics* 68.8, pp. 839–864. ISSN: 1364-6826. DOI: `10.1016/j.jastp.2006.01.008`.

Rishbeth, H. and R. G. Roble (1992). “Cooling of the Upper Atmosphere by Enhanced Greenhouse Gases — Modelling of Thermospheric and Ionospheric Effects”. In: *Planetary and Space Science* 40.7, pp. 1011–1026. ISSN: 0032-0633. DOI: `10.1016/0032-0633(92)90141-A`.

Roble, R. G. and R. E. Dickinson (1989). “How Will Changes in Carbon Dioxide and Methane Modify the Mean Structure of the Mesosphere and Thermosphere?” In: *Geophysical Research Letters* 16.12, pp. 1441–1444. ISSN: 1944-8007. DOI: `10.1029/GL016i012p01441`.

Roble, R. G. and E. C. Ridley (1994). “A Thermosphere-Ionosphere-Mesosphere-Electrodynamics General Circulation Model (Time-GCM): Equinox Solar Cycle Minimum Simulations (30–500 Km)”. In: *Geophysical Research Letters* 21.6, pp. 417–420. ISSN: 1944-8007. DOI: `10.1029/93GL03391`.

Roble, R. G., E. C. Ridley, A. D. Richmond, and R. E. Dickinson (1988). “A Coupled Thermosphere/Ionosphere General Circulation Model”. In: *Geophysical Research Letters* 15.12, pp. 1325–1328. ISSN: 1944-8007. DOI: `10.1029/GL015i012p01325`.

Rodney A., Viereck and Puga, Lawrence C. (1999). “The NOAA Mg II Core-to-Wing Solar Index: Construction of a 20-Year Time Series of Chromospheric Variability from Multiple Satellites”. In: *Journal of Geophysical Research: Space Physics* 104.A5, pp. 9995–10005. ISSN: 2156-2202. DOI: `10.1029/1998JA900163`.

Sakov, P. and P. R. Oke (2008a). “A Deterministic Formulation of the Ensemble Kalman Filter: An Alternative to Ensemble Square Root Filters”. In: *Tellus A* 60.2, pp. 361–371. ISSN: 1600-0870. DOI: `10.1111/j.1600-0870.2007.00299.x`.

– (2008b). “Implications of the Form of the Ensemble Transformation in the Ensemble Square Root Filters”. In: *Monthly Weather Review* 136.3, pp. 1042–1053. ISSN: 1520-0493, 0027-0644. DOI: `10.1175/2007MWR2021.1`.

Sakov, P., D. S. Oliver, and L. Bertino (2012). “An Iterative EnKF for Strongly Nonlinear Systems”. In: *Monthly Weather Review* 140.6, pp. 1988–2004. ISSN: 1520-0493, 0027-0644. DOI: `10.1175/MWR-D-11-00176.1`.

Sarris, T. E., E. R. Talaat, M. Palmroth, I. Dandouras, E. Armandillo, G. Kervalishvili, S. Buchert, et al. (2020). “Daedalus: A Low-Flying Spacecraft for in Situ Exploration of the Lower Thermosphere–Ionosphere”. In: *Geoscientific Instrumentation, Methods and Data Systems* 9.1, pp. 153–191. ISSN: 2193-0856. DOI: `10.5194/gi-9-153-2020`.

Schindelegger, M., T. Sakazaki, and M. Green (2023). “Chapter 16 - Atmospheric Tides—An Earth System Signal”. In: *A Journey Through Tides.* Ed. by M. Green and J. C. Duarte. Elsevier, pp. 389–416. ISBN: 978-0-323-90851-1. DOI: `10.1016/B978-0-323-90851-1.00007-8`.

Schreiner, W., J. Weiss, R. Anthes, J. Braun, V. Chu, J. Fong, D. Hunt, et al. (2020). “COSMIC-2 Radio Occultation Constellation: First Results”. In: *Geophysical Research Letters* 47.4, e2019GL086841. ISSN: 1944-8007. DOI: `10.1029/2019GL086841`.

Schuh, W.-D. (2017). “Signalverarbeitung in der Physikalischen Geodäsie”. In: *Erdmessung und Satellitengeodäsie: Handbuch der Geodäsie, herausgegeben von Willi Freeden und Reiner Rummel.* Ed. by R. Rummel. Springer Reference Naturwissenschaften. Berlin, Heidelberg: Springer, pp. 73–121. ISBN: 978-3-662-47100-5. DOI: `10.1007/978-3-662-47100-5_15`.

Schunk, R. and A. Nagy (2009). *Ionospheres: Physics, Plasma Physics, and Chemistry.* 2nd ed. Cambridge Atmospheric and Space Science Series. Cambridge: Cambridge University Press. ISBN: 978-0-521-87706-0. DOI: `10.1017/CBO9780511635342`.

Schunk, R. W., L. Scherliess, J. J. Sojka, D. C. Thompson, D. N. Anderson, M. Codrescu, C. Minter, et al. (2004). “Global Assimilation of Ionospheric Measurements (GAIM)”. In: *Radio Science* 39.1. ISSN: 1944-799X. DOI: `10.1029/2002RS002794`.

Schwabe, H. (1844). “Sonnen — Beobachtungen Im Jahre 1843”. In: *Astronomische Nachrichten* 21.15, pp. 234–235. DOI: `10.1002/asna.18440211505`.

Sehnal, L. (1988). “Thermospheric Total Density Model TD.” In: *Bulletin of the Astronomical Institutes of Czechoslovakia* 39, pp. 120–127. ISSN: 0004-6248. URL: `https://ui.adsabs.harvard.edu/abs/1988BAICz..39..120S` (visited on 11/18/2022).

Sentman, L. H. (1961). *Free Molecule Flow Theory and Its Application to the Determination of Aerodynamic Forces.* AD0265409. Sunnyvale: Lockheed Missiles and Space Company, p. 111. URL: `https://apps.dtic.mil/sti/citations/AD0265409` (visited on 08/29/2023).

Shapiro, R. (1970). “Smoothing, Filtering, and Boundary Effects”. In: *Reviews of Geophysics* 8.2, pp. 359–387. ISSN: 1944-9208. DOI: `10.1029/RG008i002p00359`.

– (1975). “Linear Filtering”. In: *Mathematics of Computation* 29.132, pp. 1094–1097. ISSN: 0025-5718, 1088-6842. DOI: `10.1090/S0025-5718-1975-0389356-X`.

Sheng, C., G. Lu, S. C. Solomon, W. Wang, E. Doornbos, L. A. Hunt, and M. G. Mlynczak (2017). “Thermospheric Recovery during the 5 April 2010 Geomagnetic Storm”. In: *Journal of Geophysical Research: Space Physics* 122.4, pp. 4588–4599. ISSN: 2169-9402. DOI: `10.1002/2016JA023520`.

Shimojo, M. and K. Iwai (2023). “Over Seven Decades of Solar Microwave Data Obtained with Toyokawa and Nobeyama Radio Polarimeters”. In: *Geoscience Data Journal* 10.1, pp. 114–129. ISSN: 2049-6060. DOI: `10.1002/gdj3.165`.

Siegel, P. H. (2007). “THz Instruments for Space”. In: *IEEE Transactions on Antennas and Propagation* 55.11, pp. 2957–2965. ISSN: 1558-2221. DOI: `10.1109/TAP.2007.908557`.

Siemes, C., J. de Teixeira da Encarnação, E. Doornbos, J. van den IJssel, J. Kraus, R. Pereštý, L. Grunwaldt, et al. (2016). “Swarm Accelerometer Data Processing from Raw Accelerations to Thermospheric Neutral Densities”. In: *Earth, Planets and Space* 68.1, p. 92. ISSN: 1880-5981. DOI: `10.1186/s40623-016-0474-5`.

Siemes, C., J. van den IJssel, and P. Visser (2024). “Uncertainty of Thermosphere Mass Density Observations Derived from Accelerometer and GNSS Tracking Data”. In: *Advances in Space Research* 73.10, pp. 5043–5063. ISSN: 0273-1177. DOI: `10.1016/j.asr.2024.02.057`.

Silberstein, R. (1959). “The Origin of the Current Nomenclature for the Ionospheric Layers”. In: *Journal of Atmospheric and Terrestrial Physics* 13.3, p. 382. ISSN: 0021-9169. DOI: `10.1016/0021-9169(59)90130-8`.

SILSO World Data Center (1818–2024). *The International Sunspot Number.* URL: `http://www.sidc.be/silso/datafiles` (visited on 11/13/2024).

skewness (2025). URL: `https://de.mathworks.com/help/stats/skewness.html#f1132178` (visited on 04/14/2025).

Smith, G. L., S. F. Schmidt, and L. A. McGee (1962). *Application of Statistical Filter Theory to the Optimal Estimation of Position and Velocity on Board a Circumlunar Vehicle.* NASA-TR-R-135. URL: `https://ntrs.nasa.gov/citations/19620006857` (visited on 02/01/2023).

Smith, R. E. (1998). *The Marshall Engineering Thermosphere (MET) Model.* NASA/CR-1998-207946/VOL1. URL: `https://ntrs.nasa.gov/citations/19980201847` (visited on 11/14/2022).

Smoluchowski von Smolan, M. (1898). “Ueber Wärmeleitung in Verdünnten Gasen”. In: *Annalen der Physik* 300.1, pp. 101–130. ISSN: 1521-3889. DOI: `10.1002/andp.18983000110`.

Snow, M., J. Machol, R. Viereck, T. Woods, M. Weber, D. Woodraska, and J. Elliott (2019). “A Revised Magnesium II Core-to-Wing Ratio From SORCE SOLSTICE”. In: *Earth and Space Science* 6.11, pp. 2106–2114. ISSN: 2333-5084. DOI: `10.1029/2019EA000652`.

Solomon, S. C. and L. Qian (2005). “Solar Extreme-Ultraviolet Irradiance for General Circulation Models”. In: *Journal of Geophysical Research: Space Physics* 110.A10. ISSN: 2156-2202. DOI: `10.1029/2005JA011160`.

ISO 21348 (2007). *Space Environment (Natural and Artificial) — Process for Determining Solar Irradiances.* Standard ISO 21348:2007(E). Geneva, CH: International Organization for Standardization. URL: `https://www.iso.org/standard/39911.html`.

Staff of the royal aircraft establishment (1957). “Observations on the Orbit of the First Russian Earth Satellite”. In: *Nature* 180.4593, pp. 937–941. ISSN: 1476-4687. DOI: `10.1038/180937a0`.

Stallcop, J. R., H. Partridge, and E. Levin (1991). “Resonance Charge Transfer, Transport Cross Sections, and Collision Integrals for N+(3P)–N(4S) and O+(4S)–O(3P) Interactions”. In: *The Journal of Chemical Physics* 95.9, pp. 6429–6439. ISSN: 0021-9606. DOI: `10.1063/1.461563`.

Stammer, D. and A. Cazenave, eds. (2017). *Satellite Altimetry Over Oceans and Land Surfaces.* Boca Raton: CRC Press. 643 pp. ISBN: 978-1-315-15177-9. DOI: `10.1201/9781315151779`.

Stern, R. G. (2008). *Reentry Breakup and Survivability Characteristics of the Vehicle Atmospheric Survivability Project (VASP) Vehicles:* Fort Belvoir, VA: Defense Technical Information Center. DOI: `10.21236/ADA491628`.

Storz, M. (2012). “HASDM Validation Tool Using Energy Dissipation Rates”. In: *AIAA/AAS Astrodynamics Specialist Conference and Exhibit.* American Institute of Aeronautics and Astronautics. DOI: `10.2514/6.2002-4889`.

Storz, M., B. R. Bowman, and J. Branson (2002). “High Accuracy Satellite Drag Model (HASDM)”. In: *AIAA/AAS Astrodynamics Specialist Conference and Exhibit.* Guidance, Navigation, and Control and Co-located Conferences. American Institute of Aeronautics and Astronautics. DOI: `10.2514/6.2002-4886`.

Strogatz, S. H. (2019). *Nonlinear Dynamics and Chaos: With Applications to Physics, Biology, Chemistry, and Engineering.* 2nd ed. Boca Raton: CRC Press. 532 pp. ISBN: 978-0-429-49256-3. DOI: `10.1201/9780429492563`.

Suggs, R.J. and Suggs, R.M. (2007). *Marshall Engineering Thermosphere Model, Version MET-2007.* Technical Memorandum NASA/TM—2017–218238. Huntsville, Alabama: Marshall Space Flight Center. URL: `https://ntrs.nasa.gov/api/citations/20170005172/downloads/20170005172.pdf`.

Sugiura, M. (1963). *Hourly Values of Equatorial Dst for the Igy.* NASA-TM-X-55238. URL: `https://ntrs.nasa.gov/citations/19650020355` (visited on 02/16/2024).

Sulzer, M. P. (2015). “RADAR | Incoherent Scatter Radar”. In: *Encyclopedia of Atmospheric Sciences (Second Edition).* Ed. by G. R. North, J. Pyle, and F. Zhang. Oxford: Academic Press, pp. 422–428. ISBN: 978-0-12-382225-3. DOI: `10.1016/B978-0-12-382225-3.00330-3`.

Sutton, E. K. (2018). “A New Method of Physics-Based Data Assimilation for the Quiet and Disturbed Thermosphere”. In: *Space Weather* 16.6, pp. 736–753. ISSN: 1542-7390. DOI: `10.1002/2017SW001785`.

Tapley, B. D., S. Bettadpur, M. Watkins, and C. Reigber (2004). “The Gravity Recovery and Climate Experiment: Mission Overview and Early Results”. In: *Geophysical Research Letters* 31.9. ISSN: 1944-8007. DOI: `10.1029/2004GL019920`.

Tapping, K. F. (2013). “The 10.7 Cm Solar Radio Flux (F10.7)”. In: *Space weather : the international journal of research & applications* 11.7, pp. 394–406. ISSN: 1542-7390. DOI: `10.1002/swe.20064`.

Testut, C.-E., P. Brasseur, J.-M. Brankart, and J. Verron (2003). “Assimilation of Sea-Surface Temperature and Altimetric Observations during 1992–1993 into an Eddy Permitting Primitive Equation Model of the North Atlantic Ocean”. In: *Journal of Marine Systems*. The Use of Data Assimilation in Coupled Hydrodynamic, Ecological and Bio-geo-chemical Models of the Ocean. Selected Papers from the 33rd International Liege Colloquium on Ocean Dynamics, Held in Liege, Belgium on May 7-11th, 2001. 40–41, pp. 291–316. ISSN: 0924-7963. DOI: `10.1016/S0924-7963(03)00022-8`.

Thayer, J. P., W. K. Tobiska, M. D. Pilinski, and E. K. Sutton (2021). “Remaining Issues in Upper Atmosphere Satellite Drag”. In: *Space Weather Effects and Applications*. American Geophysical Union (AGU), pp. 111–140. ISBN: 978-1-119-81557-0. DOI: `10.1002/9781119815570.ch5`.

Tippett, M. K., J. L. Anderson, C. H. Bishop, T. M. Hamill, and J. S. Whitaker (2003). “Ensemble Square Root Filters”. In: *Monthly Weather Review* 131.7, pp. 1485–1490. ISSN: 1520-0493, 0027-0644. DOI: `10.1175/1520-0493(2003)131<1485:ESRF>2.0.CO;2`.

Tobiska, W. K., B. R. Bowman, and S. D. Bouwer (2008a). *Solar and Geomagnetic Indices for the JB2008 Thermosphere Density Model*. SET TR 2008-002. Space Environment Technologies. URL: `https://spacewx.com/wp-content/uploads/2020/11/SET_TR2008_002.pdf`.

Tobiska, W. K., S. D. Bouwer, and B. R. Bowman (2008b). “The Development of New Solar Indices for Use in Thermospheric Density Modeling”. In: *Journal of Atmospheric and Solar-Terrestrial Physics* 70.5, pp. 803–819. ISSN: 1364-6826. DOI: `10.1016/j.jastp.2007.11.001`.

Tobiska, W. K. and B. R. Bowman (2005). “Improvements in Modeling Thermospheric Densities Using a New Schumann-Runge Continuum Index”. In: 2005, SA33A–08. URL: `http://sol.spacenvironment.net/~JB2008/pubs/JB2006_AAS_2006_237.pdf` (visited on 11/03/2023).

Todd, J. F. J. (1991). “Recommendations for Nomenclature and Symbolism for Mass Spectroscopy (Including an Appendix of Terms Used in Vacuum Technology). (Recommendations 1991)”. In: *Pure and Applied Chemistry* 63.10, pp. 1541–1566. ISSN: 1365-3075. DOI: `10.1351/pac199163101541`.

Todling, R. and S. E. Cohn (1994). “Suboptimal Schemes for Atmospheric Data Assimilation Based on the Kalman Filter”. In: *Monthly Weather Review* 122.11, pp. 2530–2557. ISSN: 1520-0493, 0027-0644. DOI: `10.1175/1520-0493(1994)122<2530:SSFADA>2.0.CO;2`.

Touboul, P., B. Foulon, M. Rodrigues, and J. P. Marque (2004). “In Orbit Nano-g Measurements, Lessons for Future Space Missions”. In: *Aerospace Science and Technology* 8.5, pp. 431–441. ISSN: 1270-9638. DOI: `10.1016/j.ast.2004.01.006`.

Tuan Pham, D., J. Verron, and M. Christine Roubaud (1998). “A Singular Evolutive Extended Kalman Filter for Data Assimilation in Oceanography”. In: *Journal of Marine Systems* 16.3, pp. 323–340. ISSN: 0924-7963. DOI: `10.1016/S0924-7963(97)00109-7`.

USSA66 (1966). *U.S. Standard Atmosphere Supplements, 1966*. NASA-CR-88870. URL: `https://ntrs.nasa.gov/citations/19670028571` (visited on 11/15/2022).

USSA62 (1962). *U.S. Standard Atmosphere, 1962: ICAO Standard Atmosphere to 20 Kilometers, Proposed ICAO Extension to 32 Kilometers, Tables and Data to 700 Kilometers*. URL: `https://ntrs.nasa.gov/citations/19630003300` (visited on 11/15/2022).

USSA76 (1976). *U.S. Standard Atmosphere, 1976*. NOAA-S/T-76-1562. URL: `https://ntrs.nasa.gov/citations/19770009539` (visited on 11/15/2022).

Vadas, S. L., E. Becker, C. Figueiredo, K. Bossert, B. J. Harding, and L. C. Gasque (2023). “Primary and Secondary Gravity Waves and Large-Scale Wind Changes Generated by the Tonga Volcanic Eruption on 15 January 2022: Modeling and Comparison With ICON-MIGHTI Winds”. In: *Journal of Geophysical Research: Space Physics* 128.2. ISSN: 2169-9402. DOI: `10.1029/2022JA031138`.

Vallado, D. A. and D. Finkleman (2014). “A Critical Assessment of Satellite Drag and Atmospheric Density Modeling”. In: *Acta Astronautica* 95, pp. 141–165. ISSN: 0094-5765. DOI: `10.1016/j.actaastro.2013.10.005`.

Van Leeuwen, P. J., H. R. Künsch, L. Nerger, R. Potthast, and S. Reich (2019). “Particle Filters for High-Dimensional Geoscience Applications: A Review”. In: *Quarterly Journal of the Royal Meteorological Society* 145.723, pp. 2335–2365. ISSN: 1477-870X. DOI: `10.1002/qj.3551`.

VanZandt, T. E., W. L. Clark, and J. M. Warnock (1972). “Magnetic Apex Coordinates: A Magnetic Coordinate System for the Ionospheric F 2 Layer”. In: *Journal of Geophysical Research (1896-1977)* 77.13, pp. 2406–2411. ISSN: 2156-2202. DOI: `10.1029/JA077i013p02406`.

Vazquez, T., S. Vuppala, I. Ayodeji, L. Song, N. Grimes, and T. Evans-Nguyen (2021). “In Situ Mass Spectrometers for Applications in Space”. In: *Mass Spectrometry Reviews* 40.5, pp. 670–691. ISSN: 1098-2787. DOI: `10.1002/mas.21648`.

Verlaan, M. and A. W. Heemink (1997). “Tidal Flow Forecasting Using Reduced Rank Square Root Filters”. In: *Stochastic Hydrology and Hydraulics* 11.5, pp. 349–368. ISSN: 1435-151X. DOI: `10.1007/BF02427924`.

Vetra-Carvalho, S., P. van Leeuwen, L. Nerger, A. Barth, M. U. Altaf, P. Brasseur, P. Kirchgessner, et al. (2018). “State-of-the-Art Stochastic Data Assimilation Methods for High-Dimensional Non-Gaussian Problems”. In: *Tellus A: Dynamic Meteorology and Oceanography* 70.1, pp. 1–43. DOI: `10.1080/16000870.2018.1445364`.

Vielberg, K. (2024). “Thermosphere and Radiation Effects in Forward and Inverse Non-Gravitational Force Modelling”. PhD thesis. Bonn: Rheinische Friedrich-Wilhelms-Universität. DOI: `10.48565/bonndoc-213`.

Vielberg, K., C. Lück, A. Corbin, E. Forootan, A. Löcher, and J. Kusche (2021). *TND-IGG RL01: Thermospheric Neutral Density from Accelerometer Measurements of GRACE, CHAMP and Swarm.* PANGAEA. DOI: `10.1594/PANGAEA.931347`.

Viereck, R., L. Puga, D. McMullin, D. Judge, M. Weber, and W. K. Tobiska (2001). “The Mg II Index: A Proxy for Solar EUV”. In: *Geophysical Research Letters* 28.7, pp. 1343–1346. ISSN: 1944-8007. DOI: `10.1029/2000GL012551`.

Villanueva, G. L., M. D. Smith, S. Protopapa, S. Faggi, and A. M. Mandell (2018). “Planetary Spectrum Generator: An Accurate Online Radiative Transfer Suite for Atmospheres, Comets, Small Bodies and Exoplanets”. In: *Journal of Quantitative Spectroscopy and Radiative Transfer* 217, pp. 86–104. ISSN: 00224073. DOI: `10.1016/j.jqsrt.2018.05.023`.

Vono, M., N. Dobigeon, and P. Chainais (2022). “High-Dimensional Gaussian Sampling: A Review and a Unifying Approach Based on a Stochastic Proximal Point Algorithm”. In: *SIAM Review* 64.1, pp. 3–56. ISSN: 0036-1445. DOI: `10.1137/20M1371026`.

Von Zahn, U., W. Köhnlein, K. H. Fricke, U. Laux, H. Trinks, and H. Volland (1977). “Esro 4 Model of Global Thermospheric Composition and Temperatures during Times of Low Solar Activity”. In: *Geophysical Research Letters* 4.1, pp. 33–36. ISSN: 1944-8007. DOI: `10.1029/GL004i001p00033`.

Wagner, W. E. and C. E. Velez (1972). “Goddard Trajectory Determination Subsystem: Mathematical Specifications”. URL: `https://ntrs.nasa.gov/citations/19720023166` (visited on 11/18/2022).

Wallace, J. M. and P. V. Hobbs (2006). “3 - Atmospheric Thermodynamics”. In: *Atmospheric Science (Second Edition)*. Ed. by J. M. Wallace and P. V. Hobbs. 2nd ed. San Diego: Academic Press, pp. 63–111. ISBN: 978-0-12-732951-2. DOI: `10.1016/B978-0-12-732951-2.50008-9`.

Wang, P., Z. Chen, X. Deng, J.-S. Wang, R. Tang, H. Li, S. Hong, et al. (2023). “The Short-Time Prediction of Thermospheric Mass Density Based on Ensemble-Transfer Learning”. In: *Space Weather* 21.10. ISSN: 1542-7390. DOI: `10.1029/2023SW003576`.

Wang, S., L. Weng, H. Fang, Y. Xie, and S. Yang (2014). “Intra-Annual Variations of the Thermospheric Density at 400 Km Altitude from 1996 to 2006”. In: *Advances in Space Research*. Recent Advances in Equatorial, Low- and Mid-Latitude Mesosphere, Thermosphere-Ionosphere System Studies 54.3, pp. 327–332. ISSN: 0273-1177. DOI: `10.1016/j.asr.2013.12.011`.

Wang, W., T. L. Killeen, A. G. Burns, and R. G. Roble (1999). “A High-Resolution, Three-Dimensional, Time Dependent, Nested Grid Model of the Coupled Thermosphere–Ionosphere”. In: *Journal of Atmospheric and Solar-Terrestrial Physics* 61.5, pp. 385–397. ISSN: 1364-6826. DOI: `10.1016/S1364-6826(98)00079-0`.

Wang, W. (1998). “A Thermosphere-Ionosphere Nested Grid (TING) Model.” Thesis. URL: `http://deepblue.lib.umich.edu/handle/2027.42/131568` (visited on 02/14/2024).

Wang, X., C. H. Bishop, and S. J. Julier (2004). “Which Is Better, an Ensemble of Positive–Negative Pairs or a Centered Spherical Simplex Ensemble?” In: *Monthly Weather Review* 132.7, pp. 1590–1605. ISSN: 1520-0493, 0027-0644. DOI: `10.1175/1520-0493(2004)132<1590:WIBAEO>2.0.CO;2`.

Weimer, D. R. (2005). “Improved Ionospheric Electrodynamic Models and Application to Calculating Joule Heating Rates”. In: *Journal of Geophysical Research: Space Physics* 110.A5. ISSN: 2156-2202. DOI: `10.1029/2004JA010884`.

Whitaker, J. S. and T. M. Hamill (2002). “Ensemble Data Assimilation without Perturbed Observations”. In: *Monthly Weather Review* 130.7, pp. 1913–1924. ISSN: 1520-0493, 0027-0644. DOI: `10.1175/1520-0493(2002)130<1913:EDAWPO>2.0.CO;2`.

Wiltberger, M., W. Wang, A. G. Burns, S. C. Solomon, J. G. Lyon, and C. C. Goodrich (2004). “Initial Results from the Coupled Magnetosphere Ionosphere Thermosphere Model: Magnetospheric and Ionospheric Responses”. In: *Journal of Atmospheric and Solar-Terrestrial Physics*. Towards an Integrated Model of the Space Weather System 66.15, pp. 1411–1423. ISSN: 1364-6826. DOI: `10.1016/j.jastp.2004.03.026`.

Woodbury, M. A. (1950). *Inverting Modified Matrices*. Statistical Research Group, Memo. Rep. No. 42. Princeton University, Princeton, N. J., p. 4. URL: `https://mathscinet.ams.org/mathscinet-getitem?mr=38136`.

Woods, T. N., F. G. Eparvier, S. M. Bailey, P. C. Chamberlin, J. Lean, G. J. Rottman, S. C. Solomon, et al. (2005). “Solar EUV Experiment (SEE): Mission Overview and First Results”. In: *Journal of Geophysical Research: Space Physics* 110.A1. DOI: `10.1029/2004JA010765`.

Woods, T. N. and G. J. Rottman (2002). “Solar Ultraviolet Variability Over Time Periods of Aeronomic Interest”. In: *Atmospheres in the Solar System: Comparative Aeronomy*. American Geophysical Union (AGU), pp. 221–233. ISBN: 978-1-118-66957-0. DOI: `10.1029/130GM14`.

Woods, T., J. Harder, and M. Snow (2021). *SORCE Combined XPS, SOLSTICE, and SIM Solar Spectral Irradiance 24-Hour Means V001*. Version 001. DOI: `10.5067/9PRENS3AL461`.

Wu, L. (2022). *Rarefied Gas Dynamics: Kinetic Modeling and Multi-Scale Simulation*. Singapore: Springer Nature. ISBN: 978-981-19287-4-1. DOI: `10.1007/978-981-19-2872-7`.

Xiong, C., H. Lühr, M. Schmidt, M. Bloßfeld, and S. Rudenko (2018). “An Empirical Model of the Thermospheric Mass Density Derived from CHAMP Satellite”. In: *Annales Geophysicae* 36.4, pp. 1141–1152. ISSN: 0992-7689. DOI: `10.5194/angeo-36-1141-2018`.

Yamazaki, Y., J. Matzka, C. Stolle, G. Kervalishvili, J. Rauberg, O. Bronkalla, A. Morschhauser, et al. (2022). “Geomagnetic Activity Index Hpo”. In: *Geophysical Research Letters* 49.10. ISSN: 1944-8007. DOI: `10.1029/2022GL098860`.

Yamazaki, Y. and A. D. Richmond (2013). “A Theory of Ionospheric Response to Upward-Propagating Tides: Electrodynamic Effects and Tidal Mixing Effects”. In: *Journal of Geophysical Research: Space Physics* 118.9, pp. 5891–5905. ISSN: 2169-9402. DOI: `10.1002/jgra.50487`.

“Space Weather” (2019a). In: *Geomagnetism, Aeronomy and Space Weather: A Journey from the Earth’s Core to the Sun*. Ed. by A. Yau, E. Petrovsky, M. Mandea, and M. Korte. Special Publications of the International Union of Geodesy and Geophysics. Cambridge: Cambridge University Press, pp. 207–264. ISBN: 978-1-108-41848-5. DOI: `10.1017/9781108290135`.

“Why Study the Geomagnetic Field?” (2019b). In: *Geomagnetism, Aeronomy and Space Weather: A Journey from the Earth’s Core to the Sun*. Ed. by A. Yau, E. Petrovsky, M. Mandea, and M. Korte. Special Publications of the International Union of Geodesy and Geophysics. Cambridge: Cambridge University Press, pp. 7–29. ISBN: 978-1-108-41848-5. DOI: `10.1017/9781108290135.003`.

Yue, J., W. Yu, N. Pedatella, S. Bruinsma, N. Wang, and H. Liu (2023). “Contribution of the Lower Atmosphere to the Day-to-Day Variation of Thermospheric Density”. In: *Advances in Space Research*. COSPAR Space Weather Roadmap 2022: Scientific Research and Applications 72.12, pp. 5460–5475. ISSN: 0273-1177. DOI: `10.1016/j.asr.2022.06.011`.

Zahorjan, J., E. Lazowska, and D. Eager (1989). “Speedup Versus Efficiency in Parallel Systems”. In: *IEEE Transactions on Computers* 38.03, pp. 408–423. ISSN: 1557-9956. DOI: `10.1109/12.21127`.

Zeitler, L., A. Corbin, K. Vielberg, S. Rudenko, A. Löcher, M. Bloßfeld, M. Schmidt, et al. (2021). “Scale Factors of the Thermospheric Density: A Comparison of Satellite Laser Ranging and Accelerometer Solutions”. In: *Journal of Geophysical Research: Space Physics* 126.12. ISSN: 2169-9402. DOI: `10.1029/2021JA029708`.

Zhang, X., J. M. Forbes, and M. E. Hagan (2010). “Longitudinal Variation of Tides in the MLT Region: 1. Tides Driven by Tropospheric Net Radiative Heating”. In: *Journal of Geophysical Research: Space Physics* 115.A6. ISSN: 2156-2202. DOI: `10.1029/2009JA014897`.

Zupanski, M. (2005). “Maximum Likelihood Ensemble Filter: Theoretical Aspects”. In: *Monthly Weather Review* 133.6, pp. 1710–1726. ISSN: 1520-0493, 0027-0644. DOI: `10.1175/MWR2946.1`.

Zupanski, M., I. M. Navon, and D. Zupanski (2008). “The Maximum Likelihood Ensemble Filter as a Non-Differentiable Minimization Algorithm”. In: *Quarterly Journal of the Royal Meteorological Society* 134.633, pp. 1039–1050. ISSN: 1477-870X. DOI: `10.1002/qj.251`.

List of Figures

List of Tables

List of Setups

A. Derivations

A.1. Aerostatic Equation

The following derivation is taken from Prölss (2004). Considering only gravity and pressure force, the atmosphere is in equilibrium if both forces compensate at any height. Given a surface area A at height z (see Figure A.1), one can write

$$F_p(z) = F_g(z), \tag{A.1}$$

with the pressure force $F_p(z)$ pressing the surface upwards and the gravitational force $F_g(z)$ pulling the surface to the ground. Inserting the definitions of the forces, one obtains:

$$\begin{aligned}
A\,p(z) &= A\int_z^\infty \rho(z')\,g(z')\,dz' \\
&\quad \Big\downarrow \text{ reducing } A \\
p(z) &= \int_z^\infty \rho(z')\,g(z')\,dz' \\
&\quad \Big\downarrow \text{ differentiate w.r.t. } z \\
\frac{dp(z)}{dz} &= \frac{d}{dz}\int_z^\infty \rho(z')\,g(z')\,dz' \\
&\quad \Big\downarrow \ \frac{d}{dx}\textstyle\int_a^x f(t)dt = -\frac{d}{dx}\int_x^a f(t)dt = f(x) \\
\frac{dp(z)}{dz} &= -\,\rho(z)\,g(z)
\end{aligned} \tag{A.2}$$

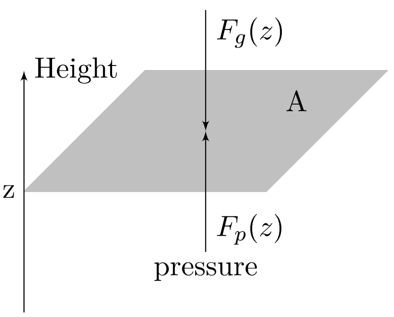

Figure A.1.: The gray plane can be considered as a massless impermeable membrane. The air column above causes the force F_G due to gravity. It is counterbalanced by the pressure force F_p from below (adapted from Prölss (2004, Figure 2.14)).

A.2. Barometric Law

By inserting the ideal gas law into aerostatic equation one obtains

$$\frac{dp(z)}{dz} = -\,\rho(z)\,g(z) = -\frac{\overline{m}(z)p(z)}{k_B T(z)}\,g(z) = -\frac{p(z)}{H(z)}. \tag{A.3}$$

This is a first order ordinary differential equation, which is solved by rearranging it to a separable equation:

$$\begin{aligned}
\frac{dp(h)}{dh} &= -\frac{p(h)}{H(h)} && \Big\downarrow \text{divide by } p(h) \\
\frac{dp(h)}{dh}\frac{1}{p(h)} &= -\frac{1}{H(h)} && \Big\downarrow \text{integrate both sides} \\
\int_{h_0}^{h}\frac{dp(z)}{dz}\frac{1}{p(z)}dz &= -\int_{h_0}^{h}\frac{1}{H(z)}dz && \Big\downarrow \textstyle\int \frac{f'(x)}{f(x)}dx = \ln x \\
\ln(p(z))\Big|_{h_0}^{h} &= -\int_{h_0}^{h}\frac{1}{H(z)}dz && \Big\downarrow \ln(a)-\ln(b) = \ln\left(\tfrac{a}{b}\right) \\
\ln\left(\frac{p(h)}{p(h_0)}\right) &= -\int_{h_0}^{h}\frac{1}{H(z)}dz \\
\frac{p(h)}{p(h_0)} &= \exp\left(-\int_{h_0}^{h}\frac{1}{H(z)}dz\right) \\
p(h) &= p(h_0)\exp\left(-\int_{h_0}^{h}\frac{1}{H(z)}dz\right)
\end{aligned} \tag{A.4}$$

A.3. Number Density Scale Height

Here, the instructions given by Prölss (2004, p.38) are used to derive an equation for the number density profile. By replacing the pressure in Equation 2.18 with Equation 2.14 we find an expression for the number density

$$p(h) = p(h_0)\exp\left(-\int_{h_0}^{h}\frac{1}{H(z)}dz\right) \qquad \Big\downarrow p(h) = C(h)T(h)k_B \tag{A.5}$$

$$C(h)T(h)k_B = C(h_0)T(h_0)k_B\exp\left(-\int_{h_0}^{h}\frac{1}{H(z)}dz\right) \qquad \Big\downarrow \text{eliminate } k_B \text{, divide by } T(h) \tag{A.6}$$

$$C(h) = C(h_0)\frac{T(h_0)}{T(h)}\exp\left(-\int_{h_0}^{h}\frac{1}{H(z)}dz\right). \tag{A.7}$$

The pressure scale height is defined as (see Equation A.3)

$$H(h) = -p(h)\frac{1}{\frac{dp(h)}{dh}}. \tag{A.8}$$

Analogously one can define the number density scale height with

$$H_C(h) = -C(h)\frac{1}{\frac{dC(h)}{dh}}. \tag{A.9}$$

The derivative of Equation A.7 is obtained by applying the product rule

$$\begin{aligned}\frac{dC(h)}{dh} =& C(h_0)T(h_0)\left(-\frac{1}{T(h)^2}\frac{dT(h)}{dh}\right)\exp\left(-\int_{h_0}^{h}\frac{1}{H(z)}dz\right) \qquad \text{(A.10)}\\ &+\left(-\frac{1}{H(z)}\right)\exp\left(-\int_{h_0}^{h}\frac{1}{H(z)}dz\right)C(h_0)\frac{T(h_0)}{T(h)} \qquad \text{factorize}\\ =& -C(h_0)\frac{T(h_0)}{T(h)}\exp\left(-\int_{h_0}^{h}\frac{1}{H(z)}dz\right)\left(\frac{1}{T(h)}\frac{dT(h)}{dh}+\frac{1}{H(z)}\right) \qquad \text{use Eq. A.7}\\ =& -C(h)\left(\frac{1}{T(h)}\frac{dT(h)}{dh}+\frac{1}{H(z)}\right)\end{aligned}$$

In the next step we divide the equation by $C(h)$ and see that we have the reciprocal of Equation A.9 on the left-hand side:

$$-\frac{dC(h)}{dh}\frac{1}{C(h)} = \frac{1}{T(h)}\frac{dT(h)}{dh}+\frac{1}{H(z)} \tag{A.11}$$

$$\frac{1}{H_C(h)} = \frac{1}{T(h)}\frac{dT(h)}{dh}+\frac{1}{H(z)} \tag{A.12}$$

A.4. Density Change by Transport and Expansion

Following (Prölss, 2004, p.129), one can assess the effect of a temperature increase on the neutral density using Equation A.7. Let $C_1(h)$ be the neutral density at temperature $T_1(h)$, and $C_2(h)$ be the neutral density at a higher temperature $T_2(h) > T_1(h)$. Then, the density ratio is

$$\frac{C_2(h)}{C_1(h)} = \frac{C_2(h_0)}{C_1(h_0)}\frac{\frac{T_2(h_0)}{T_2(h)}\exp\left(-\int_{h_0}^{h}\frac{1}{H_2(z)}dz\right)}{\frac{T_1(h_0)}{T_1(h)}\exp\left(-\int_{h_0}^{h}\frac{1}{H_1(z)}dz\right)}. \tag{A.13}$$

Assuming constant lower boundary condition, i.e., $C_2(h_0) = C_1(h_0)$ and $T_2(h_0) = T_1(h_0)$ and making use of the exponent quotient rule, we get

$$\frac{C_2(h)}{C_1(h)} = \frac{T_1(h)}{T_2(h)}\exp\left(-\int_{h_0}^{h}\frac{1}{H_2(z)}dz+\int_{h_0}^{h}\frac{1}{H_1(z)}dz\right) \tag{A.14}$$

$$\frac{C_2(h)}{C_1(h)} = \frac{T_1(h)}{T_2(h)}\exp\left(\int_{h_0}^{h}-\frac{1}{H_2(z)}+\frac{1}{H_1(z)}dz\right). \tag{A.15}$$

Using Equation 2.19, assuming gravitational acceleration and mean molecular mass are equal at both altitudes, one can express H_2 as function of H_1

$$H_2 = \frac{T_2}{T_1}H_1. \tag{A.16}$$

Inserting yields

$$
\left.
\begin{aligned}
\frac{C_2(h)}{C_1(h)} &= \frac{T_1(h)}{T_2(h)} \exp\left(\int_{h_0}^{h} \frac{1}{H_1(z)} - \frac{T_1(z)}{T_2(z)}\frac{1}{H_1(z)} dz\right) \\
\frac{C_2(h)}{C_1(h)} &= \underbrace{\frac{T_1(h)}{T_2(h)}}_{\text{temperature-induced}} \quad \underbrace{\exp\left(\int_{h_0}^{h}\left(1-\frac{T_1(z)}{T_2(z)}\right)\frac{1}{H_1(z)}dz\right)}_{\text{transport-induced}} .
\end{aligned}
\right) \swarrow \ \text{factorize } \frac{1}{H_1(z)} \tag{A.17}
$$

Since $T_2(h) > T_1(h)$ the first term describes the temperature-induced decline of the neutral density and the second term the transport-induced increase (Prölss, 2004, p.129).

Substituting $\frac{T_1(h)}{T_2(h)}$ with $s(h)$ and finding parameters for which transport-induced increase is greater than the temperature-induced decrease we obtain

$$
\exp\left(\int_{h_0}^{h} \frac{1-s(z)}{H_1(z)} dz\right) > \frac{1}{s(h)} \tag{A.18}
$$

Using trapezoidal rule $\int_a^b f(x)dx \approx (b-a)\frac{f(a)+f(b)}{2}$ we get the approximation

$$
\int_{h_0}^{h} \frac{1-s(z)}{H_1(z)} dz \approx (h-h_0)\frac{\dfrac{1-s(h)}{H_1(h)} + \dfrac{1-s(h_0)}{H_1(h_0)}}{2} \tag{A.19}
$$

Since $s(h_0) = \frac{T_1(h_0)}{T_2(h_0)}$ is one by definition, this simplifies to

$$
\int_{h_0}^{h} \frac{1-s(z)}{H_1(z)} dz \approx (h-h_0)\frac{1-s(h)}{2H_1(h)} . \tag{A.20}
$$

Inserting the approximation for the integral yields

$$
\exp\left((h-h_0)\frac{1-s(h)}{2H_1(h)}\right) > \frac{1}{s(h)} . \tag{A.21}
$$

Using the substitution $\Delta = \frac{h-h_0}{H_1(h)}$ which can be interpreted as the height above the lower layer expressed as a multiple of the scale height we get

$$
\exp\left(\Delta\frac{1-s(h)}{2}\right) > \frac{1}{s(h)} . \tag{A.22}
$$

Figure A.2 shows that at two scale heights above h_0, the transport-induced increase dominates the temperature-induced decrease.

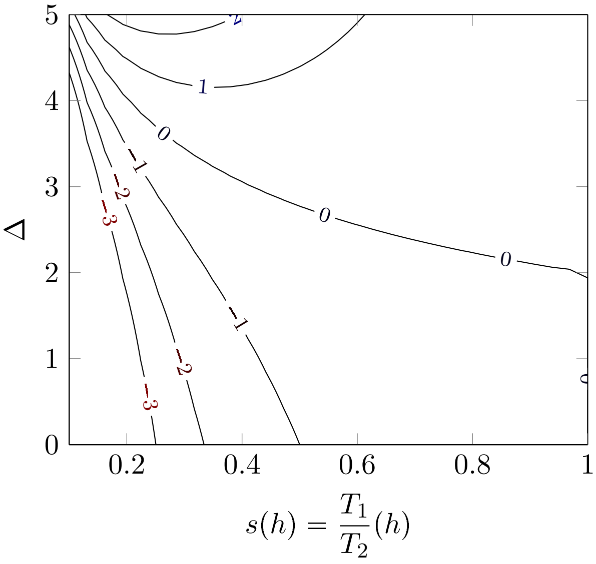

Figure A.2.: Contour plot of $f(\Delta, s(h)) = \exp\left(\Delta^{\frac{1-s(h)}{2}}\right) - \frac{1}{s(h)}$. For values of $f(\Delta, s(h)) > 0$ there is a net density increase due to transport.

A.5. Geopotential Height

We start from the aerodynamic equilibrium using geometric altitude z as vertical coordinate

$$\frac{dp(z)}{dz} = -\rho(z)\, g(z). \tag{A.23}$$

Inserting ideal gas law we get

$$\begin{aligned}
\frac{dp(z)}{dz} &= -\frac{p(z)\overline{M}(z)}{RT(z)}\, g(z) \\
&\qquad \big\downarrow \text{ isolate } g \\
-\frac{RT(z)}{p(z)\overline{M}(z)}\frac{dp(z)}{dz} &= g(z) \\
&\qquad \big\downarrow \text{ integrate both sides w.r.t. } z \\
-R\int_{z_1}^{z_2} \frac{T(z)}{p(z)\overline{M}(z)}\frac{dp(z)}{dz} dz &= \int_{z_1}^{z_2} g(z) dz \\
&\qquad \big\downarrow \text{ use the definition of geopotential} \\
-R\int_{z_1}^{z_2} \frac{T(z)}{p(z)\overline{M}(z)}\frac{dp(z)}{dz} dz &= C(z_2) - C(z_1) \\
&\qquad \big\downarrow \text{ divide by } g_0 \\
-\frac{R}{g_0}\int_{z_1}^{z_2} \frac{T(z)}{p(z)\overline{M}(z)}\frac{dp(z)}{dz} dz &= \frac{C(z_2) - C(z_1)}{g_0} \\
&\qquad \big\downarrow H_{\text{pot}} = \frac{C}{g_0} \text{ (see Equation 2.25)} \\
-\frac{R}{g_0}\int_{z_1}^{z_2} \frac{T(z)}{p(z)\overline{M}(z)}\frac{dp(z)}{dz} dz &= H_{\text{pot}}(z_2) - H_{\text{pot}}(z_1).
\end{aligned} \tag{A.24}$$

After rearranging, we get the following expression for the geopotential height:

$$H_{\text{pot}}(z_2) = H_{\text{pot}}(z_1) - \frac{R}{g_0}\int_{z_1}^{z_2} \frac{T(z)}{p(z)\overline{M}(z)}\frac{dp(z)}{dz} dz. \tag{A.25}$$

To transform this equation to pressure coordinates, we substitute the geometric height z with pressure p

$$H_{\text{pot}}(z(p_2)) = H_{\text{pot}}(z(p_1)) - \frac{R}{g_0} \int_{p_1}^{p_2} \frac{T(z(p))}{p(z(p))\overline{M}(z(p))} \frac{dp(z(p))}{dz} \frac{dz(p)}{dp} dp. \tag{A.26}$$

From the inverse function theorem, we get

$$\frac{dz(p)}{dp} = \frac{1}{\frac{dp(z)}{dz}}. \tag{A.27}$$

Thus, $\frac{dp(z(p))}{dz}\frac{dz(p)}{dp}$ is the identity. Moreover, we define $T(z(p)) := T(p)$, $\overline{M}(z(p)) := \overline{M}(p)$, and $H_{\text{pot}}(z(p)) := H_{\text{pot}}(p)$. And finally, we see that $p(z(p)) = p$ and get

$$H_{\text{pot}}(p_2) = H_{\text{pot}}(p_1) - \frac{R}{g_0} \int_{p_1}^{p_2} \frac{T(p)}{p\overline{M}(p)} dp. \tag{A.28}$$

Using Equation 2.15 this can be expressed as integral over the reciprocal mass density:

$$H_{\text{pot}}(p_2) = H_{\text{pot}}(p_1) - \frac{1}{g_0} \int_{p_1}^{p_2} \frac{1}{\rho(p)} dp \tag{A.29}$$

A.5.1. Geopotential Height of a Pressure Level

The pressure level k is defined as

$$k(p) = \ln \frac{p_0}{p} = \ln p_0 - \ln p \tag{A.30}$$

and has the derivative

$$\frac{dk(p)}{dp} = -\frac{1}{p}. \tag{A.31}$$

Substituting the pressure in Equation A.28, one gets

$$\begin{aligned} H_{\text{pot}}(p_2) =& H_{\text{pot}}(p_1) - \frac{R}{g_0} \int_{p_1}^{p_2} \frac{T(p)}{p\overline{M}(p)} dp && \Big\rangle \text{ substitute pressure with pressure level} \\ H_{\text{pot}}(p(k_2)) =& H_{\text{pot}}(p(k_1)) - \frac{R}{g_0} \int_{k_1}^{k_2} \frac{T(p(k))}{p(k)\overline{M}(p(k))} \frac{dp(k)}{dk} dk && \Big\rangle \text{ Inverse function theorem, } T(p(k)) := T(k),\ \overline{M}(p(k)) := \overline{M}(k) \\ H_{\text{pot}}(k_2) =& H_{\text{pot}}(k_1) + \frac{R}{g_0} \int_{k_1}^{k_2} \frac{T(k)}{\overline{M}(k)} dk \end{aligned} \tag{A.32}$$

A.5.2. Relation between Geometric and Geopotential Height

The geopotential of a spherical Earth with homogeneous density distribution is given by

$$W(r) = \frac{\mu_\oplus}{r} \tag{A.33}$$

for $r \geqslant R_\oplus$. The corresponding gravitational acceleration is

$$g(r) = -\frac{d}{dr}W(r) = \frac{\mu_\oplus}{r^2}. \tag{A.34}$$

Inserting Equation A.33 into Equation 2.23 gives the geopotential number of a point with geometric height z above the Earth's surface:

$$\begin{aligned} C =& \frac{\mu_\oplus}{R_\oplus} - \frac{\mu_\oplus}{R_\oplus + z} \\ =& \frac{\mu_\oplus\, z}{R_\oplus(R_\oplus + z)}. \end{aligned} \tag{A.35}$$

Inserting this into Equation 2.25 yields

$$H_\text{pot} = \frac{1}{g_0}\frac{\mu_\oplus\, z}{R_\oplus(R_\oplus + z)}. \tag{A.36}$$

Using Equation A.34 for the gravity at Earth's surface $g_0 = g(R_\oplus) = \frac{\mu_\oplus}{{R_\oplus}^2}$ yields

$$\begin{aligned} H_\text{pot} =& \frac{{R_\oplus}^2}{\mu_\oplus}\frac{\mu_\oplus\, z}{R_\oplus(R_\oplus + z)} \\ =& \frac{R_\oplus\, z}{R_\oplus + z}. \end{aligned} \tag{A.37}$$

The inverse function is

$$\begin{aligned} H_\text{pot}(R_\oplus + z) =& zR_\oplus \\ H_\text{pot}R_\oplus + H_\text{pot}z =& zR_\oplus \\ H_\text{pot}z - zR_\oplus =& -H_\text{pot}R_\oplus \\ z(H_\text{pot} - R_\oplus) =& -H_\text{pot}R_\oplus \\ z =& -\frac{H_\text{pot}R_\oplus}{H_\text{pot} - R_\oplus} \\ z =& \frac{R_\oplus H_\text{pot}}{R_\oplus - H_\text{pot}}. \end{aligned} \tag{A.38}$$

A.6. (Ensemble) Kalman Filter

A.6.1. Kalman Filter

To find the optimal state $\boldsymbol{x}$, the objective function (also given in Equation 6.46)

$$\begin{aligned} J(\boldsymbol{x}) =& \frac{1}{2}\Big(\boldsymbol{x} - \boldsymbol{x}^f\Big)^\mathsf{T} \boldsymbol{P}^{f^{-1}}\Big(\boldsymbol{x} - \boldsymbol{x}^f\Big) \\ &+ \frac{1}{2}\Big(\boldsymbol{H}\boldsymbol{x} - \boldsymbol{y}^o\Big)^\mathsf{T} \boldsymbol{R}^{-1}\Big(\boldsymbol{H}\boldsymbol{x} - \boldsymbol{y}^o\Big). \end{aligned} \tag{A.39}$$

is minimized. Here, all time indices are dropped since all variables are given at the same epoch. The derivatives of the quadratic forms present in Equation A.39 are generally given by

$$\frac{\partial(\boldsymbol{x}+\boldsymbol{b})^{\intercal}\boldsymbol{N}(\boldsymbol{x}+\boldsymbol{b})}{\partial\boldsymbol{x}} = 2\boldsymbol{N}(\boldsymbol{x}+\boldsymbol{b}) \tag{A.40}$$

$$\frac{\partial(\boldsymbol{A}\boldsymbol{x}+\boldsymbol{b})^{\intercal}\boldsymbol{N}(\boldsymbol{A}\boldsymbol{x}+\boldsymbol{b})}{\partial\boldsymbol{x}} = 2\boldsymbol{A}^{\intercal}\boldsymbol{N}(\boldsymbol{A}\boldsymbol{x}+\boldsymbol{b}) \quad \text{with} \quad \boldsymbol{N}^{\intercal} = \boldsymbol{N}. \tag{A.41}$$

Thus, the derivative of Equation A.39 is

$$\nabla J(\boldsymbol{x}) = \boldsymbol{P}^{f^{-1}}(\boldsymbol{x}-\boldsymbol{x}^f) + \boldsymbol{H}^{\intercal}\boldsymbol{R}^{-1}(\boldsymbol{H}\boldsymbol{x}-\boldsymbol{y}^o). \tag{A.42}$$

Setting the derivative to zero and solving for $\boldsymbol{x}$ yields

$$\begin{aligned}
0 =& \boldsymbol{P}^{f^{-1}}(\boldsymbol{x}-\boldsymbol{x}^f) + \boldsymbol{H}^{\intercal}\boldsymbol{R}^{-1}(\boldsymbol{H}\boldsymbol{x}-\boldsymbol{y}^o) && \quad \text{multiply out the brackets} \\
=& \boldsymbol{P}^{f^{-1}}\boldsymbol{x} - \boldsymbol{P}^{f^{-1}}\boldsymbol{x}^f + \boldsymbol{H}^{\intercal}\boldsymbol{R}^{-1}\boldsymbol{H}\boldsymbol{x} - \boldsymbol{H}^{\intercal}\boldsymbol{R}^{-1}\boldsymbol{y}^o && \quad \text{factorize x} \\
=& (\boldsymbol{P}^{f^{-1}} + \boldsymbol{H}^{\intercal}\boldsymbol{R}^{-1}\boldsymbol{H})\boldsymbol{x} - \boldsymbol{P}^{f^{-1}}\boldsymbol{x}^f - \boldsymbol{H}^{\intercal}\boldsymbol{R}^{-1}\boldsymbol{y}^o && \quad \text{multiply with } (\boldsymbol{P}^{f^{-1}} + \boldsymbol{H}^{\intercal}\boldsymbol{R}^{-1}\boldsymbol{H})^{-1} \\
\boldsymbol{x} =& (\boldsymbol{P}^{f^{-1}} + \boldsymbol{H}^{\intercal}\boldsymbol{R}^{-1}\boldsymbol{H})^{-1}(\boldsymbol{P}^{f^{-1}}\boldsymbol{x}^f + \boldsymbol{H}^{\intercal}\boldsymbol{R}^{-1}\boldsymbol{y}^o)
\end{aligned} \tag{A.43}$$

In the next step, the Sherman Morrison-Woodbury formula (Woodbury, 1950)

$$(\boldsymbol{A}+\boldsymbol{U}\boldsymbol{C}\boldsymbol{V})^{-1} = \boldsymbol{A}^{-1} - \boldsymbol{A}^{-1}\boldsymbol{U}(\boldsymbol{C}^{-1}+\boldsymbol{V}\boldsymbol{A}^{-1}\boldsymbol{U})^{-1}\boldsymbol{V}\boldsymbol{A}^{-1} \tag{A.44}$$

is applied, which yields

$$\begin{aligned}
\boldsymbol{x} =& \left(\boldsymbol{P}^f - \boldsymbol{P}^f\boldsymbol{H}^{\intercal}(\boldsymbol{R}+\boldsymbol{H}\boldsymbol{P}^f\boldsymbol{H}^{\intercal})^{-1}\boldsymbol{H}\boldsymbol{P}^f\right)(\boldsymbol{P}^{f^{-1}}\boldsymbol{x}^f + \boldsymbol{H}^{\intercal}\boldsymbol{R}^{-1}\boldsymbol{y}^o) && \quad \text{eliminate the brackets} \\
\boldsymbol{x} =& \underbrace{\boldsymbol{P}^f\boldsymbol{P}^{f^{-1}}}_{\mathbb{1}}\boldsymbol{x}^f \\
&+\boldsymbol{P}^f\boldsymbol{H}^{\intercal}\boldsymbol{R}^{-1}\boldsymbol{y}^o \\
&-\boldsymbol{P}^f\boldsymbol{H}^{\intercal}(\boldsymbol{R}+\boldsymbol{H}\boldsymbol{P}^f\boldsymbol{H}^{\intercal})^{-1}\boldsymbol{H}\underbrace{\boldsymbol{P}^f\boldsymbol{P}^{f^{-1}}}_{\mathbb{1}}\boldsymbol{x}^f \\
&-\boldsymbol{P}^f\boldsymbol{H}^{\intercal}(\boldsymbol{R}+\boldsymbol{H}\boldsymbol{P}^f\boldsymbol{H}^{\intercal})^{-1}\boldsymbol{H}\boldsymbol{P}^f\boldsymbol{H}^{\intercal}\boldsymbol{R}^{-1}\boldsymbol{y}^o.
\end{aligned} \tag{A.45}$$

Multiplying the second term with $(\boldsymbol{R}+\boldsymbol{H}\boldsymbol{P}^f\boldsymbol{H}^{\intercal})^{-1}(\boldsymbol{R}+\boldsymbol{H}\boldsymbol{P}^f\boldsymbol{H}^{\intercal})$ does not change the result since it is equal to the identity matrix. The result is

$$\begin{aligned}
\boldsymbol{x} =& \boldsymbol{x}^f \\
&+\boldsymbol{P}^f\boldsymbol{H}^{\intercal}\underbrace{(\boldsymbol{R}+\boldsymbol{H}\boldsymbol{P}^f\boldsymbol{H}^{\intercal})^{-1}(\boldsymbol{R}+\boldsymbol{H}\boldsymbol{P}^f\boldsymbol{H}^{\intercal})}_{\mathbb{1}}\boldsymbol{R}^{-1}\boldsymbol{y}^o \\
&-\boldsymbol{P}^f\boldsymbol{H}^{\intercal}(\boldsymbol{R}+\boldsymbol{H}\boldsymbol{P}^f\boldsymbol{H}^{\intercal})^{-1}\boldsymbol{H}\boldsymbol{x}^f \\
&-\boldsymbol{P}^f\boldsymbol{H}^{\intercal}(\boldsymbol{R}+\boldsymbol{H}\boldsymbol{P}^f\boldsymbol{H}^{\intercal})^{-1}\boldsymbol{H}\boldsymbol{P}^f\boldsymbol{H}^{\intercal}\boldsymbol{R}^{-1}\boldsymbol{y}^o.
\end{aligned} \tag{A.46}$$

The previous step enables the factorization of $\boldsymbol{P}^f\boldsymbol{H}^\top(\boldsymbol{R}+\boldsymbol{H}\boldsymbol{P}^f\boldsymbol{H}^\top)^{-1}$ in the second, third and fourth term:

$$\boldsymbol{x} =\boldsymbol{x}^f + \boldsymbol{P}^f\boldsymbol{H}^\top(\boldsymbol{R}+\boldsymbol{H}\boldsymbol{P}^f\boldsymbol{H}^\top)^{-1}\left((\boldsymbol{R}+\boldsymbol{H}\boldsymbol{P}^f\boldsymbol{H}^\top)\boldsymbol{R}^{-1}\boldsymbol{y}^o - \boldsymbol{H}\boldsymbol{x}^f - \boldsymbol{H}\boldsymbol{P}^f\boldsymbol{H}^\top\boldsymbol{R}^{-1}\boldsymbol{y}^o\right) \tag{A.47}$$

Eliminating the inner brackets gives

$$\begin{aligned}
\boldsymbol{x} &=\boldsymbol{x}^f + \boldsymbol{P}^f\boldsymbol{H}^\top(\boldsymbol{R}+\boldsymbol{H}\boldsymbol{P}^f\boldsymbol{H}^\top)^{-1}\left(\underbrace{\boldsymbol{R}\boldsymbol{R}^{-1}}_{\mathbb{1}}\boldsymbol{y}^o + \boldsymbol{H}\boldsymbol{P}^f\boldsymbol{H}^\top\boldsymbol{R}^{-1}\boldsymbol{y}^o - \boldsymbol{H}\boldsymbol{x}^f - \boldsymbol{H}\boldsymbol{P}^f\boldsymbol{H}^\top\boldsymbol{R}^{-1}\boldsymbol{y}^o\right) \qquad \text{(A.48)}\\
\boldsymbol{x} &=\boldsymbol{x}^f + \boldsymbol{P}^f\boldsymbol{H}^\top(\boldsymbol{R}+\boldsymbol{H}\boldsymbol{P}^f\boldsymbol{H}^\top)^{-1}\left(\boldsymbol{y}^o - \boldsymbol{H}\boldsymbol{x}^f\right).
\end{aligned}$$

Finally, defining the Kalman matrix as $K := \boldsymbol{P}^f\boldsymbol{H}^\top(\boldsymbol{R}+\boldsymbol{H}\boldsymbol{P}^f\boldsymbol{H}^\top)^{-1}$ and denoting the state optimizing Equation A.39 with $\boldsymbol{x}^a$, simplifies the equation to

$$\boldsymbol{x}^a =\boldsymbol{x}^f + \boldsymbol{K}\left(\boldsymbol{y}^o - \boldsymbol{H}\boldsymbol{x}^f\right). \tag{A.49}$$

The covariance matrix of the optimal state $\boldsymbol{x}^a$ can be derived by variance propagation. First the partials of Equation A.49 are computed:

$$\frac{\partial\boldsymbol{x}^a}{\partial\boldsymbol{x}^f} =\mathbb{1} - \boldsymbol{K}\boldsymbol{H} \tag{A.50}$$

$$\frac{\partial\boldsymbol{x}^a}{\partial\boldsymbol{y}^o} =\boldsymbol{K} \tag{A.51}$$

Since $\boldsymbol{x}^f$ and $\boldsymbol{y}^o$ are assumed to be uncorrelated, error propagation yields

$$\begin{aligned}
\boldsymbol{P}^a &= \left[\frac{\partial\boldsymbol{x}^a}{\partial\boldsymbol{x}^f}\right]\boldsymbol{P}^f\left[\frac{\partial\boldsymbol{x}^a}{\partial\boldsymbol{x}^f}\right]^\top + \left[\frac{\partial\boldsymbol{x}}{\partial\boldsymbol{y}^o}\right]\boldsymbol{R}\left[\frac{\partial\boldsymbol{x}}{\partial\boldsymbol{y}^o}\right]^\top && \text{(A.52)}\\
& && \text{insert derivatives}\\
&=(\mathbb{1} - \boldsymbol{K}\boldsymbol{H})\boldsymbol{P}^f(\mathbb{1} - \boldsymbol{K}\boldsymbol{H})^\top + \boldsymbol{K}\boldsymbol{R}\boldsymbol{K}^\top && (\boldsymbol{U}+\boldsymbol{V})^\top = \boldsymbol{U}^\top + \boldsymbol{V}^\top\\
& && (\boldsymbol{U}\boldsymbol{V})^\top = \boldsymbol{V}^\top\boldsymbol{U}^\top\\
&=(\mathbb{1} - \boldsymbol{K}\boldsymbol{H})\boldsymbol{P}^f(\mathbb{1} - \boldsymbol{H}^\top\boldsymbol{K}^\top) + \boldsymbol{K}\boldsymbol{R}\boldsymbol{K}^\top\\
&=(\boldsymbol{P}^f - \boldsymbol{K}\boldsymbol{H}\boldsymbol{P}^f)(\mathbb{1} - \boldsymbol{H}^\top\boldsymbol{K}^\top) + \boldsymbol{K}\boldsymbol{R}\boldsymbol{K}^\top && \text{eliminate brackets}\\
&=\boldsymbol{P}^f - \boldsymbol{K}\boldsymbol{H}\boldsymbol{P}^f \underbrace{-\boldsymbol{P}^f\boldsymbol{H}^\top\boldsymbol{K}^\top + \boldsymbol{K}\boldsymbol{H}\boldsymbol{P}^f\boldsymbol{H}^\top\boldsymbol{K}^\top + \boldsymbol{K}\boldsymbol{R}\boldsymbol{K}^\top}_{0}.
\end{aligned}$$

The expression above the bracket is zero since

$$\begin{aligned}
\boldsymbol{K}\boldsymbol{H}\boldsymbol{P}^f\boldsymbol{H}^\top\boldsymbol{K}^\top + \boldsymbol{K}\boldsymbol{R}\boldsymbol{K}^\top - \boldsymbol{P}^f\boldsymbol{H}^\top\boldsymbol{K}^\top &\overset{!}{=}0 && \text{(A.53)}\\
& && \text{factorize } \boldsymbol{K}\\
\boldsymbol{K}\left(\boldsymbol{H}\boldsymbol{P}^f\boldsymbol{H}^\top\boldsymbol{K}^\top + \boldsymbol{R}\boldsymbol{K}^\top\right) - \boldsymbol{P}^f\boldsymbol{H}^\top\boldsymbol{K}^\top &=0\\
& && \text{factorize } \boldsymbol{K}^\top\\
\boldsymbol{K}\left(\boldsymbol{H}\boldsymbol{P}^f\boldsymbol{H}^\top + \boldsymbol{R}\right)\boldsymbol{K}^\top - \boldsymbol{P}^f\boldsymbol{H}^\top\boldsymbol{K}^\top &=0\\
& && \text{insert defintion of } \boldsymbol{K}\\
\boldsymbol{P}^f\boldsymbol{H}^\top\underbrace{\left(\boldsymbol{H}\boldsymbol{P}^f\boldsymbol{H}^\top + \boldsymbol{R}\right)^{-1}\left(\boldsymbol{H}\boldsymbol{P}^f\boldsymbol{H}^\top + \boldsymbol{R}\right)}_{\mathbb{1}}\boldsymbol{K}^\top - \boldsymbol{P}^f\boldsymbol{H}^\top\boldsymbol{K}^\top &=0.
\end{aligned}$$

Thus, the VCM of the optimal state is

$$\boldsymbol{P}^a = \boldsymbol{P}^f - \boldsymbol{K}\boldsymbol{H}\boldsymbol{P}^f. \tag{A.54}$$

A.6.2. Equivalent Expression for Analysis Error

Using the Sherman Morrison-Woodbury formula (Woodbury, 1950) the Kalman Gain (Equation 6.49) can be expressed as (e.g., Bocquet and Farchi, 2024, Equation 1.24)

$$\boldsymbol{K} = \left(\boldsymbol{P}^{f^{-1}} + \boldsymbol{H}^\intercal\boldsymbol{R}^{-1}\boldsymbol{H}\right)^{-1}\boldsymbol{H}^\intercal\boldsymbol{R}^{-1}. \tag{A.55}$$

Inserting A.55 into Equation 6.50 gives

$$\begin{aligned}
\boldsymbol{P}^a =& (\mathbb{1} - \boldsymbol{K}\boldsymbol{H})\boldsymbol{P}^f && \text{insert Equation A.55}\\
=& (\mathbb{1} - \underbrace{(\boldsymbol{P}^{f^{-1}} + \boldsymbol{H}^\intercal\boldsymbol{R}^{-1}\boldsymbol{H})^{-1}\boldsymbol{H}^\intercal\boldsymbol{R}^{-1}}_{\boldsymbol{K}}\boldsymbol{H})\boldsymbol{P}^f && \text{replace identity}\\
=& \Big[\underbrace{\left(\boldsymbol{P}^{f^{-1}} + \boldsymbol{H}^\intercal\boldsymbol{R}^{-1}\boldsymbol{H}\right)^{-1}\left(\boldsymbol{P}^{f^{-1}} + \boldsymbol{H}^\intercal\boldsymbol{R}^{-1}\boldsymbol{H}\right)}_{\mathbb{1}}\\
&- \left(\boldsymbol{P}^{f^{-1}} + \boldsymbol{H}^\intercal\boldsymbol{R}^{-1}\boldsymbol{H}\right)^{-1}\boldsymbol{H}^\intercal\boldsymbol{R}^{-1}\boldsymbol{H}\Big]\boldsymbol{P}^f && \text{factorize } \left(\boldsymbol{P}^{f^{-1}} + \boldsymbol{H}^\intercal\boldsymbol{R}^{-1}\boldsymbol{H}\right)^{-1}\\
=& \left(\boldsymbol{P}^{f^{-1}} + \boldsymbol{H}^\intercal\boldsymbol{R}^{-1}\boldsymbol{H}\right)^{-1}\Big[\boldsymbol{P}^{f^{-1}} + \underbrace{\boldsymbol{H}^\intercal\boldsymbol{R}^{-1}\boldsymbol{H} - \boldsymbol{H}^\intercal\boldsymbol{R}^{-1}\boldsymbol{H}}_{0}\Big]\boldsymbol{P}^f\\
=& \left(\boldsymbol{P}^{f^{-1}} + \boldsymbol{H}^\intercal\boldsymbol{R}^{-1}\boldsymbol{H}\right)^{-1}\underbrace{\boldsymbol{P}^{f^{-1}}\boldsymbol{P}^f}_{\mathbb{1}}\\
=& \left(\boldsymbol{P}^{f^{-1}} + \boldsymbol{H}^\intercal\boldsymbol{R}^{-1}\boldsymbol{H}\right)^{-1}.
\end{aligned} \tag{A.56}$$

Comparing this with Equation A.55 gives an equation of the gain matrix depending on the error of the analysis step

$$\boldsymbol{K} = \boldsymbol{P}^a\boldsymbol{H}^\intercal\boldsymbol{R}^{-1}. \tag{A.57}$$

A.6.3. Kalman Gain from Ensemble

$$\begin{aligned}
\boldsymbol{K} =& \boldsymbol{P}^f\boldsymbol{H}^\intercal(\boldsymbol{R} + \boldsymbol{H}\boldsymbol{P}^f\boldsymbol{H}^\intercal)^{-1}\\
=& \frac{\hat{\boldsymbol{X}}^f\left(\hat{\boldsymbol{X}}^f\right)^\intercal}{n_e - 1}\boldsymbol{H}^\intercal\left(\boldsymbol{R} + \boldsymbol{H}\frac{\hat{\boldsymbol{X}}^f\left(\hat{\boldsymbol{X}}^f\right)^\intercal}{n_e - 1}\boldsymbol{H}^\intercal\right)^{-1} && \boldsymbol{S} = \boldsymbol{H}\hat{\boldsymbol{X}}^f\\
=& \frac{\hat{\boldsymbol{X}}^f\boldsymbol{S}^\intercal}{n_e - 1}\left(\boldsymbol{R} + \frac{\boldsymbol{S}\boldsymbol{S}^\intercal}{n_e - 1}\right)^{-1}
\end{aligned} \tag{A.58}$$

An equivalent formulation can be found by expanding the fraction with $(n_e - 1)$

$$\begin{aligned}
\boldsymbol{K} &= \frac{\hat{\boldsymbol{X}}^f \boldsymbol{S}^\top}{n_e - 1} \left(\frac{(n_e - 1)\boldsymbol{R} + \boldsymbol{S}\boldsymbol{S}^\top}{n_e - 1} \right)^{-1} && \\
& && \Big\downarrow\ (a\boldsymbol{A})^{-1} = a^{-1}\boldsymbol{A}^{-1} \\
&= \frac{\hat{\boldsymbol{X}}^f \boldsymbol{S}^\top}{n_e - 1} (n_e - 1) \left((n_e - 1)\boldsymbol{R} + \boldsymbol{S}\boldsymbol{S}^\top \right)^{-1} && \\
& && \Big\downarrow\ \text{eliminate } n_e\text{-1} \\
&= \hat{\boldsymbol{X}}^f \boldsymbol{S}^\top \left((n_e - 1)\boldsymbol{R} + \boldsymbol{S}\boldsymbol{S}^\top \right)^{-1} &&
\end{aligned} \tag{A.59}$$

Using the definition of the VCM of the innovation $\boldsymbol{F} = (n_e - 1)\boldsymbol{R} + \boldsymbol{S}\boldsymbol{S}^\top$, one finally gets

$$\boldsymbol{K} = \hat{\boldsymbol{X}}^f \boldsymbol{S}^\top \boldsymbol{F}^{-1} \tag{A.60}$$

A.6.4. Quadratic Analyzed Ensemble

Starting from Equation 6.50 and skipping the indices, one obtains

$$\begin{aligned}
\boldsymbol{P}^a &= (\mathbb{1} - \boldsymbol{K}\boldsymbol{H})\boldsymbol{P}^f && \\
& && \Big\downarrow\ \text{express VCM via ensemble} \\
\frac{\hat{\boldsymbol{X}}^a \left(\hat{\boldsymbol{X}}^a\right)^\top}{n_e - 1} &= (\mathbb{1} - \boldsymbol{K}\boldsymbol{H}) \frac{\hat{\boldsymbol{X}}^f \left(\hat{\boldsymbol{X}}^f\right)^\top}{n_e - 1} && \\
& && \Big\downarrow\ \text{eliminate } n_e\text{-1} \\
\hat{\boldsymbol{X}}^a \left(\hat{\boldsymbol{X}}^a\right)^\top &= (\mathbb{1} - \boldsymbol{K}\boldsymbol{H}) \hat{\boldsymbol{X}}^f \left(\hat{\boldsymbol{X}}^f\right)^\top && \\
& && \Big\downarrow\ \text{pull } \hat{\boldsymbol{X}}^f \text{ into brackets} \\
\hat{\boldsymbol{X}}^a \left(\hat{\boldsymbol{X}}^a\right)^\top &= (\hat{\boldsymbol{X}}^f - \boldsymbol{K}\boldsymbol{H}\hat{\boldsymbol{X}}^f) \left(\hat{\boldsymbol{X}}^f\right)^\top && \\
& && \Big\downarrow\ \boldsymbol{S} = \boldsymbol{H}\hat{\boldsymbol{X}}^f \\
\hat{\boldsymbol{X}}^a \left(\hat{\boldsymbol{X}}^a\right)^\top &= (\hat{\boldsymbol{X}}^f - \boldsymbol{K}\boldsymbol{S}) \left(\hat{\boldsymbol{X}}^f\right)^\top &&
\end{aligned} \tag{A.61}$$

Inserting the expression for the gain matrix derived in Appendix A.6.3 yields

$$\begin{aligned}
\hat{\boldsymbol{X}}^a \left(\hat{\boldsymbol{X}}^a\right)^\top &= (\hat{\boldsymbol{X}}^f - \hat{\boldsymbol{X}}^f \boldsymbol{S}^\top \boldsymbol{F}^{-1}\boldsymbol{S}) \left(\hat{\boldsymbol{X}}^f\right)^\top && \\
& && \Big\downarrow\ \text{factorize } \hat{\boldsymbol{X}}^f \\
&= \hat{\boldsymbol{X}}^f (\mathbb{1} - \boldsymbol{S}^\top \boldsymbol{F}^{-1}\boldsymbol{S}) \left(\hat{\boldsymbol{X}}^f\right)^\top &&
\end{aligned} \tag{A.62}$$

A.6.5. Ensemble of Analyzed Model Perturbation

$$\begin{aligned}
\hat{\boldsymbol{X}}^a \left(\hat{\boldsymbol{X}}^a\right)^\top &= \hat{\boldsymbol{X}}^f \left(\mathbb{1} - \boldsymbol{S}^\top \boldsymbol{F}^{-1}\boldsymbol{S}\right) \left(\hat{\boldsymbol{X}}^f\right)^\top && \\
& && \Big\downarrow\ \mathbb{1} - \boldsymbol{S}^\top \boldsymbol{F}^{-1}\boldsymbol{S} := \boldsymbol{T}\boldsymbol{T}^\top \\
\hat{\boldsymbol{X}}^a \left(\hat{\boldsymbol{X}}^a\right)^\top &= \hat{\boldsymbol{X}}^f \boldsymbol{T}\boldsymbol{T}^\top \left(\hat{\boldsymbol{X}}^f\right)^\top && \\
& && \Big\downarrow\ \boldsymbol{A}^\top \boldsymbol{B}^\top = (\boldsymbol{B}\boldsymbol{A})^\top \\
\hat{\boldsymbol{X}}^a \left(\hat{\boldsymbol{X}}^a\right)^\top &= \hat{\boldsymbol{X}}^f \boldsymbol{T} (\hat{\boldsymbol{X}}^f \boldsymbol{T})^\top && \\
\hat{\boldsymbol{X}}^a &= \hat{\boldsymbol{X}}^f \boldsymbol{T} &&
\end{aligned} \tag{A.63}$$

A.6.6. Rewrite Transform Matrix Product

Applying the Sherman Morrison-Woodbury formula (Woodbury, 1950) to the right-hand side of Equation 6.62 yields

$$
\begin{aligned}
\boldsymbol{T}\boldsymbol{T}^{\intercal} &= \mathbb{1} - \boldsymbol{S}^{\intercal}\boldsymbol{F}^{-1}\boldsymbol{S} && \Big\downarrow \text{Sherman Morrison-Woodbury} \\
&= \left(\mathbb{1} + \boldsymbol{S}^{\intercal}(\boldsymbol{F} - \boldsymbol{S}\boldsymbol{S}^{\intercal})^{-1}\boldsymbol{S}\right)^{-1} && \Big\downarrow \text{insert defintion of } \boldsymbol{F} \\
&= \left(\mathbb{1} + \boldsymbol{S}^{\intercal}((n_e - 1)\boldsymbol{R} + \boldsymbol{S}\boldsymbol{S}^{\intercal} - \boldsymbol{S}\boldsymbol{S}^{\intercal})^{-1}\boldsymbol{S}\right)^{-1} \\
&= \left(\mathbb{1} + \boldsymbol{S}^{\intercal}((n_e - 1)\boldsymbol{R})^{-1}\boldsymbol{S}\right)^{-1} && \Big\downarrow (a\boldsymbol{A})^{-1} = a^{-1}\boldsymbol{A}^{-1} \\
&= \left(\mathbb{1} + \boldsymbol{S}^{\intercal}\frac{1}{n_e - 1}\boldsymbol{R}^{-1}\boldsymbol{S}\right)^{-1}
\end{aligned}
\tag{A.64}
$$

B. Solar- and Geomagnetic indices

B.1. Solar Indices

The F10.7 index is discussed in Section 2.3.1.2. Here additional indices used by models discussed in Chapter 5 are summarized.

B.1.1. F30

The F30 index (de Wit and S. Bruinsma, 2017; de Wit et al., 2014) is a proxy for solar EUV radiation similar to the F10.7 index but measured at a wavelength of 30 cm. It is constructed from radio polarimeters observations at 30 cm which have been conducted since 1 March 1957, first from the Toyokawa Observatory and later from Nobeyama Observatory, both in Japan (Shimojo and Iwai, 2023). de Wit and S. Bruinsma (2017) recommend using F30 over F10.7 for thermospheric applications since it enables a more accurate neutral density modeling.

B.1.2. S10

The S10 index (Tobiska et al., 2008b; Tobiska and Bowman, 2005) (sometimes also called S10.7 and formerly called S_{EUV}) is derived from the observations of the Solar Extreme-ultraviolet Monitor (SEM) installed on the Solar and Heliospheric Observatory (SOHO, Domingo et al., 1995) satellite located on the Lagrange Point 1. It observes solar EUV emission from 26 to 34 nm every 15 s since 1995. The emissions in that band are dominated by the chromospheric He II line at 30.4 nm (see Figure 2.8). To calculate the S10 index the emissions are integrated over the observed wavelengths, normalized by the daily mean value, and converted to solar flux units via linear regression to the F10.7 index (Tobiska and Bowman, 2005, Equation 1).

B.1.3. Y10

The Y10 index (Tobiska et al., 2008a) is a combination of two indices. The Xb10 index, which represents the solar X-ray emission at 0.1–0.8 nm, and the L10 index, which represents the Lyman-α emission. Both the X-ray and Lyman-α emissions are deposited into the mesosphere and lower thermosphere. During solar maximum, the X-ray emissions are dominant, while Lyman-α is the dominant driver during solar minimum conditions (see Figure 2.8). The Y10 index “is weighted to represent mostly Xb10 during solar maximum and to represent mostly Lyman-α during moderate and low solar activity” (Tobiska et al., 2008a) using the F10.7 index.

B.1.4. Mg II core-to-wing

Near 280 nm, the solar spectrum (see Figure 2.8) has absorption lines associated with singly ionized magnesium (Mg II). The core-to-wing ratio was first described by Heath and Schlesinger (1986). It is the ratio of the irradiance at the peaks (cores) of absorption lines of MG II to the irradiance in the nearby continua (wings). See Snow et al. (2019, Figure 2) for a detailed spectrum.

The Mg II core-to-wing ratio (Heath and Schlesinger, 1986; Rodney A., Viereck and Puga, Lawrence C., 1999; Snow et al., 2019; Viereck et al., 2001) has been derived from different satellite missions. It is highly correlated to the variability of the solar spectral irradiance in the ultra violate range. An advantage of the Mg II core-to-wing ratio is that instrumental errors affecting both cores and wings are eliminated.

Viereck et al. (2001) argues that MG II core-to-wing ratio is a better proxy for EUV than F10.7.

B.1.5. M10

The M10 index (Tobiska et al., 2008b; Tobiska and Bowman, 2005) (sometimes also M10.7 index) is basically the Mg II core-to-wing index converted to solar flux units via linear regression with the F10.7 index.

B.2. Geomagnetic Indices

The Kp index is discussed in Section 2.3.2.2. Here additional indices used by models discussed in Chapter 5 are summarized.

B.2.1. AP index

The AP index is the Kp indexed transformed to a linear scale (see Figure 2.17).

B.2.2. Hpo index

The Hpo index (Yamazaki et al., 2022) is a Kp-like index with higher temporal resolution and without an upper limit. The probability density distribution of Hpo was designed to be similar to the distribution of the Kp-index (see Figure 2.17). There are two products, the Hp60 and Hp30 index, with 60 and 30 minutes temporal resolution, respectively.

B.2.3. D_{st} index

The disturbance storm-time index (Sugiura, 1963) is determined from near-equatorial observatories. Those observatories are sensitive to the equatorial ring current (e.g., Baumjohann, 2012, Section 3.6) that is located several Earth radii above the ground. During geomagnetic storms, the enhanced ring current, which flows westwards, decreases the horizontal component of the magnetic field (mostly pointing towards north) in the equatorial region on the ground (Love and Remick, 2007). This effect does not depend on the longitude. D_{st} can be computed continuously also for quiet conditions. It has a temporal resolution of one minute.

C. TIE-GCM

C.1. Sensitivity

It is quite easy to find out how a state variable simulated by a model responds to changes in a model parameter. One can simply perturb a single parameter within a range while holding all other parameters constant. However, this approach does not provide information about the combined response when perturbing multiple parameters simultaneously. Moreover, when analyzing the responses, one must keep in mind that the effect depends on the chosen perturbation. Choosing realistic perturbations is crucial to rank the parameters by their sensitivity. Even for unrealistic perturbations, one can compare the sensitivity of a single parameter at different altitudes.

Here, the sensitivity is investigated for solar minimum conditions (F10.7: 70 sfu, the IMF is zero in the x and y component and 0.01 nT in z direction, the solar wind velocity is $400\,\mathrm{km\,s^{-1}}$, and the solar wind density is $4\,\mathrm{cm^{-3}}$). The initial state is the climatological state included in the TIE-GCM data. The climatological state is forwarded cyclically over five days to reach a steady state using the 5°-version. I analyze the last forecast of the model run.

The average impact of the lower boundaries on the neutral mass density is illustrated in Figure C.1. The influence of a global offset in the lower boundary conditions on the neutral mass density decreases with altitude. Within the analyzed range, the impact of the neutral wind on the neutral density is rather small at all altitudes. Changing the wind speed by $\pm 10\,\mathrm{m\,s^{-1}}$ ($\pm$20 %) changes the neutral mass density by not more than $\pm$0.2 %. In contrast, a 40 K (20 %) warmer neutral temperature at the lower boundary increases the neutral mass density at 400 km by 5 %. The minimal value of geopotential height is limited to 95 km in the TIE-GCM. Thus, all the lines corresponding to perturbations less than -2 km give the same result. Note that realistic perturbations for lower boundary conditions should be derived from ensemble runs of the model providing the lower boundaries in the future.

Figure C.2 and Figure C.3 contain the impact of some model parameters and the external forcings on the neutral mass density, respectively. For all external forcings, the influence increases with altitude.

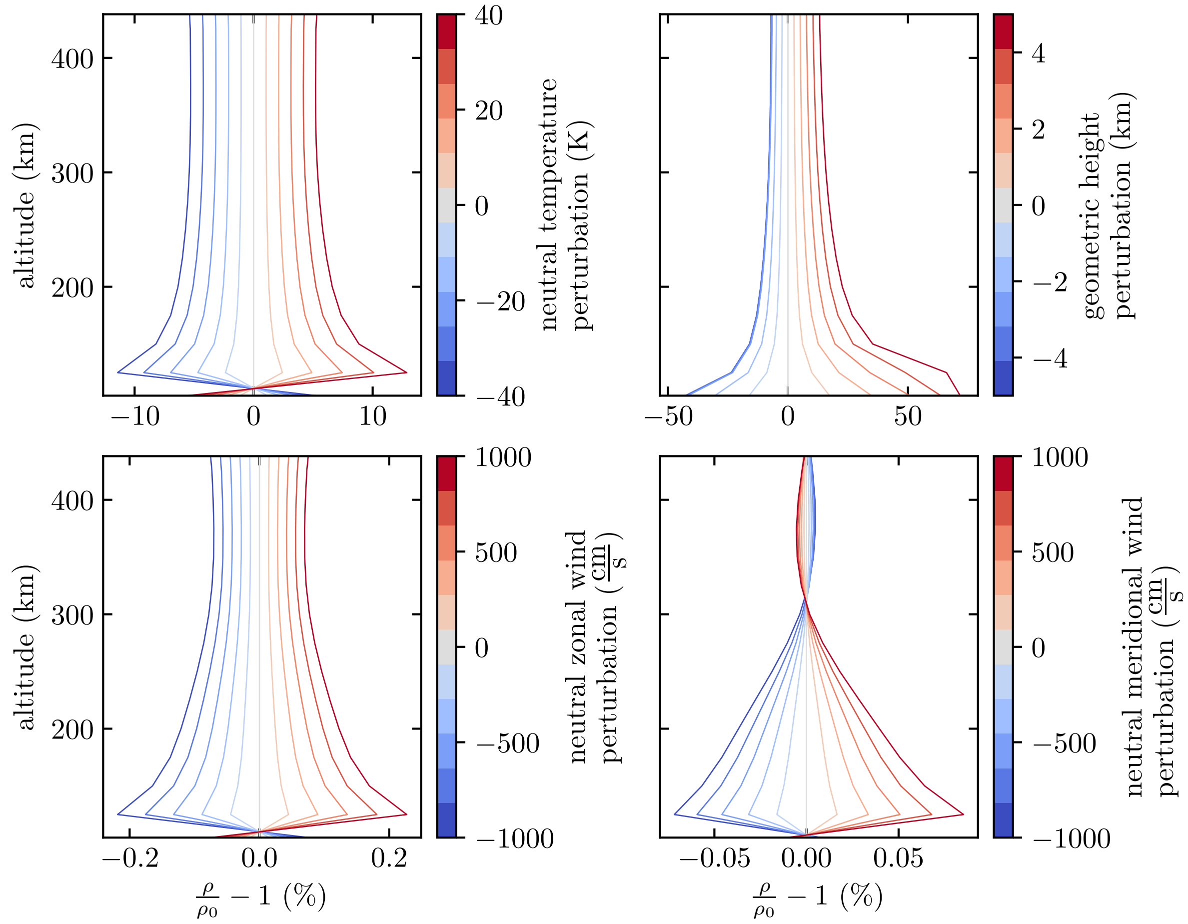

Figure C.1.: Sensitivity of horizontally averaged neutral mass density w.r.t. lower boundary conditions. The original TIE-GCM data was interpolated to a regular grid (described in Section 7.6). Each cell was weighted by its surface area (Appendix C.4).

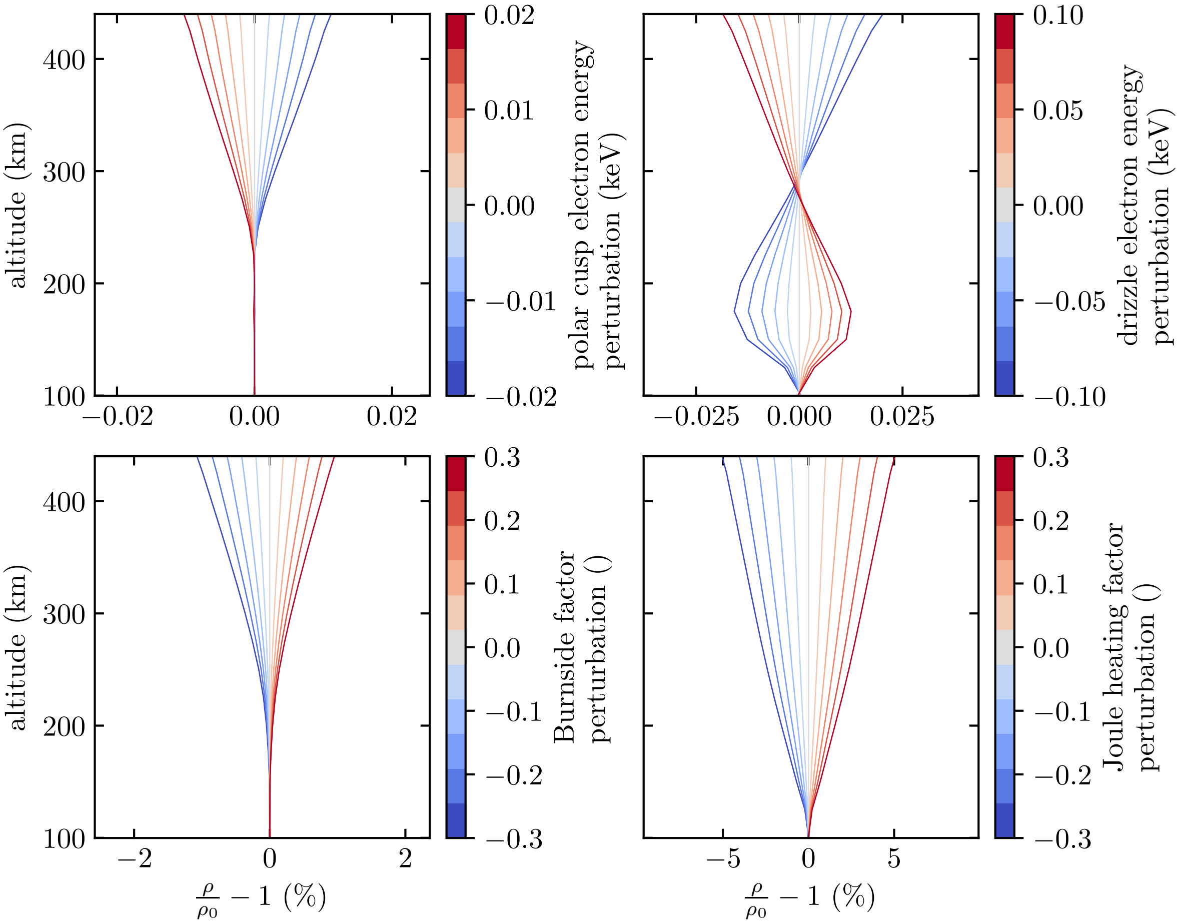

Figure C.2.: Sensitivity of horizontally averaged neutral mass density w.r.t. some model parameters. The original TIE-GCM data was interpolated to a regular grid (described in Section 7.6). Each cell was weighted by its surface area (Appendix C.4). The maximal absolute perturbations of all shown parameters are 20 % of the default value.

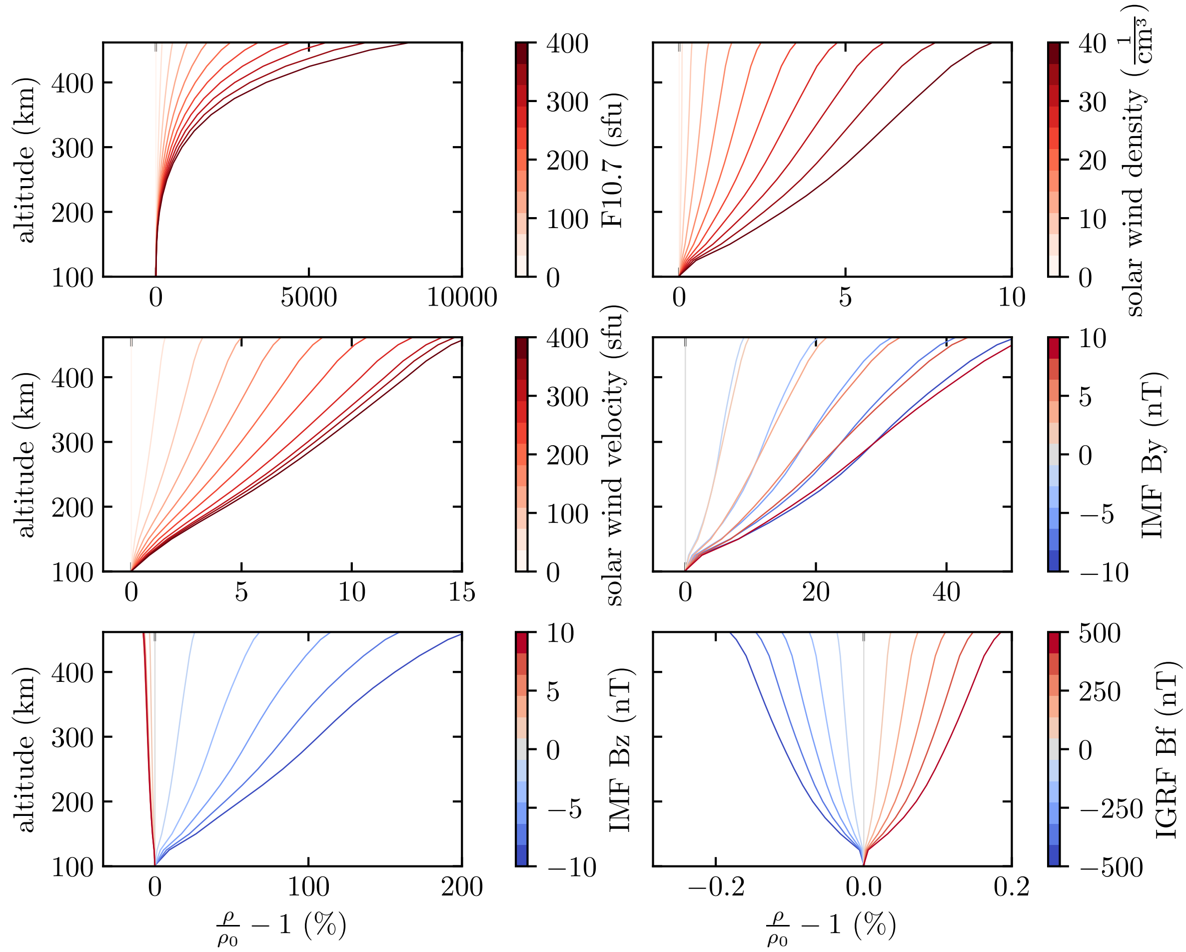

Figure C.3.: Sensitivity of horizontally averaged neutral density w.r.t. external forcing. The original TIE-GCM data was interpolated to a regular grid (described in Section 7.6). Each cell was weighted by its surface area (Appendix C.4).

C.2. Parallelization

The TIE-GCM 2.0 is parallelized by subdividing the model grid into subdomains horizontally. There is no parallelization along the vertical direction. This is illustrated in Figure C.4 for an exemplary configuration using eight subdomains[1]. For computing the horizontal gradients, each subdomain requires the data at the rim from the neighboring domains. This data is made available by halo cells located around each subdomain. The exchange of the periodic cells in longitude is implemented explicitly. However, this is actually not necessary since this is covered by the halo exchange. I suspect this exchange was not removed when the parallelization was implemented.

I use the fully parallelized implementation of PDAF. Thus, each ensemble member is computed in parallel, and all members are computed in parallel. Each subdomain of each ensemble is assigned to its own physical processor core. The processor cores communicate via the MPI. Each of this processor cores is represented by a so called *rank* within the MPI. An exemplary layout of the MPI ranks is illustrated in Figure C.5.

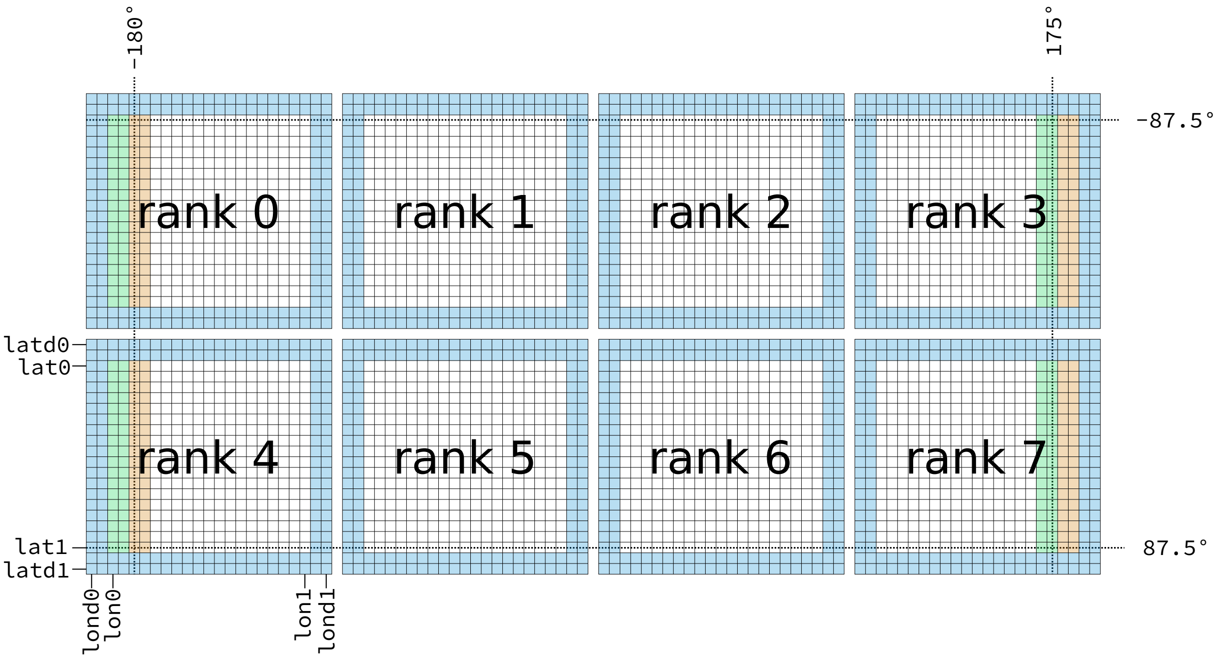

Figure C.4.: Distribution of the model grid on eight subdomains and processor cores for 5° resolution. The blue cells are the halo cells (called ghost cells in TIE-GCM code) that contain the data from the neighboring subdomains (not on the poles). The green and orange cells are periodic cells in longitude that are also exchanged. Since there are already the halo cells, they are actually unnecessary.

---

[1] Do not confuse these subdomains with those used for domain localization (Section 6.4.2). Here a subdomain is the part of the complete domain that is assigned to a single physical processor core.

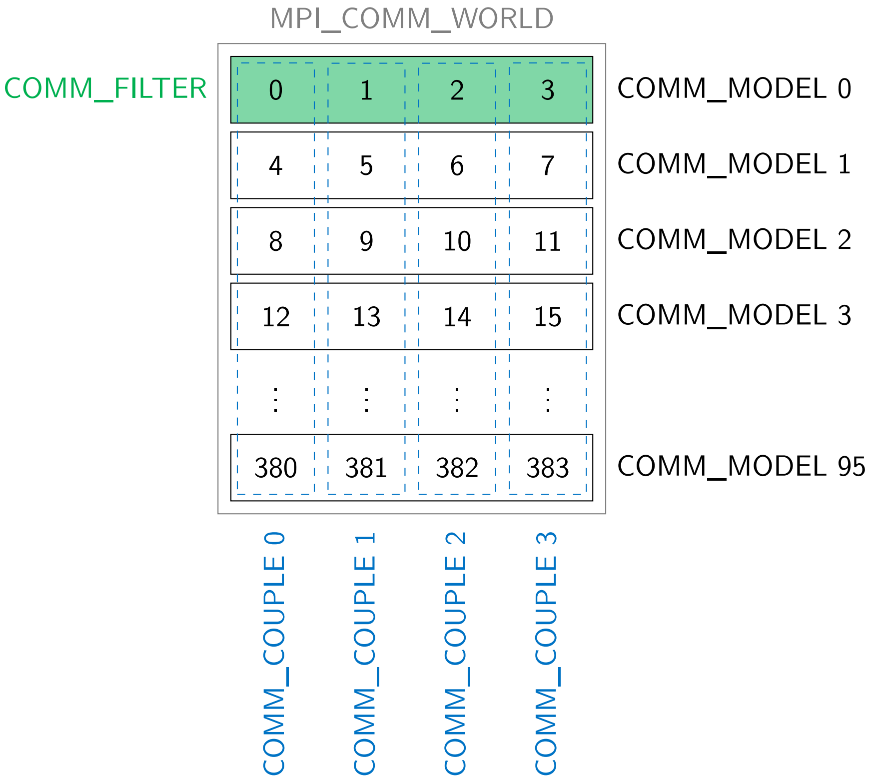

Figure C.5.: Exemplary MPI layout of the fully parallel PDAF implementation with 96 ensemble members each distributed over 4 physical processor cores. For this configuration, each number represents a MPI rank, physical processor core, and subdomain at the same time. The MPI communicators are illustrated by rectangles. Each row corresponds to an ensemble member or a model instance. Each column corresponds to a subdomain of the model.

C.3. Scaling

It is not possible to reduce the execution time of a computer program immeasurably by distributing its computations over an ever-increasing number of processor cores. Typically, it is not possible to parallelize all of the program's computations, which means that the other processor cores must wait until the serial computations are finished. In addition, the communication between the processor cores slows down the execution.

According to Amdahl's law (Amdahl, 1967), the theoretical speedup S_A of a program parallelized using n processor cores with equal performance and serial fraction f is (e.g., Gustafson, 2011, p. 53)

$$S_A(n,f) = \frac{1}{f + \dfrac{1-f}{n}}. \tag{C.1}$$

One can measure the speedup S by dividing the time T_1 required to execute a program on a single processor core by the time T_n required to execute the same program with n processor

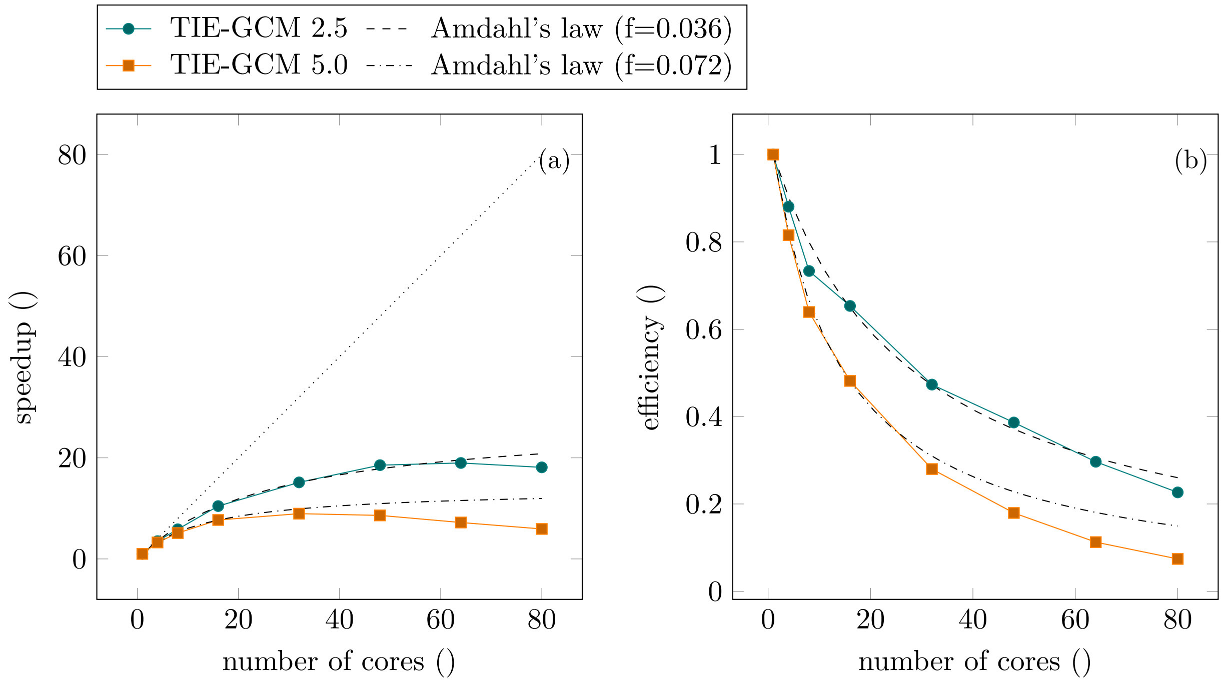

Figure C.6.: Strong scaling behavior of TIE-GCM 2.0 compiled without PDAF coupling. The benchmarks were computed on the JURECA cluster using the default TIE-GCM 2.0 setup. The results were written to a file every sixtieth step. On other clusters, a similar behavior was observed. The dashed and dashed-dotted lines were fitted to the data points.

cores (e.g., Zahorjan et al., 1989)

$$S(n) = \frac{T_1}{T_n}. \tag{C.2}$$

The efficiency (Zahorjan et al., 1989) E using n processor core is

$$E(n) = \frac{S(n)}{n}. \tag{C.3}$$

The speedup and efficiency of the TIE-GCM 2.0 are plotted in Figure C.6. Note that the file I/O and the solver for partial differential equations in the TIE-GCM 2.0 are not parallelized limiting the speedup. Data is written at every sixtieth step. My analysis indicates that the standalone TIE-GCM with 5° resolution should not use more than four physical processor cores and the TIE-GCM with 2.5° not more than eight physical processor cores, to maintain an efficiency above 70 %. In panel B.6a one can see that the speedup fo the 5° version degenerates when using more than 32 physical processor cores. That means the program runs longer with 64 than with 32 physical processor cores. This is likely due to the overhead introduced by the halo communication. I estimated the serial fraction by fitting Amdahl's law through the data points. The estimated serial fraction of the TIE-GCM 2.0 is 7.2 % and 3.6 % for 5° and 2.5° horizontal resolution, respectively. The fraction increases when writing results more frequently.

C.4. Account for Different Volumes of Grid Cells when Computing Statistics

The grid cells in the TIE-GCM all have varying volumes. The cells become smaller towards the poles because the number of cells per longitudinal ring is constant. Additionally, the height of the cells increases with altitude since pressure coordinates are used for the vertical component. Furthermore, two grid cells located at the same pressure will not have the same height since a surface of constant pressure deviates from a sphere.

For a three-dimensional grid defined by polar coordinates (λ, ϕ, r)

$$\begin{bmatrix} x \\ y \\ z \end{bmatrix} = \begin{bmatrix} r\sin(\phi) sin(\lambda) \\ r\sin(\phi) cos(\lambda) \\ r\cos(\phi) \end{bmatrix} \tag{C.4}$$

with radius $r \in \mathbb{R}^+$, longitude $\lambda \in [-\pi, \pi)$, and latitude $\phi \in [-\frac{\pi}{2}, \frac{\pi}{2}]$ the volume of a grid cell is given by

$$V = \int_{r_0}^{r_1} \int_{\lambda_0}^{\lambda_1} \int_{\phi_0}^{\phi_1} r^2 \cos(\phi)\, d\phi d\lambda dr \tag{C.5}$$

$$= \frac{1}{3}(r_1^3 - r_0^3)(\lambda_1 - \lambda_0)\,(\sin(\phi_1) - \sin(\phi_0))\,. \tag{C.6}$$

Note that Equation C.6 ignores the fact that each vertex of a grid cell has a different altitude. It assumes that the upper vertices and lower vertices have the same altitude. However, the error is neglect-able when using the average altitude at the top and bottom.

When computing statistics, one can weight each cell with the corresponding volume to account for the differences in volume.

When averaging cells at the same vertical coordinate, one can weight them by the surface area

$$S = \int_{\lambda_0}^{\lambda_1} \int_{\phi_0}^{\phi_1} r^2 \cos(\phi)\, d\phi d\lambda \tag{C.7}$$

$$= r^2(\lambda_1 - \lambda_0)\,(\sin(\phi_1) - \sin(\phi_0))\,. \tag{C.8}$$

Since in this scenario the radius r is constant, one can ignore it for the weighting. In case the longitudinal spacing $\lambda_1 - \lambda_0$ of all gird cells is equal one can simply use $\sin(\phi_1) - \sin(\phi_0)$ as weights.

D. Additional Figures

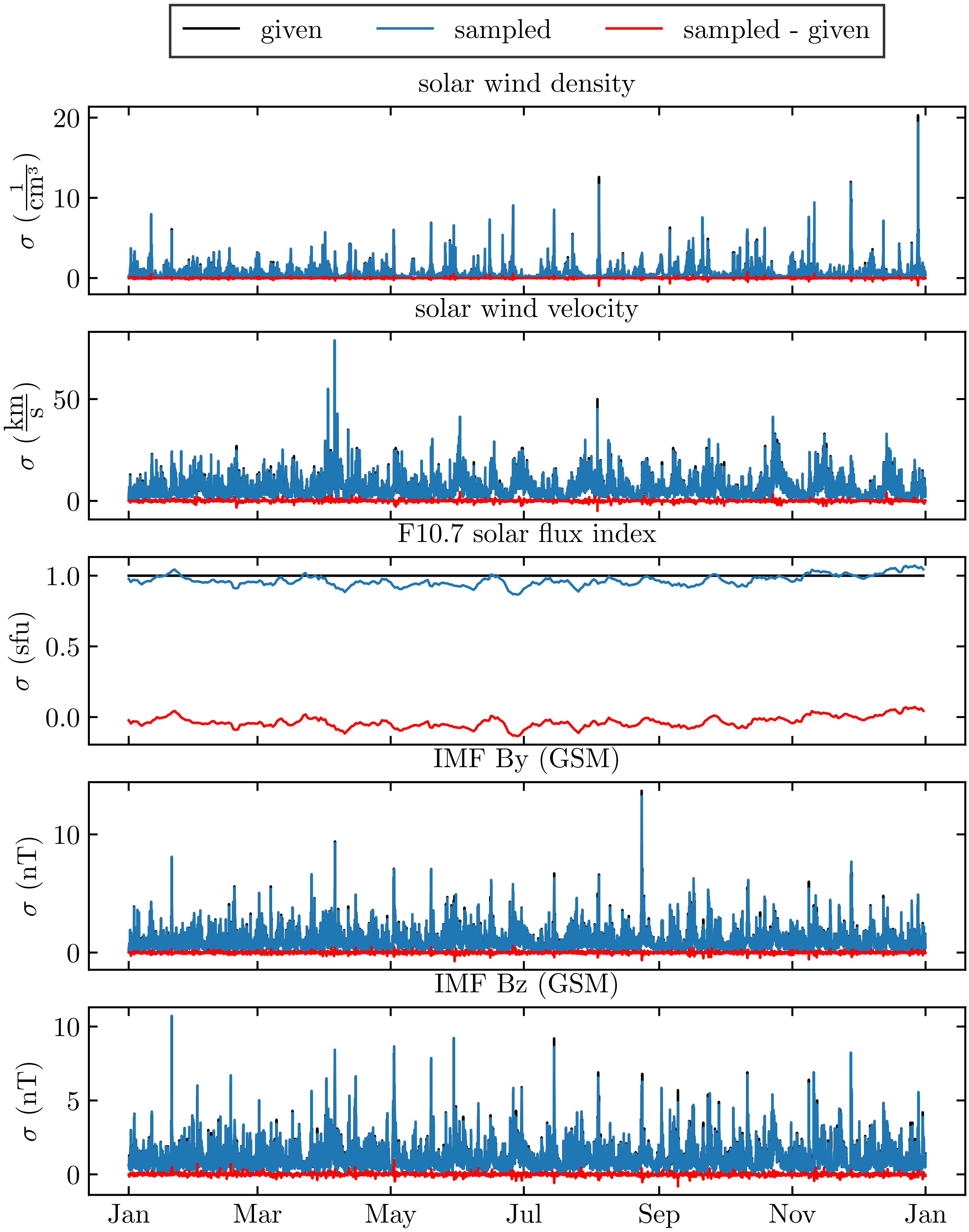

Figure D.1.: For the year 2010 the standard deviation of the external forcings described in Section 7.2 are plotted. The black line corresponds to the given standard deviations (see Table 7.2). The blue line is the standard deviation computed from the ensemble of perturbations sampled via Equation 7.2. The red line is the difference between the given and the sampled standard deviation. Compared with the absolute values the error is negligible.

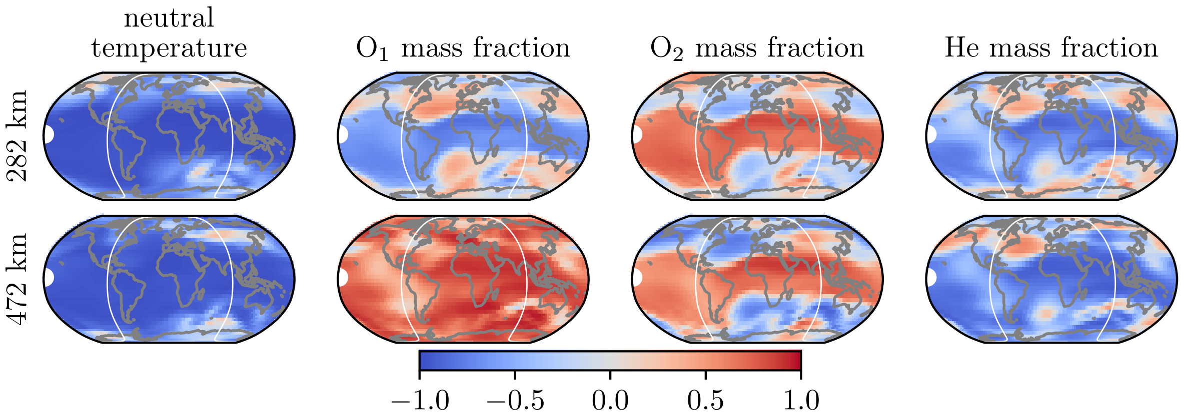

(a) Correlations of neutral mass density with other neutral state variables

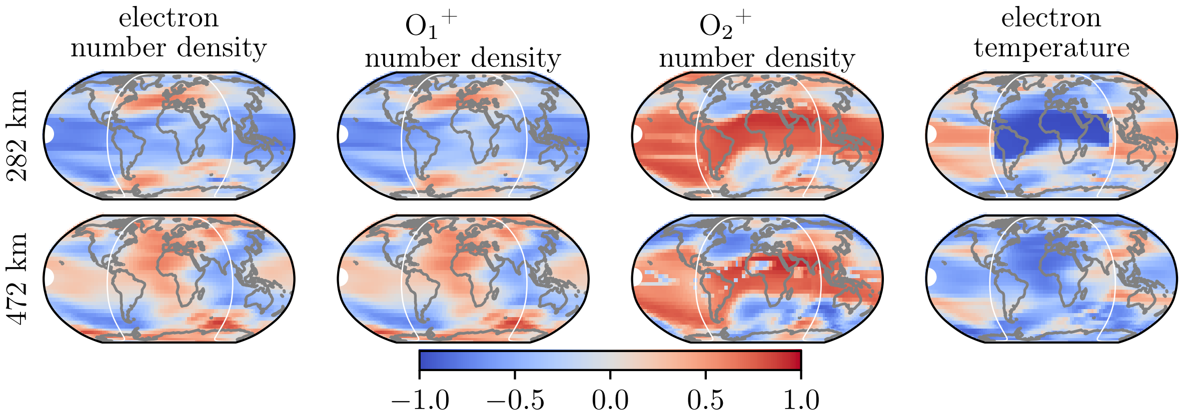

(b) Correlations of neutral mass density with state variables associated with charge carriers

Figure D.2.: Each map contains the correlation between neutral mass density and a state variable provided at the top of each column. Each row of maps correspond to a pressure levels. The average altitude of each pressure level is provided on the left of each row. The correlations are computed from an ensemble with 96 members at 27 March 2010 00:00 UTC+0 after forwarding the TIE-GCM 5° 10 days. The ensemble was generated using configuration P 4 (Table 8.1). The correlations in each map corresponds to a diagonal of a sub matrix surrounded by black lines in Figure 8.4.

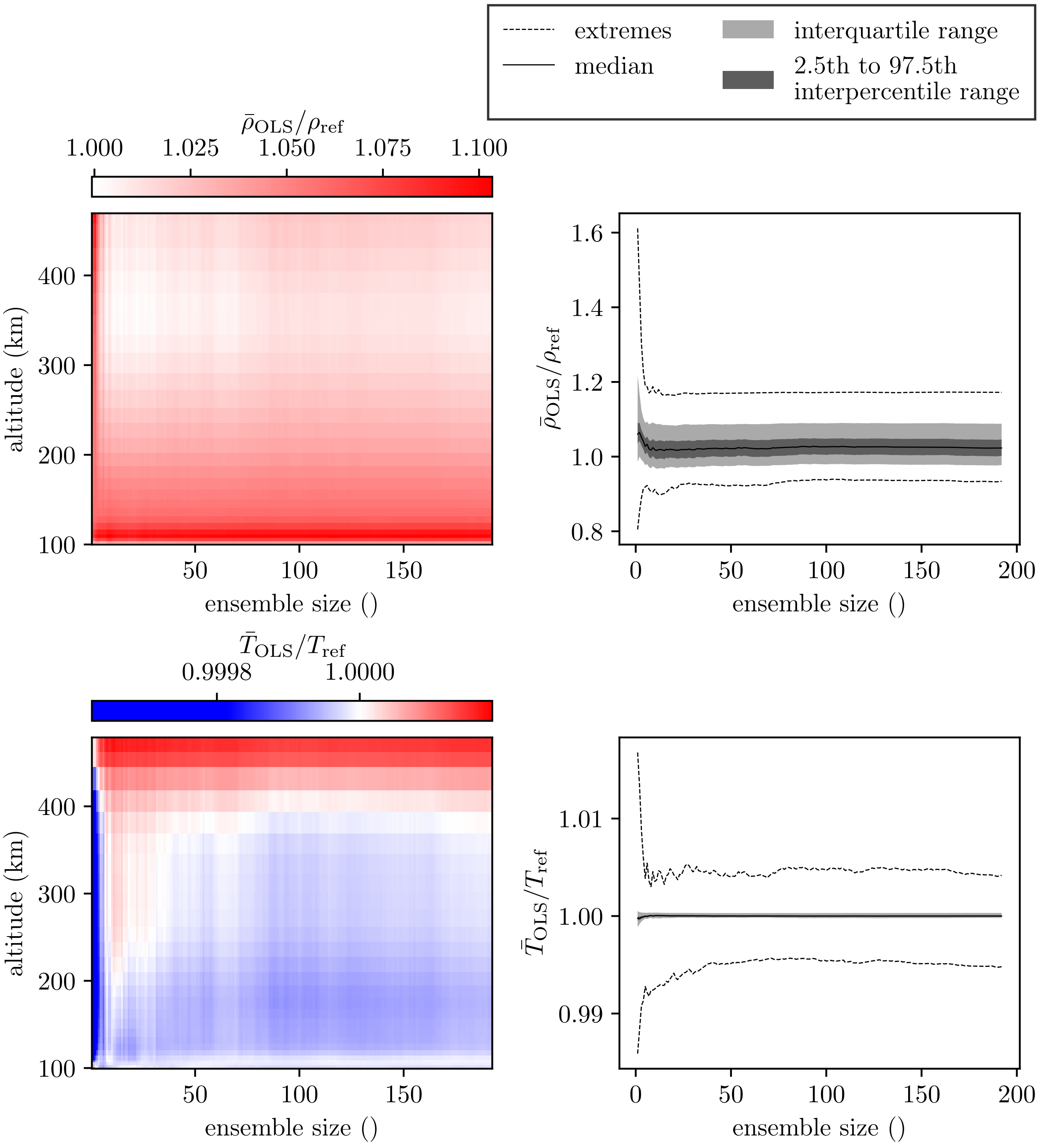

Figure D.3.: The panels in the upper row show the mass density ratio of the OLS (P 4) and reference run (single instance run without perturbations) depending on the ensemble size. The lower rows show the corresponding ratio for the neutral temperature. All grid cells from 26 March 2010 till 27 March 2010 have been used to calculate the average ratios. Weights are computed according to Appendix C.4. For ensemble sizes larger than 10, the differences w.r.t. the reference run become small. At low altitudes, the OLS computes a mass density that is up to 10 % larger compared to the reference run independent of the ensemble size. At higher altitudes, the density is also larger for the OLS but at a much smaller percentage.

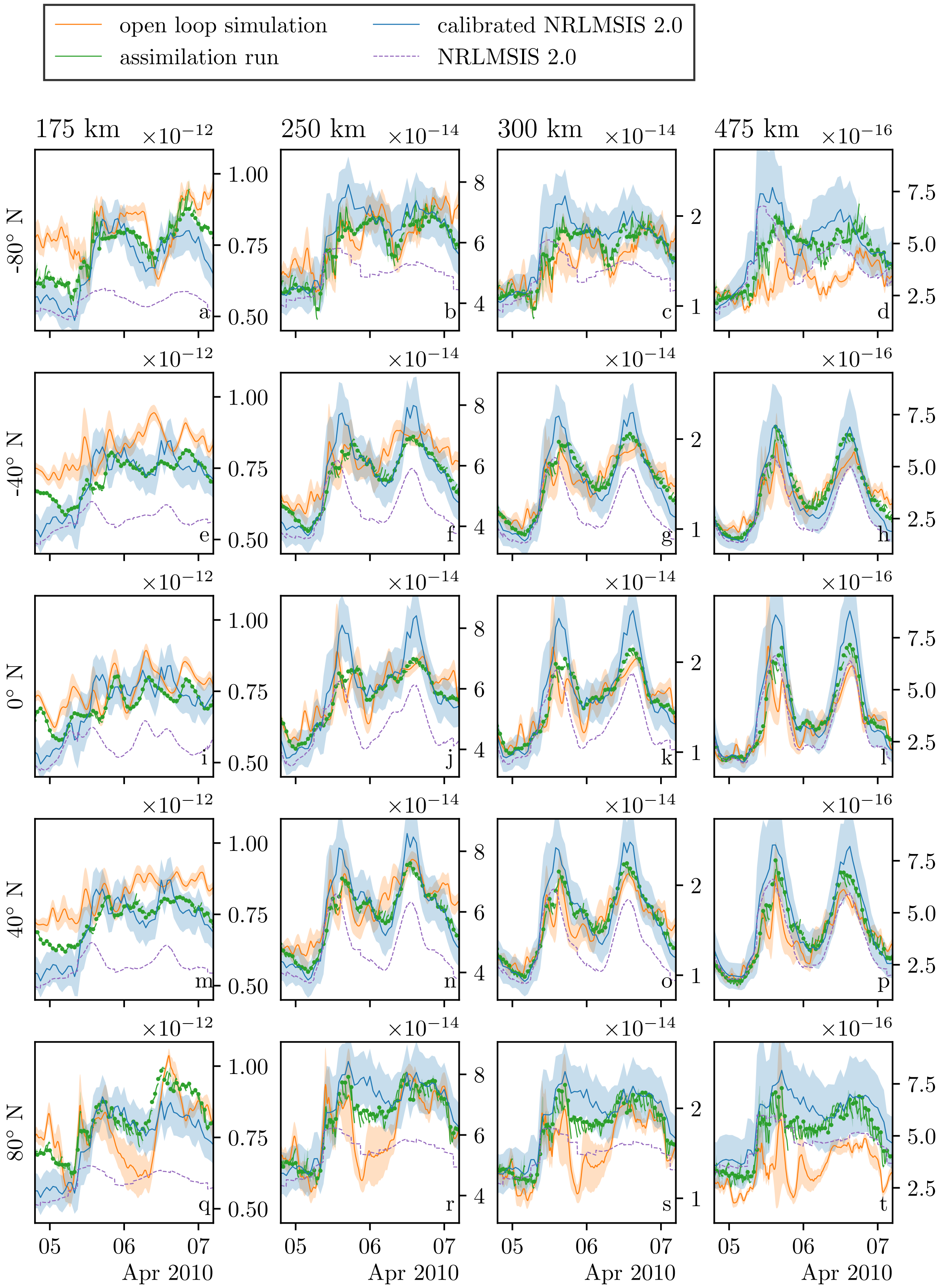

Figure D.4.: Each panel contains time series of mass density ($\mathrm{g\,cm^{-3}}$) for different cells of the data grid. Each row corresponds to a geocentric latitude and each column to an ellipsoidal height. The longitude is always 0°E. The panels of each column share the same y-axis. The error bands show the standard deviation.

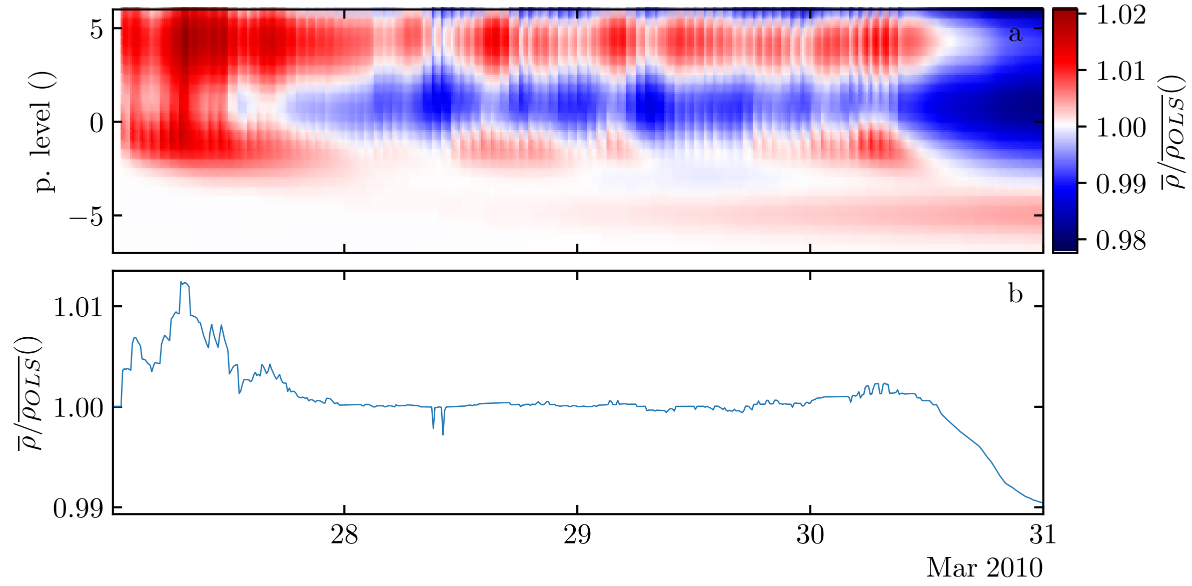

Figure D.5.: Each column in panel a is a height profile of the ratio of the ensemble mean of the neutral mass density $\overline{\rho}$ for experiment E 03 (Setup 6 and the OLS $\overline{\rho_{\mathrm{OLS}}}$. The average ensemble mean at each pressure level is weighted according to Appendix C.4. Panel b shows the median of the average ratio for each point in time.

E. Coordinate Systems

This thesis includes various coordinate systems which are suited for different applications. This chapter gives a compact overview of the used coordinate systems.

E.1. Transformation between Celestial and Terrestrial Reference System

Satellite orbits are best computed in quasi-inertial geocentric reference systems fixed to the stars (celestial reference system). Atmospheric models are typically computed on a non-inertial, geocentric reference system co-rotating with Earth (terrestrial reference system). Thus, to bring observations along an orbit and models together, the transformation between both systems is required.

By convention, the International Terrestrial Reference System (ITRS) defined in the *IERS Conventions* (2010, Section 4.1.4), and the geocentric celestial reference system (GCRS) also defined in the *IERS Conventions* (2010, Section 2.1) are employed. Both systems share the same origin and scale and differ by a set of time-dependent rotations. The transformation from a point in the GCRS $\boldsymbol{x}_{\mathrm{GCRS}}$ and the same point in the ITRS $\boldsymbol{x}_{\mathrm{ITRS}}$ reads (*IERS Conventions* 2010, Equation 5.1)

$$\boldsymbol{x}_{\mathrm{GCRS}} = \boldsymbol{Q}(t)\boldsymbol{R}(t)\boldsymbol{W}(t)\boldsymbol{x}_{\mathrm{ITRS}}, \tag{E.1}$$

where $\boldsymbol{Q}(t)$ is the rotation caused by precession and nutation, $\boldsymbol{R}(t)$ is the daily rotation of Earth, and $\boldsymbol{W}(t)$ represents polar motion (for example, Dehant and Mathews, 2015).

In this thesis, the values for the rotations are taken from the IERS EOP 14C04 time series (Bizouard et al., 2019).

E.2. Geocentric Solar Coordinates

The x axes of the GSE and GSM coordinate systems (e.g. M. A. Hapgood, 1992) are aligned to the Sun-Earth line (see Figure E.1). Such coordinate systems are useful to investigate phenomena occurring on the day or night-side of Earth. GSE and GSM differ in the definition of the z axis. The Z axis of the GSE system is the ecliptic pole, whereas the z axis of the GSM system is aligned to the projection of the dipole axis to the YZ plane of the GSE system. For both systems, the y axis completes the right-hand system. The transformation between the GSE and GSM system is a single rotation around the common x axis (e.g. M. A. Hapgood, 1992, Eq. 6). This transformation depends mainly on the daily rotation, the orbit of Earth around the Sun and the wandering of the dipole axis.

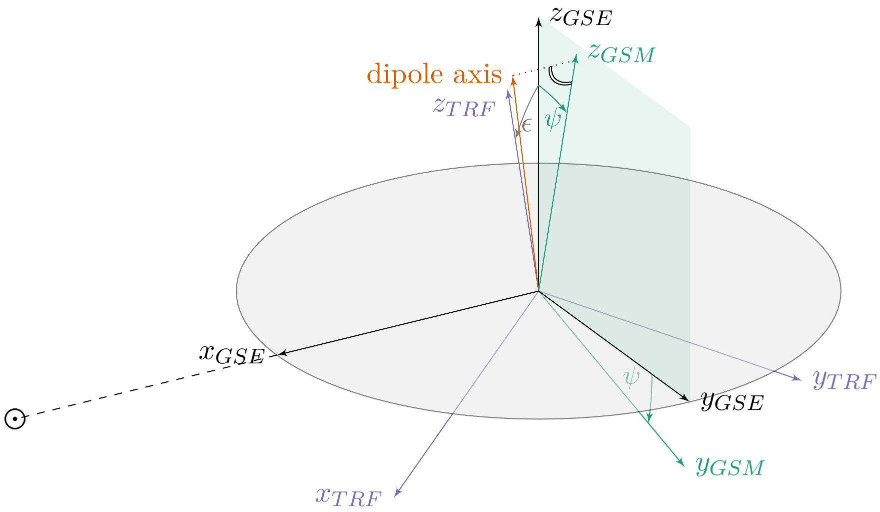

Figure E.1.: The gray circle illustrates the ecliptic. ϵ indicates the obliquity and the Sun is indicated by $\odot$. GSE and GSM system differ only by a rotation (ψ) around the common x axis which points from the Earth towards the Sun. The z axis of the GSE system is the ecliptic pole. The z axis of the GSM system is aligned to the projection of the dipole axis on the YZ plane (green square) of the GSE system.

E.3. Magnetic Apex Coordinates

Magnetic Apex Coordinates (Laundal and Richmond, 2017; VanZandt et al., 1972) are used to describe magnetic field lines. The apex is the point of a field line with the largest altitude. An individual dipole field line is constructed by

$$r(\phi) = A\, R_\oplus \cos^2(\phi) \tag{E.2}$$

from the condition that field lines are co-aligned with the magnetic field (Prölss, 2004, p.216). $A = \dfrac{R_\oplus + h_A}{R_\oplus}$ is the apex radius or shell parameter, h_A is the geometric distance between Earth surface and the apex, and r is the distance between the geocenter and the point on a field line given by the latitude ϕ. See Figure E.2 for an illustration of a field line.

The apex latitude ϕ_A is the intersection of a field line with apex radius A and the surface of Earth. Setting $r(\phi) = R_\oplus$ and solving Equation E.2 for ϕ yields

$$\begin{aligned} R_\oplus &= AR_\oplus \cos^2(\phi_A) && \\ & && \Big\downarrow \text{ eliminate } R_\oplus \\ 1 &= A\cos^2(\phi_A) && \\ & && \Big\downarrow \text{ apply square root} \\ 1 &= \sqrt{A}\cos(\phi_A) && \\ & && \Big\downarrow \text{ solve for } \phi_A \\ \phi_A &= \pm \arccos\left(\frac{1}{\sqrt{A}}\right) && \\ & && \Big\downarrow \text{ insert definition of } A \\ &= \pm \arccos\left(\sqrt{\frac{R_\oplus}{R_\oplus + h_A}}\right) && \end{aligned} \tag{E.3}$$

The first coordinate of magnetic apex coordinates is either the apex radius or the apex latitude. It specifies an apex shell. The second coordinate is the apex longitude specifying a single field

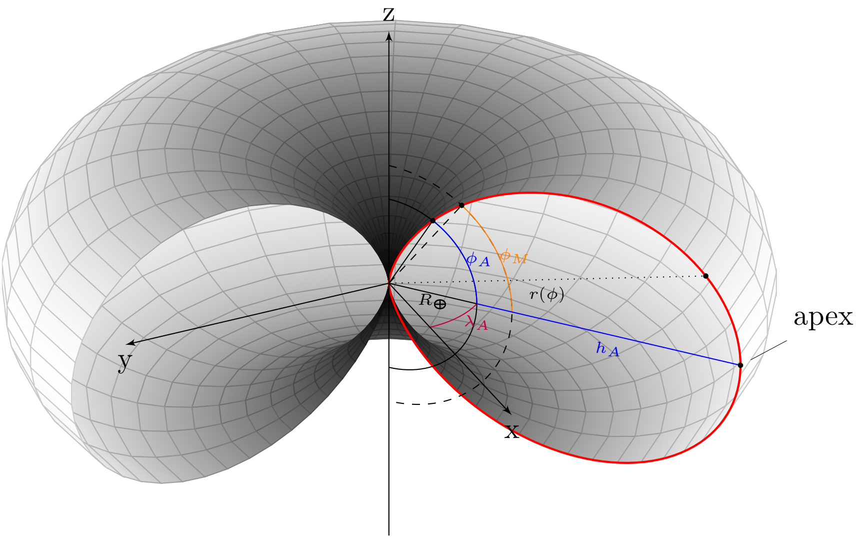

Figure E.2.: The apex shell is defined by the apex height h_A or apex latitude ϕ_A. A single field line (red line) is defined by the apex longitude λ_A. The third coordinate is the height above the reference surface, which is indicated by the color map. This definition is ambiguous because there are two points of the same height for each field line. To solve this, the sign of ϕ_A is used: a positive value indicates a point above the magnetic equator, a negative one below.

line. The third coordinate is the height above Earth's surface. Instructions on how to transform geographic coordinates to apex coordinates are found in (VanZandt et al., 1972).

Modified apex coordinates (Richmond, 1995) define the apex latitude not on Earth's surface, but on a reference surface with altitude h_R above Earth (dashed half circle in Figure E.2)

$$\phi_M = \pm \arccos\left(\sqrt{\frac{R_\oplus^{eq} + h_R}{R_\oplus^{eq} + h_A}}\right) \tag{E.4}$$

This is useful since only field lines that intersect with the reference surface are defined. Field lines below this surface are not represented by modified apex coordinates (see Figure E.3). This facilitates looping over all latitudes in models that are not extended to the ground as the TIE-GCM.

Ignoring that apex and modified apex coordinates use different Earth radii, one can directly transform them into each other via

$$\phi_M = \pm \arccos\left(\sqrt{\frac{1}{A}\frac{R_\oplus + h_R}{R_\oplus}}\right). \tag{E.5}$$

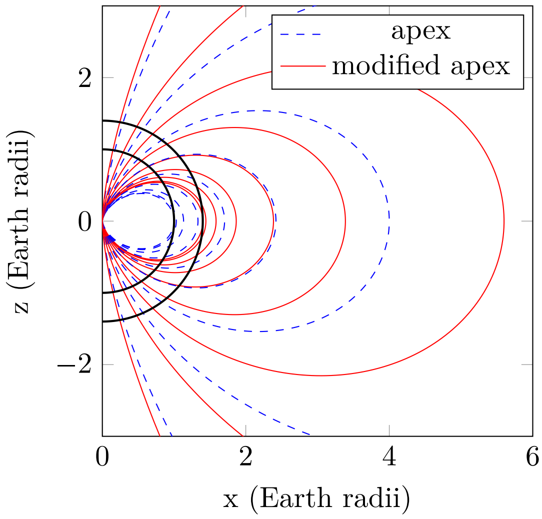

Figure E.3.: Field lines associated with apex and modified apex latitudes in the interval $0°, 10°, \ldots, 80°$. For this illustration, the ratio $\frac{R_\oplus + h_R}{R_\oplus} = 1.4$ is used. Modified apex coordinates represent only field lines extending beyond the reference surface, while apex coordinates represent all field lines above Earth's surface.

Back cover picture: Eight ensemble members of a TIE-GCM 2.0 5° open loop simulation are visualized by mapping the mass density at pressure levels 25, 20, and 15 using the waterman butterfly projection.